Multiconfigurational Simulations of X-ray Absorption Spectroscopy: Insights into Actinyl Covalency

Kurtis Stanistreet-Welsh

Department of Chemistry

Lancaster University

A thesis submitted for the degree of

Doctor of Philosophy

December, 2024

Multiconfigurational Simulations of X-ray Absorption Spectroscopy: Insights into Actinyl Covalency

Kurtis Stanistreet-Welsh.

Department of Chemistry, Lancaster University

A thesis submitted for the degree of *Doctor of Philosophy*. December, 2024.

Abstract

Multiconfigurational Restricted Active Space Self-Consistent Field (RASSCF) theory calculations are employed to simulate oxygen K-edge and actinide $M_{4/5}$-edge XANES spectra of the actinyls from uranyl to plutonyl. Both XANES techniques are routinely used to determine ground-state (GS) covalency in actinide systems, but relies on the assumption that ground- and probed core-excited state (CES) bonding orbitals do not undergo substantial orbital relaxation. This assumption is addressed in each stage of the thesis through a combination of Quantum Theory of Atoms in Molecules (QTAIM) and orbital composition analysis. The influence of actinyl model on the accuracy of simulated spectra and orbital relaxation, is investigated for uranyl O K-edge XANES (chapter 3). The ability of the RASSCF methodology to manage systems with unpaired electrons was investigated through simulations of actinyl(VI) O K-edge and An $M_{4/5}$-edge spectra (chapter 4). Finally, the ability of RASSCF simulations to correctly capture the shift behavior of An $M_{4/5}$-edge spectra due to a change in oxidation state was investigated through simulations of actinyls in both the +6 and +5 oxidation states. Further investigation sought to establish a relationship between the energy separation of An $M_{4/5}$-edge peaks and axial covalency. Changes in bonding orbitals between the GS and CESs in each chapter are quantified and rationalized in the context of QTAIM analysis. The RASSCF methodology detailed in this thesis lays the foundation for future actinide XANES studies or adaption to other types of spectroscopy that access the core-state. The results of this thesis represent a notable contribution to the field, with the O K-edge simulations being the first such RASSCF simulations of this edge to be reported for

the actinides. Similarly, the final results chapter demonstrates the ability of RASSCF simulations to capture the correct shift behavior for the actinides due to a change in oxidation state for the first time.

Declaration

I, Kurtis Stanistreet-Welsh confirm that the work presented in this thesis is my own work, and has not been submitted for the award of a higher degree elsewhere. Where information has been derived from other sources, I confirm that this has been indicated in the thesis.

Kurtis Stanistreet-Welsh

Publications

Published:

This thesis is based upon the following publications, which form the basis of chapters 3 and 4:

1. Bounding [AnO2]2+ (An = U, Np) covalency by simulated O K-edge and An M-edge X-ray absorption near-edge spectroscopy

   K. Stanistreet-Welsh and A. Kerridge, Phys. Chem. Chem. Phys., 2023, 25, 23753-23760, DOI: 10.1039/d3cp03149g

2. Quantifying Covalency and Environmental Effects in RASSCF-Simulated O K-Edge XANES of Uranyl

   K. Stanistreet-Welsh and A. Kerridge, Inorganic Chemistry, 2024, 63, 15115–15126, DOI: 10.1021/acs.inorgchem.4c02144

In Preparation:

This work is under preparation and forms the basis of chapter 5.

1. Probing covalency in RASSCF An $M_{4/5}$-edge XANES simulations of actinyls in different oxidation states

   K. Stanistreet-Welsh and A. Kerridge, Inorganic Chemistry, 2025

Work not included in this thesis:

1. Structure of Uranium(V) Methyl and Uranium(IV) Ylide Complexes

   P. Rungthanaphatsophon, **K. Stanistreet-Welsh**, R. J. Ward, S. P. Kelley, W. W. Lukens, A. Kerridge and J. R. Walensky, Organometallics, 2023, 42, 1404–1410, DOI: 10.1021/acs.organomet.3c00040

Acknowledgements

First, my gratitude goes to the many staff members of Lancaster University Chemistry Department for all their help in many different matters across the years, in both my time as an undergraduate and throughout my postgraduate studies. In particular, I'd like to acknowledge the researchers in theoretical chemistry who in their courses or through my participation in their research projects, inspired me to keep perusing my interests in computational chemistry. I'd also like to thank the department for all the many opportunities that were given to me, especially the chance to participate in teaching and other roles.

I'd also like to thank my close friends and family for their constant support as I undertook my postgraduate studies. The breaks from study and research to spend time with you all was invaluable.

Most of all, I'd like to thank my PhD supervisor Dr Andrew Kerridge for both his support and encouragement, as well as his mentorship over the course of my PhD. I thank you for the many opportunities you provided to me, all of which have made me grow as a scientist and as a person over these four years. I want to thank you for all the time you gave me and especially thank you for your patience and trust. The freedom you gave me to explore all the avenues I found interesting over my PhD has made this one of the most rewarding experiences thus far in my journey through science.

Finally, I'd like to thank my parents, without whose constant support and sacrifice none of this would have been possible. Thank you for your unwavering belief in me and for continually supporting my aspiration to be a scientist.

Contents

List of Tables

List of Figures

Chapter 1

Introduction

In this chapter, an overview of the current understanding of actinide covalency is discussed, with particular focus on actinyl covalency and the influence of oxidation state on the stability of actinyl systems. The importance of fundamental research into actinide covalency is discussed in the context of solving challenges in the management of spent nuclear fuels. X-ray absorption near-edge spectroscopy (XANES) is introduced as a useful tool for probing actinide covalency as well as for determining oxidation state. The key literature studies that pair XANES and theoretical simulations are outlined, covering the main actinide systems of interest and exploring the features of XANES spectra that contain useful covalency and oxidation state information. While most of the relevant literature is discussed in this chapter, additional studies and details are covered in the opening sections of the results chapters. This chapter finishes by outlining the structure and main areas of focus for this thesis.

1.1 Actinide Electronic Structure

Developing a fundamental knowledge of the actinide electronic structure and the nature of their bonding is key to the future developments of applications in a number of areas beneficial to society: from energy generation,[1–3] to chemical processes,[4–7] catalysis,[8–12] nuclear medicine[13–15] magnets,[16–18] and aspects of national security.[19, 20] With countries around the world aiming to de-carbonise energy production substantially by 2050, demand for nuclear energy is set to triple in the coming decades as governments

make nuclear power part of their official road maps for net-zero.[21–23] Therefore, this introduction highlights the particular role foundational research in actinide electronic structure can have on improving strategies for managing spent nuclear fuels at the back end of the nuclear fuel cycle and ultimately improves the prospects of using this energy source over fossil fuels.[24, 25]

1.1.1 Managing Spent-Fuels

The impact of actinides on our modern societies is substantial when considering their role in electricity generation alone, with the actinide dioxides, predominantly UO_2, being the most widely used nuclear fuels.[26, 27] Nuclear power is one of the most viable, clean and promising alternatives to fossil fuel intensive electricity generation but further research is required in order to provide solutions to some of the drawbacks that come with this power generation approach. Challenges remain around the best strategies for both the short and long term storage of spent nuclear fuels, which also brings concerns around the risks of environmental contamination by radionuclides either due to containment failure in storage or in the worst case scenario of a reactor meltdown.[28–30] These problems have sparked research into nuclear waste management through the separation and reprocessing of spent nuclear fuels[27, 31–34] strategies for safe disposal and long term storage,[35, 36] and the development of remediation approaches for cleaning contaminated sites.[37–40]

Research into actinide bonding is key for making progress in the areas outlined above. For instance, efficient, safe and economically viable ways of utilizing spent nuclear fuels is still under investigation and a key area that requires more fundamental research.[41–45] Spent fuel contains a significant number of radionuclides, which include minor actinides, making it a long term radiation hazard. Spent fuel contains ^{235}U, ^{239}Pu, some minor actinides (Np, Am, Cm) and their fission products (^{90}Sr, ^{137}Cr, ^{99}Tc).[41, 46, 47] To reduce the radiation hazard of spent nuclear fuel, long-lived alpha emitting minor actinides are converted into more stable elements by partitioning and transmutation processes.[27, 46, 48–50] The separation and reprocessing of spent fuels relies on knowledge of actinide-ligand bonding to design more efficient and highly selective ligands that are capable of separating the minor-actinide from the lanthanides in spent fuels and waste.[32, 33, 51, 52] These highly selective and stable ligands which target actinides, also hold promise medical

applications in nuclear medicine.[13–15]

An understanding of actinide oxidation state is also crucial for areas of application, since it directly influences electronic structure, thus determining both the physical and chemical bonding characteristics.[53–57] Understanding the properties of actinides in various oxidation states is key for the development of strategies for treating nuclear waste. For example, knowing the oxidation state is key for developing new containers for nuclear waste to reside within.[58–63] Research is crucial in this regard since for example the oxidation of UO_2 is associated with a large volume expansion, which is capable of rupturing confinement barriers.[58] Understanding the interaction of spent fuel with the confinement materials is also crucial for ensuring safe long-terms storage. High level nuclear waste with low Pu content is typically generated from the reprocessing of spent fuels and confined within borosilicate glass matrices.[61, 62, 64, 65] However, formation of separate phases distributed across the glass can cause a combination of swelling and/or poor leeching performance in the case of ground-water intrusion.[66, 67] The Pu oxidation state is found to influence its solubility through the glass matrices and is therefore a key variable to control when manufacturing glass materials for confinement.[68, 69]

In the worst-case scenarios of containment failure and nuclear waste enters the environment, the mobility of actinide species through the aqueous environment of the natural world is highly dependent on the oxidation state.[50, 57, 70, 71] Strategies to immobilise actinides in contaminated sites therefore relies on fundamental knowledge of actinide behaviour in various oxidation states.[72, 73] In general, higher oxidation states tend to be more soluble in aqueous environments,[59, 60, 74] and therefore immobilisation strategies can target the reduction of An(VI) compounds to An(IV), since the latter are less soluble.[50, 70, 71, 75, 76] For instance, in U(VI) in contaminated sites, uranium species are soluble and mobile raising the potential for contamination to spread,[75] therefore, immobilisation strategies can target the redox properties to convert uranium to its U(IV) form. This can be achieved practically in a number of ways such as using microorganisms,[76, 77] or by exploiting iron oxide-rich materials which act as U sinks.[75, 78, 79]

1.1.2 Defining Covalency

Covalency is a fundamental concept for rationalising chemical bonding in systems, but despite its usefulness, no formal definition exists. One theoretical framework in which to view covalency is within perturbation theory as a deviation from the ionic limit.[53, 80, 81] At the ionic limit, metal-ligand bonding is purely Coulombic with no orbital mixing. Deviations from the ionic limit involve some degree of metal-ligand orbital mixing and represents a covalent contribution. In metal-ligand systems, the mixing of metal ϕ_M and ligand ϕ_L atomic orbitals generates hybridised bonding ψ_{ML} and anti-bonding molecular orbitals ψ^*_{ML} as shown in fig. 1.1. The bonding orbital ψ_{ML} can be expressed within

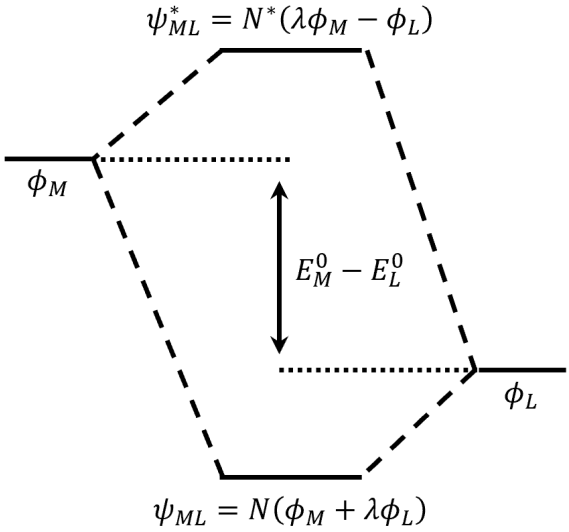

Figure 1.1: Qualitative orbital energy diagram showing relative energies of metal (ϕ_M) and ligand (ϕ_L) atomic orbitals as well as the bonding (ψ_{ML}) and anti-bonding (ψ^*_{ML}) molecular orbitals.

perturbation theory at first order as follows,

$$\psi_{\mathrm{ML}} = N(\phi_M + \lambda\phi_L) = \frac{\phi_{\mathrm{M}} + \lambda\phi_{\mathrm{L}}}{\sqrt{1 + 2\lambda S_{\mathrm{ML}} + \lambda^2}} \tag{1.1}$$

where S_{ML} is the overlap integral and the mixing coefficient λ is a measure of covalent character, defined to first order as,

$$\lambda = \frac{H_{\mathrm{ML}}}{\Delta E_{\mathrm{ML}}} \propto \frac{-S_{ML}}{E^0_M - E^0_L} \tag{1.2}$$

The off-diagonal Hamiltonian matrix element H_{ML} between the two orbitals is approximately proportional to the overlap between the two orbitals, while ΔE_{ML} is the energy difference between them.[53, 82] Any non-zero value of λ is a deviation from the ionic limit and indicates a covalent component to the metal-ligand bonding in the original sense of Heitler and London.[83] The limit $\lambda = 1$, is characteristic of homonuclear diatomics such as H_2 at the bond equilibrium. The mixing coefficient as defined in eq. (1.2) reveals two mechanisms by which covalent interactions may manifest: (1) either through spatial overlap of orbitals and/or (2) near degeneracy of orbital energy levels. Therefore, covalent interactions are maximised by large values of H_{ML}, corresponding to orbital overlap-driven covalency, and/or through better energy match between orbital energies as expressed by ΔE_{ML}, which corresponds to energy degeneracy driven covalency.[53, 80, 83] The energy associated with the covalent mixing can also be derived, in this case from the second-order correction to the energy,

$$\Delta E = \frac{|H_{ML}|^2}{\Delta E_{ML}} = \lambda H_{ML} \tag{1.3}$$

The bond stabilisation ΔE is dependent on the magnitude of the Hamiltonian matrix element H_{ML}, which is proportional to the orbital overlap S_{ML}, and makes clear that overlap driven covalency has the greatest impact on the bond energy.[53] Furthermore, two bonds with the same orbital mixing coefficient, λ, can have different covalent contributions to the bond energy since the magnitude of the Hamiltonian matrix element can differ for the two bonds.[53] Additional details on the derivation of the outlined expressions can be found in the relevant perturbation molecular orbital theory literature.[84, 85]

1.1.3 Actinide Covalency

While covalency in the d-block, that of the transitions metals, is commonplace, the nature of bonding in the f-elements, that of the actinides and lanthanides, is still debated.[81, 86–89] The lanthanides are considered to bond largely through ionic interactions,[86, 90] although this is not universal, and examples of covalent systems are known.[86, 90, 91] Some of the first evidence that actinides might engage in covalency with ligands dates back to the 1950s when Seaborg and co-workers rationalised findings for americium on an ion-exchange resin as evidence for covalent mixing between the An(5f) and Cl(3p) orbitals.[92,

93] Following this, the nodal properties of the 5f-orbitals led Streitwieser and co-workers to predict the existence of the actinocenes.[94–96]

Since this time, a large body of work has demonstrated actinide covalency in a number of different systems. The actinides can be considered as having intermediate bonding properties between the transition metals and lanthanides.[89, 97] Some of the most commonly known examples of actinide systems are the actinlys,[98] actinide hexahalides and the actinide sandwhich complexes.[81, 87] While the understanding of actinide covalency has grown over the years, debate still remains as to the specific role of 5f/6d/6p/7s orbitals in bonding, as well as the degree to which the actinide 5f- and 6d-orbitals participate in covalency across the actinide series.[35, 53, 69] Figure 1.2 presents the radial distribution functions for atomic orbitals known to participate in actinide bonding.

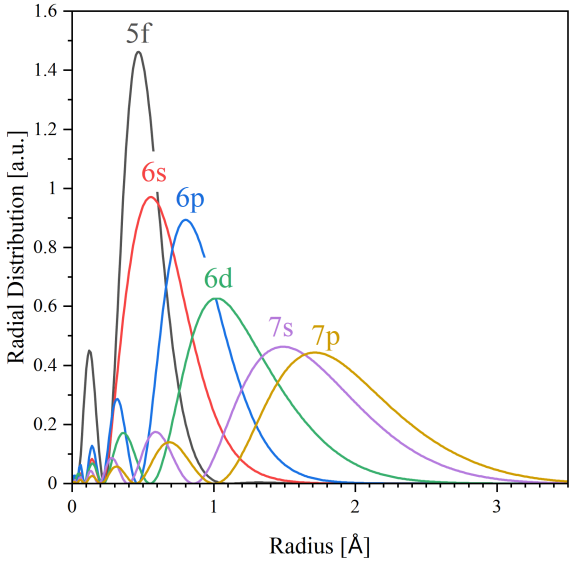

Figure 1.2: Radial distribution functions of atomic orbitals that are thought to participate in actinide-bonding. RDF's are plotted for the U^{6+} ion with single electron occupancy. The ground-state of U^{6+} was obtained from a scalar-relativistic CAS(12,14)/ANO-RCC-TZVP (without h-functions) calculation.

Covalent bonding is found to occur largely through orbital mixing of the actinide 6d- and 5f-orbitals with ligand atomic orbitals.[35, 47, 52, 53, 69, 80, 81, 98] These orbitals explain the existence and stability of actinide-ligand multiple bonding,[99–104] actinide-arene

δ-interactions,[105–107]and molecular actinide-metal bonds.[108, 109] Given the known involvement of the 6d- and 5f-orbitals in actinide covalency, the relative contributions to bonding interactions is of high interest to the community.[53, 69, 80, 81, 88, 98]

Early in the actinide series, the 5f and 6d orbitals are near-degenerate, across the series the 5f-orbitals fall lower in energy due to imperfect screening of the increasing effective nuclear charge by successive additional 5f-electrons. The radial extension of the 5f and 6d orbitals also differ as shown in fig. 1.2. The 6d orbitals are more diffuse and radially extended compared with the 5f orbitals, meaning the 6d-orbitals are more accessible for bonding with nearby ligands. [53] The 5f-orbitals are more active in covalency in the early actinyls, but become less involved across the series as the 5f orbitals become less diffuse and more core-like.[69] This contraction of the 5f-orbitals reduces the capability of the 5f orbitals to overlap with ligand orbitals.[53] This tends to lead to more complex chemistry in the lighter actinides akin to that seen in the d-block.[53] Additional orbital interactions are also thought to be important to establish a full picture of actinide bonding, these being the 6s, 6p, 7s, and 7p orbitals, and have been found to directly influence bonding interactions.[54, 69, 80, 110, 111] Figure 1.2 shows the significant radial extension of these orbitals. Of particular interest is the participation of the actinide 6p orbital, since its involvement is thought to enhance the axial bond strength through a 'pushing from below' mechanism.[112, 113] Overall, while studies suggest an increase in orbital mixing across the actinide series, as indicated in eq. (1.3) this does not necessarily come with a strengthening of the actinide-ligand bond.[47, 53, 114, 115]

Understanding the nature of actinide covalency and making improvements to our current theoretical models has been made difficult due to the limited ability to probe d- and f-element electronic structures. The developments in cyclotron technology has led to highly versatile and accurate X-ray absorption techniques, and offers a promising experimental route to directly probing the role of actinide atomic orbitals in covalent bonding. Additional details on covalency trends and electronic structure for actinides is given in a number of reviews.[53, 54, 116, 117]

1.2 The Actinyls

Studies on the actinyls, both theoretical and experimental, have provided crucial and foundational insights into the nature of electronic structure and bonding in the actinides.[54, 113, 118–120] An understanding of actinyl electronic structure is crucial for their application in the nuclear fuel cycle, decontamination of radioactive sites, the prevention of nuclear waste contamination through the environment, as well as the separation and reprocessing of spent nuclear fuels. An increase demand for nuclear energy has spurred interest into tackling the problems associated with nuclear waste. Two main areas of interest have emerged, including research into the reprocessing and recycling of spent nuclear fuel, and into understanding how nuclear waste can be safely stored long-term. [43–46] Understanding the properties of actinyls in different oxidation states, particularly the changes in bonding interactions, is highly relevant for developing solutions to the waste problem. For instance, in the event nuclear material comes into contact with the natural environment, the formation of high oxidation state actinyls is highly likely.[56, 121] The ability of the actinyls to persist and migrate through the environment depends on the oxidation state, which will change the degree to which they interact with various species found in the natural environment. For example, if nuclear material was to enter an aquifer system, the resulting actinyl ions will form complexes with various ionic ligands naturally found within water, each of which will affect the mobility differently.[122] [123] Understanding the covalency of actinyls in these oxidation states is key to the rational development of newly enhanced extractants with ligands capable of selectively binding to the actinyls.[41, 53, 118, 124–126] As such, these systems are of high interest to the community.

Out of all the actinyls, uranyl is of key interest due to its involvement in the uranium-based nuclear fuel cycle and makes an appearance in various stages of the front- and back-end portions of the cycle. The nuclear fuel cycle consists of the various industrial processes required to product electricity from uranium in nuclear power plants.[1, 127] The front-end stages of the cycle before power generation involve the mining, milling, conversion and enrichment.[1, 127, 128] Uranium ore can be obtained via conventional mining in open-pits or underground tunnels, which is then transported to mills to be

crushed and dissolved in acidic or alkaline leaching solutions which contain appropriate oxidising agents to form uranium ore concentrates (UOC) or "yellowcake".[129] Depending on the leaching solution used, yellowcake can contain a variety of uranium compounds alongside the main compound of interest U_3O_8, such as different uranium oxides and uranyl containing compounds including uranyl hydroxide, uranyl sulfate, and uranyl peroxide.[129, 130] An increasing proportion of the worlds uranium is coming from in situ leach (ISL) mining which essentially combines the mining and milling processes together using leaching solutions to dissolve uranium at the deposits and extract the resulting mixture via wells to the surface. In this approach, various uranyl compounds of different types depending on the composition of the leaching solution and surrounding environment can form in the process.[130–132] Uranyl compounds can also appear at this stage if yellowcake is left in storage for long periods of time, with studies showing the formation of uranyl containing metaschoepite and schoepite minerals depending on the storage conditions and timescale.[129] Regardless of the uranium extraction approach to obtain yellowcake, the resulting product sold from the mills is pure U_3O_8.[127, 128] At this stage in the cycle, U_3O_8 is first transformed into UF_6 gas for enrichment and then converted to UO_2 pellets which are manufactured into fuel rods for commercial use.[128, 129] Depending on the process used, hydrolysis of UF_6 to uranyl fluoride UO_2F_2 can arise. This is a useful molecule of note for regulators since UO_2F_2 is rarely encountered outside of nuclear fuel or weapons production, and can leave traces on equipment or within the environment.[129]

Once used in power generation and after some time cooling in water ponds, two options are available for the spent fuel: either it is recycled or directly sent for disposal.[1, 128] Spent fuel consists of 96% U, 1% Pu and 3% other high-level radioactive products, meaning a large portion of usable uranium remains.[1, 127] Recycling of spent fuel is an area of key research interest since it hold promise in making nuclear energy more sustainable by more efficiently utilizing the existing uranium resources.[133, 134] Furthermore, the ability to separate the components of spent fuel could also aid in reducing the radiotoxicity of waste for safer long-term storage. Both potential benefits rely on highly selective and efficient extraction and separation processes,[43–46] and a variety of ligands have been developed to act as potential extractants. [41, 124, 126] [33, 133] [46, 135, 136] [125, 137] Despite

advancements, the PUREX process is the only commercially viable separation process used globally today and works by dissolving the fuel in nitric acid to form uranyl and plutonium ions which are then extracted using TBP (tributyl phosphate) ligands.[**Nash2011**, 1, 125, 127–129, 133, 138–140] The separated uranium and plutonium can then be kept separate for alternative use, combined to form mixed oxide (MOX) fuel for use in specialized reactors or the uranium is recycled back into UO_2 fuel. The other highly radioactive fissle products and minor actinides still require long term storage as waste.[1, 127, 128] Regardless of the strategy undertaken nuclear waste is still inevitable and requires a long term solution for its safe disposal.

International consensus has arrived at the use of deep geological repositories as the best long-term solution to store nuclear waste. Research has focused on understanding how the conditions in these environments may affect the storage of spent nuclear fuel and what potential interactions between species in the environment and the fuel may arise given large enough timescales. Although the spent fuel is protected within specialized encasements, after several thousand years, it is foreseeable that some groundwater will infiltrate the barriers and eventually interact with the spent fuel. In this case, oxidation of spent fuel from U(IV) to U(VI) can occur and the formation of uranyl containing compounds is expected.[1, 36, 141] For example, the formation of uranyl peroxides is highly likely since studies have identified the formation of these compounds due to water radiolysis when waste from the Fukushima and Chernobyl incidents has came into contact with the environment.[36, 142–147]

Overall, the actinyls are important for understanding the fundamental covalency that arises in actinide-ligand systems and their potential to contribute to a range of applications makes them a key system of interest in actinide research.

1.2.1 Molecular Structure and Oxidation State

The actinyls are among the most well studied actinide molecular systems that exhibit covalency and are characterised by short, strong, and col-linear An=O bonds.[53, 54, 57] The linear structure ($D_{\infty h}$) of the actinyls is maintained across the actinide series regardless of the $5f^n$ occupancy.[53, 54, 57] Actinyls in the strictest sense refers to $[An(VI)O_2]^{2+}$ cations, but the name has been widely extended to include both $[AnO_2]^{+}$

and $[AnO_2]^{3+}$ ions as well, and are typically indicated as actinyl(V) and actinyl(VI).[57] The pentavalent actinyls tend to be more prevalent in acidic solutions, while the hexavalent actinyls are present across a wider pH range.[124] For example, americyl(V) is less common and energetically unfavourable compared to americyl(VI),[46, 148] but can nonetheless be stabilised in acidic conditions.[46, 149]

The oxidation state of the actinyls is a key property that influences the characteristics of the systems, and is ultimately linked to the covalency and bonding stability of the actinyl unit.[150] While the actinyl unit is shared across a wide variety of compounds in various oxidation states, the most stable forms under ambient conditions are U(VI), Np(V), Pu(IV) and Am(II), for the early actinides.[57] While the most stable actinyls have been identified for the early actinides (U-Pu), penta- and hexa-valent actinyls for the later actinides from Am to Cf have also been reported.[46, 151] Accessing higher oxidation states for the later actinides is a challenge since past Am, the An(II) and An(III) structures become the most stable, therefore bypassing this relies on careful consideration of both the experimental conditions and ligands utilised to stabilise actinide species.[46, 152] Dau et al.[151] reported the first synthesis of bare Bk(V) and Cf(V) actinyls, followed by Kovacs et al.[153] who reported stable $An(V)O_2(NO_3)_2$ complexes across a number of actinides from Pu, Am, Cm, Bk, and Cf. Additionally, Vasiliu et al.[152] has also reported stable curly(VI) and berkelyl(VI) complexes.

Of all the actinyls, uranyl(VI) is the most studied due to its prevalence as a structural motif in hexavalent coordination chemistry,[53, 54, 57] and due to uranium being one of the few actinides stable and safe enough to explore with experiments in a laboratory. For these reasons, uranyl tends to appear the most in theoretical and experimental studies of the actinyl systems.[100] Uranyl(VI) is considered chemically inert due to the strong covalent U-O bonds,[54] being highly stable in both solution and solid state, and by extension within the natural environment.[54, 70, 80, 120] In contrast, uranyl(V) is much less studied, likely due to its non-trivial synthesis[154, 155] and its instability in aqueous conditions, whereby it disproportionates to uranyl(VI) and uranyl(IV).[36, 54, 150] Despite the the relative instability compared to its hexavalent counter-part, uranyl(V) compounds have been identified in nature.[124] Neptunium forms neptunyl(V) as its most stable actinyl, however, neptunium can exist over a range of oxidation states from +3 to +7, and the

neptunyl(VI) system is relatively accessible.[54, 57, 69] Experiments involving plutonium are difficult due to the high radiotoxocity, but plutonyl in the +6 oxidation state has nonetheless been stabilised and investigated in aqueos medium.[124] Actinyls tend to be studied in either aqueous or crystal environments, whereby a variety of ligands can interact to form weak bonds to the actinide centre in the equatorial plane perpendicular to the axial actinyl unit.[53, 54, 57] For example, the dianionic actinyl tetrahailides $[AnO_2X_4]^{2-}$ tend to be popular analytes for spectroscopic and computational studies.[98, 113, 118–120, 156] These crystals can be isolated as large crystals in high yields and are air and moisture stable, making them an ideal system to study with a variety of experiments. Actinlys in aqueous solution form aquo complexes. A number of studies have investigated the electronic structure of actinyl aquo complexes, which present a variety of oxidation states,[56] and can be considered as the prototypical actinide environmental species.[121, 157] Studies have come to a reasonable consensus that actinyl ions form $[AnO_2(H_2O)_5]^{n+}$ penta-aquo complexes in the +5 and +6 oxidation states, particularly at low pH.[56, 157, 158]

1.2.2 Electronic Structure and Bonding

The most important orbitals that contribute to actinyl bonding are present in fig. 1.3,[54] and labelled with respect to the centrosymmetric $D_{\infty h}$ point-group. In this symmetry, the actinide 5f- and 6d-orbitals are orthogonal and restricted from mixing, forming their own unique sets of interactions with the oxygen 2p-orbitals. [53] The MO diagram expresses the interaction of atomic orbitals for a general actinyl system and the energy ordering should be viewed as qualitative and subject to change for specific systems.

Actinide ions posses two primary shells, the 5f and 6d orbitals, which both participate in bonding, forming σ and π bonding interactions with oxygen ligands in the actinyls.[54, 57, 159] The bonding orbitals originating from actinide 5f and oxygen 2p in-phase combinations span $2\pi_u$ and $3\sigma_u$, while bonding orbitals originating from actinide 6d and oxygen 2p in-phase combinations span $1\pi_g$ and $3\sigma_g$.[53, 54] These orbitals contribute to an overall nominal bond order of three.[54] While the order of the anti-bonding orbitals has largely been confirmed from XAS experiments.[54] The relative energy ordering of the bonding orbitals is not obvious,[53, 57] but in terms of contribution to bonding,

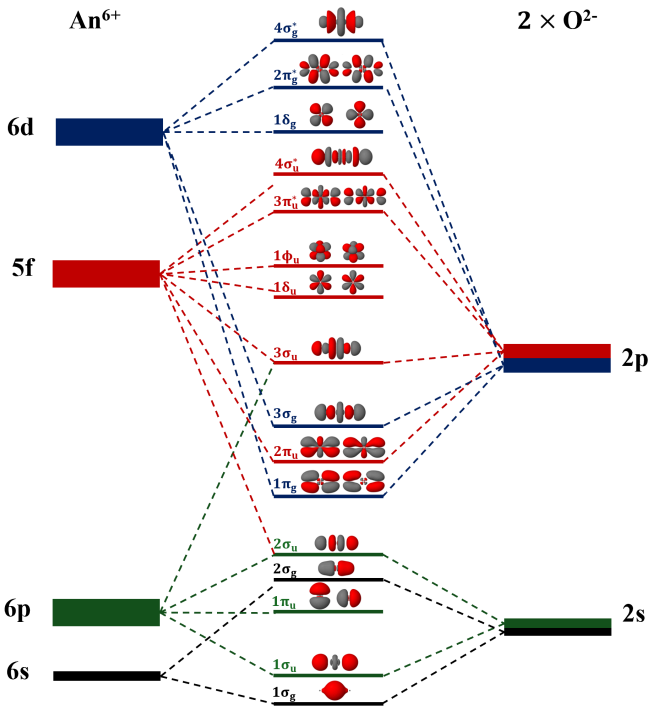

Figure 1.3: Qualatative molecular orbital diagram for a general actinyl system. Diagram is adapted with permission from R. G. Denning, *The Journal of Physical Chemistry A*, 2007, **111**, 4125–4143. Copyright 2024 American Chemical Society.

it is assumed that the σ orbitals contribute greater to the bond strength than the π orbitals. Both experimental and computational studies point to the $3\sigma_u$ orbital being at relatively higher energy than the other bonding orbitals due to a destabilising "pushing from below" mechanism.[53] The "pushing from below" (PFB) mechanism was proposed as an explanation for the higher than expected orbital energy of the $3\sigma_u$ in actinyl systems,[113] and was initially identified in uranyl(VI). At the time the $3\sigma_u$ bonding orbital being the highest occupied molecular orbital (HOMO) was surprising, since a strong covalent σ-interaction resulting from the combination of actinide 5f and oxygen 2p orbitals was expected to a stabilising interaction.[112] The destabilised $3\sigma_u$ HOMO is rationalised through a PFB mechanism, whereby a pseudo-core An 6p-orbital admixes with the otherwise σ_u An(5f)+O(2p) combination. This repulsive filled-filled interaction accounts for the destabilisation of the σ_u orbital pushing it to higher energy relative to the other valence orbitals. This interaction also, somewhat un-intuitively, leads to

greater An(5f) participation due to better orbital energy matching upon destabilisation, and leads to an enhanced axial U-O bond strength.[69, 70, 120, 160] The PFB mechanism was best shown theoretically for uranyl by Kaltsoyannis et al.[113] Here it was shown that the inclusion of U(6p) orbital in valence electronic structure resulted in a significant destabilisation of the $3\sigma_u$ orbital compared to a frozen U(6p) calculation. The orbital composition of the valence orbitals were found to be largely unperturbed by the inclusion of the 6p, while the $3\sigma_u$ orbital had enhanced U(5f) contribution to the bonding. The $1\phi_u$ and $1\delta_u$ orbitals are formally non-bonding 5f orbitals and excluded from mixing with oxygen ligands under $D_{\infty h}$ symmetry. In uranyl, the $1\delta_u$ orbital is considered to be of lower energy due to spin-orbit coupling, and so is ordered as such in fig. 1.3.[53, 57] Similarly the $1\delta_g$ orbitals are non-bonding 6d orbitals and excluded from mixing with oxygen ligands due to symmetry.

In the ground-state of the early hexavalent actinyls, from U to Pu, all molecular orbitals up to and including the $3\sigma_u$ are doubly occupied by electrons. Moving across the actinyl series, the non-bonding 5f-orbitals are progressively filled with electrons depending on the oxidation state but remain the lowest unoccupied molecular orbitals (LUMOs) in most cases for the actinyls.[53, 54, 57] The ground-state of uranyl(VI) is closed shell up to $3\sigma_u$. In neptunyl(VI), a single additional electron is present, while for plutonyl(VI), two additional electrons are present. These additional electrons are confirmed by a mixture of electron paramagnetic resonance (EPR) and magnetic susceptibility experiments to reside within the non-bonding 5f-orbitals.[57, 161, 162] Across the series, this gives ground-states of $^1\sum^+_{0+g}$, $^2\Phi_{5/2u}$, and $^3H_{4g}$ for uranyl, neptunyl and plutonyl, respectively.[57] EPR experiments reveal additional details about the electronic configurations of the ground-states, identifying a $1\phi^1_u$ and $1\phi^1_u 1\delta^1_u$ electronic ground-state configuration for neptunyl and plutonyl, respectively.

1.3 X-ray Absorption Spectroscopy (XAS)

X-ray absorption spectroscopy (XAS) involves measuring, directly or indirectly, the absorption of X-ray photons by a system as a function of the incident energy. XAS is a highly versatile tool, capable of measuring spectra for virtually all the elements of the periodic table, and can be applied to all three of the standard phases. For actinide-ligand

systems, XAS can be view from the perspective of the metal or ligand by tuning the energy of the incident X-rays to induce core-excitations from either the metal or ligand atom at the appropriate energy scale for the atom of interest.[163, 164]

The development of new synchrotrons and improvement in technology means the vast majority of XAS experiments are preformed in these such facilities, which offer high intensity X-rays over a range of energy scales.[163, 164] Access to these facilities is limited and highly competitive, which has prompted the development of some in-house laboratory scale X-ray sources to perform more routine experiments.[163] Regardless of the X-ray source, all XAS measurements fundamentally involve the absorption of an X-ray photon by an element within a sample, leading to the excitation of a core-electron and the generation of a short-lived core-hole state. Once formed, the collapse of the core-hole state occurs via a system relax through either X-ray fluorescence or Auger processes, both of which enable an indirect measurement of the absorption by application of the Beer law. The absorption can also be obtained directly by measuring the number of photons transmitted through the sample.[165] Convectional XAS leads to peaks in the spectra which are dependent on the lifetime of the core-hole, which tends to give broad peaks.[50] Other techniques exists to improve peak resolution such as high energy resolution fluorescence detected spectroscopy (HERFDS), which obtains the XAS spectrum by tuning the detector to measure a specific single and dominant emission/decay process. Another technique involves measuring absorption in combination with X-ray emission spectroscopy (XES) over a range of energies, typically referred to as resonant inelastic X-ray scattering (RIXS). Both of these techniques involve an emission process into a final state and the peak broadening no longer depends on the core-hole state, but rather the final valence states. In these states, the valence hole lifetime broadening is much smaller and results in higher resolution peaks.[50, 66, 69, 165, 166]

1.4 X-ray Absorption Near-Edge Spectroscopy (XANES)

Figure 1.4 presents a general qualitative XAS spectrum split into different regions and an energy level diagram showing K- and M-edge core-excitations.

The XAS spectrum contains two main regions either side of the absorption edge, the pre-edge and post-edge regions. The pre-edge region is targeted by X-ray absorption near-

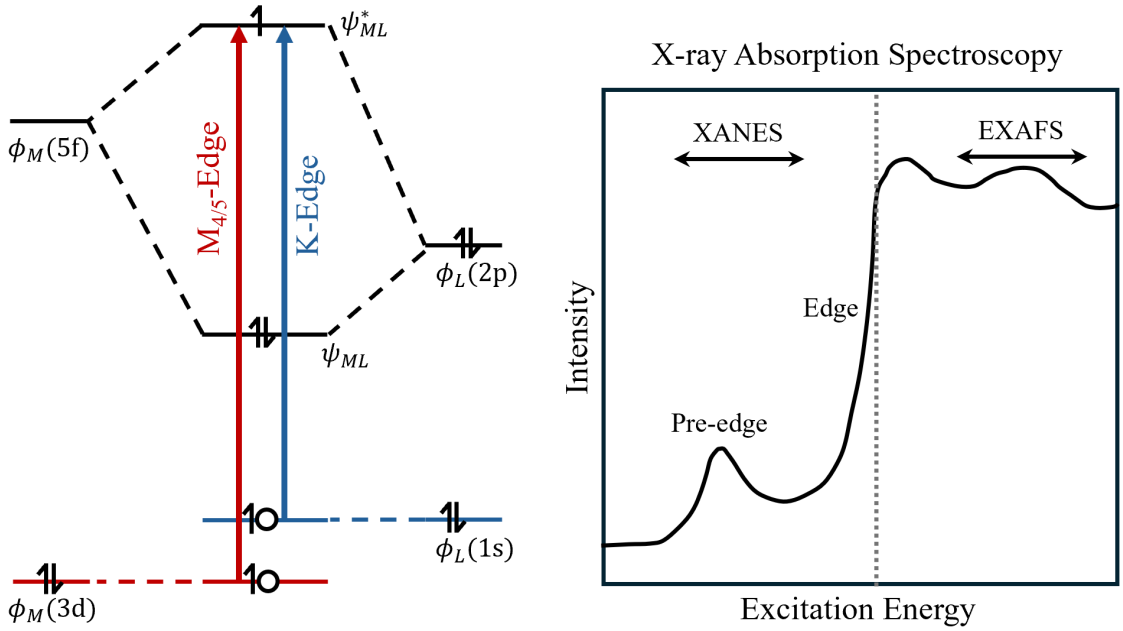

Figure 1.4: Energy diagram (left) showing the core-excitation processes for the two main XANES edges covered in this thesis. A qualitative plot (right) of an XAS spectrum and its splitting into XANES and EXAFS regions. Pre-edge features are generated by core-excitation processes shown in the energy diagram.

edge spectroscopy (XANES) which contains pre-edge peaks corresponding to excitations from core-orbitals on the absorbing atom into empty valence orbitals of the system. The sudden absorption edge corresponds to the ionisation energy of the core-electron and the type of transition is labelled K-, L- or M-edges depending on which shell of the absorbing atoms the ionisation occurs from. The same labelling system is used for XANES, with K-edge spectra generated by core-excitations from 1s-orbitals, L-edge spectra from 2s- or 2p-orbitals, and M-edge spectra from 3s-, 3p-, or 3d-orbitals. Additional subscripts are added to specify which atomic orbital in particular is targeted, for instance, excitations from the 3s-, 3p-, and 3d- orbitals are labelled M_1-, $M_{2/3}$-, and $M_{4,5}$-edges, respectively. [165] By applying principals of MO theory the XANES spectra can be interpreted to extract electronic structure information.

From this point and throughout the rest of the thesis, "XANES" will represent a catch-all term, encompassing any experimental technique that results in a spectrum that targets the pre-edge region of the XAS spectrum. The post-edge oscillating region of

the XAS spectrum corresponds to the interference effects of a propagating core-electron wave with electrons on neighbouring atoms. Spectroscopy targeting the post-edge region corresponds to extended X-ray absorption fine structure (EXAFS) spectroscopy and is useful in geometry identification.[165]

1.4.1 Accuracy of XANES Measurements

Progress in the development of synchrotrons and beamline technology over recent years has progressed XAS experiments to exceptional accuracy,[167] but errors due to uncertainty inevitably still exists. Uncertainty in measured XAS energies can come from both intrinsic and extrinsic factors. In XAS experiments, the generated core-excited states have a limited lifetime due to the instability of the generated core-hole which decays quickly on the order of femo-seconds. Due to the Heisenberg uncertainty principle, the limited lifetime of the state due to the core-hole introduces an intrinsic uncertainty in the energyof the state, which manifests as a broadening of the measured spectral features.[168] Extrinsic contributions also exist and originate from the components of XAS experiments which all require an X-ray source, a monochromator and detector. These components of experiment introduce an extrinsic instrumental uncertainty in the energy measurements. Most XAS experiments are performed at synchrotrons which act as the X-ray source and provide a wide range of stable x-ray beams with wide energy ranges. The monochromator enables a particular X-ray energy from the synchrotron to be accessed and re-directed toward the sample. These two aspects of the experiment combined largely determine the resolution of the XAS experiment with both the beamline and the quality/choice of crystals in the monochromator contributing to the energy resolution. This introduces an instrumental broadening to the spectral features in the measured XAS spectrum.[167, 168] Some additional considerations are also important to note when interpreting the energy position of peaks. As mentioned by Vitova et al.[69] and demonstrated within this thesis, peaks within a XANES spectrum do not necessarily correspond to a single well-defined electron transition, instead a peak can be comprised of a multitude of transitions due to multiconfigurational character as well as spin-orbit coupling effects. Additional broadening can also arise from structural changes in the excited states if the particular excitations deviate more from purely vertical transitions. These features of the system and states can

also broaden the peak, introducing ambiguity in being able to determine the exact energy for a particular electronic transition and using these experimental values as benchmarks to compare with simulated spectra. In chapters 3 and 4 of this thesis, simulations are compared to two different types of XAS experiments, and the experimental uncertainty is breifly discussed.

In chapter 3, O K-edge XAS of uranyl reported by Denning et al.[98] was performed on the ID12B beamline of the European synchrotron facility (ESRF) using the Dragon monochromator with excitation energies tuned from 520-580 eV. The XAS was recorded via Fluroescence detection, meaning all emitted photons were recorded in the energy range specified. X-ray monochromators have improved substantially for O K-edge from a 2 eV resolution reported in 1980 to $\tilde{0}$.04 eV resolution for the Dragon monochromator by Chen and Sette.[167, 169, 170] This means with high-quality sources and monochromators that the energy resolution offered by experiment is in principle better than the O K-edge core-hole lifetime broadening which is on the order of $\tilde{0}$.3 eV.[167] Denning discusses the potential sources of spectral broadening in the measured XAS spectrum presented in chapter 3.[98] As discussed, the oxygen 1s core-hole with a $\tilde{3}$fs lifetime contributes $\tilde{0}$.3 eV to the intrinsic spectral broadening. Denning also identifies structural changes in the crystal within the core-excited state due to the generation of a phonon which causes the U-O bond to lengthen (vibrate) and contribute a potential 0.9 eV to the spectral broadening. The extrinsic instrumental broadening was reported to be a total of 0.8 eV. The final FWHM values of the peaks in the XAS spectrum ranges from 1.4 - 2.0 eV and defines the total resolution of the experimental energies.

In chapter 4, An $M_{4/5}$-edge XANES reported by Vitova is utilized as an experimental reference.[69] Here, the energies are taken from XANES spectra which are slices of 3d4d-RIXS maps for the actinyls from uranyl to plutonyl. In this case, the RIXS broadening still depends on the instrumental resolution (beamline and spectrometer) and the core-hole lifetime, but with the addition of the final valence state lifetime since RIXS involves two states in the spectroscopic process. The core-state and valence-state lifetimes are reported by Vitova to be on the order of 3.2 - 3.4 eV and 0.3 - 0.5 eV, respectively, depending on the actinyl in question. The final resolution capable of the experiment was reported to be on the order of 1 - 1.2 eV.

1.4.2 Oxidation State Determination

The energy of the XAS edge can be utilized as an indicator of the oxidation state of the absorbing atom. As the atom gains or loses an electron through redox processes, an oxidation-state shift can be detected in the resulting XAS spectrum, typically shifting 1-2 eV for a unit change in oxidation state.[50, 165] The L_3-edge has been a popular choice for determining oxidation state, but is limited in its spectral resolution due to a large core-hole lifetime broadening.[66, 171, 172] Instead, the $M_{4/5}$-edge has become a popular edge for oxidation state determination, particularly for the actinides, offering high sensitivity (as low as 2% contribution) in a variety of species and high resolution.[69, 72, 75, 150, 166, 173–178]Oxidation state determination using $M_{4/5}$-edge XANES has been demonstrated for uranium,[69, 173, 174, 179, 180] neptunium,[69, 181, 182] and plutonium systems.[66, 69, 72, 175, 183] The high sensitivity even enables oxidation state determination in mixed actinide oxides, which is not easily possible by other spectroscopic techniques.[50, 66, 184] In An $M_{4/5}$-edge XANES, peaks are generated by electric-dipole allowed core-excitations from actinide 3d core-orbitals into the actinide valence 5f-based anti-bonding orbitals (fig. 1.4), with peak intensity driven by the degree of 5f character in the anti-bonding orbital. The energy position of the pre-edge peaks corresponds to the energy difference between the core 3d- and actinide 5f-shell, which upon the gain or loss of an electron to the actinide centre, changes the excitation energy and results in a detectable oxidation-state shift.[50] Oxidation state determination can then be practically performed by comparing the XANES spectrum of the species of interest (and its oxidation-state shift) with well-known reference compounds,[50, 184] as well as theoretical calculations in order to gain more in-depth interpretation.

1.4.3 Probing Actinide-Ligand Covalency

The use of XANES to probe covalency was first pioneered by Hedman, Solomon and colleagues in transitions metal complexes.[185–189] Since then, the approach has been developed and utilised in the study of actinide-ligand covalency and successfully used to study covalency of a variety of different actinide systems.[69, 81, 88, 98, 100, 114, 190, 191] XANES probes covalency by directly measuring the orbital mixing between metal and ligand atomic orbitals, with this information contained directly in the XANES peaks.

Covalency in the context to XANES experiments refers back to section 1.1.2, were orbital mixing is encapsulated in eq. (1.3), derived by considering covalency as a perturbation from the ionic limit in the original sense of Heitler and London.[83]

The ability to extract orbital mixing information from the XANES peaks is best outlined in the work of Hedman and Solomon for ligand K-edge XANES, but the determination can be adapted to other edges.[185, 187, 188, 192] In this section, the determination of orbital mixing in a molecular orbital from a ligand K-edge XANES peak is explained in context to actinide(5f)-ligand(2p) bonding which takes place in the actinyls. The hybridisation of a metal $\phi_M(5f)$ orbital and valence ligand $\phi_L(2p)$ orbital, results in an anti-bonding orbital ψ^*_{ML} defined as,

$$\psi^*_{ML} = (1-\alpha^2)^{1/2}|\phi_M(5f)\rangle - \alpha|\phi_L(2p)\rangle \tag{1.4}$$

where α^2 represents the ligand 2p character contained within a normalised symmetry adapted molecular orbital. Now consider a ligand K-edge core-excitation into the anti-bonding orbital, $1s \rightarrow \psi^*_{ML}$. The electric-dipole intensity of this transition is given by,

$$I\big(\phi_L(1s) \rightarrow \psi^*_{ML}\big) = K|\langle\phi_L(1s)|\mathbf{r}|\psi^*_{ML}\rangle|^2 \tag{1.5}$$

where K is a constant. Substitution of ψ^*_{ML} into the above intensity expression combined with the localised nature of the ligand-1s orbitals, results in the following simplified expression,

$$I\big(\phi_L(1s) \rightarrow \psi^*_{ML}\big) = \alpha^2 K|\langle\phi_L(1s)|\mathbf{r}|\phi_L(2p)\rangle|^2 \tag{1.6}$$

$$= \alpha^2 I\big(\phi_L(1s) \rightarrow \phi_L(2p)\big) \tag{1.7}$$

where $K|\langle\phi_L(1s)|\mathbf{r}|\phi_L(2p)\rangle|^2$ represents the intensity of a pure $\phi_L(1s) \rightarrow \phi_L(2p)$ transition. The final equation therefore indicates that the strength of peaks observed in XANES is simply the intensity of a $1s \rightarrow 2p$ transition weighted by α^2, the covalent character contained in the anti-bonding orbital. For greater details on the exact derivation of the expressions and theoretical background on extracting covalent information from experimental XANES peaks, the reader is directed to a number of useful reviews and studies.[185, 187, 188, 192] Overall, equations 1.4 - 1.7, reveal that the pre-edge peaks

in ligand K-edge XANES are generated by electric-dipole allowed core-excitations from ligand 1s-orbitals into actinide-ligand anti-bonding orbitals, with the peak intensity driven by the p-character in the anti-bonding orbital. Following measurement of peak intensity, orthogonality arguments then allows quantification of ligand p-orbital contribution to the bonding orbitals in the core-excited state.[167, 188, 191–193] Assuming only minimal changes to the bonding orbitals upon core-excitation, the experimentally probed orbital mixing can be considered as representative of the ground-state bonding, and therefore XANES is a probe of GS covalency. Analogous arguments can also be applied to $M_{4/5}$-edge XANES.

In practice, most studies utilizing XANES to probe covalency pair experimental spectra with theoretical simulations, with this combination proving to be successful in revealing insights into actinide-ligand bonding. Accurate simulation of experimental spectra aids in the characterisation of XANES peaks and enables in-depth quantification of covalent interactions and the verification of oxidation state. In the proceeding section, a summary of the key actinide systems investigated by pairing theoretical methods with both ligand K-edge and metal $M_{4/5}$-edge XANES experiments is outlined. This combination relies on the ability of theoretical methods to accurately model transitions from the ground- to core-excited states.

1.5 Pairing Theory & XANES to Probe Actinide Covalency

1.5.1 Density Functional Theory Simulations

The simulation of XANES involves the calculation of core-excited states, and a number of different approaches are available to obtain these states. Approaches that use some aspect of DFT tend to be the most popular choice due to the good overall balance between ease of use, scalability, accuracy and computational cost.[194] Simulating such states in the actinides comes with added complexity, with actinide systems presenting strong electron correlation, pronounced relativistic effects and substantial multiconfigurational character.

One of the most straightforward approaches is to simply use the energy differences between the Kohn-Sham orbitals as an indication of the excitation energy. This was the approach taken by Su et al.[81] for an investigation into the actinide hexachlorides. To

obtain oscillator strengths for a specific core excitation, the transition-dipole approximation between the occupied MO and the virtual MOs can be utilized.[81] Overall, this approach gives both the excitation energy and the transition-dipole strength, which is enough to generate an approximation to the XANES spectrum. The ΔSCF approach is also a simple but effective scheme. Here the difference in total energy between the ground-state and the core-excited states, obtain as non-Aufbau solutions, gives the excitation energy. This approach is usually paired with the use of certain constraints to avoid variational collapse of the core-excited state.[195] The ΔSCF approach was taken by Denning et al.[98] to calculate the core-excitations responsible for peaks in the uranyl O K-edge XAS spectrum. This approach comes with the advantage of capturing the orbital relaxations in the presence of the core-hole which accounts for a large part of the error in other approaches. The disadvantage comes for systems were a large number of core-excitations are possible and the one state at a time approach of ΔSCF can quickly become impractical. The main alternative to the two outlined approaches thus far is to make use of some form of time-dependent DFT (TDDFT). TDDFT comes with the advantage that the excited-states are obtained efficiently in a single calculation.[195–197] However, the bottom-up approach of TDDFT algorithms in standard codes makes the use of pure linear-response TDDFT prohibitively expensive since all the lower energy valence states would be obtained first before the higher energy core-excited states are reached.[195–197] To avoid this, restrictions are implemented on the single excitation space to only include the orbitals of interest, in this case, the core-orbitals and the unoccupied valence orbitals.[194, 195, 198, 199] This restricted excitation window (REW) approach was first introduced by Stener and co-workers,[200] and the details on theory can be found in a number of studies.[194, 195, 199, 200] REW TDDFT enables virtual orbitals to relax and mix in the presence of the core-hole, but such relaxations are excluded for orbitals not included in the accessible excitation space, which include the bonding orbitals. The omission of orbital relaxations accounts for a significant amount of the error in these calculations and motivates the need for large energy shifts to align simulated and experimental spectra. While the shift primarily accounts for the lack of orbital relaxations, it is important to note that regardless of the DFT approach taken to simulate actinides, some shift is likely inevitable, since approximations in the introduction of relativistic effects and errors associated with the

exchange-correlation functional used, will also contribute. Lastly, an alternative approach to using generalised TDDFT approaches is to make use of TDDFT codes specifically designed and implemented for XAS simulations, such as the freely available FDMNES code.[201–203]

1.5.2 Ligand K-edge Case Studies

Ligand K-edge has been used as a tool for exploring the covalency in a number of key actinide systems including: Actinide hexachlorides,[81, 87, 92, 193] actinide oxides,[49, 204–206] actinide sandwich complexes,[97, 114, 190] the actinyls,[98, 100, 125, 198, 207, 208], as well as metallocene dichlorides,[88] and other interesting actinide systems.[87, 89, 209, 210] The majority of experimental ligand K-edge studies are paired with density functional theory calculations, with studies focusing on C,[114, 190] N,[211] O,[49, 98, 125, 167, 198, 204, 206, 210, 212, 213] and Cl[81, 87, 88, 92, 100, 214] K-edges depending on the ligands in question. These studies have lay the foundation of interesting results and strong evidence for actinide 5f and 6d orbital mixing with p-orbitals in various ligands.

The actinide hexachlorides are highly useful complexes to study since the octrahedral symmetry forbids the 5f and 6d orbitals from mixing and therefore the bonding orbitals formed by each can be probed separately.[81] Cl K-edge has proven useful in identifying covalency in these systems with a prominent example being that of $[AmCl_6]^{3-}$. Cross et al.[92] reported the Cl K-edge XANES spectrum of $[AmCl_6]^{3-}$ with direct evidence of both Am 5f- and 6d-orbitals participating in hybridisation with chlorine 3p ligands. The contributions from the Am 6d-orbitals were found to be greater than those of the 5f, determining a 10% Cl 3p-character per bond using the methods established by Solomon, Hedman, Hodgson and co-workers.[92, 192] In 2012, Minasian et al.[87] presented the Cl K-edge XANES for $[UCl_6]^{2-}$ for the first time. Paired with hybrid TDDFT calculations, results indicated that both the uranium 5f- and 6d-orbitals are involved in bonding interactions, but greater contributions come from the 6d orbitals. This finding was in contradiction to the ground-state DFT calculations which predicted greater 5f participation in bonding. Similar findings have been found in other systems, with Kozimor et al.[88] finding greater 6d orbital participation in bonding than the 5f for thorium and uranium metallocene dichlorides, suggesting that this result could be characteristic of

a variety of actinide systems. Later in 2018, Su et al.[81] published a comprehensive investigation of the early actinide $[AnCl_6]^{2-}$ An=Th, U, Np, Pu, systems using Cl K-edge XANES to quantify the actinide 5f- and 6d-orbital participation in bonding. The study found that 6d-orbitals participate to a greater degree than the 5f-orbitals in covalent bonding, but interestingly found that the 5f participation increased across the actinide series, pointing to increased energy degeneracy driven covalency due to better energy alignment of 5f and ligand p-orbitals. This finding was supported by DFT calculations which found increasing 5f contributions to bonding from Th to Pu alongside the better energy match of Cl(3p) and An(5f) orbitals. This study highlights a particular sensitivity of actinide 5f-orbital bonding to energy degeneracy driven covalency as compared with actinide 6d-orbital bonding. Although DFT simulations reported in the studies outlined are able to predict key features of Cl K-edge XANES in most cases, they require a substantially large 64 eV energy shift to align the predicted spectrum with experiment, with the shift accounting for the omission of orbital relaxation effects, and errors associated with relativistic stabilisation and the exchange-correlation functional.[87, 88]

Bonding in actinide sandwhich complexes have also been of interest to the community.[114, 190] In 2013, Minasian et al.[114] used C K-edge XANES to probe actinide-carbon mixing in thorocene and uranocene. Carbon K-edge XANES provided experimental evidence of both 5f- and 6d-orbital mixing in the bonding between the actinide centres and COT ligands. Both the experimental and theoretical results indicate an increase in 5f-δ bonding between actinides and ligands from Th to U as the 5f-orbitals decreased in energy. The C K-edge and TDDFT results also suggested evidence for ϕ-type bonding in thorocene for the first time. [114] This result was interesting since 5f-orbital mixing was thought to increase with the later actinides, but the ϕ-orbital bonding in thorium provided an unusual case where mixing is greatest for the earlier actinide. Later in 2020, ab initio multiconfigurational simulations reported by Ganguly et al.[97] showed that ϕ-bonding is only present in the core-excited state, hence its appearance as a feature in the XANES spectrum, but its does not occur within the ground-state of either system. Qiao et al in 2021[190] utilized a combination of DFT and ab initio multiconfigurational calculations to report uranium 5f-δ bonding in the $[U(C_7H_7)_2]^-$ system. Similar to the actinocenes, ϕ-bonding was identified in the core-excited state

only. Compared to uranocene, the $[U(C_7H_7)_2]^-$ system presented stronger δ-covalency. No concrete explanation was offered for this observation, but it was hypothesised that better energy match between 5f and ligand orbitals could occur as the 5f-orbitals decrease in energy with the increasing oxidation state from uranocene to $[U(C_7H_7)_2]^-$.[190] The prediction of ϕ-bonding by DFT approaches in the ground-state of thorocene, which was later shown by multiconfigurational calculations not to be the case, highlights the care that must be taken in taking simulated results at face value. In all studies reported here for carbon K-edge simulations, DFT calculations required a shift in the region of 10-20 eV to align simulation with experiment.[114, 190]

In 2002, Denning et al.[98] published polarised O K-edge XAS for uranyl in a $Cs_2UO_2Cl_4$ crystal for the first time to distinguish between σ and π-bonding interactions. Paired with DFT calculations, the study confirmed uranium 5f- and 6d-orbital participation in actinyl bonding and provided some of the first experimental evidence for the involvement the U 6p pseudo-core orbital in σ_u bonding.[69, 98, 167] Since then, studies have used oxygen, nitrogen and chlorine K-edge XANES to investigate various aspects of uranyl covalency and in particular its bonding to a variety of equatorial ligands.[100, 167, 198, 211] Fillaux et al.[198] has examined the effect of two different equatorial ligand environments on the covalency of the uranyl bonds, observing that electron donating and electron withdrawing groups have measurable effect on XANES features. In particular, it was found that differences in the bonding of cynaide ion and pyrridine ligands to uranyl result in changes to the uranyl anti-bonding orbitals and leads to an additional peak in the system which contains the former ligands. [198] In 2022, Zhang et al.[125] investigated the covalent bonding of monodenate organophospouros TRPO ligands to uranyl. TRPO ligands exhibit exceptional selectively toward uranyl ions, and finds application in the aptly named TRPO process. A combination of O K-edge and DFT simulations point to both 6d and 5f-orbital interactions between ligands and the uranium centre, forming both σ and π-bonding interactions to the uranyl unit. Although the 6d contributions are larger, the limited U 5f-interactions that occur, were found to be sufficiently responsible for the exceptional selectivity of the TRPO ligands for uranyl ions.[125]

Other systems such as the actinide oxidies including UO_2, NpO_2 and PuO_2 have been subject to investigation by a combination of O K-edge XANES and DFT. In all cases,

strong evidence for An 5f- and 6d-orbital hybridisation with oxygen 2p-orbitals is found in the experimental O K-edge XANES spectra.[49, 125, 167, 198, 204–206, 212] Studies on the actinide oxides point to a decreasing 5f-orbital energy relative to 6d across the actinide series from U to Pu, confirming the same orbital behaviour as in other systems such as the actinide hexachlorides. Overall studies involving simulations of O K-edge core-excited states tend to require shifts of 10-20 eV to align theory with experimental excitation energies.

Overall, the studies outlined showcase the usefulness of ligand K-edge for probing actinide-ligand bonding. In all cases, studies indicate the involvement of both actinide 6d- and 5f-orbitals in bonding, with the former tending form stronger interactions with ligands. [81, 87, 88, 92, 125] Studies point to the decrease in 5f-orbital energy across the series which could account for the weaker interaction of the 5f-orbitals with ligands. However, other studies suggest that the decrease in actinide 5f-orbital energy comes along with increased energy degeneracy driven covalency as these orbitals approach the energy of the ligand atomic orbitals.[81, 190]

1.5.3 Actinide $M_{4/5}$-Edge Case Studies

Actinide (An) $M_{4/5}$-edge XANES has been a well established tool for determining oxidation state, however, the technique can also offer information regarding the manifestation of 5f-covalency in actinide systems.[177, 184] Vitova et al.[215] reported polarisation dependent U M_4-edge XANES spectra on the $Cs_2UO_2Cl_4$ crystal. The generated spectra can be considered as good representations of the general characteristics found in U M_4-edge XANES spectra. The spectrum consists of three well resolved and progressively lower intensity peaks from low to high energy, corresponding to core-excitations from core 3d-orbitals into the non-bonding 5f orbitals (peak 1), π_u^* orbitals (peak 2), and σ_u^* orbitals, respectively.[215] The emergence of peaks 2 and 3 themselves, often referred to as charge transfer satellites in the context of An $M_{4/5}$-edge, are evidence of U(5f) and O(2p) hybridisation. Studies to date, appear not to use the intensity of An $M_{4/5}$-edge XANES peaks as a measure of orbital mixing and thus ground-state covalency as is done routinely in ligand K-studies. Instead, due to the characteristic appearance of a highly resolved non-bonding 5f peak in systems, studies have focused on using the relative energy position

of peaks with respect to the non-bonding 5f peak to determine the relative destabilisation of the anti-bonding orbitals. This experimentally determined relative separation of the anti-bonding orbitals is then used to infer information about the energy stabilisation of the bonding orbitals and thus gives insight into the nature of covalency in the actinide system being examined. A number of studies have investigated covalency in systems using An $M_{4/5}$-edge XANES, with focus predominately on the actinyls and actinide oxide systems.[35, 150, 166, 177, 178]

In 2021, Amidani et al.[184] published U M_4-edge XANES spectra for a variety of U(VI) compounds in differing local environments, including the $Cs_2UO_2Cl_4$ uranyl crystal. The study demonstrates the sensitivity of U M_4-edge XANES to changes in U-O bond lengths as a consequence of the local geometry configurations. It was found that the relative separation of the peaks attributed to the non-bonding 5f and σ_u^* orbitals correlated with decreasing U-O bond lengths. As pointed out by Amidani, this relationship between U-O bond length and peak separation is associated with the energy stabilisation/destabilisation of the σ_u^* orbital, which has been identified in uranyl containing compounds and explained by the PFB mechanism. In this mechanism, shorter and stronger axial U-O bonds come with increased An(5f) contribution to the covalency due to the interaction with the actinide pseudo-core 6p-orbital. This results in a destabilisation of both the σ_u and σ_u^* orbitals, manifesting as a larger separation between the final peak associated with the σ_u^* and the first peak associated to the non-bonding 5f orbitals.

Utilizing the energy separation between the non-bonding 5f peak and the σ_u^* peak (σ_u^*-shift), a number of studies have examined changes in covalency due to a change in oxidation state. For example, Zegke et al.[176] examined the covalency differences between a uranyl(V) and uranyl(VI) complex. In this study, the U M_4-edge XANES first confirmed the oxidation states of the two complexes, with the uranyl(V) spectral profile shifted approximately 1 eV lower in energy compared to uranyl(VI). Examining the differences in peak separations between the two complexes confirmed a lower axial covalency in the uranyl(V) complex. A similar finding has also been demonstrated by Vitova et al.[70] using U M_4-edge XANES on uranyl(V/VI) systems, finding lower covalency in uranyl(V). In this study, Vitova also examined a Fe-bound uranyl(V) system which causes a redistribution of electron density from the uranyl bond to the Fe(II) centre, weakening the axial bond

and resulting in a reduced peak separation in the XANES spectrum compared with the unbound uranyl(V) system. Lower covalency in uranyl(V) compared to uranyl(VI) has also been demonstrated by electrochemical experiments.[69]

Reduced covalency due to a change in oxidation state has been demonstrated in other actinyls as well, such as neptunyl(VI) and neptunyl(V), with the latter presenting the smallest σ_u^*-shift and therefore corresponding to weaker axial covalency.[182] A comprehensive investigation of the actinyl(VI) systems in aqueous environment using An $M_{4/5}$-edge XANES was reported by Vitova et al.,[69] enabling an examination of covalency differences between the actinyls from uranyl to plutonyl. With the successive addition of electrons to the 5f shell from uranyl to plutonyl, the resulting Coulombic repulsion between electrons was expected to affect the covalent mixing. In U M_4-edge XANES, three peaks corresponding to the non-bonding 5f orbitals, the π_u^* and σ_u^* orbitals are resolved. In both the Np and Pu M_5-edge XANES, only the σ_u^* peak is resolved from the main non-bonding 5f orbital peak. From uranyl to plutonyl, the bond distances contract suggesting a strengthening of covalency across the series. However, the trend in σ_u^*-shift from the XANES spectra suggested greater covalency in uranyl followed by neptunyl and then plutonyl, which is the opposite trend to that of the bond lengths. While Vitova et al. entertained the idea that the XANES results could suggest that energy degeneracy driven covalency may have greater impact on the chemical bonding across the actinyl series, it was not until the work of Autschbach and co-workers covered in the next section,[207] was this puzzle partially resolved.

1.5.4 Multiconfigurational RASSCF Simulations: A Promising Alternative

The key advantage that DFT based approaches outlined in the previous sections offer is their scalability to a large variety of systems with reasonable computational cost.[194, 216] In the TDDFT approaches, excited states are obtained as a perturbation of the ground-state electron density and can all be obtained within a single calculation set-up. These approaches are largely black-box with user input limited to the selection of the exchange-correlation functional that is to be used in the calculation, making these approaches highly user-friendly. As discussed in section 1.5.1, TDDFT approaches

typically need adapting since there algorithms are implemented as bottom-up approaches, calculating all lower energy valence excited states first before reaching the core-excited states of interest.[195–197] Depending on the system, such TDDFT calculations would be impractical if there exist large numbers of valence states. Instead, REW-TDDFT can be employed whereby the bonding orbitals are frozen such that the core-excited states become the lowest energy excited-state solutions possible for calculation. [194, 195, 199, 200] This constraint means that the bonding orbitals in the core-excited states are not optimized for the presence of the core-hole, introducing a substantial energy error, which as demonstrated in the previous section, requires large energy shifts in order to correct. A promising alternative is to utilize a DFT ΔSCF approach whereby the GS and CESs are individually calculated by constraining the orbital occupations to represent the different possible CESs of the system.[195] This approach accounts for the differential orbital relaxations between states but can quickly become impractical if the number of CESs is high. Regardless of the DFT approach implemented, fundamental limitations of the theory remain. Practical implementations of DFT do not provide a consistent theoretical framework in which different systems are treated, with different choices of exchange-correlation functional changing the quality of the physics being described for the system and thus the nature of the states. Furthermore, DFT remains a single determinant approach limited to describing single electronic configurations.[216] In open-shell systems with degenerate and near-degenerate partially occupied orbitals, like those in neptunyl and plutonyl, single electronic configuration descriptions ultimately fail to capture the possible electron correlation. The key advantage of multiconfigurational approaches such as RASSCF is that they provide a consistent theoretical framework in which to treat systems that exhibit multiconfigurational character by incorporating many determinants to capture electron correlation.[217–220] User input is moved from picking an exchange-correlation functional in DFT to picking the size of the active-space and the constraints set upon it. Since the approach is variational, in-principle the calculation quality can be systematically improved by a combination of increasing the size of the active space and loosening constraints. In the context of XANES simulations, RASSCF calculations enable orbital relaxation in the presence of the core-hole and therefore accounts for the most significant error contribution to predicting the absolute energy of XANES peaks. While

this approach offers advantages over DFT, the main drawback of RASSCF approaches is the high computational cost. Systems with limited symmetry which reduce to C1 point groups mean that smaller calculations performed separately for sets of states belonging to a particular symmetry of higher-order point-groups are now all combined into a single costly calculation to obtain all the states belonging to a single symmetry. This limits the systems that can be simulated to those which tend to be smaller and more symmetrical. Lastly, the cost of calculations increases with the number of electron configurations to be optimised,[52, 216] which puts limitations on the size the active spaces and can therefore rule-out some systems from being considered or limit the quality of the description. Despite the limitations, the next section demonstrates the emergence of a number of applications of RASSCF to successfully simulate XANES for a variety of systems. As computing power improves into the future, the set of possible systems which can be simulated with these methods will likely increase, and therefore contributions made today will set the standard for future research in the future.

1.5.5 Multiconfigurational RASSCF Case Studies

A number of studies have emerged using Restricted Active Space Self-Consistent Field (RASSCF) theory[217–220] calculations to simulate both ligand K-edge and An $M_{4/5}$-edge XANES spectra for a number of actinide systems.[97, 190, 191, 193, 207, 221–223] RAS approaches facilitate the treatment of multiconfigurational states, but crucially, allow for orbital relaxation of orbitals in the presence of the core-hole and excited core-electron. By calculating the ground- and core-excited states separately, orbital relaxation and thus any variation in covalency between the states is captured, and can be quantitatively investigated. With RAS approaches able to capture orbital relaxation, it enables the key assumption in the interpretation of XANES spectra as direct probes of GS covalency to be addressed. The established interpretation assumes that the orbital mixing of the bonding orbitals in the core-excited states are also reflective of the ground-state orbital mixing. For this assumption to be valid, the orbitals in the GS and core-excited state remain similar after core-excitation has occurred. This assumption neglects to consider the impact of the core-hole and excited core-electron on the bonding orbitals, which may undergo substantial orbital relaxation to reflect the differing electronic structures.

In 2018, Autschbach and co-workers introduced the first RASSCF simulation of An $M_{4/5}$-edge XANES for actinyl systems.[207] While RASSCF calculations have been utilised before to simulate XANES in transition metal complexes, the study by Autschbach and co-workers was the first of a number of studies establishing RAS approaches as an effective method of simulating XANES for actinide systems. The RAS An $M_{4/5}$-edge simulations for the actinyls, from uranyl to plutonyl, successfully reproduced the experimental spectra. Vitova et al.[69] highlighted the puzzling finding that the XANES spectra presented larger energy splitting between the main peak attributed to the non-bonding 5f orbitals and the σ_u^* peak (σ_u^*-shift) for uranyl than for neptunyl and plutonyl, an indicator of greater axial An-O covalency in the former over the latter systems. The puzzle comes from the fact that the An-O distances contract from uranyl to plutonyl, suggesting an increased covalency from U to Pu. Vitova et al. hypothesised that the decrease in covalency from uranyl to plutonyl indicated by the XANES σ_u^*-shift could be driven by an increasing energy degeneracy covalency across the actinyl series. The increase in covalency from uranyl to plutonyl as indicated in the reduction of bond lengths was then explained by an increase in energy degeneracy driven covalency.[69] Autschbach and co-workers were able to demonstrate that the actinyl XANES spectra did not reflect the ground-state covalency,[207] which increases from uranyl to plutonyl inline with contracting bond lengths and increasing bond orders, but rather reflected a weakened σ_u covalency in the core-excited state from plutonyl to uranyl. The ability to analyse the GS and CESs separately in RAS simulations was a key component that made solving the puzzle possible. Additional analysis of the bonding orbitals in the GS and CESs found limited orbital relaxation in uranyl, but substantial relaxation for the σ_u orbitals in the CESs of neptunyl and plutonyl. Such relaxations render the measured peak intensities from the XANES spectra unrepresentative of the actual GS orbital mixing, invalidating XANES as a probe of GS covalency in this instance.

Since this first publication, Autschbach and co-workers have to date, demonstrated the ability of RAS approaches to successfully reproduce the experimental XANES spectra for a number of systems and edges including the Cl K-edge of $[AmCl_6]^{3-}$,[207] the An $N_{4/5}$-edge and C K-edges of $An(C_8H_8)_2$ An=Th, U,[97] the C K-edge of $[U(C_7H_7)_2]^-$,[190] and the Cl K-edge of $[AnCl_6]^{2-}$.[193] From the studies performed thus far, substantial

orbital relaxation has been identified between the GS and CESs in An $M_{4/5}$-edge XANES for the actinyls, while limited relaxation is found between states in carbon K-edge of $[U(C_7H_7)_2]^-$ and Cl K-edge of the actinide hexachlorides. As such, the degree to which orbital relaxation effects render XANES an valid/invalid probe of GS covalency is likely to vary depending on the edge and system being investigated. Another consideration is whether the peaks that present themselves in XANES spectra are solely a feature of the CES, or whether they also indicate a feature of the GS. For instance, all the peaks in the Cl K-edge XANES of the actinide hexachlorides can be linked directly to 5f- and 6d-bonding orbitals in the ground-state. This is not the case for thorocene, with Autschbach and co-workers demonstrating that previous work reporting possible ϕ-bonding in the ground-state only occurs in the core-excited state. It was shown that the ϕ-bonding orbitals are accessible for population by the core-electrons, hence its appearance as a feature in the XANES spectrum, but is inaccessible to electrons in the ground-state.

RASSCF simulations outside of the contributions of Autschbach and co-workers is limited. To date, only a handful of other research groups including that of Polly, Kerridge and Li have published works using RASSCF simulations to simulate XANES for actinide systems.[208, 221–223] Polly et al. has simulated uranyl U M_4-edge XANES and further demonstrated the ability of RASSCF simulations to successfully reproduce the 3d4f-RIXS maps of uranyl.[208] While contributions from the Kerridge group make up the work outlined in chapters 3 and 4 of this thesis. Overall, the body of work thus far showcases the potential pitfalls of interpreting XANES in terms of ground-state covalency, and highlights the important contribution RAS-level simulations have and will continue to make in understanding the validity of XANES as a probe of GS covalency.

1.6 Thesis Outline

In this chapter, an overview of the current understanding of actinide covalency was provided and the importance of foundational research into covalency was highlighted through applications in spent nuclear fuel management. Actinide covalency was discussed in context to the actinyl systems, discussing the main orbital contributions to bonding and the influence of oxidation state on actinyl stability. The pairing of XANES and theoretical simulations as an important tool for probing the electronic structure of acinide systems was

introduced. Following this, case studies covering ligand K-edge and actinide $M_{4/5}$-edge for key actinide systems of interest were discussed. The chapter ended by discussing the recent simulations of XANES by multiconfigurational RASSCF methods, which in-part, inspired the research documented in the results chapters of this thesis.

In chapter 2, the theoretical background behind electronic structure methods is outlined. A brief overview of quantum mechanics in the context of molecular systems is presented, followed by a detailed examination of Hartree-Fock theory. Methods for introducing electron correlation are then covered, beginning first with an outline of density functional theory before discussing multiconfigurational wavefunction approaches. Discussions cover RASSCF theory and perturbation theory. The chapter ends by giving a brief overview of how relativstic effects are implemented into the Molcas code used to simulate XANES in this thesis.

There is two main aims for this thesis. The first aim is to establish whether RASSCF approaches can simulate key aspects of both ligand K-edge and actinide $M_{4/5}$-edge XANES spectra, which are amongst the most useful edges for probing actinide covalency. Focus is on whether simulations can accurately predict the absolute and relative position of XANES peaks compared with experiment, and the ability to replicate the main features of the experimental spectral profiles. The thesis also aims to examine whether the models used for actinyl systems affects the quality of the simulated spectrum. The second aim of this thesis is to assess the validity of XANES as a probe of GS covalency. A major assumption for using XANES as a probe of GS covalency is to assume that the bonding orbitals in the GS and the experimentally probed CESs are equivalent. This may not be case, since substantial orbital relaxation can occur as the electronic structure adjusts to the core-hole and excited electron. RASSCF is well suited to test this assumption, since the GS and core-excited states (CESs) are obtained and optimised separately, meaning any changes in orbital composition due to the core-hole can be measured by analysing the two states separately.

Chapter 3 begins by detailing the RAS(SD) methodology which is then adapted for use throughout the thesis to obtain the required spin-free ground- and core-excited states of various spin-multiplicities and state symmetries using RASSCF theory. The O K-edge XANES of uranyl in progressively more representative models of the $Cs_2UO_2Cl_4$ crystal

used in the experiment of Denning et al.[98] are presented. Models include $[UO_2]^{2+}$, $[UO_2Cl_4]^{2-}$ and a $Cs_2UO_2Cl_4$ point-charge model. Assignment of the simulated XANES spectra is discussed in greater depth compared to the other results chapters to ensure that a full account of the assignment process is shown. In chapters 4 and 5, less detail around the overall peak assignments is provided in the interest of avoiding redundancy. The aim of chapter 3 is to examine the degree to which the actinyl model impacts the resulting simulated XANES spectra and covalency analysis of the ground- and core-excited states. The chapter explores the degree to which bonding orbitals in the GS and CESs are similar and whether the conclusions drawn from the analysis change depending on the model examined. Other features are also examined such as the validity of assigning a peak to a single core-excitation or the degree to which a peak can be attributed to the occupation of a particular anti-bonding orbital in the CES.

In chapter 4, $[AnO_2]^{2+}$ models are utilized to simulate the O K-edge XANES spectra across the acctinyl series from uranyl to plutonyl. Here, the adaptability of the RAS(SD) approach to handle an increasing number of unpaired electrons is showcased. Simulations of actinide $M_{4/5}$-edge XANES is also introduced, representing a challenge for simulations since the spin-orbit coupling is more pronounced for the 3d-shell. Capturing the correct splitting due to spin-orbit coupling is a crucial feature for simulations, since it is required to obtain the separate M_4- and M_5-edge spectra for a given system. The differences in bonding orbitals between the GS and CESs due to orbital relaxations is investigated to determine the degree to which K-edge and M-edge XANES are valid probes of GS actinyl covalency. The chapter proposes that the actual ground-state actinide contribution can be bound by the ligand K-edge and actinide M-edge XANES contributions.

In the final results chapter (chapter 5), the An $M_{4/5}$-edge XANES spectra of the actinyls from uranyl to plutonyl in the +6 and +5 oxidation state is simulated. The chapter shows the ability of the RAS(SD) methodology to handle an increased number of unpaired electrons. The ability of the RASSCF approach to capture the correct and expected red-shift of XANES spectra due to a reduction of An(VI) to An(V) in an actinyl system was also examined. The chapter outlines an explanation for the origin of the oxidation-state shift in XANES spectra due to oxidation states by using a combination of state energies and QTAIM analysis. Continuing the investigation from chapter 4, the

degree to which bonding orbitals are similar between the GS and CESs is also assessed for actinyls in both oxidation states. The chapter ends by examining whether the separation of the $5f_{\delta/\phi}$ and 5f-σ_u^* peaks correlates with actinyl axial covalency.

Finally, a summary of the key findings and concluding remarks is included within chapter 6.

References

[1] L. Rodríguez-Penalonga and B. Y. Moratilla Soria, *Energies*, 2017, **10**, DOI: 10.3390/en10081235.

[2] D. A. Andersson, C. R. Stanek, C. Matthews and B. P. Uberuaga, *MRS Bulletin*, 2023, **48**, 1154–1162, DOI: 10.1557/s43577-023-00631-3.

[3] D. Butler, *Nature*, 2004, **429**, 238–240, DOI: https://doi.org/10.1038/429238a.

[4] W. J. Evans and S. A. Kozimor, *Coordination Chemistry Reviews*, 2006, **250**, Actinide Chemistry, 911–935, DOI: https://doi.org/10.1016/j.ccr.2006.01.017.

[5] C. Janiak, *Coordination Chemistry Reviews*, 2006, **250**, Metallocene Complexes as Catalysts for Olefin Polymerization, 66–94, DOI: https://doi.org/10.1016/j.ccr.2005.02.016.

[6] T. J. Marks, in *Progress in Inorganic Chemistry*, John Wiley & Sons, Ltd, 1979, pp. 223–333, DOI: https://doi.org/10.1002/9780470166260.ch4.

[7] H. S. La Pierre and K. Meyer, in *Progress in Inorganic Chemistry Volume 58*, John Wiley & Sons, Ltd, 2014, ch. 5, pp. 303–416, DOI: https://doi.org/10.1002/9781118792797.ch05.

[8] R. J. Batrice, I. S. Karmel, G. Yardeni and M. S. Eisen, in *Encyclopedia of Inorganic and Bioinorganic Chemistry*, American Cancer Society, 2018, pp. 1–23, DOI: https://doi.org/10.1002/9781119951438.eibc2564.

[9] P. L. Arnold, J. M. Purkis, R. Rutkauskaite, D. Kovacs, J. B. Love and J. Austin, *ChemCatChem*, 2019, **11**, 3786–3790, DOI: 10.1002/cctc.201900037.

[10] P. L. Arnold, T. Ochiai, F. Y. T. Lam, R. P. Kelly, M. L. Seymour and L. Maron, *Nature Chemistry*, 2020, **12**, 654–659, DOI: 10.1038/s41557-020-0457-9.

[11] E. Barnea and M. S. Eisen, *Coordination Chemistry Reviews*, 2006, **250**, Actinide Chemistry, 855–899, DOI: https://doi.org/10.1016/j.ccr.2005.12.007.

[12] M. S. Eisen and T. J. Marks, *Journal of Molecular Catalysis*, 1994, **86**, 23–50, DOI: https://doi.org/10.1016/0304-5102(93)E0210-8.

[13] R. Abergel, J. Aris, W. E. Bolch, S. A. Dewji, A. Golden, D. A. Hooper, D. Margot, C. G. Menker, T. Paunesku, D. Schaue and G. E. Woloschak, *International Journal of Radiation Biology*, 2022, **98**, 267–275, DOI: 10.1080/09553002.2022.2027542.

[14] V. Frantellizzi, L. Cosma, G. Brunotti, A. Pani, A. Spanu, S. Nuvoli, F. De Cristofaro, L. Civitelli and G. De Vincentis, *Cancer Biotherapy and Radiopharmaceuticals*, 2020, **35**, 437–445, DOI: 10.1089/cbr.2019.3105.

[15] A. Morgenstern, C. Apostolidis, C. Kratochwil, M. Sathekge, L. Krolicki and F. Bruchertseifer, *Curr Radiopharm*, 2018, **11**, 200–208.

[16] N. Magnani and R. Caciuffo, *Inorganics*, 2018, **6**, DOI: 10.3390/inorganics6010026.

[17] K. R. Meihaus and J. R. Long, *Dalton Transactions*, 2015, **44**, 2517–2528, DOI: 10.1039/C4DT02391A.

[18] S. T. Liddle and J. v. Slageren, in *Lanthanides and Actinides in Molecular Magnetism*, John Wiley & Sons, Ltd, 2015, ch. 10, pp. 315–340, DOI: https://doi.org/10.1002/9783527673476.ch10.

[19] M. B. Chadwick, *Nuclear Technology*, 2021, **207**, iii–viii, DOI: 10.1080/00295450.2021.1903301.

[20] S. K. Hanson and W. J. Oldham, *Nuclear Technology*, 2021, **207**, S295–S308, DOI: 10.1080/00295450.2021.1951538.

[21] D. for Energy Security & Net Zero, *CIVIL NUCLEAR: ROADMAPTO 2050*, 2024, https://www.gov.uk/government/publications/civil-nuclear-roadmap-to-2050 (visited on 09/13/2024).

[22] U. D. of State, *Declaration to Triple Nuclear Energy*, 2023, https://www.state.gov/declaration-to-triple-nuclear-energy/ (visited on 09/13/2024).

[23] E. Directorate-General for Internal Market, Industry and SMEs, *The Net-Zero Industry Act: Accelerating the transition to climate neutrality*, https://single-market-economy.ec.europa.eu/industry/sustainability/net-zero-industry-act_en (visited on 09/13/2024).

[24] G. Choppin, J.-O. Liljenzin, J. Rydberg and C. Ekberg, in *Radiochemistry and Nuclear Chemistry (Fourth Edition)*, ed. G. Choppin, J.-O. Liljenzin, J. Rydberg and C. Ekberg, Academic Press, Oxford, Fourth Edition, 2013, pp. 685–751, DOI: https://doi.org/10.1016/B978-0-12-405897-2.00021-5.

[25] R. Taylor, W. Bodel and G. Butler, *Energies*, 2022, **15**, DOI: 10.3390/en15072472.

[26] J. G. Tobin, S.-W. Yu, R. Qiao, W. L. Yang, C. H. Booth, D. K. Shuh, A. M. Duffin, D. Sokaras, D. Nordlund and T.-C. Weng, *Phys. Rev. B*, 2015, **92**, 045130, DOI: 10.1103/PhysRevB.92.045130.

[27] J. Veliscek-Carolan, *Journal of Hazardous Materials*, 2016, **318**, 266–281, DOI: https://doi.org/10.1016/j.jhazmat.2016.07.027.

[28] B. Szpunar, J. Szpunar, V. Milman and A. Goldberg, *Solid State Sciences*, 2013, **24**, 44–53, DOI: https://doi.org/10.1016/j.solidstatesciences.2013.06.013.

[29] B. Dorado, M. Freyss, B. Amadon, M. Bertolus, G. Jomard and P. Garcia, *Journal of Physics: Condensed Matter*, 2013, **25**, 333201, DOI: 10.1088/0953-8984/25/33/333201.

[30] Y. Yun, O. Eriksson and P. M. Oppeneer, *Journal of Nuclear Materials*, 2009, **385**, 510–516, DOI: https://doi.org/10.1016/j.jnucmat.2008.12.311.

[31] P. J. Panak and A. Geist, *Chemical Reviews*, 2013, **113**, 1199–1236, DOI: 10.1021/cr3003399.

[32] H. H. Dam, D. N. Reinhoudt and W. Verboom, *Chemical Society Reviews*, 2007, **36**, 367–377, DOI: 10.1039/B603847F.

[33] A. Leoncini, J. Huskens and W. Verboom, *Chem. Soc. Rev.*, 2017, **46**, 7229–7273, DOI: 10.1039/C7CS00574A.

[34] F. v. Hippel, R. Ewing, R. Garwin and A. Macfarlane, *Nature*, 2012, **485**, 167–168, DOI: 10.1038/485167a.

[35] P. S. Bagus, B. Schacherl and T. Vitova, *Inorganic Chemistry*, 2021, **60**, 16090–16102, DOI: 10.1021/acs.inorgchem.1c01331.

[36] R. C. Ewing, *Nature Materials*, 2015, **14**, 252–257, DOI: 10.1038/nmat4226.

[37] A. B. Kersting, D. W. Efurd, D. L. Finnegan, D. J. Rokop, D. K. Smith and J. L. Thompson, *Nature*, 1999, **397**, 56–59, DOI: 10.1038/16231.

[38] M. Denecke, N. Bryan, S. Kalmykov, K. Morris and F. Quinto, in *Experimental and Theoretical Approaches to Actinide Chemistry*, John Wiley & Sons, Ltd, 2018, ch. 8, pp. 378–444, DOI: https://doi.org/10.1002/9781119115557.ch8.

[39] K. Ollila, E. Myllykylä, M. Tanhua-Tyrkkö and T. Lavonen, *Journal of Nuclear Materials*, 2013, **442**, 320–325, DOI: https://doi.org/10.1016/j.jnucmat.2013.09.019.

[40] M. Jonsson, F. Nielsen, O. Roth, E. Ekeroth, S. Nilsson and M. M. Hossain, *Environmental Science & Technology*, 2007, **41**, 7087–7093, DOI: 10.1021/es070832y.

[41] M. Duan, P. Li, H. Zhao, F. Xie and J. Ma, *Inorganic Chemistry*, 2019, **58**, 3425–3434, DOI: 10.1021/acs.inorgchem.8b03538.

[42] J. Li, X. Dai, L. Zhu, C. Xu, D. Zhang, M. A. Silver, P. Li, L. Chen, Y. Li, D. Zuo, H. Zhang, C. Xiao, J. Chen, J. Diwu, O. K. Farha, T. E. Albrecht-Schmitt, Z. Chai and S. Wang, *Nature Communications*, 2018, **9**, 3007, DOI: 10.1038/s41467-018-05380-5.

[43] S. Ion, *Chem*, 2016, **1**, 663–665, DOI: https://doi.org/10.1016/j.chempr.2016.10.008.

[44] M. S. Dresselhaus and I. L. Thomas, *Nature*, 2001, **414**, 332–337, DOI: 10.1038/35104599.

[45] R. Taylor, *Chem*, 2016, **1**, 662–663, DOI: https://doi.org/10.1016/j.chempr.2016.10.004.

[46] A. Jennifer G, Y. Gao, G. Schreckenbach and E. Varathan, *Dalton Trans.*, 2022, **51**, 10006–10019, DOI: 10.1039/D2DT01142E.

[47] N. Kaltsoyannis, *Inorganic Chemistry*, 2013, **52**, 3407–3413, DOI: 10.1021/ic3006025.

[48] F. W. Lewis, L. M. Harwood, M. J. Hudson, A. Geist, V. N. Kozhevnikov, P. Distler and J. John, *Chem. Sci.*, 2015, **6**, 4812–4821, DOI: 10.1039/C5SC01328C.

[49] J.-L. Chen, P. Blaha and N. Kaltsoyannis, *The Journal of Physical Chemistry C*, 2023, **127**, 17994–18000, DOI: 10.1021/acs.jpcc.3c03143.

[50] K. O. Kvashnina and S. M. Butorin, *Chem. Commun.*, 2022, **58**, 327–342, DOI: 10.1039/D1CC04851A.

[51] P. J. Panak and A. Geist, *Chemical Reviews*, 2013, **113**, 1199–1236, DOI: 10.1021/cr3003399.

[52] M. P. Jensen and A. H. Bond, *Journal of the American Chemical Society*, 2002, **124**, 9870–9877, DOI: 10.1021/ja0178620.

[53] M. L. Neidig, D. L. Clark and R. L. Martin, *Coordination Chemistry Reviews*, 2013, **257**, 394–406, DOI: 10.1016/j.ccr.2012.04.029.

[54] R. G. Denning, *The Journal of Physical Chemistry A*, 2007, **111**, 4125–4143, DOI: 10.1021/jp071061n.

[55] A. Kovacs, R. J. M. Konings, J. K. Gibson, I. Infante and L. Gagliardi, *Chemical Reviews*, 2015, **115**, 1725–1759, DOI: 10.1021/cr500426s.

[56] P. J. Hay, R. L. Martin and G. Schreckenbach, *The Journal of Physical Chemistry A*, 2000, **104**, 6259–6270, DOI: 10.1021/jp000519h.

[57] S. Matsika and R. M. Pitzer, *The Journal of Physical Chemistry A*, 2000, **104**, 4064–4068, DOI: 10.1021/jp993767q.

[58] R. McEachern and P. Taylor, *Journal of Nuclear Materials*, 1998, **254**, 87–121, DOI: https://doi.org/10.1016/S0022-3115(97)00343-7.

[59] D. Shoesmith, *Journal of Nuclear Materials*, 2000, **282**, 1–31, DOI: https://doi.org/10.1016/S0022-3115(00)00392-5.

[60] D. J. Wronkiewicz, J. K. Bates, S. F. Wolf and E. C. Buck, *Journal of Nuclear Materials*, 1996, **238**, Spent Fuels, 78–95, DOI: https://doi.org/10.1016/S0022-3115(96)00383-2.

[61] C. Jantzen, *Journal of Non-Crystalline Solids*, 1986, **84**, The physics and chemistry of glass and glass making, 215–225, DOI: https://doi.org/10.1016/0022-3093(86)90780-5.

[62] E. Vernaz, S. Gin and C. Veyer, in *Comprehensive Nuclear Materials*, ed. R. J. Konings, Elsevier, Oxford, 2012, pp. 451–483, DOI: https://doi.org/10.1016/B978-0-08-056033-5.00107-5.

[63] P. Chevreux, L. Tissandier, A. Laplace, T. Vitova, S. Bahl, F. L. Guyadec and E. Deloule, *Journal of Nuclear Materials*, 2021, **544**, 152666, DOI: https://doi.org/10.1016/j.jnucmat.2020.152666.

[64] M. Ojovan and W. Lee, in *An Introduction to Nuclear Waste Immobilisation (Second Edition)*, ed. M. Ojovan and W. Lee, Elsevier, Oxford, Second Edition, 2014, pp. 245–282, DOI: https://doi.org/10.1016/B978-0-08-099392-8.00017-6.

[65] C. Kaushik, *Procedia Materials Science*, 2014, **7**, 2nd International Summer School on Nuclear Glass Wasteform: Structure, Properties and Long-Term Behavior, SumGLASS 2013, 16–22, DOI: https://doi.org/10.1016/j.mspro.2014.10.004.

[66] S. Bahl, S. Peuget, I. Pidchenko, T. Pruessmann, J. Rothe, K. Dardenne, J. Delrieu, D. Fellhauer, C. Jégou, H. Geckeis and T. Vitova, *Inorganic Chemistry*, 2017, **56**, 13982–13990, DOI: 10.1021/acs.inorgchem.7b02118.

[67] X. Deschanels, S. Peuget, J. Cachia and T. Charpentier, *Progress in Nuclear Energy*, 2007, **49**, Options for the Long-Term Management of Separated Plutonium, 623–634, DOI: https://doi.org/10.1016/j.pnucene.2007.05.001.

[68] G. Calas, L. Galoisy, L. Cormier, G. Ferlat and G. Lelong, *Procedia Materials Science*, 2014, **7**, 2nd International Summer School on Nuclear Glass Wasteform: Structure, Properties and Long-Term Behavior, SumGLASS 2013, 23–31, DOI: https://doi.org/10.1016/j.mspro.2014.10.005.

[69] T. Vitova, I. Pidchenko, D. Fellhauer, P. S. Bagus, Y. Joly, T. Pruessmann, S. Bahl, E. Gonzalez-Robles, J. Rothe, M. Altmaier, M. A. Denecke and H. Geckeis, *Nature Communications*, 2017, **8**, 16053, DOI: 10.1038/ncomms16053.

[70] T. Vitova, R. Faizova, J. I. Amaro-Estrada, L. Maron, T. Pruessmann, T. Neill, A. Beck, B. Schacherl, F. F. Tirani and M. Mazzanti, *Chem. Sci.*, 2022, **13**, 11038–11047, DOI: 10.1039/D2SC03416F.

[71] V. Vallet, L. Maron, B. Schimmelpfennig, T. Leininger, C. Teichteil, O. Gropen, I. Grenthe and U. Wahlgren, *The Journal of Physical Chemistry A*, 1999, **103**, 9285–9289, DOI: 10.1021/jp991609t.

[72] K. O. Kvashnina, A. Y. Romanchuk, I. Pidchenko, L. Amidani, E. Gerber, A. Trigub, A. Rossberg, S. Weiss, K. Popa, O. Walter, R. Caciuffo, A. C. Scheinost, S. M. Butorin and S. N. Kalmykov, *Angewandte Chemie International Edition*, 2019, **58**, 17558–17562, DOI: https://doi.org/10.1002/anie.201911637.

[73] N. Armaroli and V. Balzani, *Energy Environ. Sci.*, 2011, **4**, 3193–3222, DOI: 10.1039/C1EE01249E.

[74] G. Bernhard, G. Geipel, V. Brendler and H. Nitsche, *Journal of Alloys and Compounds*, 1998, **271-273**, 201–205, DOI: https://doi.org/10.1016/S0925-8388(98)00054-1.

[75] Z. Pan, Y. Roebbert, A. Beck, B. Bartova, T. Vitova, S. Weyer and R. Bernier-Latmani, *Environmental Science & Technology*, 2022, **56**, 1753–1762, DOI: 10.1021/acs.est.1c06865.

[76] M. Molinas, R. Faizova, A. Brown, J. Galanzew, B. Schacherl, B. Bartova, K. L. Meibom, T. Vitova, M. Mazzanti and R. Bernier-Latmani, *Environmental Science & Technology*, 2021, **55**, 4753–4761, DOI: 10.1021/acs.est.0c06633.

[77] D. R. Lovley, E. J. P. Phillips, Y. A. Gorby and E. R. Landa, *Nature*, 1991, **350**, 413–416, DOI: 10.1038/350413a0.

[78] T. Scott, G. Allen, P. Heard and M. Randell, *Geochimica et Cosmochimica Acta*, 2005, **69**, 5639–5646, DOI: https://doi.org/10.1016/j.gca.2005.07.003.

[79] E. J. O'Loughlin, S. D. Kelly, R. E. Cook, R. Csencsits and K. M. Kemner, *Environmental Science & Technology*, 2003, **37**, 721–727, DOI: 10.1021/es0208409.

[80] A. Kerridge, *Chemical Communications*, 2017, **53**, 6685–6695, DOI: 10.1039/C7CC00962C.

[81] J. Su, E. R. Batista, K. S. Boland, S. E. Bone, J. A. Bradley, S. K. Cary, D. L. Clark, S. D. Conradson, A. S. Ditter, N. Kaltsoyannis, J. M. Keith, A. Kerridge, S. A. Kozimor, M. W. Löble, R. L. Martin, S. G. Minasian, V. Mocko, H. S. L. Pierre, G. T. Seidler, D. K. Shuh, M. P. Wilkerson, L. E. Wolfsberg and P. Yang, *Journal of the American Chemical Society*, 2018, **140**, 17977–17984, DOI: 10.1021/jacs.8b09436.

[82] R. Hoffmann, *The Journal of Chemical Physics*, 2004, **39**, 1397–1412, DOI: 10.1063/1.1734456.

[83] W. Heitler and F. London, *Zeitschrift für Physik*, 1927, **44**, 455–472, DOI: 10.1007/BF01397394.

[84] D.-K. Seo, G. Papoian and R. Hoffmann, *International Journal of Quantum Chemistry*, 2000, **77**, 408–420, DOI: https://doi.org/10.1002/(SICI)1097-461X(2000)77:1<408::AID-QUA41>3.0.CO;2-1.

[85] L. Rincón, *Journal of Molecular Structure: THEOCHEM*, 2005, **731**, 213–217, DOI: https://doi.org/10.1016/j.theochem.2005.04.032.

[86] M. W. Löble, J. M. Keith, A. B. Altman, S. C. E. Stieber, E. R. Batista, K. S. Boland, S. D. Conradson, D. L. Clark, J. L. Pacheco, S. A. Kozimor, R. L. Martin, S. G. Minasian, A. C. Olson, B. L. Scott, D. K. Shuh, T. Tyliszczak, M. P. Wilkerson and R. A. Zehnder, *Journal of the American Chemical Society*, 2015, **137**, 2506–2523, DOI: 10.1021/ja510067v.

[87] S. G. Minasian, J. M. Keith, E. R. Batista, K. S. Boland, D. L. Clark, S. D. Conradson, S. A. Kozimor, R. L. Martin, D. E. Schwarz, D. K. Shuh, G. L. Wagner, M. P. Wilkerson, L. E. Wolfsberg and P. Yang, *Journal of the American Chemical Society*, 2012, **134**, 5586–5597, DOI: 10.1021/ja2105015.

[88] S. A. Kozimor, P. Yang, E. R. Batista, K. S. Boland, C. J. Burns, D. L. Clark, S. D. Conradson, R. L. Martin, M. P. Wilkerson and L. E. Wolfsberg, *Journal of the American Chemical Society*, 2009, **131**, 12125–12136, DOI: 10.1021/ja9015759.

[89] T. Dumas, D. Guillaumont, C. Fillaux, A. Scheinost, P. Moisy, S. Petit, D. K. Shuh, T. Tyliszczak and C. D. Auwer, *Physical Chemistry Chemical Physics*, 2016, **18**, 2887–2895, DOI: 10.1039/C5CP05820A.

[90] T. Vitova, P. W. Roesky and S. Dehnen, *Communications Chemistry*, 2022, **5**, 12, DOI: 10.1038/s42004-022-00630-6.

[91] A. B. Altman, J. I. Pacold, J. Wang, W. W. Lukens and S. G. Minasian, *Dalton Transactions*, 2016, **45**, 9948–9961, DOI: 10.1039/C6DT00358C.

[92] J. N. Cross, J. Su, E. R. Batista, S. K. Cary, W. J. Evans, S. A. Kozimor, V. Mocko, B. L. Scott, B. W. Stein, C. J. Windorff and P. Yang, *Journal of the American Chemical Society*, 2017, **139**, 8667–8677, DOI: 10.1021/jacs.7b03755.

[93] R. M. Diamond, K. J. Street and G. T. Seaborg, *Journal of the American Chemical Society*, 1954, **76**, 1461–1469, DOI: 10.1021/ja01635a001.

[94] D. F. Starks, T. C. Parsons, A. Streitwieser and N. Edelstein, *Inorganic Chemistry*, 1974, **13**, 1307–1308, DOI: 10.1021/ic50136a011.

[95] A. J. Streitwieser and N. Yoshida, *Journal of the American Chemical Society*, 1969, **91**, 7528–7528, DOI: 10.1021/ja01054a061.

[96] A. J. Streitwieser and U. Mueller-Westerhoff, *Journal of the American Chemical Society*, 1968, **90**, 7364–7364, DOI: 10.1021/ja01028a044.

[97] G. Ganguly, D.-C. Sergentu and J. Autschbach, *Chemistry – A European Journal*, 2020, **26**, 1776–1788, DOI: 10.1002/chem.201904166.

[98] R. G. Denning, J. C. Green, T. E. Hutchings, C. Dallera, A. Tagliaferri, K. Giarda, N. B. Brookes and L. Braicovich, *The Journal of Chemical Physics*, 2002, **117**, 8008–8020, DOI: 10.1063/1.1510445.

[99] A. R. Fox and C. C. Cummins, *Journal of the American Chemical Society*, 2009, **131**, 5716–5717, DOI: 10.1021/ja8095812.

[100] L. P. Spencer, P. Yang, S. G. Minasian, R. E. Jilek, E. R. Batista, K. S. Boland, J. M. Boncella, S. D. Conradson, D. L. Clark, T. W. Hayton, S. A. Kozimor, R. L. Martin, M. M. MacInnes, A. C. Olson, B. L. Scott, D. K. Shuh and M. P. Wilkerson, *Journal of the American Chemical Society*, 2013, **135**, 2279–2290, DOI: 10.1021/ja310575j.

[101] H. S. La Pierre and K. Meyer, *Inorganic Chemistry*, 2013, **52**, 529–539, DOI: 10.1021/ic302412j.

[102] T. Vent-Schmidt, L. Andrews, K. S. Thanthiriwatte, D. A. Dixon and S. Riedel, *Inorganic Chemistry*, 2015, **54**, 9761–9769, DOI: 10.1021/acs.inorgchem.5b01383.

[103] J. L. Brown, E. R. Batista, J. M. Boncella, A. J. Gaunt, S. D. Reilly, B. L. Scott and N. C. Tomson, *Journal of the American Chemical Society*, 2015, **137**, 9583–9586, DOI: 10.1021/jacs.5b06667.

[104] E. P. Wildman, G. Balázs, A. J. Wooles, M. Scheer and S. T. Liddle, *Nature Communications*, 2016, **7**, 12884, DOI: 10.1038/ncomms12884.

[105] S. T. Liddle, *Coordination Chemistry Reviews*, 2015, **293-294**, 41st International Conference on Coordination Chemistry, Singapore, July 2014, 211–227, DOI: https://doi.org/10.1016/j.ccr.2014.09.011.

[106] B. M. Gardner, F. Tuna, E. J. L. McInnes, J. McMaster, W. Lewis, A. J. Blake and S. T. Liddle, *Angewandte Chemie International Edition*, 2015, **54**, 7068–7072, DOI: https://doi.org/10.1002/anie.201501728.

[107] P. L. Diaconescu, P. L. Arnold, T. A. Baker, D. J. Mindiola and C. C. Cummins, *Journal of the American Chemical Society*, 2000, **122**, 6108–6109, DOI: 10.1021/ja994484e.

[108] J. A. Hlina, J. R. Pankhurst, N. Kaltsoyannis and P. L. Arnold, *Journal of the American Chemical Society*, 2016, **138**, 3333–3345, DOI: 10.1021/jacs.5b10698.

[109] B. Oelkers, M. V. Butovskii and R. Kempe, *Chemistry – A European Journal*, 2012, **18**, 13566–13579, DOI: https://doi.org/10.1002/chem.201200783.

[110] S. K. Cary, M. Vasiliu, R. E. Baumbach, J. T. Stritzinger, T. D. Green, K. Diefenbach, J. N. Cross, K. L. Knappenberger, G. Liu, M. A. Silver, A. E. DePrince, M. J. Polinski, S. M. V. Cleve, J. H. House, N. Kikugawa, A. Gallagher, A. A. Arico, D. A. Dixon and T. E. Albrecht-Schmitt, *Nature Communications*, 2015, **6**, 6827, DOI: 10.1038/ncomms7827.

[111] M. J. Polinski, E. B. Garner, R. Maurice, N. Planas, J. T. Stritzinger, T. G. Parker, J. N. Cross, T. D. Green, E. V. Alekseev, S. M. V. Cleve, W. Depmeier, L. Gagliardi, M. Shatruk, K. L. Knappenberger, G. Liu, S. Skanthakumar, L. Soderholm, D. A.

Dixon and T. E. Albrecht-Schmitt, *Nature Chemistry*, 2014, **6**, 387–392, DOI: 10.1038/nchem.1896.

[112] L. C. Motta and J. Autschbach, *Nature Communications*, 2023, **14**, 4307, DOI: 10.1038/s41467-023-39626-8.

[113] N. Kaltsoyannis, *Inorganic Chemistry*, 2000, **39**, 6009–6017, DOI: 10.1021/ic000891b.

[114] S. G. Minasian, J. M. Keith, E. R. Batista, K. S. Boland, D. L. Clark, S. A. Kozimor, R. L. Martin, D. K. Shuh and T. Tyliszczak, *Chemical Science*, 2014, **5**, 351–359, DOI: 10.1039/C3SC52030G.

[115] I. Kirker and N. Kaltsoyannis, *Dalton Trans.*, 2011, **40**, 124–131, DOI: 10.1039/C0DT01018A.

[116] M. Pepper and B. E. Bursten, *Chemical Reviews*, 1991, **91**, 719–741, DOI: 10.1021/cr00005a005.

[117] S. Matsika, Z. Zhang, S. R. Brozell, J.-P. Blaudeau, Q. Wang and R. M. Pitzer, *The Journal of Physical Chemistry A*, 2001, **105**, 3825–3828, DOI: 10.1021/jp003085z.

[118] P. D. Dau, J. Su, H.-T. Liu, D.-L. Huang, J. Li and L.-S. Wang, *The Journal of Chemical Physics*, 2012, **137**, 064315, DOI: 10.1063/1.4742062.

[119] K. Pierloot and E. van Besien, *The Journal of Chemical Physics*, 2005, **123**, 204309, DOI: 10.1063/1.2121608.

[120] N. Kaltsoyannis, *Chem. Soc. Rev.*, 2003, **32**, 9–16, DOI: 10.1039/B204253N.

[121] G. A. Shamov and G. Schreckenbach, *The Journal of Physical Chemistry A*, 2005, **109**, 10961–10974, DOI: 10.1021/jp053522f.

[122] K. Newcomb, S. P. Tiwari, N. Rai and E. J. Maginn, *Phys. Chem. Chem. Phys.*, 2018, **20**, 15753–15763, DOI: 10.1039/C8CP01944D.

[123] S. P. Tiwari, N. Rai and E. J. Maginn, *Phys. Chem. Chem. Phys.*, 2014, **16**, 8060–8069, DOI: 10.1039/C3CP54556C.

[124] A. Jennifer G, Y. Gao, G. Schreckenbach and E. Varathan, *Inorganic Chemistry*, 2023, **62**, 6920–6933, DOI: 10.1021/acs.inorgchem.3c00022.

[125] Y. Zhang, W. Duan, Y. Yang, T. Jian, Y. Qiao, G. Ren, N. Zhang, L. Zheng, W. Yan, J. Wang, J. Chen, S. G. Minasian and T. Sun, *Inorganic Chemistry*, 2022, **61**, 92–104, DOI: 10.1021/acs.inorgchem.1c02236.

[126] M. Yang, W. Ding and D. Wang, *New J. Chem.*, 2017, **41**, 63–74, DOI: 10.1039/C6NJ01615D.

[127] B. M. T. Costa Peluzo and E. Kraka, *International Journal of Molecular Sciences*, 2022, **23**, DOI: 10.3390/ijms23094655.

[128] W. N. Association, *Nuclear Fuel Cycle Overview*, https://world-nuclear.org/information-library/nuclear-fuel-cycle/introduction/nuclear-fuel-cycle-overview (visited on 12/06/2024).

[129] K. J. Pastoor, R. S. Kemp, M. P. Jensen and J. C. Shafer, *Inorganic Chemistry*, 2021, **60**, 8347–8367, DOI: 10.1021/acs.inorgchem.0c03390.

[130] A. H. Kaksonen, A.-M. Lakaniemi and O. H. Tuovinen, *Journal of Cleaner Production*, 2020, **264**, 121586, DOI: 10.1016/j.jclepro.2020.121586.

[131] M. B. Kurmanseiit, M. S. Tungatarova, A. Kaltayev and J.-J. Royer, *Minerals*, 2022, **12**, DOI: 10.3390/min12111340.

[132] G. Li and J. Yao, *Mining*, 2024, **4**, 120–148, DOI: 10.3390/mining4010009.

[133] M. S. M. J. N. Mathur and K. L. Nash, *Solvent Extraction and Ion Exchange*, 2001, **19**, 357–390, DOI: 10.1081/SEI-100103276.

[134] C. W. Abney, R. T. Mayes, T. Saito and S. Dai, *Chemical Reviews*, 2017, **117**, 13935–14013, DOI: 10.1021/acs.chemrev.7b00355.

[135] A. Alka, V. S. Shetti and M. Ravikanth, *Coordination Chemistry Reviews*, 2019, **401**, 213063, DOI: https://doi.org/10.1016/j.ccr.2019.213063.

[136] E. Varathan, Y. Gao and G. Schreckenbach, *The Journal of Physical Chemistry A*, 2021, **125**, 920–932, DOI: 10.1021/acs.jpca.0c08760.

[137] J. Chen, X. He and J. Wang, *Radiochimica Acta*, 2014, **102**, 41–51, DOI: doi:10.1515/ract-2014-2093.

[138] R. Kusaka and M. Watanabe, *Phys. Chem. Chem. Phys.*, 2018, **20**, 29588–29590, DOI: 10.1039/C8CP04558E.

[139] F. Baumgärtner and D. Ertel, *Journal of radioanalytical chemistry*, 1980, **58**, 11–28, DOI: 10.1007/BF02533770.

[140] T. Robin, in *Reprocessing and Recycling of Spent Nuclear Fuel*, Elsevier, 2015, pp. 2–2.

[141] N. Rodríguez-Villagra, L. J. Bonales, A. Milena-Pérez and H. Galán, *MRS Advances*, 2023, **8**, 207–213, DOI: 10.1557/s43580-022-00476-z.

[142] C. R. Armstrong, M. Nyman, T. Shvareva, G. E. Sigmon, P. C. Burns and A. Navrotsky, *Proceedings of the National Academy of Sciences*, 2012, **109**, 1874–1877, DOI: 10.1073/pnas.1119758109.

[143] Y. Kumagai, R. Kusaka, M. Nakada, M. Watanabe, D. Akiyama, A. Kirishima, N. Sato and T. Sasaki, *Journal of Nuclear Science and Technology*, 2022, **59**, 961–971, DOI: 10.1080/00223131.2021.2023055.

[144] B. Grambow, A. Nitta, A. Shibata, Y. Koma, S. Utsunomiya, R. Takami, K. Fueda, T. Ohnuki, C. Jegou, H. Laffolley and C. Journeau, *Journal of Nuclear Science and Technology*, 2022, **59**, 1–24, DOI: 10.1080/00223131.2021.1966347.

[145] T. S. Akira Kirishima, Masahiko Hirano and N. Sato, *Journal of Nuclear Science and Technology*, 2015, **52**, 1240–1246, DOI: 10.1080/00223131.2015.1017545.

[146] S. O. Odoh, J. Shamblin, C. A. Colla, S. Hickam, H. L. Lobeck, R. A. K. Lopez, T. Olds, J. E. S. Szymanowski, G. E. Sigmon, J. Neuefeind, W. H. Casey, M. Lang, L. Gagliardi and P. C. Burns, *Inorganic Chemistry*, 2016, **55**, 3541–3546, DOI: 10.1021/acs.inorgchem.6b00017.

[147] V. V. Gurzhiy, B. E. Burakov, B. Y. Zubekhina and A. V. Kasatkin, *Materials*, 2023, **16**, DOI: 10.3390/ma16134533.

[148] G. P. Horne, T. S. Grimes, W. F. Bauer, C. J. Dares, S. M. Pimblott, S. P. Mezyk and B. J. Mincher, *Inorganic Chemistry*, 2019, **58**, 8551–8559, DOI: 10.1021/acs.inorgchem.9b00854.

[149] J. D. Burns, T. C. Shehee, A. Clearfield and D. T. Hobbs, *Analytical Chemistry*, 2012, **84**, 6930–6932, DOI: 10.1021/ac3018394.

[150] L. Köhler, M. Patzschke, S. Bauters, T. Vitova, S. M. Butorin, K. O. Kvashnina, M. Schmidt, T. Stumpf and J. März, *Chemistry – A European Journal*, 2022, **28**, e202200119, DOI: https://doi.org/10.1002/chem.202200119.

[151] P. D. Dau, M. Vasiliu, K. A. Peterson, D. A. Dixon and J. K. Gibson, *Chemistry – A European Journal*, 2017, **23**, 17369–17378, DOI: https://doi.org/10.1002/chem.201704193.

[152] M. Vasiliu, T. Jian, J. K. Gibson, K. A. Peterson and D. A. Dixon, *Inorganic Chemistry*, 2020, **59**, 4554–4566, DOI: 10.1021/acs.inorgchem.9b03690.

[153] A. Kovács, P. D. Dau, J. Marçalo and J. K. Gibson, *Inorganic Chemistry*, 2018, **57**, 9453–9467, DOI: 10.1021/acs.inorgchem.8b01450.

[154] P. L. Arnold, J. B. Love and D. Patel, *Coordination Chemistry Reviews*, 2009, **253**, 38th International Conference on Coordination Chemistry, 1973–1978, DOI: https://doi.org/10.1016/j.ccr.2009.03.014.

[155] R. Faizova, R. Scopelliti, A.-S. Chauvin and M. Mazzanti, *Journal of the American Chemical Society*, 2018, **140**, 13554–13557, DOI: 10.1021/jacs.8b07885.

[156] N. Kaltsoyannis, P. J. Hay, J. Li, J.-P. Blaudeau and B. E. Bursten, in *The Chemistry of the Actinide and Transactinide Elements*, ed. L. R. Morss, N. M. Edelstein and J. Fuger, Springer Netherlands, Dordrecht, 2006, pp. 1893–2012, DOI: 10.1007/1-4020-3598-5_17.

[157] S. Spencer, L. Gagliardi, N. C. Handy, A. G. Ioannou, C.-K. Skylaris, A. Willetts and A. M. Simper, *The Journal of Physical Chemistry A*, 1999, **103**, 1831–1837, DOI: 10.1021/jp983543s.

[158] D. Rios, M. C. Michelini, A. F. Lucena, J. Marçalo, T. H. Bray and J. K. Gibson, *Inorganic Chemistry*, 2012, **51**, 6603–6614, DOI: 10.1021/ic3001625.

[159] P. S. Bagus, C. J. Nelin, K. M. Rosso, B. Schacherl and T. Vitova, *Inorganic Chemistry*, 2024, **63**, 1793–1802, DOI: 10.1021/acs.inorgchem.3c03158.

[160] K. Pierloot, E. van Besien, E. van Lenthe and E. J. Baerends, *The Journal of Chemical Physics*, 2007, **126**, 194311, DOI: 10.1063/1.2735297.

[161] D. M. Gruen and J. Hutchison, Clyde A., *The Journal of Chemical Physics*, 1954, **22**, 386–393, DOI: 10.1063/1.1740080.

[162] M. P. B. Bleaney, P.M. Llewellyn and G. Hall, *The London, Edinburgh, and Dublin Philosophical Magazine and Journal of Science*, 1954, **45**, 992–993, DOI: 10.1080/14786440908520515.

[163] P. Zimmermann, S. Peredkov, P. M. Abdala, S. DeBeer, M. Tromp, C. Müller and J. A. van Bokhoven, *Coordination Chemistry Reviews*, 2020, **423**, 213466, DOI: https://doi.org/10.1016/j.ccr.2020.213466.

[164] W. Malzer, C. Schlesiger and B. Kanngießer, *Spectrochimica Acta Part B: Atomic Spectroscopy*, 2021, **177**, 106101, DOI: https://doi.org/10.1016/j.sab.2021.106101.

[165] J. K. Kowalska, F. A. Lima, C. J. Pollock, J. A. Rees and S. DeBeer, *Israel Journal of Chemistry*, 2016, **56**, 803–815, DOI: https://doi.org/10.1002/ijch.201600037.

[166] S. M. Butorin, K. O. Kvashnina, A. L. Smith, K. Popa and P. M. Martin, *Chemistry – A European Journal*, 2016, **22**, 9693–9698, DOI: https://doi.org/10.1002/chem.201505091.

[167] F. Frati, M. O. J. Y. Hunault and F. M. F. de Groot, *Chemical Reviews*, 2020, **120**, 4056–4110, DOI: 10.1021/acs.chemrev.9b00439.

[168] P. P. Paufler, *Journal of Synchrotron Radiation*, 2011, **18**, 818–818.

[169] C. T. Chen and F. Sette, *Review of Scientific Instruments*, 1989, **60**, 1616–1621, DOI: 10.1063/1.1141044.

[170] C. T. Chen and F. Sette, *Physica Scripta*, 1990, **1990**, 119, DOI: 10.1088/0031-8949/1990/T31/016.

[171] S. D. Conradson, *Applied Spectroscopy*, 1998, **52**, 252A–279A, DOI: 10.1366/0003702981944599.

[172] M. O. Krause and J. H. Oliver, *Journal of Physical and Chemical Reference Data*, 1979, **8**, 329–338, DOI: 10.1063/1.555595.

[173] K. O. Kvashnina, S. M. Butorin, P. Martin and P. Glatzel, *Physical Review Letters*, 2013, **111**, 253002, DOI: 10.1103/PhysRevLett.111.253002.

[174] G. Leinders, R. Bes, J. Pakarinen, K. Kvashnina and M. Verwerft, *Inorganic Chemistry*, 2017, **56**, 6784–6787, DOI: 10.1021/acs.inorgchem.7b01001.

[175] T. Vitova, I. Pidchenko, S. Biswas, G. Beridze, P. W. Dunne, D. Schild, Z. Wang, P. M. Kowalski and R. J. Baker, *Inorganic Chemistry*, 2018, **57**, 1735–1743, DOI: 10.1021/acs.inorgchem.7b02326.

[176] M. Zegke, X. Zhang, I. Pidchenko, J. A. Hlina, R. M. Lord, J. Purkis, G. S. Nichol, N. Magnani, G. Schreckenbach, T. Vitova, J. B. Love and P. L. Arnold, *Chem. Sci.*, 2019, **10**, 9740–9751, DOI: 10.1039/C8SC05717F.

[177] S. M. Butorin, A. Modin, J. R. Vegelius, K. O. Kvashnina and D. K. Shuh, *The Journal of Physical Chemistry C*, 2016, **120**, 29397–29404, DOI: 10.1021/acs.jpcc.6b09335.

[178] S. M. Butorin, K. O. Kvashnina, J. R. Vegelius, D. Meyer and D. K. Shuh, *Proc. Natl. Acad. Sci.*, 2016, **113**, 8093.

[179] R. Bès, K. Kvashnina, A. Rossberg, G. Dottavio, L. Desgranges, Y. Pontillon, P. Solari, S. Butorin and P. Martin, *Journal of Nuclear Materials*, 2018, **507**, 145–150, DOI: https://doi.org/10.1016/j.jnucmat.2018.04.046.

[180] R. Bès, M. Rivenet, P.-L. Solari, K. O. Kvashnina, A. C. Scheinost and P. M. Martin, *Inorganic Chemistry*, 2016, **55**, 4260–4270, DOI: 10.1021/acs.inorgchem.6b00014.

[181] B. Schacherl, C. Joseph, P. Lavrova, A. Beck, C. Reitz, T. Pruessmann, D. Fellhauer, J.-Y. Lee, K. Dardenne, J. Rothe, H. Geckeis and T. Vitova, *Analytica Chimica Acta*, 2022, **1202**, 339636, DOI: https://doi.org/10.1016/j.aca.2022.339636.

[182] T. Vitova, I. Pidchenko, D. Schild, T. Prüßmann, V. Montoya, D. Fellhauer, X. Gaona, E. Bohnert, J. Rothe, R. J. Baker and H. Geckeis, *Inorganic Chemistry*, 2020, **59**, 8–22, DOI: 10.1021/acs.inorgchem.9b02463.

[183] T. Vitova, I. Pidchenko, D. Fellhauer, T. Pruessmann, S. Bahl, K. Dardenne, T. Yokosawa, B. Schimmelpfennig, M. Altmaier, M. Denecke, J. Rothe and H. Geckeis, *Chem. Commun.*, 2018, **54**, 12824–12827, DOI: 10.1039/C8CC06889E.

[184] L. Amidani, M. Retegan, A. Volkova, K. Popa, P. M. Martin and K. O. Kvashnina, *Inorganic Chemistry*, 2021, **60**, 16286–16293, DOI: 10.1021/acs.inorgchem.1c02107.

[185] S. E. Shadle, J. E. Penner-Hahn, H. J. Schugar, B. Hedman, K. O. Hodgson and E. I. Solomon, *Journal of the American Chemical Society*, 1993, **115**, 767–776, DOI: 10.1021/ja00055a057.

[186] S. E. Shadle, B. Hedman, K. O. Hodgson and E. I. Solomon, *Journal of the American Chemical Society*, 1995, **117**, 2259–2272, DOI: 10.1021/ja00113a015.

[187] B. Hedman, K. O. Hodgson and E. I. Solomon, *Journal of the American Chemical Society*, 1990, **112**, 1643–1645, DOI: 10.1021/ja00160a062.

[188] T. Glaser, B. Hedman, K. O. Hodgson and E. I. Solomon, *Accounts of Chemical Research*, 2000, **33**, 859–868, DOI: 10.1021/ar990125c.

[189] M. L. Baker, M. W. Mara, J. J. Yan, K. O. Hodgson, B. Hedman and E. I. Solomon, *Coordination Chemistry Reviews*, 2017, 182–208, DOI: 10.1016/j.ccr.2017.02.004.

[190] Y. Qiao, G. Ganguly, C. H. Booth, J. A. Branson, A. S. Ditter, D. J. Lussier, L. M. Moreau, D. R. Russo, D.-C. Sergentu, D. K. Shuh, T. Sun, J. Autschbach and S. G. Minasian, *Chemical Communications*, 2021, **57**, 9562–9565, DOI: 10.1039/D1CC03414F.

[191] D.-C. Sergentu and J. Autschbach, *Dalton Transactions*, 2022, **51**, 1754–1764, DOI: 10.1039/D1DT04075H.

[192] E. I. Solomon, B. Hedman, K. O. Hodgson, A. Dey and R. K. Szilagyi, *Coordination Chemistry Reviews*, 2005, **249**, 97–129, DOI: 10.1016/j.ccr.2004.03.020.

[193] D.-C. Sergentu and J. Autschbach, *Chemical Science*, 2022, **13**, 3194–3207, DOI: 10.1039/D1SC06454A.

[194] Y. Zhang, J. D. Biggs, D. Healion, N. Govind and S. Mukamel, *The Journal of Chemical Physics*, 2012, **137**, 194306, DOI: 10.1063/1.4766356.

[195] N. A. Besley and F. A. Asmuruf, *Phys. Chem. Chem. Phys.*, 2010, **12**, 12024–12039, DOI: 10.1039/C002207A.

[196] M. E. Casida, *Journal of Molecular Structure: THEOCHEM*, 2009, **914**, Time-dependent density-functional theory for molecules and molecular solids, 3–18, DOI: https://doi.org/10.1016/j.theochem.2009.08.018.

[197] S. Hirata and M. Head-Gordon, *Chemical Physics Letters*, 1999, **314**, 291–299, DOI: https://doi.org/10.1016/S0009-2614(99)01149-5.

[198] C. Fillaux, D. Guillaumont, J.-C. Berthet, R. Copping, D. K. Shuh, T. Tyliszczak and C. D. Auwer, *Phys. Chem. Chem. Phys.*, 2010, **12**, 14253–14262, DOI: 10.1039/C0CP00386G.

[199] K. Lopata, B. E. Van Kuiken, M. Khalil and N. Govind, *Journal of Chemical Theory and Computation*, 2012, **8**, 3284–3292, DOI: 10.1021/ct3005613.

[200] M. Stener, G. Fronzoni and M. de Simone, *Chemical Physics Letters*, 2003, **373**, 115–123, DOI: https://doi.org/10.1016/S0009-2614(03)00543-8.

[201] J. Rehr and A. Ankudinov, *Coordination Chemistry Reviews*, 2005, **249**, Synchrotron Radiation in Inorganic and Bioinorganic Chemistry, 131–140, DOI: https://doi.org/10.1016/j.ccr.2004.02.014.

[202] S. Team, *The FDMNES Project*, https://fdmnes.neel.cnrs.fr/ (visited on 09/14/2024).

[203] O. Bunău and Y. Joly, *Journal of Physics: Condensed Matter*, 2009, **21**, 345501, DOI: 10.1088/0953-8984/21/34/345501.

[204] X.-D. Wen, M. W. Löble, E. R. Batista, E. Bauer, K. S. Boland, A. K. Burrell, S. D. Conradson, S. R. Daly, S. A. Kozimor, S. G. Minasian, R. L. Martin, T. M. McCleskey, B. L. Scott, D. K. Shuh and T. Tyliszczak, *Journal of Electron Spectroscopy and Related Phenomena*, 2014, **194**, Core-Level Spectroscopies of Actinides, 81–87, DOI: https://doi.org/10.1016/j.elspec.2014.03.005.

[205] A. Modin, Y. Yun, M.-T. Suzuki, J. Vegelius, L. Werme, J. Nordgren, P. M. Oppeneer and S. M. Butorin, *Phys. Rev. B*, 2011, **83**, 075113, DOI: 10.1103/PhysRevB.83.075113.

[206] C. Fillaux, J.-C. Berthet, S. D. Conradson, P. Guilbaud, D. Guillaumont, C. Hennig, P. Moisy, J. Roques, E. Simoni, D. K. Shuh, T. Tyliszczak, I. Castro-Rodriguez and C. Den Auwer, *Comptes Rendus Chimie*, 2007, **10**, 859–871, DOI: https://doi.org/10.1016/j.crci.2006.12.012.

[207] D.-C. Sergentu, T. J. Duignan and J. Autschbach, *The Journal of Physical Chemistry Letters*, 2018, **9**, 5583–5591, DOI: 10.1021/acs.jpclett.8b02412.

[208] R. Polly, B. Schacherl, J. Rothe and T. Vitova, *Inorganic Chemistry*, 2021, **60**, 18764–18776, DOI: 10.1021/acs.inorgchem.1c02364.

[209] T. Dumas, D. Guillaumont, P. Moisy, D. K. Shuh, T. Tyliszczak, P. L. Solari and C. Den Auwer, *Chem. Commun.*, 2018, **54**, 12206–12209, DOI: 10.1039/C8CC05176C.

[210] E. Dalodière, M. Virot, V. Morosini, T. Chave, T. Dumas, C. Hennig, T. Wiss, O. Dieste Blanco, D. K. Shuh, T. Tyliszcak, L. Venault, P. Moisy and S. I. Nikitenko, *Scientific Reports*, 2017, **7**, 43514, DOI: 10.1038/srep43514.

[211] C. D. Pemmaraju, R. Copping, S. Wang, M. Janousch, S. J. Teat, T. Tyliszcak, A. Canning, D. K. Shuh and D. Prendergast, *Inorganic Chemistry*, 2014, **53**, 11415–11425, DOI: 10.1021/ic501107a.

[212] A. Modin, M.-T. Suzuki, J. Vegelius, Y. Yun, D. K. Shuh, L. Werme, J. Nordgren, P. M. Oppeneer and S. M. Butorin, *Journal of Physics: Condensed Matter*, 2015, **27**, 315503, DOI: 10.1088/0953-8984/27/31/315503.

[213] L. Amidani, T. Dumas, D. K. Shuh, S. M. Butorin, C. J. Sahle, A. Longo and K. O. Kvashnina, *The Journal of Physical Chemistry C*, 2023, **127**, 3077–3084, DOI: 10.1021/acs.jpcc.2c07771.

[214] J. M. Kasper, X. Li, S. A. Kozimor, E. R. Batista and P. Yang, *Journal of Chemical Theory and Computation*, 2022, **18**, 2171–2179, DOI: 10.1021/acs.jctc.1c00851.

[215] T. Vitova, J. C. Green, R. G. Denning, M. Löble, K. Kvashnina, J. J. Kas, K. Jorissen, J. J. Rehr, T. Malcherek and M. A. Denecke, *Inorganic Chemistry*, 2015, **54**, 174–182, DOI: 10.1021/ic5020016.

[216] C. J. Cramer, *Essentials of Computational Chemistry : Theories and Models*, John Wiley & Sons, Incorporated, New York, UNITED KINGDOM, 2004.

[217] J. Olsen, B. O. Roos, P. Jo/rgensen and H. J. A. Jensen, *The Journal of Chemical Physics*, 1988, **89**, 2185–2192, DOI: 10.1063/1.455063.

[218] B. O. Roos, in John Wiley and Sons, Ltd, 1987, pp. 399–445, DOI: 10.1002/9780470142943.ch7.

[219] P. A. Malmqvist, A. Rendell and B. O. Roos, *The Journal of Physical Chemistry*, 1990, **94**, 5477–5482, DOI: 10.1021/j100377a011.

[220] B. O. Roos, P. R. Taylor and P. E. M. Sigbahn, *Chemical Physics*, 1980, **48**, 157–173, DOI: 10.1016/0301-0104(80)80045-0.

[221] K. Stanistreet-Welsh and A. Kerridge, *Phys. Chem. Chem. Phys.*, 2023, **25**, 23753–23760, DOI: 10.1039/D3CP03149G.

[222] K. Stanistreet-Welsh and A. Kerridge, *Inorganic Chemistry*, 2024, **63**, 15115–15126, DOI: 10.1021/acs.inorgchem.4c02144.

[223] J. N. Ehrman, K. Shumilov, A. J. Jenkins, J. M. Kasper, T. Vitova, E. R. Batista, P. Yang and X. Li, *JACS Au*, 2024, **4**, 1134–1141, DOI: 10.1021/jacsau.3c00838.

Chapter 2

Theoretical Background

2.1 Preliminary Comments

The content of this chapter is adapted from the detailed books covering the foundations of quantum chemistry and include the works of Szabo and Ostlund,[1] Helgaker,[2] Jensen,[3] and Cramer.[4] Additional references are made for areas that require acknowledgment to particular studies or papers. Effort has been made to include examples to expand on concepts were appropriate and when possible.

2.2 Molecular Quantum Mechanics

2.2.1 The Schrödinger Equation

The time-independent non-relativistic Schrödinger equation governs the nature of a stationary quantum state (particles, atoms and molecules) and can be solved to obtain the wavefunction. The wavefunction provides a complete description of the quantum state, which can be acted upon by operators to obtain any observable property of the state, and in principle, any experimentally reported property. The time-independent non-relativistic Schrödinger equation takes the form

$$\hat{H}\Psi = E\Psi \tag{2.1}$$

and contains the Hamiltonian operator $\hat{H}$ which acts on the wavefunction Ψ to return the total energy of the state, E. In the context of molecules, Ψ is a many electron wavefunction,

$\hat{H}$ is the molecular Hamiltonian, and E is the total energy of the molecular state. Solving the Schrödinger equation analytically for anything other than a simple one-electron system (H_2^+ or H-atom) becomes intractable since such systems represent a many-body problem. Therefore, to make progress, it is inevitable to introduce approximate methods of solving eq. (2.1).

2.2.1.1 The Molecular Hamiltonian

The Hamiltonian operator in eq. (2.1) encapsulates the interactions for the particles that make up the system and can be split into the total kinetic ($\hat{T}$) energy of all particles and the total potential ($\hat{V}$) energy between particle pairs. The molecular Hamiltonian $\hat{H}$, therefore contains all possible particle interactions that contribute to the total energy. The kinetic energy can be split into that from the electrons $\hat{T}_\mathrm{e}$, and from the nuclei $\hat{T}_\mathrm{N}$. The potential energy can be split into that of nuclear-nuclear $\hat{V}_{NN}$ repulsion, electron-electron $\hat{V}_{ee}$ repulsion, and electron-nuclear $\hat{V}_{Ne}$ attraction. The molecular Hamiltonian can then be expressed as

$$\hat{H} = \hat{T} + \hat{V} = \hat{T}_\mathrm{e} + \hat{T}_\mathrm{N} + \hat{V}_\mathrm{Ne} + \hat{V}_\mathrm{ee} + \hat{V}_\mathrm{NN} \tag{2.2}$$

In atomic units, the operators in eq. (2.2) can be written explicitly to give a full expression for the molecular Hamiltonain of a N-electron and M-nuclei system as

$$\hat{H} = -\sum_{i=1}^{N} \frac{1}{2}\nabla_i^2 - \sum_{A=1}^{M} \frac{1}{2M_A}\nabla_A^2 - \sum_{i=1}^{N}\sum_{A=1}^{M} \frac{Z_A}{r_{iA}} + \sum_{i=1}^{N}\sum_{j>i}^{N} \frac{1}{r_{ij}} + \sum_{A=1}^{M}\sum_{B>A}^{M} \frac{Z_A Z_B}{R_{AB}} \tag{2.3}$$

where M_A is the ratio of the mass of nucleus A to the mass of an electron, Z_A and Z_B are the charges of nucleus A and B, respectively. The distances r_{iA}, r_{ij}, and R_{AB} are defined by the position vectors of the nuclei $\mathbf{R_A}$ and electrons $\mathbf{r_i}$, such that, $r_{iA} = |r_{iA}| = |\mathbf{r_i} - \mathbf{R_A}|$, $r_{ij} = |r_{ij}| = |\mathbf{r_i} - \mathbf{r_j}|$ and $R_{AB} = |R_{AB}| = |\mathbf{R_A} - \mathbf{R_B}|$. The Laplacian operators ∇_i^2 and ∇_A^2 involve differentiation with respect to the coordinates of the electron or nucleus, respectively. In the general case, the Laplacian can be written in Cartesian form

$$\nabla_k^2 = \frac{\partial^2}{\partial^2 x_k} + \frac{\partial^2}{\partial^2 y_k} + \frac{\partial^2}{\partial^2 z_k} \tag{2.4}$$

2.2.1.2 The Born-Oppenheimer Approximation

To further reduce the complexity of solving the Schrödinger equation, the Born-Oppenheimer approximation can be made. This approximation fixes the positions of the nuclei, thereby eliminating the kinetic term for the nuclei ($\hat{T}_N$) and turning the nuclear-nuclear repulsion term ($\hat{V}_{NN} = E_{NN}$) into a constant. Any constant added to an operator only adds to the operator eigenvalues with no effect on the eigenfunctions. Therefore, it is usual to drop the nuclear-nuclear energy constant from the Hamiltonian and add it as a final correction to the electronic energy at the end of a calculation. The remaining terms describe the motion of N-electrons in a field of fixed M-nuclei and constitutes the electronic Hamiltonian $\hat{H}_{\text{elec}}$

$$\hat{H}_{\text{elec}} = -\sum_{i=1}^{N} \frac{1}{2}\nabla_i^2 - \sum_{i=1}^{N}\sum_{A=1}^{M} \frac{Z_A}{r_{iA}} + \sum_{i=1}^{N}\sum_{j>i}^{N} \frac{1}{r_{ij}} \tag{2.5}$$

This assumes the system can be approximated by considering the electrons as moving through a field of fixed nuclei. Since the nuclei are so much greater in mass compared to the electron their motion is much slower in comparison, and from the reference frame of the electrons, the nuclei are almost stationary. Solving the Schrödinger equation using the electronic Hamiltonian

$$\hat{H}_{\text{elec}}\Psi_{\text{elec}} = E_{\text{elec}}\Psi_{\text{elec}} \tag{2.6}$$

yields the electronic wavefunction Ψ_{elec}, which provides a description of the electronic structure at a fixed set of nuclear coordinates. Since the nuclear-repulsion term is negated from the electronic Hamiltonian, to obtain the total energy E_{tot}, the repulsion must be taken into consideration after solving and obtaining the electronic energy E_{elec}

$$E_{\text{tot}} = E_{\text{elec}} + \sum_{A=1}^{M}\sum_{B>A}^{M} \frac{Z_A Z_B}{R_{AB}} \tag{2.7}$$

2.2.1.3 Orbitals and the Pauli Exclusion Principle:

A fundamental property of electrons is their intrinsic spin and is a key requirement in theoretical models to form a complete description of electron behaviour. The spin information in a non-relativistic framework can be incorporated as an additional coordinate

of the wavefunction. Each electron in an N-electron system is described by three spatial ($\mathbf{r}$) and one spin coordinate (ω), which is collectively denoted by $\mathbf{x} = \{\mathbf{r}, \omega\}$, giving an electronic wavefunction that is a function of electron coordinates $\Psi(\mathbf{x_1}, \mathbf{x_2}, \cdots, \mathbf{x}_N)$. However, since the electronic Hamiltonian only depends on the spatial coordinates of the electrons, simply including the spin as a coordinate does not automatically lead to a wavefunction that satisfies the anti-symmetry requirements of fermionic wavefunctions. The anti-symmetry requirement is a manifestation of the Pauli exclusion principle and leads to the requirement that fermionic wavefunctions must change sign upon the interchange of any two electron coordinates

$$\Phi(\mathbf{x_1}, \cdots, \mathbf{x}_i, \cdots, \mathbf{x}_j, \cdots, \mathbf{x}_N) = -\Phi(\mathbf{x_1}, \cdots, \mathbf{x}_j, \cdots, \mathbf{x}_i, \cdots, \mathbf{x}_N) \tag{2.8}$$

This requirement must be incorporated into the many-electron wavefunction. To proceed, a sensible approach to constructing the many-electron wavefunction is to first consider single-electron wavefunctions for each electron and use these single-electron constructions to form a complete molecular wavefunction. For a given electron coordinate $\mathbf{x}$, which has spatial and spin components, the single electron wavefunction that describes the state of this electron at a particular position vector $\mathbf{r}$ is referred to as an orbital. The spatial distribution of an electron can be described by a spatial orbital $\psi(\mathbf{r})$, such that $|\psi(\mathbf{r})|^2 \, \mathrm{d}\mathbf{r}$ is the probability of finding the electron in the small volume element $\mathrm{d}\mathbf{r}$ surrounding $\mathbf{r}$. To account for the spin-component of the electron ω, a set of two orthonormal spin-functions $\alpha(\omega)$ and $\beta(\omega)$, for spin-up ($\uparrow$) and spin-down ($\downarrow$) electrons, can be introduced. The wavefunction that describes both the spatial and spin components of a single electron coordinate is a spin-orbital, $\chi(\mathbf{x})$. For each spatial orbital $\psi(\mathbf{r})$, two different spin-orbitals can be defined by the product of the spatial orbital with the $\alpha(\omega)$ and $\beta(\omega)$ spin-functions as follows

$$\chi(\mathbf{x}) = \begin{cases} \psi(\mathbf{r})\alpha(\omega) \\ \text{or} \\ \psi(\mathbf{r})\beta(\omega) \end{cases} \tag{2.9}$$

These two undefined spin-functions (α and β) which take unspecified spin-variables (ω) as inputs, need only operate such that they satisfy normalization conditions and orthogonality

conditions to form an orthonormal set

$$\int \alpha^*(\omega)\alpha(\omega)\,\mathrm{d}\omega = \int \beta^*(\omega)\beta(\omega)\,\mathrm{d}\omega = \langle\alpha|\alpha\rangle = \langle\beta|\beta\rangle = 1 \tag{2.10}$$

$$\int \alpha^*(\omega)\beta(\omega)\,\mathrm{d}\omega = \int \beta^*(\omega)\alpha(\omega)\,\mathrm{d}\omega = \langle\alpha|\beta\rangle = \langle\beta|\alpha\rangle = 0 \tag{2.11}$$

2.2.1.4 Hartree-Products

Having considered single electron wavefunctions as spin-orbitals, the many-electron wavefunction can now be constructed. To simplify the problem, a fictional system whereby the electrons do not interact with each other is considered by setting $\hat{V}_{\mathrm{ee}} = 0$. This reduces the electronic Hamiltonian to the sum of one-electron energy operators

$$\hat{H}_{\mathrm{elec}} = \sum_{i=1}^{N} \hat{h}(i) \tag{2.12}$$

where $\hat{h}(i)$ is the operator describing the kinetic and potential energy of electron-i as follows

$$\hat{h}(i) = -\frac{1}{2}\nabla_i^2 - \sum_{A=1}^{M} \frac{Z_A}{r_{iA}} \tag{2.13}$$

The first term is the kinetic energy of electron-i and the second term is the combined potential energy from the Coulomb interactions of electron-i with all the fixed nuclei A. For each individual electron with coordinate $\mathbf{x}_i$, is contained in a spin-orbital χ_j, which is an eigenfunction of the one-electron energy operator $\hat{h}(i)$ forming the eigenvalue equation

$$\hat{h}(i)\chi_j(\mathbf{x}_i) = \epsilon_j\chi_j(\mathbf{x}_i) \tag{2.14}$$

Solving eq. (2.14) returns the orbital energy eigenvalue ϵ_j for the eigenfunction $\chi_j(\mathbf{x}_i)$. Because $\hat{H}_{\mathrm{elec}}$ is a sum of one-electron Hamiltonians in this case, a wavefunction which is a simple product of spin-orbitals for each electron, known as a Hartree-Product (HP)

$$\Psi^{\mathrm{HP}}(\mathbf{x_1}, \mathbf{x_2}, \cdots, \mathbf{x}_N) = \prod_{i=1}^{N} \chi_i(\mathbf{x}_i) = \chi_1(\mathbf{x_1})\chi_2(\mathbf{x_2})\cdots\chi_i(\mathbf{x}_N) \tag{2.15}$$

is an eigenfunction of $\hat{H}_{\text{elec}}$. This can be seen by applying the Hamiltonian to the the HP wavefunction Ψ^{HP}

$$\hat{H}_{\text{elec}}\Psi^{\text{HP}} = \Big[\sum_i \hat{h}(i)\Big] \cdot \prod_{i=1}^{N} \chi_i(\mathbf{x}_i) \tag{2.16}$$

$$= \Big[\hat{h}(1) + \hat{h}(2) + \cdots + \hat{h}(i)\Big]\Big[\chi_1(\mathbf{x_1})\chi_2(\mathbf{x_2})\cdots\chi_i(\mathbf{x}_i)\Big] \tag{2.17}$$

$$= \Big\{\hat{h}(1)\chi_1(\mathbf{x_1})\chi_2(\mathbf{x_2})\cdots\chi_i(\mathbf{x}_i)\Big\} + \cdots + \Big\{\chi_1(\mathbf{x_1})\chi_2(\mathbf{x_2})\cdots\hat{h}(i)\chi_i(\mathbf{x}_i)\Big\}$$

$$= \Big\{\epsilon_1\chi_1(\mathbf{x_1})\chi_2(\mathbf{x_2})\cdots\chi_i(\mathbf{x}_i)\Big\} + \cdots + \Big\{\chi_1(\mathbf{x_1})\chi_2(\mathbf{x_2})\cdots\epsilon_i\chi_i(\mathbf{x}_i)\Big\}$$

$$= \Big[\epsilon_1 + \epsilon_2 + \cdots + \epsilon_i\Big]\prod_{i=1}^{N}\chi_i(\mathbf{x}_i) = E_{\text{elec}}\Psi^{\text{HP}} \tag{2.18}$$

which returns the eigenvalue E_{elec}, which is just the sum of the spin-orbital energies ϵ_i. The HP wavefunction is an eigenfunction of the Hamiltonian since the latter consists of one-electron operators which act only on a specific electron i, maintaining the independent electron approximation ($V_{ee} = 0$). Each application of the one-electron operator returns an orbital energy and the total one-electron wavefunction (spin-orbital) for each term in eq. (2.17). Since the HP wavefunction appears in each term, it can be factored out leaving the sum of orbital energies in eq. (2.18) as the eigenvalue of $\hat{H}_{\text{elec}}$. Constructing the wavefunction as a product of independent electron wavefunctions, means the HP wavefunction is uncorrelated. This can be shown by considering the simultaneous probability of finding electron-one in the volume element $\mathrm{d}\mathbf{x_1}$ centered at $\mathbf{x_1}$, electron-two in $\mathrm{d}\mathbf{x_2}$ centred at $\mathbf{x_2}$, ect. written as

$$|\Psi^{\text{HP}}(\mathbf{x}_1, \cdots, \mathbf{x}_N)|^2\,\mathrm{d}\mathbf{x_1}\cdots\mathrm{d}\mathbf{x}_N = |\chi_1(\mathbf{x_1})|^2\,\mathrm{d}\mathbf{x_1}|\chi_2(\mathbf{x_2})|^2\,\mathrm{d}\mathbf{x_2}\cdots|\chi_i(\mathbf{x}_N)|^2\,\mathrm{d}\mathbf{x}_N \tag{2.19}$$

The probability of finding an electron in a particular orbital is independent of the position of electrons in the other orbitals, since the total probability is a product of independent probabilities. This contradicts with reality, since electrons repel one another and therefore their motion is correlated. The Hartree product also does not account for the distinguishability of the electrons. As written in eq. (2.15), the Hartree-product treats the electrons as distinguishable particles, since electron-one is in orbital-one, electron-two is in orbital-two, ect. and implies that the location of every electron in space is known exactly at any given moment. Lastly, the wavefunction does not satisfy the anti-symmetry principle violating the Pauli exclusion principle. This can be addressed by the use of Slater

determinants.

2.2.1.5 Slater Determinants

The indistinguishability of electrons and anti-symmetry principle can be enforced through the construction of Slater determinants. Consider the two-electron case in which a single electron occupies the spin-orbitals χ_1 and χ_2. Two possible Hartree products can be constructed to reflect the possible position of electrons in the spin-orbitals

$$\Psi^{\mathrm{HP}}(\mathbf{x_1}, \mathbf{x_2}) = \chi_1(\mathbf{x_1})\chi_2(\mathbf{x_2}) \tag{2.20}$$

$$\Psi^{\mathrm{HP}}(\mathbf{x_2}, \mathbf{x_1}) = \chi_1(\mathbf{x_2})\chi_2(\mathbf{x_1}) \tag{2.21}$$

In these HP wavefunctions, the electrons are clearly distinguishable and an exchange of electron coordinates returns a positive wavefunction. By taking the appropriate linear combination of the two Hartree products and normalising with a factor of $\frac{1}{\sqrt{2}}$, a Slater determinant wavefunction Ψ^{SD} is formed

$$\Psi^{\mathrm{SD}}(\mathbf{x_1}, \mathbf{x_2}) = \frac{1}{\sqrt{2}}(\chi_1(\mathbf{x_1})\chi_2(\mathbf{x_2}) - \chi_1(\mathbf{x_2})\chi_2(\mathbf{x_1})) \tag{2.22}$$

The minus sign in the combination ensures that the wavefunction is anti-symmetric with respect to the interchange of electron coordinates, such that

$$\Psi(\mathbf{x_1}, \mathbf{x_2}) = -\Psi(\mathbf{x_2}, \mathbf{x_1}) \tag{2.23}$$

The Slater determinant also clearly restricts two electrons from occupying the same spin-orbital as required by the Pauli exclusion principle and easily tested, since if $i = j$ in eq. (2.22) the wavefunction vanishes. The Slater determinant can be conveniently written in a linear algebra form

$$\Psi(\mathbf{x_1}, \mathbf{x_2}) = \frac{1}{\sqrt{2}} \begin{vmatrix} \chi_1(\mathbf{x_1}) & \chi_2(\mathbf{x_1}) \\ \chi_1(\mathbf{x_2}) & \chi_2(\mathbf{x_2}) \end{vmatrix} \tag{2.24}$$

which can be generalised for an N-electron system with a normalisation factor $\frac{1}{\sqrt{N!}}$ as

$$\Psi(\mathbf{x_1}, \mathbf{x_2}, \cdots, \mathbf{x_N}) = \frac{1}{\sqrt{N!}} \begin{vmatrix} \chi_1(\mathbf{x_1}) & \chi_2(\mathbf{x_1}) & \cdots & \chi_N(\mathbf{x_1}) \\ \chi_1(\mathbf{x_2}) & \chi_2(\mathbf{x_2}) & \cdots & \chi_N(\mathbf{x_2}) \\ \vdots & \vdots & \ddots & \vdots \\ \chi_1(\mathbf{x_N}) & \chi_2(\mathbf{x_N}) & \cdots & \chi_N(\mathbf{x_N}) \end{vmatrix} \tag{2.25}$$

The Slater determinant has N-electrons occupying N-spin orbitals without specifying which electron is in which orbital, thus maintaining the indistinguishability of the electrons. Interchanging the coordinates of two electrons corresponds to interchanging two rows of the Slater determinant, which changes the sign of the determinant, satisfying the anti-symmetry requirement. Two electrons occupying the same spin-orbital corresponds to having two columns of the determinant be equal, which makes the determinant zero, satisfying the Pauli exclusion principle. Assuming the electron order runs numerically and showing only the diagonal elements, the determinants can be written in short-hand as

$$\Psi(\mathbf{x_1}, \mathbf{x_2}, \cdots, \mathbf{x_N}) = |\chi_1 \chi_2 \cdots \chi_N\rangle \tag{2.26}$$

2.2.1.6 Emergent Exchange Effects from the Anti-symmetry Principle

The construction of the many-electron wavefunction as a Slater determinant also introduces exchange effects which manifest for electrons with parallel spin. The exchange effects can be understood by considering the joint probability of finding two electrons at their respective coordinate $\mathbf{x_1}$ and $\mathbf{x_2}$. The two-electron Slater determinant is

$$\Psi(\mathbf{x_1}, \mathbf{x_2}) = |\chi_1(\mathbf{x_1})\chi_2(\mathbf{x_2})\rangle = \frac{1}{\sqrt{2}} \begin{vmatrix} \chi_1(\mathbf{x_1}) & \chi_2(\mathbf{x_1}) \\ \chi_1(\mathbf{x_2}) & \chi_2(\mathbf{x_2}) \end{vmatrix} \tag{2.27}$$

and can be expanded to

$$\Psi(\mathbf{x_1}, \mathbf{x_2}) = \frac{1}{\sqrt{2}}[\chi_1(\mathbf{x_1})\chi_2(\mathbf{x_2}) - \chi_2(\mathbf{x_1})\chi_1(\mathbf{x_2})] \tag{2.28}$$

In the case whereby two electrons have opposite spin and occupy different spatial orbitals, the two spin-orbitals

$$\chi_1(\mathbf{x_1}) = \psi_1(\mathbf{r_1})\alpha(\omega_1) \tag{2.29}$$

$$\chi_2(\mathbf{x_2}) = \psi_2(\mathbf{r_2})\beta(\omega_2) \tag{2.30}$$

can be formed. Substituting these spin-orbitals into the anti-symmetric wavefunction eq. (2.28) and simplifying the result, gives

$$\Psi(\mathbf{x_1},\mathbf{x_2}) = \frac{1}{\sqrt{2}}[\psi_1(\mathbf{r_1})\psi_2(\mathbf{r_2})\alpha(\omega_1)\beta(\omega_2) - \psi_1(\mathbf{r_2})\psi_2(\mathbf{r_1})\alpha(\omega_2)\beta(\omega_1)] \tag{2.31}$$

Using eq. (2.19) the simultaneous probability of electron-one being in $\mathrm{d}\mathbf{x_1}$ and electron-two in being $\mathrm{d}\mathbf{x_2}$ can be written (dropping $\mathrm{d}\mathbf{x_1}\mathrm{d}\mathbf{x_2}$ for brevity) as

$$|\Psi(\mathbf{x_1},\mathbf{x_2})|^2 = \Psi(\mathbf{x_1},\mathbf{x_2})^*\Psi(\mathbf{x_1},\mathbf{x_2}) \tag{2.32}$$

$$= \frac{1}{2}|\psi_1(\mathbf{r_1})\psi_2(\mathbf{r_2})\alpha(\omega_1)\beta(\omega_2) - \psi_1(\mathbf{r_2})\psi_2(\mathbf{r_1})\alpha(\omega_2)\beta(\omega_1)|^2 \tag{2.33}$$

expanding to

$$= \frac{1}{2}\Big\{ \underbrace{|\psi_1(\mathbf{r_1})|^2|\psi_2(\mathbf{r_2})|^2|\alpha(\omega_1)|^2|\beta(\omega_2)|^2}_{\text{Term}_1} + \underbrace{|\psi_1(\mathbf{r_2})|^2|\psi_2(\mathbf{r_1})|^2|\beta(\omega_1)|^2|\alpha(\omega_2)|^2}_{\text{Term}_2}$$
$$- \big[\psi_1^*(\mathbf{r_1})\psi_2(\mathbf{r_1})\psi_2^*(\mathbf{r_2})\psi_1(\mathbf{r_2})\alpha^*(\omega_1)\beta(\omega_1)\beta^*(\omega_2)\alpha(\omega_2)$$
$$\underbrace{+\psi_2^*(\mathbf{r_1})\psi_1(\mathbf{r_1})\psi_1^*(\mathbf{r_2})\psi_2(\mathbf{r_2})\beta^*(\omega_1)\alpha(\omega_1)\alpha^*(\omega_2)\beta(\omega_2)\big]}_{\text{Cross-Terms}}\Big\} \tag{2.34}$$

The probability of finding electron-one in $\mathrm{d}\mathbf{r_1}$ at $\mathbf{r_1}$ and simultaneously finding electron-two in $\mathrm{d}\mathbf{r_2}$ at $\mathbf{r_2}$ is given as $P(\mathbf{r_1},\mathbf{r_2})\,\mathrm{d}\mathbf{r_1}\,\mathrm{d}\mathbf{r_2}$ and is obtain by integrating over spin coordinates ω_1 and ω_2

$$P(\mathbf{r_1},\mathbf{r_2})\,\mathrm{d}\mathbf{r_1}\,\mathrm{d}\mathbf{r_2} = \int |\Psi(\mathbf{x_1},\mathbf{x_2})|^2\,\mathrm{d}\mathbf{r_1}\,\mathrm{d}\mathbf{r_2}\,\mathrm{d}\omega_1\,\mathrm{d}\omega_2 \tag{2.35}$$

$$= \int \mathrm{d}\omega_1 \int \mathrm{d}\omega_2 \left(\Psi(\mathbf{x_1},\mathbf{x_2})\,\mathrm{d}\mathbf{r_1}\,\mathrm{d}\mathbf{r_2}\right) \tag{2.36}$$

$$= \int \mathrm{d}\omega_1 \int \mathrm{d}\omega_2 \left(\frac{1}{2}[\text{Term}_1 + \text{Term}_2 - \text{Cross-Terms}]\right) \tag{2.37}$$

Each spin-function that appears in the terms of eq. (2.34) are integrated using the normalisation and orthogonality properties of the spin functions expressed in eqs. 2.10-2.11.

$$\text{Term}_1 = |\psi_1(\mathbf{r_1})|^2|\psi_2(\mathbf{r_2})|^2 \int |\alpha(\omega_1)|^2\,\mathrm{d}\omega_1 \int |\beta(\omega_2)|^2\,\mathrm{d}\omega_2 = |\psi_1(\mathbf{r_1})|^2|\psi_2(\mathbf{r_2})|^2 \tag{2.38}$$

$$\text{Term}_2 = |\psi_1(\mathbf{r_2})|^2|\psi_2(\mathbf{r_1})|^2 \int |\alpha(\omega_2)|^2\,\mathrm{d}\omega_2 \int |\beta(\omega_1)|^2\,\mathrm{d}\omega_1 = |\psi_1(\mathbf{r_2})|^2|\psi_2(\mathbf{r_1})|^2 \tag{2.39}$$

For the Cross-Terms, integration over the spin coordinates causes the terms to vanishes, since the functions are orthonormal

$$\int \alpha^*(\omega_1)\beta(\omega_1)\,\mathrm{d}\omega_{\mathbf{1}} \int \beta^*(\omega_2)\alpha(\omega_2)\,\mathrm{d}\omega_{\mathbf{2}} = \langle\alpha|\beta\rangle \cdot \langle\beta|\alpha\rangle = 0 \tag{2.40}$$

$$\int \beta^*(\omega_1)\alpha(\omega_1)\,\mathrm{d}\omega_{\mathbf{1}} \int \alpha^*(\omega_2)\beta(\omega_2)\,\mathrm{d}\omega_{\mathbf{2}} = \langle\beta|\alpha\rangle \cdot \langle\alpha|\beta\rangle = 0 \tag{2.41}$$

$$\tag{2.42}$$

Therefore, the probability of finding two electrons simultaneously at two points in space is non-zero

$$P(\mathbf{r_1}, \mathbf{r_2})\,\mathrm{d}\mathbf{r_1}\,\mathrm{d}\mathbf{r_2} = \frac{1}{2}\left[|\psi_1(\mathbf{r_1})|^2|\psi_2(\mathbf{r_2})|^2 + |\psi_1(\mathbf{r_2})|^2|\psi_2(\mathbf{r_1})|^2\right]\mathrm{d}\mathbf{r_1}\,\mathrm{d}\mathbf{r_2} \tag{2.43}$$

The first term is the product of the probability of finding each electron in a volume element when electron-one occupies ψ_1 and electron-two occupies ψ_2. The second term is the product of the probability when electron-one occupies ψ_2 and electron-two occupies ψ_1. Since the electrons are indistinguishable, the overall probability is the average of the two independent probability terms as shown in eq. (2.43), and thus the motion of the two electrons with opposite spin is uncorrelated. This is particularly obvious if $\psi_1 = \psi_2$, for in that case

$$P(\mathbf{r_1}, \mathbf{r_2}) = |\psi_1(\mathbf{r_1})|^2|\psi_1(\mathbf{r_2})|^2 \neq 0 \tag{2.44}$$

and since the probability cannot be zero, there is a finite probability of finding two electrons with opposite spins at the same point in space. If the two electrons have the same spin, the spin-orbitals take the form

$$\chi_1(\mathbf{x_1}) = \psi_1(\mathbf{r_1})\beta(\omega_1) \tag{2.45}$$

$$\chi_2(\mathbf{x_2}) = \psi_2(\mathbf{r_2})\beta(\omega_2) \tag{2.46}$$

Following similar steps above, in this case the cross terms do not vanish.

$$\begin{aligned} P(\mathbf{r_1}, \mathbf{r_2}) = \frac{1}{2}\Big\{ & |\psi_1(\mathbf{r_1})|^2|\psi_2(\mathbf{r_2})|^2 + |\psi_1(\mathbf{r_2})|^2|\psi_2(\mathbf{r_1})|^2 \\ & - \left[\psi_1^*(\mathbf{r_1})\psi_2(\mathbf{r_1})\psi_2^*(\mathbf{r_2})\psi_1(\mathbf{r_2}) \right. \\ & \left. + \psi_2^*(\mathbf{r_1})\psi_1(\mathbf{r_1})\psi_1^*(\mathbf{r_2})\psi_2(\mathbf{r_2})\right]\Big\} \end{aligned} \tag{2.47}$$

The cross terms mean that the total probability can longer be represented as the average of two independent probabilities. The probability of finding an electron is now dependent on the position of the other electron, thus the electrons are correlated. This demonstrates the exchange correlation (Fermi correlation) that arises due to electrons with parallel spins. Now, if the two electrons are placed at the same point in space, $i = j$ in eq. (2.47), the resulting probability is zero $P(\mathbf{r_1}, \mathbf{r_1}) = 0$, and the Pauli exclusion principle is enforced. As demonstrated, the same effects do not arise for electrons with opposite spins. Since the motion of opposite spins remains uncorrelated, it is customary to refer to single determinant wavefunctions as uncorrelated in general.

2.2.2 Orbital Basis Sets for Molecules

2.2.2.1 Slater and Gaussian Orbitals

Just as the many-electron wavefunction can be constructed from single electron orbitals, the molecular basis set can be constructed from atomic basis functions. This constitutes the atoms-in-molecules approach to designing basis sets. The idea being that a basis set for the molecule can be constructed through basis functions optimised for each atomic centre. The general form of an atomic function in polar coordinates is obtained from solving the Schrödinger equation for a single electron which yields functions $\psi_{nlm}(r, \theta, \phi)$ in the form

$$\psi_{nlm}(r, \theta, \phi) = R_{nl}(r) Y_{lm}(\theta, \phi) \tag{2.48}$$

which is a product of a radial $R_{nl}(r)$ and angular $Y_{lm}(\theta, \phi)$ function. This form applies to the one-electron wavefunctions for the Hydrogenic systems for example, and leads quite naturally to Laguerre functions. These functions form a complete orthonormal set of functions that combine a fixed-exponent exponential decay with a polynomial in r. However, forming basis functions that retain the exact characteristics of hydrogenic orbitals fails in practice in adopting characteristics of other atoms. This is due to the inflexibility of using a fixed exponent, which restricts the ability of functions to mimic characteristics of other centres. This can be resolved by using variable exponents in the form of Slater functions. However, introducing variable exponents means the resulting functions are no longer orthogonal, and results in overlap integrals having to be explicitly

considered in calculations.

The Slater orbitals take the functional form.

$$\phi^{\mathrm{SF}}_{\zeta,n,l,m}(r,\theta,\psi) = NY_{l,m}(\theta,\psi)r^{n-1}e^{-\zeta r} \tag{2.49}$$

were N is a normalisation constant and $Y_{l,m}$ are spherical harmonic functions. The exponential dependence on r mirrors that of the exact orbitals for the hydrogen atom but STOs do not have any radial nodes, these are introduced through taking linear combinations of STOs. In practice, Slater determinants are a hindrance in the calculations since four-centre two-electron integrals cannot be performed analytically. The use of Gaussian functions avoids this issue due to the specific mathematical properties of the functions, reducing the two-electron integrals from a four-centre to a solvable two-centre problem. This is explored in more detail for the H_2 molecule as an example in section 2.2.2.2.

Gaussian orbitals can be written in either polar or Cartesian coordinates as

$$\phi_{\zeta,n,l,m}(r,\theta,\psi) = NY_{l,m}(\theta,\psi)r^{2n-2-l}e^{-\zeta r^2} \tag{2.50}$$

$$\phi_{\zeta,n,l,m}(x,y,z) = Nx^{lx}y^{ly}z^{lz}e^{-\zeta r^2} \tag{2.51}$$

where the l_x, l_y and l_z terms determine the type of orbital (s,p,d,f,...). The r^2 dependence in the exponential makes the GTOs inferior to STO at the two extremes of r. The form of the exponential functions at $\mathbf{r} = 0$, means the two functions differ at the atomic nucleus. The Slater function has a finite slope representing a nuclear 'cusp', while the Gaussian function has a zero slope demonstrated by taking the differential with respect to $\mathbf{r}$

$$\frac{d}{dr}e^{-\zeta r}\Big|_{r=0} \neq 0 \tag{2.52}$$

$$\frac{d}{dr}e^{-\zeta r^2}\Big|_{r=0} = 0 \tag{2.53}$$

At large values of $\mathbf{r}$, the Gaussian functions decay more rapidly than the Slater, with the behaviour of the latter aligning more closely with the known characteristics of the hydrogenic atomic orbitals. This makes Slater functions inherently more accurate than the Gaussian functions, meaning more Gaussian functions are required in order to obtain a basis set with identical accuracy to that of a basis formed from Slater functions. However, the increased number of functions required in Gaussian basis sets is more than

compensated for by the increase in computational efficiency gained by enabling analytical solutions to the two-electron integrals.

2.2.2.2 Minimal Basis H_2 Model

The hydrogen molecule offers a simple model by which to consider the how basis functions optimised for atomic centres come to form molecular orbitals. Additionally, it can be demonstrated how the choice of basis function, Slater or Gaussian, aids in molecular calculations. Lets consider two H-atoms centred at $\mathbf{R_1}$ and $\mathbf{R_2}$ separated at distance $\mathbf{R_{12}} = |\mathbf{R_1} - \mathbf{R_2}|$, each with a single electron residing in an s-orbital ($1s^1$ electronic configurations). An atomic function representing the 1s-orbital is centered on each hydrogen atom R_1 and R_2, and defined as $\phi_1(\mathbf{r} - \mathbf{R_1})$ and $\phi_2(\mathbf{r} - \mathbf{R_2})$. The exact form of the 1s atomic orbital for hydrogen is the normalised Slater function centred at $\mathbf{R}$

$$\phi_{1s}^{SF}(\zeta, \mathbf{r} - \mathbf{R}) = \left(\frac{\zeta^3}{\pi}\right)^{1/2} \exp\big(-|\mathbf{r} - \mathbf{R}|\big) \tag{2.54}$$

where ζ is the orbital exponent. The two atomic orbitals $\phi_1(\mathbf{r} - \mathbf{R_1})$ and $\phi_2(\mathbf{r} - \mathbf{R_2})$ can be assumed normalised but not orthogonal, meaning the overlap takes the form

$$S_{12} = \int \phi_1^*(\mathbf{r})\phi_2(\mathbf{r})\,\mathrm{d}\mathbf{r} \tag{2.55}$$

The overlap depends on the position of the two atoms R_{12}, returning a value of unity when $R_{12} = 0$, a value of zero when $R_{12} = \infty$, and a non-zero value otherwise. At distances approaching the bond length, a linear combination of atomic orbitals generates a symmetric (gerade) and un-symmetric (un-gerade) bonding (ψ_1) and anti-bonding (ψ_2^*) molecular orbital, respectively. These take the form

$$\psi_1 = \frac{1}{\sqrt{2(1 + S_{12})}}(\phi_1 + \phi_2) \tag{2.56}$$

$$\psi_2^* = \frac{1}{\sqrt{2(1 - S_{12})}}(\phi_1 - \phi_2) \tag{2.57}$$

This combination of the two 1s hydrogen atomic orbitals is a special case of a more general linear combination of atomic orbitals scheme (eq. (2.58)) used to generate sets of spatial molecular orbitals $\psi_i(\mathbf{r})$, from a set of spatial basis functions $\{\phi_\mu(\mathbf{r})\}$ known as the basis set.

$$\psi_i(\mathbf{r}) = \sum_{\mu=1}^{K} C_{\mu i}\phi_\mu(\mathbf{r}) \tag{2.58}$$

The example provided for H_2 represents a minimal basis set. A higher equality description of the molecular bonding would be achieved by including additional functions in the basis set (s,p,d,f...), such that each centre has multiple basis functions. The Slater orbitals take the exact form of the hydrogen 1s-orbitals and therefore the initial expectation might be that these are the preferred route to describing the molecular orbitals. However, as noted in section section 2.2.2.1, out of the two functions, only Gaussian functions enable analytical solutions to the two-electron integrals to be obtained. This can be demonstrated for H_2 by considering the normalised 1s Gaussian function

$$\phi_{1s}^{\mathrm{GF}}(\alpha, \mathbf{r} - \mathbf{R}) = \Big(\frac{2\alpha}{\pi}\Big)^{3/4} \exp\big(-\alpha|\mathbf{r} - \mathbf{R}|^2\big) \tag{2.59}$$

where α is the orbital exponent. The two-electron integrals encountered in calculations involve the two-electron operator $(1/r_{12})$ and take the form

$$\langle \mu_A \nu_B | \lambda_C \sigma_D \rangle = \int \phi_\mu^{A*}(\mathbf{r_1}) \phi_\nu^B(\mathbf{r_1}) \frac{1}{r_{12}} \phi_\lambda^{C*}(\mathbf{r_2}) \phi_\sigma^D(\mathbf{r_2})\, \mathrm{d}\mathbf{r_1}\, \mathrm{d}\mathbf{r_2} \tag{2.60}$$

where $\{\phi_\mu^A, \phi_\nu^B, \phi_\lambda^C, \phi_\sigma^D\}$ are the basis functions consisting the basis set, which are centred on the nuclei $\{A, B, C, D\}$, each with a corresponding nuclear position $\{\mathbf{R_A}, \mathbf{R_B}, \mathbf{R_C}, \mathbf{R_D}\}$. The use of Gaussian basis functions enables the reduction of the four-centre integral to a two-centre integral problem through the application of the Gaussian product theorem. This states that the product of any two Gaussian functions generates a new Gaussian function on a third centre as follows

$$\phi_{1s}^{\mathrm{GF}}(\alpha, \mathbf{r} - \mathbf{R_A}) \phi_{1s}^{\mathrm{GF}}(\beta, \mathbf{r} - \mathbf{R_B}) = K_{AB} \phi_{1s}^{\mathrm{GF}}(p, \mathbf{r} - \mathbf{R_P}) \tag{2.61}$$

where K_{AB} is a constant, R_p is the new Gaussian center, and p is the new Gaussian exponent. Each of these parameters is easily evaluated. By applying the Gaussian product theorem to both sides of the two-electron operator $(1/r_{12})$, the four centre integral can be reduce to a two-centre integral as follows

$$\langle \mu_A \nu_B | \lambda_C \sigma_D \rangle = K_{AB} K_{CD} \int \phi_{1s}^{GF}(p, \mathbf{r_1} - \mathbf{R_P}) \frac{1}{r_{12}} \phi_{1s}^{GF}(q, \mathbf{r_1} - \mathbf{R_Q})\, \mathrm{d}\mathbf{r_1}\, \mathrm{d}\mathbf{r_2} \tag{2.62}$$

which can be readily evaluated using a variety of efficient mathematical procedures. The drawback to using Gaussian functions is that unlike the Slater functions, they lack the behaviour of known atomic orbitals. A solution to this problem, is to make use of basis

functions formed from a fixed linear combination of primitive Gaussian functions ϕ_p^{GF}. These linear combinations generate contracted Gaussian functions (CGF)

$$\phi_\mu^{\mathrm{CGF}}(\mathbf{r}-\mathbf{R_A}) = \sum_{p=1}^{L} d_{p\mu}\phi_p^{GF}(\alpha_{p\mu}, \mathbf{r}-\mathbf{R_A}) \tag{2.63}$$

where L is the length of the contraction, $d_{p\mu}$ is a contraction coefficient, and $\alpha_{p\mu}$ is the contraction exponent. By varying L, $d_{p\mu}$ and $\alpha_{p\mu}$ values, the contracted Gaussian can take on numerous forms consistent with the symmetry of the primitive functions used. In practice, the optimal values of these parameters is calculated in advance for a general set of atomic systems and then utilised in routine molecular calculations. The actual contraction coefficients and exponents can be found in databases such as the basis set exchange.[5]

2.2.2.3 Relativistic Atomic Natural Orbital (ANO) Basis Sets

The basis sets used in this thesis are the relativistic atomic natural orbital ANO-RCC basis sets of Roos et al.[6–8] These ANO basis sets contract a large number of primitive Gaussian functions into a small number of contracted Gaussian functions determined using correlated wavefunction approaches (CASSCF/CASPT2). The ANO basis sets are based on the natural orbitals that diagonalise the one-electron density matrix ρ_k for an electronic state of an atom and the contraction coefficients are simply the orbital coefficients of the natural orbitals.[9] A benefit of these approaches is that instead of using the density matrix ρ_k for one specific electronic state to obtain the contraction coefficients, the density matrix $\tilde{\rho}$ that is an average of several electronic states can be used

$$\tilde{\rho} = \sum_k \omega_k \rho_k \tag{2.64}$$

where ω_k are the weights of the different electronic states. The ANO-RCC basis sets were generated by obtaining an average density matrix for the ground-state and lowest excited state of the atom, as well as its ions and in the presence an electric field. Each density matrix was obtained from correlated wavefunctions (CASSCF/CASPT2) using the Douglas-Kroll-Hess Hamiltonian to introduce scalar relativistic effects into the contraction. The wavefunctions include the semi-core 6s and 6p electrons in the correlation treatment, which have been identified as important for a good quality description of the actinides. Equal weights, ω_i, were used for all states and the final ANOs were obtained as the

eigenfunctions of $\tilde{\rho}$. The basis set calculations themselves were performed using the built-in GENANO utility of Molcas.[9]

From uranium to plutonium, a total of 12s, 10p, 9d, 7f, 5g, and 3h basis functions in total have been obtained for the ANO-RCC basis sets. Each individual function type (s,p,d,f...) has been constructed from 26s, 23p, 17d, 13f, 5g, and 3h primitive Gaussian functions. This contraction of primitive Gaussian's into contracted Gaussian basis functions can be denoted (26s,23p,17d,13f,5g,3h)→[12s,10p,9d,7f,5g,3h]. In practice smaller contractions tend to be used, with calculations on the actinides in this thesis utilising a contraction of (26s,23p,17d,13f,5g,3h)→[9s,8p,6d,4f,2g], which corresponds to a TZVP-quality basis set.

For a practical example of how this works, consider the ANO-RCC s-functions for hydrogen, which at the TZVP quality corresponds to a contraction of (8s,4p,3d)→[3s,2p,1d]. The hydrogen centre is described with three s-type basis functions $\{\phi_\mu^{\mathrm{CGF}}\}_{\mu=1}^{3} = \{\phi_1^{\mathrm{CGF}}, \phi_2^{\mathrm{CGF}}, \phi_3^{\mathrm{CGF}}\}$ each of which (recall from eq. (2.63)) can be expanded as a linear combination of eight s-type primitive Gaussian's,

$$\phi_1^{\mathrm{CGF}} = \sum_{p=1}^{8} d_{p1}\phi_p^{\mathrm{GF}}(\alpha_p) = d_{11}\phi_1^{\mathrm{GF}}(\alpha_1) + d_{21}\phi_2^{\mathrm{GF}}(\alpha_2) + \cdots + d_{81}\phi_8^{\mathrm{GF}}(\alpha_8) \tag{2.65}$$

$$\phi_2^{\mathrm{CGF}} = \sum_{p=1}^{8} d_{p2}\phi_p^{\mathrm{GF}}(\alpha_p) = d_{12}\phi_1^{\mathrm{GF}}(\alpha_1) + d_{22}\phi_2^{\mathrm{GF}}(\alpha_2) + \cdots + d_{82}\phi_8^{\mathrm{GF}}(\alpha_8) \tag{2.66}$$

$$\phi_3^{\mathrm{CGF}} = \sum_{p=1}^{8} d_{p3}\phi_p^{\mathrm{GF}}(\alpha_p) = d_{13}\phi_1^{\mathrm{GF}}(\alpha_1) + d_{23}\phi_2^{\mathrm{GF}}(\alpha_2) + \cdots + d_{83}\phi_8^{\mathrm{GF}}(\alpha_8) \tag{2.67}$$

each with their own contraction coefficients but shared exponents. Similar procedures apply to the p- and d-basis functions of the basis set. The value of the contraction parameters themselves, are those obtained in the ANO-RCC paper by Roos et al.[8] and now stored in basis set libraries such as the basis set exchange.[5]

2.3 The Variation Principal

Up to this stage, discussion has focused on the characteristics the many-electron wavefunction must exhibit in order to correctly describe the nature of electrons in molecules. This introduced the idea of the Slater determinants which ensures the wavefunctions consisting of spin-orbitals are anti-symmetric with respect to the exchange

of two electrons. In the preceding sections, the idea of a basis set was introduced to describe the spatial component of the spin-orbitals. The exact many-electron wavefunction describes all the electronic states of a system, however, in the majority of cases it is the ground-state that is of interest. The key to finding this wavefunction is in solving the Schrödinger equation to obtain the lowest energy solution. The Schödinger equation cannot be solved exactly, except for in the simplest of cases, and therefore we are interested in finding approximate solutions. To proceed, a formal means by which to optimise the wavefunction to obtain the lowest energy solution is required. This is realised in the variation principle.

The variation principle states that the expectation value for any give trial wavefunction Φ with the Hamiltonian operator cannot be lower in energy than the exact wavefunction Ψ_0 which yields the exact ground-state energy E_0. This principle written formally as an upper bound to the exact ground-state energy

$$\frac{\langle\Phi|\,\hat{H}\,|\Phi\rangle}{\langle\Phi|\Phi\rangle} \geq E_0 \tag{2.68}$$

Not only does this bound provide a criteria by which to determine the quality of a trial/approximate wavefunction, but is also provides a means by which to optimise the approximate wavefunction. The expansion coefficients that express the molecular orbitals in terms of a linear combination of atomic orbitals (eq. (2.58)) can be varied subject to minimising the expectation value $\langle\Phi|\,\hat{H}\,|\Phi\rangle$. Therefore, the numerical parameters (orbital coefficients, CI expansion coefficients, or both) that make-up the approximate many-electron wavefunction can be varied in order to return the lower possible energy expectation value for the full electronic Hamiltonian $\hat{H}$.

2.4 Hartree-Fock Theory

2.4.1 The Hartree-Fock Equations

Hartree-Fock (HF) theory considers a single determinant and is interested in finding a set of spin-orbitals $\{\chi_a\}$ such that the single determinant $|\Psi_0\rangle$ formed from these spin-orbitals

$$|\Psi_0\rangle = |\chi_1\chi_2\cdots\chi_a\chi_b\cdots\chi_N\rangle \tag{2.69}$$

is the best possible approximation to the ground-state of the N-electron system described by an electronic Hamiltonian $\hat{H}$. The variation principle states that the optimal spin-orbitals are those than minimise the electronic energy. Since the operators of the $\hat{H}_{\text{elec}}$ electronic Hamiltonian do not include any spin-terms, the spin component of the spin-orbitals remain effectively unchanged, and it is the spatial component that is optimised to obtain a ground-state solution. By systematically varying the spin orbitals until the energy E_0 is a minimum, subject to orthogonality constraints, yields an equation for the optimal spin orbitals called the Hartree-Fock equation

$$\underbrace{h(\mathbf{x_1})\chi_i(\mathbf{x_1})}_{\hat{h}(\mathbf{x_1})} + \sum_{j\neq i}\Big[\underbrace{\int \mathrm{d}\mathbf{x_2}\,\chi_j^*(\mathbf{x_2})\chi_j(\mathbf{x_2})r_{12}^{-1}}_{\hat{J}_j(\mathbf{x_1})}\Big]\chi_i(\mathbf{x_1}) - \sum_{j\neq i}\underbrace{\Big[\int \mathrm{d}\mathbf{x_2}\chi_j^*(\mathbf{x_2})\chi_i(\mathbf{x_2})r_{12}^{-1}\Big]\chi_j(\mathbf{x_1})}_{\hat{K}_j(\mathbf{x_1})} = \epsilon_i\chi_i(\mathbf{x_1}) \tag{2.70}$$

This result takes the unsolvable many-electron problem of the electronic Hamiltonian and turns it into a series of solvable (at least approximately) one-electron problems in which the electron-electron interactions are treated as an interaction of an electron (in this case we choose electron-one $\mathbf{X_1}$) with a mean-field of all the other electrons. Each term can be considered in-term as an operator acting on a spin-orbital. The first term contains a one-electron operator called the core-Hamiltonian which acts on a spin-orbital

$$\hat{h}(\mathbf{x_1}) = -\frac{1}{2}\nabla_i^2 - \sum_A \frac{Z_A}{r_{1A}} \tag{2.71}$$

and governs the kinetic energy of an electron (chosen to be $\mathbf{X_1}$) in spin-orbital χ_i as well as the nuclear attraction of an electron in χ_i with the set of nuclei with charge Z_A. The second term is the Coulomb interaction of an electron in χ_i with the average charge distribution (mean-field) of the other electrons

$$\Big[\underbrace{\int \mathrm{d}\mathbf{x_2}\,\chi_j^*(\mathbf{x_2})\chi_j(\mathbf{x_2})r_{12}^{-1}}_{\hat{J}_j(\mathbf{x_1})}\Big]\chi_i(\mathbf{x_1}) \tag{2.72}$$

$$\hat{J}(\mathbf{x_1}) = \int \mathrm{d}\mathbf{x_2}\,\chi_j^*(\mathbf{x_2})\chi_j(\mathbf{x_2})r_{12}^{-1} \tag{2.73}$$

this operator gives the local potential at a point $\mathbf{x_1}$ due to the charge distribution of electrons in χ_j. The third term is harder to explain since it has no classical analog, arising from the anti-symmetry of the wavefunction. It appears similar in form to the Coulomb interaction but has two of the spin-orbital labels swapped/exchanged. The exchange-operator is defined based on its action on an arbitrary spin-orbital χ_i

$$\hat{K}_j(\mathbf{x_1}) \cdot \chi_i(\mathbf{x_1}) = \Big[\int \mathrm{d}\mathbf{x_2} \chi_j^*(\mathbf{x_2}) \chi_i(\mathbf{x_2}) r_{12}^{-1} \Big] \cdot \chi_j(\mathbf{x_1}) \tag{2.74}$$

This term is similar to $\hat{J}$ except in that the labels of i and j are exchanged

$$\underbrace{\chi_j^*(\mathbf{x_2})\chi_j(\mathbf{x_2}) \cdot \underbrace{\chi_i(\mathbf{x_1})}_{\text{labelled } i}}_{\text{Before}} \underset{\hat{K}}{\Rightarrow} \underbrace{\chi_j^*(\mathbf{x_2})\chi_i(\mathbf{x_2}) \cdot \underbrace{\chi_j(\mathbf{x_1})}_{\text{labelled } j}}_{\text{After}} \tag{2.75}$$

Having defined the operators, the Hartree-Fock equations can be written in a cleaner notation

$$\Big[\hat{h}(\mathbf{x_1}) + \sum_{j \neq i} \hat{J}_i(\mathbf{x_1}) - \sum_{j \neq i} \hat{K}_i(\mathbf{x_1}) \Big] \chi_i(\mathbf{x_1}) = \epsilon_i \chi_i(\mathbf{x_1}) \tag{2.76}$$

notice that if $j = i$ then

$$\begin{aligned} &\Big\{ \sum_{j \neq i} \hat{J}_i(\mathbf{x_1}) - \sum_{j \neq i} \hat{K}_i(\mathbf{x_1}) \Big\} \chi_i(\mathbf{x_1}) = \Big\{ \sum_i \hat{J}_i(\mathbf{x_1}) - \sum_i \hat{K}_i(\mathbf{x_1}) \Big\} \chi_i(\mathbf{x_1}) \\ &= \int \mathrm{d}\mathbf{x_2}\, \chi_i^*(\mathbf{x_2}) r_{12}^{-1} \chi_i^*(\mathbf{x_2}) \chi_i^*(\mathbf{x_1}) - \int \mathrm{d}\mathbf{x_2}\, \chi_i^*(\mathbf{x_2}) r_{12}^{-1} \chi_i^*(\mathbf{x_2}) \chi_i^*(\mathbf{x_1}) = 0 \end{aligned} \tag{2.77}$$

and therefore the $i \neq j$ constraint can be dropped to give

$$\Big[\hat{h}(\mathbf{x_1}) + \sum_{j} \hat{J}_j(\mathbf{x_1}) - \hat{K}_j(\mathbf{x_1}) \Big] \chi_i(\mathbf{x_1}) = \epsilon_i \chi_i(\mathbf{x_1}) \tag{2.78}$$

and in its final pseudo eigenvalue form, can be written as

$$\hat{f}(\mathbf{x_1}) \chi_i(\mathbf{x_1}) = \epsilon_i \chi_i(\mathbf{x_1}) \tag{2.79}$$

where $\hat{f}(\mathbf{x_1})$ is the one-electron Fock operator and eq. (2.79) is the pseudo-eigenvalue Hartree-Fock equation. The Fock operator can also be written in the form of the core Hamiltonian $\hat{h}(\mathbf{x_1})$ and a mean-field operator $\hat{v}^{\mathrm{HF}}(\mathbf{x_1})$ which contains the Coulomb and exchange operators

$$\hat{f}(\mathbf{x_1}) = \hat{h}(\mathbf{x_1}) + \hat{v}^{\mathrm{HF}}(\mathbf{x_1}) \tag{2.80}$$

where

$$\hat{v}^{\mathrm{HF}}(\mathbf{x_1}) = \sum_j \hat{J}_j(\mathbf{x_1}) - \hat{K}_j(\mathbf{x_1}) \tag{2.81}$$

The equation 2.79 is a pseudo-eigenvalue equation as opposed to an eigenvalue equation, as the $\hat{v}^{\mathrm{HF}}(\mathbf{x_1})$ operator is dependent on all the other electrons in the system. Note that in this case electron-one ($\mathbf{X_1}$) is chosen to represent the fact that these are one-electron operators. Putting this all together, the Fock matrix can be generalised to any electron i representing a particular electron $\mathbf{X}_i = \{\mathbf{r}, \omega\}$ consisting of a spatial and spin coordinate, giving the one-electron Fock operator

$$\hat{f}(i) = \hat{h}(i) + \hat{v}^{\mathrm{HF}}(i) = \hat{h}(i) + \sum_j \hat{J}_j(i) - \hat{K}_j(i) \tag{2.82}$$

The full Hartree-Fock Hamiltonian can be compressed into a single summation over the one-electron Fock operator

$$\hat{H}^{\mathrm{HF}} = \sum_i \hat{f}(i) \tag{2.83}$$

which is applied to each one-electron spin-orbital in the Hartree-Fock wavefunction $|\Psi_0\rangle$ to yield the Hartree-Fock equations. At this stage the Hartree-Fock equations are known, but to solve the equations requires a reformulation of the equations into a linear algebra problem that can be solved using computers, and forms the discussion in the next section.

2.4.2 The Roothaan-Hall Equations

Exact Hartree-Fock solutions to the pseudo-eigenvalue problem eq. (2.79) are only possible in practice for the atoms. For molecules, the introduction of a basis set consisting of basis functions must be introduced to expand the spin-orbitals. Furthermore, since eq. (2.79) is not actually a formal eigenvalue equation but a pseudo-eigenvalue equation, the problem must be solved by an iterative procedure. The first step is to generate the Roothaan-Hall equations.

So far, HF has been discussed in terms of a general set of spin-orbitals $\{\chi_i\}$. In this section restricted HF will be the focus of discussion. In restricted HF, the spin-orbitals use the same set of spatial functions for both α and β spin-functions and the ground-state

is represented by a closed shell restricted determinant Ψ_0

$$|\Psi_0\rangle = |\chi_1\chi_2\cdots\chi_N\rangle \tag{2.84}$$

the HF equations in terms of spin-orbitals can be converted to an equation in terms of spatial orbitals by integrating over spin coordinates, leading to the closed-shell spatial Hartree-Fock equation

$$\hat{f}(i)\psi_j(\mathbf{r}) = \epsilon_j\psi_j(\mathbf{r}) \tag{2.85}$$

where the one-electron Fock operator has the familiar form

$$\hat{f}(i) = \hat{h}(i) + \sum_{j}^{N/2} 2\hat{J}_j(i) - \hat{K}_j(i) \tag{2.86}$$

The Fock operator takes on an analogous form to that used for the spin-orbitals, except for a factor of 2 occurring with the Coulomb operator. With the spin components eliminated, the calculation of molecular orbitals ψ_j involves solving eq. (2.85). For molecules, the equations are solved by introducing a known set of spatial basis functions consisting a basis set, this was the contribution of Roothaan and Hall.[10, 11] By introducing a basis, the equations are converted from a set of differential equations to a set of linear algebra equations that can be solved with standard matrix techniques.

A set of known K basis functions can be introduced to expand the unknown molecular orbitals as a linear expansion

$$\psi_i = \sum_{\mu=1}^{K} C_{\mu i}\phi_\mu \quad i = 1, 2, \cdots, K \tag{2.87}$$

From this, the problem of calculating HF MOs reduces to the problem of calculating the set of expansion coefficients $C_{\mu i}$. The spatial HF equation, eq. (2.85), can be converted into a matrix equation by substituting the expansion of the molecular orbitals into eq. (2.85) and then introducing the set of complex conjugate basis functions ϕ_u^* in order to perform the necessary integrals. This yields the Roothaan-Hall equations

$$\underbrace{\sum_{\nu} \mathbf{F}_{\mu\nu}C_{\nu i}}_{\hat{f}\psi_j} = \underbrace{\epsilon_i \sum_{v} \mathbf{S}_{\mu\nu}C_{\nu i}}_{\epsilon_j\psi_j} \tag{2.88}$$

$$\mathbf{FC} = \mathbf{SC}\epsilon \tag{2.89}$$

which can be viewed as matrix representations of the terms in eq. (2.85). Here the Fock matrix is a representation of the Fock operator with a set of basis functions $\{\phi_\mu\}$. In this form, the integrals can be performed separately to fill the elements of the Fock and overlap matrix

$$\mathbf{F}_{\mu\nu} = \int \mathrm{d}\mathbf{r_1}\, \phi_\mu^*(\mathbf{r_1})\hat{f}(i)(\mathbf{r_1})\phi_\nu(\mathbf{r_1}) \tag{2.90}$$

$$\mathbf{S}_{\mu\nu} = \int \mathrm{d}\mathbf{r_1}\, \phi_\mu^*(\mathbf{r_1})\phi_\nu(\mathbf{r_1}) \tag{2.91}$$

The resulting $K \times K$ matrix $\mathbf{C}$ contains the expansion coefficients $C_{\mu i}$ and ϵ is a diagonal matrix of the orbital energies ϵ_i

$$C = \begin{pmatrix} C_{11} & C_{12} & \cdots & C_{1K} \\ C_{11} & C_{12} & \cdots & C_{1K} \\ \vdots & \vdots & \ddots & \vdots \\ C_{K1} & C_{K2} & \cdots & C_{KK} \end{pmatrix} \quad \epsilon = \begin{pmatrix} \epsilon_1 & & & \\ & \epsilon_2 & & \\ & & \ddots & \\ & & & \epsilon_K \end{pmatrix}$$

in the matrix $\mathbf{C}$, each column describes a molecular orbital, with column-1 containing the coefficients for ψ_1 up to column-K which contains the coefficients for ψ_K. Each of these MOs have a corresponding energy ϵ_i contained in ϵ. The final step to solving the equations is to find an explicit form of the Fock matrix, such that each part represents a term of the one-electron Fock operator $\hat{f}(i)$

$$\mathbf{F}_{\mu\nu} = \underbrace{\mathbf{H}_{\mu\nu}^{\mathrm{CORE}}}_{\hat{h}(i)} + \underbrace{\mathbf{G}_{\mu\nu}}_{\sum_j^{N/2} 2\hat{J}_j(i) - \hat{K}_j(i)} \tag{2.92}$$

$$\underbrace{\mathbf{H}_{\mu\nu}^{\mathrm{CORE}} = \mathbf{T}_{\mu\nu} + \mathbf{V}_{\mu\nu}^{\mathrm{Nuc}}}_{\hat{h}(i) = -\frac{1}{2}\nabla_i^2 - \sum_A \frac{Z_A}{r_{1A}}} \tag{2.93}$$

$$\mathbf{T}_{\mu\nu} = \int \mathrm{d}\mathbf{r_1}\, \phi_\mu^*(\mathbf{r_1})\Big[-\frac{1}{2}\nabla_i^2\Big]\phi_\mu(\mathbf{r_1}) \tag{2.94}$$

$$\mathbf{V}_{\mu\nu}^{\mathrm{Nuc}} = \int \mathrm{d}\mathbf{r_1}\, \phi_\mu^*(\mathbf{r_1})\Big[-\sum_A \frac{Z_A}{r_{1A}}\Big]\phi_\mu(\mathbf{r_1}) \tag{2.95}$$

This completely defines the one-electron terms of the core-Hamiltonian and once calculated, the matrix elements of the core-Hamiltonian are fixed for a given calculation.

The one-electron integrals themselves are efficient to solve. The second matrix $\mathbf{G}_{\mu\nu}$, encompasses the two-electron interactions and changes over the course of a calculation.

$$\mathbf{G}_{\mu\nu} = \sum_{\lambda\sigma} \mathbf{P}_{\lambda\sigma} \left[(\mu\nu|\lambda\sigma) - \frac{1}{2}(\mu\lambda|\sigma\nu) \right] \tag{2.96}$$

$(\mu\nu|\lambda\sigma)$ is short-hand for the two-electron integrals of the form

$$(\mu\nu|\lambda\sigma) = \int \mathrm{d}\mathbf{r_1}\, \mathrm{d}\mathbf{r_2} \phi^*_\mu(\mathbf{r_1}) \phi_\nu(\mathbf{r_1}) r_{12}^{-1} \phi^*_\lambda(\mathbf{r_2}) \phi_\sigma(\mathbf{r_2}) \tag{2.97}$$

For $(\mu\lambda|\sigma\nu)$, this integral takes the same form as above in eq. (2.97), but two of the labels are exchanged. As discussed previously in section 2.2.2.2, the use of Gaussian basis functions enables the two-electrons to be reduced to an integral involving just two-Gaussian functions by using the Gaussian product theorem to solve these integrals analytically. The matrix $\mathbf{P}_{\lambda\mu}$ is called the density matrix and is an important object in quantum chemistry since if we have a known set of basis function $\{\phi_\mu\}$, then $\mathbf{P}$ specifies completely the electron density $\rho(\mathbf{r})$

$$\mathbf{P}_{\mu\nu} = 2 \sum_{i}^{N/2} C_{\mu i} C^*_{\nu i} \tag{2.98}$$

$$\rho(\mathbf{r}) = 2 \sum_{i}^{N/2} |\psi_i(\mathbf{r})|^2 \tag{2.99}$$

This electron density $\rho(\mathbf{r})$, is the same entity that density functional theory (DFT) is concerned with obtaining, albeit using a different set of eigenvalue equations known as the Kohn-Sham equations.

2.4.3 The Self-Consistent Field (SCF) Procedure

The Roothaan-Hall equations transforms the HF equations into linear algebra form which can be readily coded into computers. From the matrix formulation of the HF equations, to obtaining the molecular orbitals and energies, is a set of fairly routine linear algebra steps. These involve choosing a technique to orthogonalise the basis functions to obtain a unitary overlap matrix, which turns the Roothaan-Hall equations into a standard eigenvalue equation called the transformed Roothaan-Hall equations

$$\mathbf{FC} = \mathbf{C}\epsilon \tag{2.100}$$

where the Fock matrix can be diagonalised to obtain molecular orbitals and energies. The SCF procedure performed on computers is summarised neatly in fig. 2.1. Note that the flow-chart ignores any details regarding transformations between the non-orthogonalised and orthogonalised basis which are important for a practical implementation of the SCF procedure.

Once converged, the resulting **C**, **P** and **F** matrices can be used to calculate expectation values and other quantities of interest for the molecule. The most time consuming part of the process is assembling the two-electron integrals and density matrix into **G**. The criterion for establishing convergence can vary, but the simplest approach is to observe the electronic energy of successive iterations and see if the energy converges towards a certain value.

2.4.4 Electron Correlation

For a real system with more than one-electron, the motion of the electrons is correlated as the electrons repel one another. In the molecular Hamiltonian, the instantaneous electron-electron interactions and their correlated behaviour is governed by the $\sum_{i=1}^{N}\sum_{j>i}^{N}\frac{1}{r_{ij}}$ electron repulsion term. In Hartree-Fock theory, the complicated electron-electron interactions are replaced by considering the interaction of a single electron with the mean-field of the other electrons. The use of Slater determinants in HF theory introduces exchange effects and their energy contributions are fully accounted for, these effects account for the correlation that occurs between electrons of the same spin, known as Fermi correlation. Since these only occur for electrons with the same spin, these exchange effects are not normally encompassed within the term "electron correlation" and do not form part of the correlation energy as defined in eq. (2.101). While Fermi correlation for electrons with the same spin is completely accounted for in Hartree-Fock, electrons with opposite spin remain completely uncorrelated. Instead, the Coulomb repulsion is treated as the average interaction of electrons in charge clouds rather than individual electron interactions. Therefore, the use of a single determinant in HF theory is referred to as uncorrelated since it does not account for this Coulomb correlation. It is important to note that the splitting of electron-electron interactions into those of classical Coulomb and exchange interactions arises as a convenient way to represent the energy contributions to

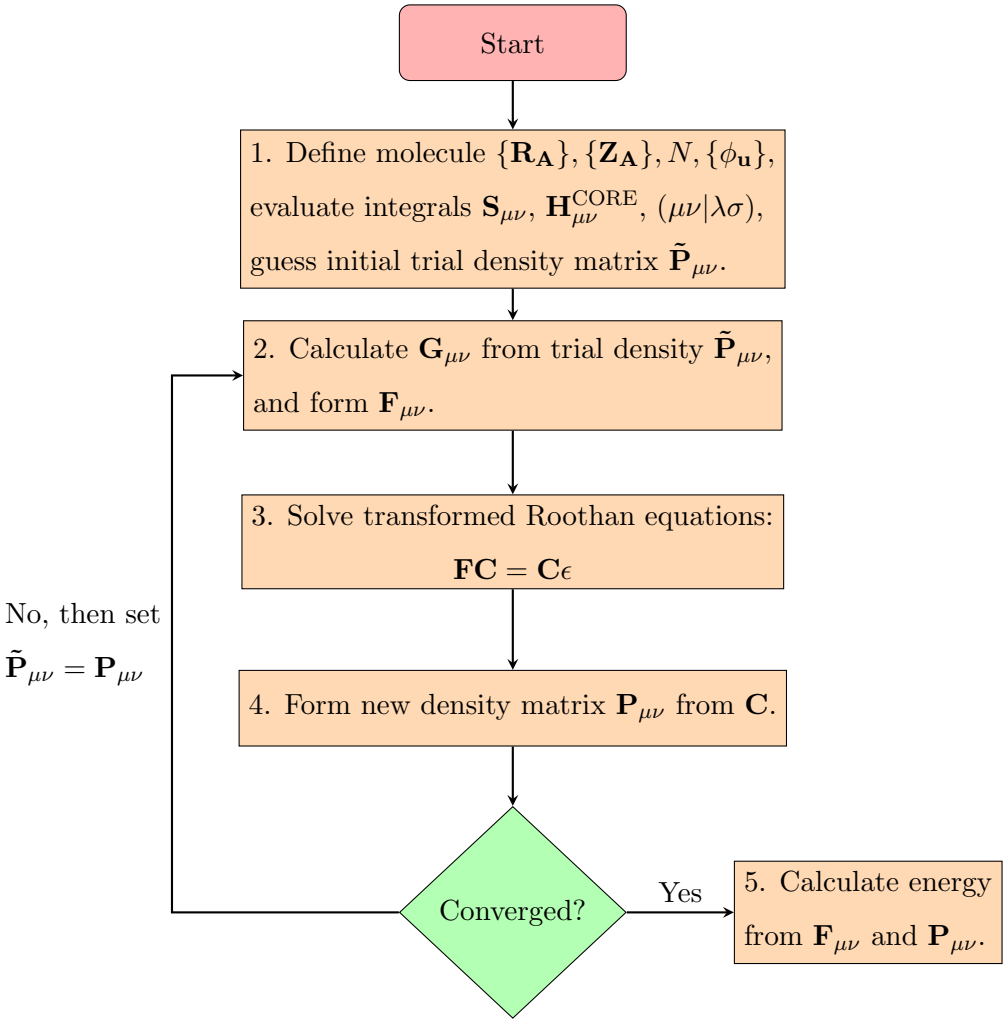

Figure 2.1: The SCF procedure for the Roothaan-Hall formulation of Hartree-Fock theory to obtain a closed-shell ground-state.

a system described by a single determinant. The actual physical interpretation of electron repulsion is contained within the electron repulsion term in the electronic Hamiltonian and does not depend on the spin of the electron. To this point, in the next section detailing density functional theory, no explicit exchange term is formulated when expressing the energy of a system in Kohn-Sham theory, only the classical Coulomb interaction is stated explicitly and used to define the error associated with not including electron correlation, which is collected into the exchange-correlation functional. The lack of correlation energy in Hartree-Fock means that the approach predicts a greater energy than the exact ground-state energy. The energy difference between the exact energy and the Hartree-Fock energy

can be used to define the electron correlation energy

$$E_{\text{corr}} = E_{\text{exact}} - E_{\text{HF}} \tag{2.101}$$

It can be useful to split electron correlation energy into a discussion of dynamic and static correlation. Dynamic correlation refers to the short-range interactions between electrons, such as two electrons in the same spatial orbital, whereby electrons avoid one another to minimise Coulomb repulsion. Static or non-dynamical correlation accounts for long-range electron correlation and is significant when multiple configurations contribute equally to an electronic state. It can be though of as electrons "avoiding" one another through the occupation of different spatial orbitals. To include correlation, approaches beyond the Hartree-Fock level are required, and often termed post Hartree-Fock methods. A straight forward way to improve upon Hartree-Fock is to simply include more Slater determinants in order to capture more possible arrangements of electrons in orbitals other than the ground-state configuration. This is the approach taken in this thesis by using the Restricted Active Space Self-Consistent Field (RASSCF) theory approach. Coupled-cluster theory is also a common approach to obtaining multiconfigurational wavefunctions but is beyond the scope of this thesis. The most popular approach to introduce electron correlation is to keep the single determinant framework but utilise the electron density as the fundamental entity by which to describe the system. This is the well-known density functional theory (DFT) approach to electronic structure. In this thesis, DFT is utilised in chapter 5 to obtain the ground-state molecular structures of the actinyl aquo complexes, and therefore the next section covers a basic introduction to DFT for ground-state systems.

2.5 Density Functional theory

2.5.1 Hohenberg-Kohn Theory

Density functional theory (DFT) offers an alternative approach to solving the Schrödinger equation for a many-electron system by using the electron density as the fundamental entity that describes the system. A good overview of the foundations and history of DFT has been outlined from the perspectives of Becke,[12] Perdew,[13, 14] as well as books from Cramer,[4] and Jensen,[15] and informs the majority of the content covered in this section.

In the 1960's, Hohenberg and Kohn established two theorems that prove the electron density can completely and exactly determine all the ground-state properties of a many-electron system.[16, 17] The details can be examined by first considering an N-electron system with an electronic Hamiltonian $\hat{H}$

$$\hat{H} = \underbrace{-\frac{1}{2}\sum_i \nabla_i^2}_{T_e} + \underbrace{\sum_i v_{\text{ext}}(r_i)}_{V_{\text{ext}}} + \underbrace{\frac{1}{2}\sum_{j\neq i}\sum_i \frac{1}{r_{ji}}}_{V_{\text{ee}}} \tag{2.102}$$

This is the same Hamiltonian introduced at the beginning of the chapter in eq. (2.5) but replaces the $\sum_{i=1}^{N}\sum_{A=1}^{M}\frac{Z_A}{r_{iA}}$ term by a function $v_{\text{ext}}(r_i)$ representing the external field potential due to the nuclei. Taking each term in turn, the first represents the kinetic energy of the electrons T_e, the second represents the potential energy of electron interactions with the nuclei V_{ext} (as a potential field) and the last term is the electron-electron interactions V_{ee}. For this Hamiltonian, there exists a unique ground-state wavefunction Ψ_0 and an associated electron density $\rho(\mathbf{r})$. In the first Hohenberg and Kohn theorem,[16] it was shown in principle that the electron density $\rho(\mathbf{r})$ can be mapped exactly to a unique external potential v_{ext} which itself contains the component information for the molecule $\{N, Z_A, R_A\}$, where Z_A and R_A are the charge and position of the nuclei. The external potential v_{ext} can further be mapped to the ground-state wavefunction Ψ_0 which as discussed, contains all information about a system including its energy. The first Hohenberg-Kohn theorem can therefore be summarise as the following mappings

$$\rho(\mathbf{r}) \rightarrow v_{\text{ext}} : \{N, Z_A, R_A\} \rightarrow \hat{H} \rightarrow \Psi_0 \rightarrow E_0 \implies E_0 = E[\rho(\mathbf{r})] \tag{2.103}$$

The ground-state energy of the system can be formulated as a functional of the electron density $E[\rho(\mathbf{r})]$ and can be split into its individual kinetic T and potential V components which are also functionals of the electron density

$$E[\rho(\mathbf{r})] = T_{\text{e}}[\rho(\mathbf{r})] + V[\rho(\mathbf{r})] \tag{2.104}$$

$$= T_{\text{e}}[\rho(\mathbf{r})] + V_{\text{ee}}[\rho(\mathbf{r})] + V_{\text{ext}}[\rho(\mathbf{r})] \tag{2.105}$$

where the potential energy can be further split into the electron-electron interactions V_{ee}

and the electron interactions with the nuclei as an external field V_{ext}, such that

$$E[\rho(\mathbf{r})] = \underbrace{T_{\text{e}}[\rho(\mathbf{r})] + V_{\text{ee}}[\rho(\mathbf{r})]}_{F_{\text{HK}}[\rho(\mathbf{r})]} + V_{\text{ext}}[\rho(\mathbf{r})] \tag{2.106}$$

$$E[\rho(\mathbf{r})] = F_{\text{HK}}[\rho(\mathbf{r})] + V_{\text{ext}}[\rho(\mathbf{r})] \tag{2.107}$$

$$= \underbrace{F_{\text{HK}}[\rho(\mathbf{r})]}_{universal} + \underbrace{\int v_{\text{ext}}(\mathbf{r}) \cdot \rho(\mathbf{r})\, \mathrm{d}\mathbf{r}}_{dependent} \tag{2.108}$$

This splits the density functional into a system dependent part and a universal part called the Hohenberg-Kohn density functional $F_{\text{HF}}[\rho(\mathbf{r})]$.[12] The latter is universal in the sense that it is independent of the molecular components $\{N, Z_A, R_A\}$. Therefore, if this functional was known exactly, which is not the case, and since it is independent of the system, one could solve the Schrödinger equation exactly for any molecular system. The second Hohenberg-Kohn theorem[16] established a variational principle such that for any given density $\tilde{p}(\mathbf{r})$ which aims to map onto the real system defined by $v_{ext}(\mathbf{r})$, then its energy is greater than the real density $\rho(\mathbf{r})$ which uniquely maps to the system as defined by $v_{ext}(\mathbf{r})$.

$$F_{\text{HF}}[\tilde{\rho}(\mathbf{r})] + \int v_{\text{ext}}(\mathbf{r}) \cdot \tilde{\rho(\mathbf{r})}\, \mathrm{d}\mathbf{r} \geq F_{\text{HF}}[\rho(\mathbf{r})] + \int v_{\text{ext}}(\mathbf{r}) \cdot \rho(\mathbf{r})\, \mathrm{d}\mathbf{r} = E_0 \tag{2.109}$$

2.5.2 Kohn-Sham Theory

To make progress, Kohn-Sham theory is considered whereby the Hamiltonian is considered for a non-interacting system of electrons (Kohn-Sham system).[17] The idea is that the density functional for the ground-state energy can be represented as a sum of terms for a non-interacting system with an electron density identical to that of the true interacting system plus correction terms to account for the missing energy associated with electron interactions. For a single closed shell Slater determinant, recall that the electron density can be constructed from a set of orbitals $\psi_i(\mathbf{r})$

$$\rho(\mathbf{r}) = 2\sum_i \psi_i^* \psi_i = |\psi_i|^2 \tag{2.110}$$

This electron density is identical for both the interacting and non-interacting systems. The kinetic energy takes the same form as found in Hartree-Fock, and can be approximated

for the Kohn-Sham system as

$$T_{\mathrm{KS}}[\rho(\mathbf{r})] = -\frac{1}{2}\sum_{i} 2\int \psi^{*}(\mathbf{r})\nabla_{i}^{2}\psi_{i}(\mathbf{r})\,\mathrm{d}(\mathbf{r}) \tag{2.111}$$

The degree to which it differs from the real interacting system ($T_{\mathrm{e}}[\rho(\mathbf{r})]$) can be written as

$$\Delta T[\rho(\mathbf{r})] = T_{\mathrm{e}}[\rho(\mathbf{r})] - T_{\mathrm{KS}}[\rho(\mathbf{r})] \tag{2.112}$$

and the classical Coulomb electron-electron interaction J can be written akin to the two-electron integrals of Hartree-Fock. For the Kohn-Sham system, the classical Coulomb interaction takes the form

$$J_{\mathrm{KS}}[\rho(\mathbf{r})] = \frac{1}{2}\int \frac{\rho(\mathbf{r_1})\rho(\mathbf{r_2})}{r_{12}}\,\mathrm{d}\mathbf{r_1}\,\mathrm{d}\mathbf{r_2} \tag{2.113}$$

with an associated error compared with the real interaction V_{ee} as

$$\Delta V[\rho(\mathbf{r})] = V_{\mathrm{ee}}[\rho(\mathbf{r})] - J_{\mathrm{KS}}[\rho(\mathbf{r})] \tag{2.114}$$

These error terms can be combined into a single term called the exchange-correlation energy E_{XC}

$$E_{\mathrm{XC}}[\rho(\mathbf{r})] = \Delta T[\rho(\mathbf{r})] + \Delta V[\rho(\mathbf{r})] \tag{2.115}$$

Collecting everything together, the total ground-state energy in Kohn-Sham theory can be expressed as

$$E[\rho(\mathbf{r})] = \underbrace{T_{\mathrm{KS}}[\rho(\mathbf{r})] + J_{\mathrm{KS}}[\rho(\mathbf{r})] + V_{\mathrm{ext}}[\rho(\mathbf{r})]}_{\text{Exact Expressions}} + \underbrace{E_{\mathrm{XC}}[\rho(\mathbf{r})]}_{\textit{Unknown}} \tag{2.116}$$

In Kohn-Sham theory, all the unknown terms can be elegantly encompassed into a single electron density functional term, E_{XC}. Finding the form of this functional has been the preoccupation of scientists in the area over the past five decades, but the exact form still remains a mystery.[12, 13] As such, approximations are required to make progress. Note that if an exact form was known, the expression would solve exactly the ground-state energy and density for the system. This is all possible without a single approximation having been made, since inserting eq. (2.115) back into eq. (2.116), yields the original Hohenberg-Kohn formulation of the ground-state energy in eq. (2.106). In a sense, the

problem is simply reformulated to be solved from the perspective of the non-interacting system and all the quantum mechanical effects from electron interactions are added as an additional E_{XC} term.

In the final step, a variational minimisation of eq. (2.116) with respect to the orbitals ψ_i yields the Kohn-Sham equations

$$-\frac{1}{2}\nabla_i^2\psi_i(\mathbf{r}) + v^{KS}(\mathbf{r})\psi_i(\mathbf{r}) = \epsilon_1\psi_i(\mathbf{r}) \tag{2.117}$$

The equations take a similar form to the Hartree-Fock equations but the effective Kohn-Sham potential is defined exactly as

$$v^{\mathrm{KS}}(\mathbf{r}) = \underbrace{v_{\mathrm{ext}}(\mathbf{r}) + \int \frac{\rho(\mathbf{r}')}{|\mathbf{r}-\mathbf{r}'|}\,\mathrm{d}\mathbf{r}'}_{Exact Expressions} + \underbrace{\frac{\delta}{\delta\rho(\mathbf{r})}(E_{\mathrm{XC}})}_{Unknown} \tag{2.118}$$

where the final term is the functional derivative of E_{XC} with respect to the electron density $\rho(\mathbf{r})$. Here, the Kohn-Sham Theory is complete and the electrons in atoms, molecules, ect. can be viewed as independent particles moving in the effective Kohn-Sham potential.

2.5.3 The Exchange-Correlation Functional

The exact and true form of the exchange-correlation functional remains unknown, and therefore approximations are required. The approximations to the exchange-correlation functional $E_{\mathrm{XC}}[\rho(\mathbf{r})]$ (or just functional for short) are discussed in the context of the Jacobs ladder of approximations introduced by Perdew.[14] The content for this section was largely derived from the work of Perdew,[13, 14] and Becke[12] as well as from the books by Cramer[4] and Jensen,[15] which provide greater detail for the interested reader.

The functional can be split into its exchange and correlation parts and the general form can be written in terms of the energy per particle or energy density $\varepsilon_{\mathrm{xc}}[\rho(\mathbf{r})]$ such that

$$E_{\mathrm{XC}}[\rho(\mathbf{r})] = E_{\mathrm{X}}[\rho(\mathbf{r})] + E_{\mathrm{C}}[\rho(\mathbf{r})] \tag{2.119}$$

$$E_{\mathrm{XC}}[\rho(\mathbf{r})] = \int \rho(\mathbf{r})\varepsilon_{\mathrm{x}}[\rho(\mathbf{r})]\,\mathrm{d}\mathbf{r} + \rho(\mathbf{r})\varepsilon_{\mathrm{c}}[\rho(\mathbf{r})]\,\mathrm{d}\mathbf{r} \tag{2.120}$$

$$E_{\mathrm{XC}}[\rho(\mathbf{r})] = \int \rho(\mathbf{r})\varepsilon_{\mathrm{xc}}[\rho(\mathbf{r})]\,\mathrm{d}\mathbf{r} \tag{2.121}$$

The quality of prediction for the ground-state energy of a system in DFT, depends on the quality of the electron density, which differs depending on the quality of the approximation

for $\varepsilon_{\text{xc}}[\rho(\mathbf{r})]$. The Jacobs ladder of exchange-correlation functional approximations is presented in fig. 2.2.[14] and provides a framework in which to judge the quality of approximations. The journey up the ladder can be viewed as a journey from complete locality to non-locality, as an increasing number of ingredients fulfill more known formal constraints of the true exchange-correlation functional and better capture the nature of the electron density in molecular systems. Each level of the ladder up to the hybrids is summarised and considered in turn.

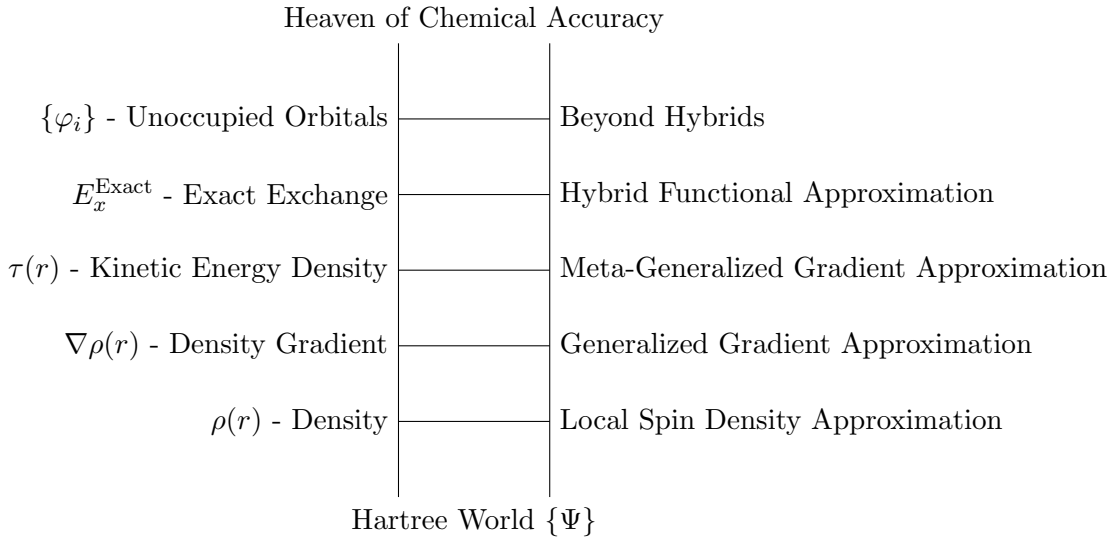

Figure 2.2: The Jacobs Ladder of density functional approximations first introduced by Perdew.[14] Adapted from J. P. Perdew, A. Ruzsinszky, J. Tao, V. N. Staroverov, G. E. Scuseria and G. I. Csonka, *The Journal of Chemical Physics*, 2005, **123**, 062201.,[13] with the permission of AIP Publishing.

The first rung of the ladder is the local density approximation (LDA), and encompass any functional whose exchange energy density at a position in space depends only on the local density value at that position. In this approximation, the exchange-correlation energy is equal to that of a Uniform Electron Gas (UEG) at a given point in space and takes the form[18]

$$E_{\text{XC}}^{\text{LDA}}[\rho(\mathbf{r})] = \int \rho(\mathbf{r})\varepsilon_{\text{xc}}^{\text{UEG}}[\rho(\mathbf{r})]\,\mathrm{d}\mathbf{r} \tag{2.122}$$

Given its reliance on the uniform electron gas, the approximation ultimately fails to capture the nature of molecules which are naturally non-uniform. The approach has its

strengths in applications to solids and surfaces where the uniform electron gas model of the electron density is most valid.[13] An approach to improving the purely local exchange-correlation functional is to introduce a dependence on the gradient of the electron density, $\nabla\rho(\mathbf{r})$. This is known as the generalised gradient approximation (GGA) and includes the well-known PBE and BLYP functionals.[19–21] The GGAs give rise to semi-local functionals in the form

$$E_{\mathrm{XC}}^{\mathrm{GGA}}[\rho(\mathbf{r})] = \int \rho(\mathbf{r})\varepsilon_{\mathrm{xc}}^{\mathrm{GGA}}[\rho(\mathbf{r}), \nabla\rho(\mathbf{r})]\,\mathrm{d}\mathbf{r} \tag{2.123}$$

The term semi-local refers to an increased knowledge of the electron density, since not only is the electron density at a specific point in space $\mathbf{r}$ known, but some additional knowledge of the electron density within some infinitesimal volume about the point $\mathbf{r}$ is gained through the gradient $\Delta\rho(\mathbf{r})$. The energy density of the GGA, $\varepsilon_{\mathrm{XC}}^{\mathrm{GGA}}$, can be modeled (ignoring spin for this discussion) by taking LDA exchange or correlation and then adding a gradient dependent term of exchange or correlation as follows

$$\varepsilon_{\mathrm{x/c}}^{\mathrm{LDA}} = \varepsilon_{\mathrm{x/c}}^{\mathrm{LDA}}[\rho(\mathbf{r})] + \Delta\varepsilon_{\mathrm{x/c}}\left[\frac{\nabla\rho(\mathbf{r})}{\rho^{4/3}(\mathbf{r})}\right] \tag{2.124}$$

This approach in principle could be expanded upon by implementing a Taylor expansion, adding greater order derivatives. The next logical step would be to include the second order derivative of the electron density, called the Laplacian $\nabla^2\rho(\mathbf{r})$. However, introducing the Laplacian introduces numerical instabilities in calculations since electron density forms cusps near nuclei which leads to discontinuities in the electron density which yield convergence issues in numerical calculations. Instead, the kinetic energy density $\tau(\mathbf{r})$ is included in meta-GGAs and takes the form

$$\tau(\mathbf{r}) = \sum_i \frac{1}{2}|\nabla\psi_i(\mathbf{r})|^2 \tag{2.125}$$

and gives the general form for a MGGA as

$$E_{\mathrm{XC}}^{\mathrm{MGGA}}[\rho(\mathbf{r})] = \int \rho(\mathbf{r})\varepsilon_{\mathrm{xc}}^{\mathrm{MGGA}}[\rho(\mathbf{r}), \nabla\rho(\mathbf{r}), \tau(\mathbf{r})]\,\mathrm{d}\mathbf{r} \tag{2.126}$$

Including the kinetic energy density enables the functional to satisfy additional known constraints of the exact exchange-correlation functional.[4] The kinetic energy density depends explicitly on the orbitals, which introduces information on how localised or

delocalised the electrons are in a given region of space. This in particular has benefits in the ability of the functionals to model bonding interactions. While the incorporating the kinetic energy density provides more detailed local information, these functionals are still considered semi-local due to the reliance on the local value and derivative of the electron density. A prominent example of a MGGA is the SCAN functional by Sun, Ruzinsky and Perdew presented in 2015.[22] This is the first MGGA that is fully constrained, fulfilling all 17 known exact constraints that a MGGA must obey. However, while SCAN is a major step in development of functionals and shows promise for ground-state properties, it is still lacking in its ability to reliably predict excited-state properties.[23] The final functionals that will be discussed in this chapter is the hybrids. In practical terms, hybrids are defined by the introduction of a percentage of exact exchange $E_{\mathrm{x}}^{\mathrm{exact}}$, which takes the form of the Hartree-Fock exchange, but with Kohn-Sham molecular orbitals used in the calculation. This defines the hybrids in terms of $E_{\mathrm{x}}^{\mathrm{HF}}$ as

$$E_{\mathrm{XC}}^{\mathrm{Hybrid}}[\rho(\mathbf{r})] = (1-\alpha)E_{\mathrm{XC}}^{\mathrm{DFT}}[\rho(\mathbf{r})] + \alpha E_{\mathrm{X}}^{\mathrm{HF}}[\rho(\mathbf{r})] \tag{2.127}$$

and directly introduces non-locality into the functional. Exact exchange enables the functional to model the exchange interactions of electrons at distance since the exchange energy of an electron depends on knowledge of the distribution of all other electrons across the molecules. The hybrids are arguably the most successful of the functionals, with the paper reporting the B3LYP hybrid functional[20, 24–28] being amongst one of the most cited papers in all science.[29] In this thesis, PBE0[30] is utilised for ground-state optimisations of actinyl aquo complexes and takes the form

$$E_{\mathrm{XC}}^{\mathrm{PBE0}}[\rho(\mathbf{r})] = \frac{1}{4}E_{\mathrm{X}}^{\mathrm{HF}}[\rho(\mathbf{r})] + \frac{3}{4}E_{\mathrm{X}}^{\mathrm{PBE}}[\rho(\mathbf{r})] + E_{\mathrm{C}}^{\mathrm{PBE}}[\rho(\mathbf{r})] \tag{2.128}$$

2.6 Multiconfigurational Methods

In Hartree-Fock theory, a single determinant is utilised to describe the many-electron wavefunction for a molecule and does not account for electron correlation. While an exact formalisation of DFT does account for all electron correlation, in practice, the exchange-correlation functional is approximated and therefore correlation is not fully accounted for. Depending on the functional approximation used, the degree to which the correlation is

captured varies from system to system. In general, the use of a single determinant in both DFT and HF approaches limits their ability to model systems where a number of electronic configurations are possible and potentially contribute to the ground-state. The approaches outlined in the proceeding sections include many electronic configurations in the description of the many-electron wavefunction to better account for electron correlation. The discussion of the CI and MCSCF methods in the proceeding sections is adapted from the detailed books of Szabo and Ostlund,[1] Helgaker[2] and Jensen.[3]

2.6.1 Configuration Interaction

One of the simplest ways to include additional electronic configurations in the total wavefunction is to make use of the additional non-Aufbau Slater determinants that can be constructed from a set of Hartree-Fock orbitals. The simplest formalism to do this is through configuration interaction. Just as the Hartree-Fock orbitals ψ can be expressed as a linear combination of known basis functions ϕ, the many-electron wavefunction $|\Phi\rangle_0$ can be expanded in a basis of Hartree-Fock Slater determinants $|\Psi\rangle_i$

$$|\Phi_0\rangle = C_0 |\Psi_{\mathrm{HF}}\rangle + \sum_i C_i |\Psi_i\rangle \tag{2.129}$$

where each additional contribution $|\Psi_i\rangle$ is a Slater determinant formed by occupying different orbitals relative to the ground-state Hartree-Fock determinant $|\Psi_{\mathrm{HF}}\rangle$. The calculation then turns into an optimisation problem to find the optimal set of expansion coefficients C, that returns the lowest energy configuration interaction energy. For a given system, if all possible Slater determinants could be constructed to represent all the possible arrangements of electrons across the orbitals, and an infinite basis set was used to construct the orbitals, then the CI wavefunction would equal the exact wavefunction of the system. In practice, only a finite basis set is possible and therefore the orbitals form a finite set. In this case, including all the possible Slater determinants for a finite basis set of orbitals constitutes a full CI expansion, and returns the exact energy for a system within the given basis set.

Configuration interaction first involves a Hartree-Fock calculation within a finite basis set in order to obtain the molecular orbitals and the ground-state Slater determinant Ψ_{HF}. Once a set of molecular orbitals is obtain, a systematic approach is required to generate

all the other possible Slater determinants. A convenient way of doing this is to designate the Hartree-Fock ground-state as the reference wavefunction and then to classify other possible (excited) determinants by how they differ from this state. This can be done by introducing new notation which states which occupied orbitals $\{ijk...\}$ are replaced by a virtual orbitals $\{abc...\}$ in the newly constructed Slater determinants. This can also be viewed as which electrons in the set of $\{ijk...\}$ orbitals in the reference determinant are promoted to the set of $\{abc...\}$ orbitals in the newly constructed excited determinants. These excited determinants can be expressed as

$$|\Psi_0\rangle = |\chi_1\chi_2\cdots\chi_i\cdots\chi_j\cdots\chi_k\cdots\chi_N\rangle \tag{2.130}$$

$$|\Psi_i^a\rangle = |\chi_1\chi_2\cdots\chi_a\cdots\chi_j\cdots\chi_k\cdots\chi_N\rangle \tag{2.131}$$

$$\left|\Psi_{ij}^{ab}\right\rangle = |\chi_1\chi_2\cdots\chi_a\cdots\chi_b\cdots\chi_k\cdots\chi_N\rangle \tag{2.132}$$

$$\left|\Psi_{ijk}^{abc}\right\rangle = |\chi_1\chi_2\cdots\chi_a\cdots\chi_b\cdots\chi_c\cdots\chi_N\rangle \tag{2.133}$$

$$\vdots$$

The newly constructed determinant $|\Psi_i^a\rangle$ in eq. (2.130) represents a singly excited determinant with an electron promoted from orbital i to a, $\left|\Psi_{ij}^{ab}\right\rangle$ represents a doubly excited determinant where two electrons are promoted from orbitals a and b to i and j, and so on. Note that the donor orbitals $\{ijk...\}$ no longer appear in the excited Slater determinants since they are unoccupied, and are replaced by the acceptor orbitals $\{ijk...\}$ which are occupied. The number of determinants that can be constructed is dependent on the number of electrons, as well as the number of orbitals that can be formed from the basis set. With the excited determinants, the full CI wavefunction can be constructed

$$|\Phi\rangle = C_0\,|\Psi_{\mathrm{HF}}\rangle + \sum_{ia} C_i^a\,|\Psi_i^a\rangle + \sum_{\substack{i<j\\a<b}} C_{ij}^{ab}\left|\Psi_{ij}^{ab}\right\rangle + \sum_{\substack{i<j<k\\a<b<c}} C_{ijk}^{abc}\left|\Psi_{ijk}^{abc}\right\rangle + \cdots \tag{2.134}$$

The problem now consists of finding the optimal expansion coefficients which will be represented by C. This can be achieved through a variational optimisation of the expectation value of the electronic energy using the electronic Hamiltonian $\hat{H}$

$$E_{\mathrm{CI}} = \min_C \frac{\langle\Phi(C)|\,\hat{H}\,|\Phi(C)\rangle}{\langle\Phi(C)|\Phi(C)\rangle} \tag{2.135}$$

and is equivalent to solving the eigenvalue problem

$$\mathbf{HC} = E\mathbf{C} \tag{2.136}$$

which can be cast into solving a set of CI secular equations in matrix form as

$$(\mathbf{H} - E\mathbf{I})\mathbf{C} = 0 \tag{2.137}$$

or

$$\begin{pmatrix} H_{00} - E & H_{01} & \cdots & H_{0j} & \cdots \\ H_{10} & H_{11} - E & \cdots & H_{1j} & \cdots \\ \vdots & \vdots & \ddots & \vdots & \cdots \\ H_{j0} & \vdots & \cdots & H_{jj} - E & \cdots \\ \vdots & \vdots & \cdots & \vdots & \ddots \end{pmatrix} \begin{pmatrix} C_0 \\ C_1 \\ \vdots \\ C_j \\ \vdots \end{pmatrix} = \begin{pmatrix} 0 \\ 0 \\ \vdots \\ 0 \\ \vdots \end{pmatrix} \tag{2.138}$$

Here $\mathbf{C}$ contains the expansion coefficients (C), E is the resulting energy of the CI expansion and H is the CI matrix with elements

$$H_{\mu\nu} = \langle \Psi_\mu | \hat{H} | \Psi_\nu \rangle \tag{2.139}$$

Solving the secular equations is equivalent to diagonalising the CI matrix. The CI energy is obtained as the lowest eigenvalue of the CI Hamiltonian matrix and the corresponding eigenvectors contains the C coefficients for the expansion of the determinants. The second lowest eigenvalue corresponds to the first excited state, the third lowest to the second excited state and so on. Taking the linear expansion in eq. (2.134) and collecting the summations into single terms gives

$$|S\rangle = \sum_{ia} C_i^a |\Psi_i^a\rangle \tag{2.140}$$

$$|D\rangle = \sum_{\substack{i<j \\ a<b}} C_{ij}^{ab} \left|\Psi_{ij}^{ab}\right\rangle \tag{2.141}$$

$$|T\rangle = \sum_{\substack{i<j<k \\ a<b<c}} C_{ijk}^{abc} \left|\Psi_{ijk}^{abc}\right\rangle \tag{2.142}$$

$$\vdots \tag{2.143}$$

each representing singly $|S\rangle$, doubly $|D\rangle$, and triply $|T\rangle$ excited determinants ect. This

enables the CI matrix to be written in a short-hand form as

$$\mathbf{H}^{\mathrm{CI}} = \begin{bmatrix} \langle \Psi_{\mathrm{HF}} | \hat{H} | \Psi_{\mathrm{HF}} \rangle & \langle \Psi_{\mathrm{HF}} | \hat{H} | \Psi_{\mathrm{D}} \rangle & \langle \Psi_{\mathrm{HF}} | \hat{H} | \Psi_{\mathrm{D}} \rangle & \langle \Psi_{\mathrm{HF}} | \hat{H} | \Psi_{\mathrm{T}} \rangle & \cdots \\ \langle \Psi_{\mathrm{S}} | \hat{H} | \Psi_{\mathrm{HF}} \rangle & \langle \Psi_{\mathrm{S}} | \hat{H} | \Psi_{\mathrm{S}} \rangle & \langle \Psi_{\mathrm{S}} | \hat{H} | \Psi_{\mathrm{D}} \rangle & \langle \Psi_{\mathrm{S}} | \hat{H} | \Psi_{\mathrm{T}} \rangle & \cdots \\ \langle \Psi_{\mathrm{D}} | \hat{H} | \Psi_{\mathrm{HF}} \rangle & \langle \Psi_{\mathrm{D}} | \hat{H} | \Psi_{\mathrm{S}} \rangle & \langle \Psi_{\mathrm{D}} | \hat{H} | \Psi_{\mathrm{D}} \rangle & \langle \Psi_{\mathrm{D}} | \hat{H} | \Psi_{\mathrm{T}} \rangle & \cdots \\ \langle \Psi_{\mathrm{T}} | \hat{H} | \Psi_{\mathrm{HF}} \rangle & \langle \Psi_{\mathrm{T}} | \hat{H} | \Psi_{\mathrm{S}} \rangle & \langle \Psi_{\mathrm{T}} | \hat{H} | \Psi_{\mathrm{D}} \rangle & \langle \Psi_{\mathrm{T}} | \hat{H} | \Psi_{\mathrm{T}} \rangle & \cdots \\ \vdots & \vdots & \vdots & \vdots & \ddots \end{bmatrix} \tag{2.144}$$

The CI matrix can be reduced, since some elements of the CI Hamiltonian cancel according to Brillouin's theorem and the Slater-Condon rules. The elements $\langle \Psi_{\mathrm{HF}} | \hat{H} | \Psi_{\mathrm{S}} \rangle = 0$ containing coupling of the singly excited determinants with the Hartree-Fock determinant are zero according to Brillouins theorem. Additionally, elements do not couple to other elements more than two steps apart and therefore $\langle \Psi_{\mathrm{HF}} | \hat{H} | \Psi_{\mathrm{T}} \rangle = 0$ and similarly if included $\langle \Psi_{\mathrm{S}} | \hat{H} | \Psi_{\mathrm{Q}} \rangle = 0$.

$$\mathbf{H}^{(\mathrm{CI})} = \begin{bmatrix} \langle \Psi_{\mathrm{HF}} | \hat{H} | \Psi_{\mathrm{HF}} \rangle & 0 & \langle \Psi_{\mathrm{HF}} | \hat{H} | \Psi_{\mathrm{D}} \rangle & 0 & \cdots \\ 0 & \langle \Psi_{\mathrm{S}} | \hat{H} | \Psi_{\mathrm{S}} \rangle & \langle \Psi_{\mathrm{S}} | \hat{H} | \Psi_{\mathrm{D}} \rangle & \langle \Psi_{\mathrm{S}} | \hat{H} | \Psi_{\mathrm{T}} \rangle & \cdots \\ \langle \Psi_{\mathrm{D}} | \hat{H} | \Psi_{\mathrm{HF}} \rangle & \langle \Psi_{\mathrm{D}} | \hat{H} | \Psi_{\mathrm{S}} \rangle & \langle \Psi_{\mathrm{D}} | \hat{H} | \Psi_{\mathrm{D}} \rangle & \langle \Psi_{\mathrm{D}} | \hat{H} | \Psi_{\mathrm{T}} \rangle & \cdots \\ 0 & \langle \Psi_{\mathrm{T}} | \hat{H} | \Psi_{\mathrm{S}} \rangle & \langle \Psi_{\mathrm{T}} | \hat{H} | \Psi_{\mathrm{D}} \rangle & \langle \Psi_{\mathrm{T}} | \hat{H} | \Psi_{\mathrm{T}} \rangle & \cdots \\ \vdots & \vdots & \vdots & \vdots & \ddots \end{bmatrix} \tag{2.145}$$

In practice, a full CI expansion is limited to only small systems with a couple of electrons. For larger systems, the expansion is truncated to only a subset of possible determinants. The first truncation is known as CIS and contains elements up to and including singly excited determinants as follows,

$$\mathbf{H}^{\mathrm{CIS}} = \begin{bmatrix} \langle \Psi_{\mathrm{HF}} | \hat{H} | \Psi_{\mathrm{HF}} \rangle & 0 \\ 0 & \langle \Psi_{\mathrm{S}} | \hat{H} | \Psi_{\mathrm{S}} \rangle \end{bmatrix} \tag{2.146}$$

This truncation can be used to approximate the excited state but makes no improvement to the ground-state energy since no excited determinants couple with the Hartree-Fock determinant. The first and cheapest approach from a computation perspective that

improves upon the ground-state energy is CISD which has a CI-truncation as follows

$$\mathbf{H}^{\mathrm{CISD}} = \begin{bmatrix} \langle \Psi_{\mathrm{HF}} | \hat{H} | \Psi_{\mathrm{HF}} \rangle & 0 & \langle \Psi_{\mathrm{HF}} | \hat{H} | \Psi_{\mathrm{D}} \rangle \\ 0 & \langle \Psi_{\mathrm{S}} | \hat{H} | \Psi_{\mathrm{S}} \rangle & \langle \Psi_{\mathrm{S}} | \hat{H} | \Psi_{\mathrm{D}} \rangle \\ \langle \Psi_{\mathrm{D}} | \hat{H} | \Psi_{\mathrm{HF}} \rangle & \langle \Psi_{\mathrm{D}} | \hat{H} | \Psi_{\mathrm{S}} \rangle & \langle \Psi_{\mathrm{D}} | \hat{H} | \Psi_{\mathrm{D}} \rangle \end{bmatrix} \tag{2.147}$$

now the doubly excited determinants couple with the HF reference and can improve the correlation treatment offer an improvement to the energy. The benefit of truncation is that it enables the CI approach to be applied to a wider array of systems, since the cost is reduced. However, this comes at the cost of size extensivity, meaning the total energy of a system will not equal the sum of the energies for the individual fragments at infinite separation, which can be a large detriment in the calculation of thermodynamic properties, bond dissociation, and other properties of molecules.

2.6.2 Multiconfigurational SCF Theory

As discussed, the single determinant construction of Hartree-Fock is only capable of representing a single electronic configuration, while in reality, the ground-state may be dominated by several configurations. Carrying out a CI calculation from a set of HF orbitals introduces a bias towards describing each state with a set of orbitals optimised for the Hartree-Fock ground-state. Instead, a more accurate approach would also optimise the orbitals that are used to describe the electronic configurations in the CI expansion. The multiconfigurational (MC)SCF approach aims to do this, simultaneously optimising the orbital and expansion coefficients, ensuring that the orbitals utilised are optimised for the particular state being described. This removes the bias toward the HF ground-state. This optimisation can be written as a variational problem

$$E_{\mathrm{MCSCF}} = \min_{\kappa, C} \frac{\langle \Phi(\kappa, C) | \hat{H} | \Phi(\kappa, C) \rangle}{\langle \Phi(\kappa, C) | \Phi(\kappa, C) \rangle} \tag{2.148}$$

whereby the wavefunction is optimised by minimising the expectation value of the MCSCF energy with respect to the expansion coefficients C and the orbital parameters represented by κ. Technically speaking, κ is the parameters of the orbital rotation operator $e^{-\hat{\kappa}}$ which tailors the orbitals to the CI expansion, but involves operators from second quantisation and is beyond the scope of this general introduction to the theory. The optimisation

of MCSCF wavefunctions represents a significant computational challenge and requires efficient and robust algorithms in order to find the true global minimum energy solution from the total solution space which may encompass a number of local solutions. Given the additional computational cost of optimising the orbitals, a truncation of the CI expansion is a necessity. The MCSCF approach is capable of capturing substantial static correlation if the truncation includes the dominating configurations in the CI expansion and configurations which are in near-degeneracy. This truncated space is typically referred to as the reference space. Dynamical correlation is still not well described by MCSCF since to completely capture the instantaneous repulsion of electrons in near spatial proximity, requires large flexibility in the wavefunction through additionally large basis sets and substantial CI expansion. Therefore, MCSCF with its necessity for truncation, is not well suited alone for capturing such correlation. Dynamic correlation can be better modelled with the addition of configurations that include excitations out of the reference space such including all singly and doubly excitations or greater.

To ensure a good description and accounting of the static correlation, the truncation involves the user manually identifying the configurations which dominate the CI expansion. Considering individual configurations is conceptually un-intuitive, especially in complex systems. A more natural approach is to consider truncation based on how the electrons might distribute across a set of orbitals to capture correlation effects. This leads naturally to the Complete Active Space (CAS) and Restricted Active Space (RAS) SCF approaches.

2.6.3 Complete/Restricted Active Space Self Consistent Field Theory

The MCSCF approach can quickly become impractical for large sets of configurations. As discussed, a truncation of the CI expansion is a requirement to take advantage of the MCSCF approach for systems with larger numbers of orbitals and electrons. A natural approach would be to target the MCSCF to only those configurations that dominate in the CI-expansion. For ground-state systems, configurations resulting from the distribution of electrons across the valence space tend to include configurations that dominate the CI expansion. Therefore, the orbital space can be utilised as the interface by which to truncate the CI expansion. This is the route taken by Complete Active Space Self-Consistent Field (CASSCF) theory.

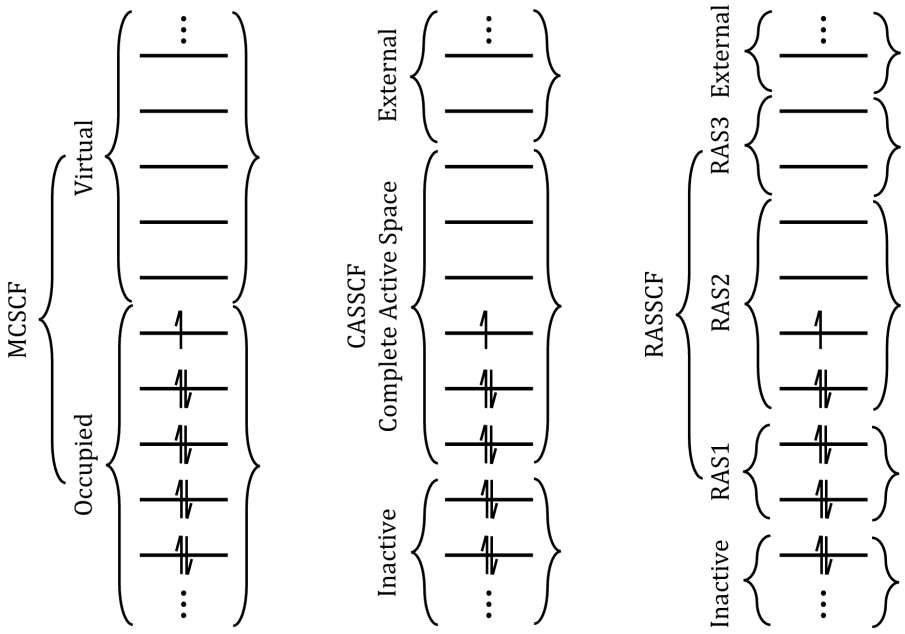

Figure 2.3: Partitioning of the orbital space in a full-CI MCSCF, CASSCF, and RASSCF calculation. CASSCF consists of three spaces including the active-space. RASSCF splits the active-space into three subspaces: RAS1/2/3.

In CASSCF, the orbital space is divided (by the user) into three subspaces classified as the inactive, active and external spaces. The inactive space consists of orbitals that are doubly occupied in all configurations. The active space consists of orbitals whose occupation takes values between 0 and 2 in the reference wavefunction, and for ground-state calculations, inevitably spans the valence orbitals. Lastly, the external space remains empty across the configurations. This set-up can be view diagrammatically in fig. 2.3.

In CASSCF, a full-CI expansion is performed on the active-space such that all the electrons occupying orbitals spanning the active space are distributed in all possible ways amongst these orbitals. This generates all the configurations which form the CASSCF wavefunction. Following the CI expansion, a MCSCF step then simultaneously optimises both the orbital and CI expansion coefficients. By defining an active space, the un-intuitive process of determining dominating configurations to the full CI-expansion is replaced by a chemically intuitive problem of picking which orbitals are relevant for the simulation at hand. The drawback of CASSCF is that the number of configurations generated increases

substantially with the number of orbitals in the active space, limiting CASSCF to approx 12-16 orbitals in most cases.[31]

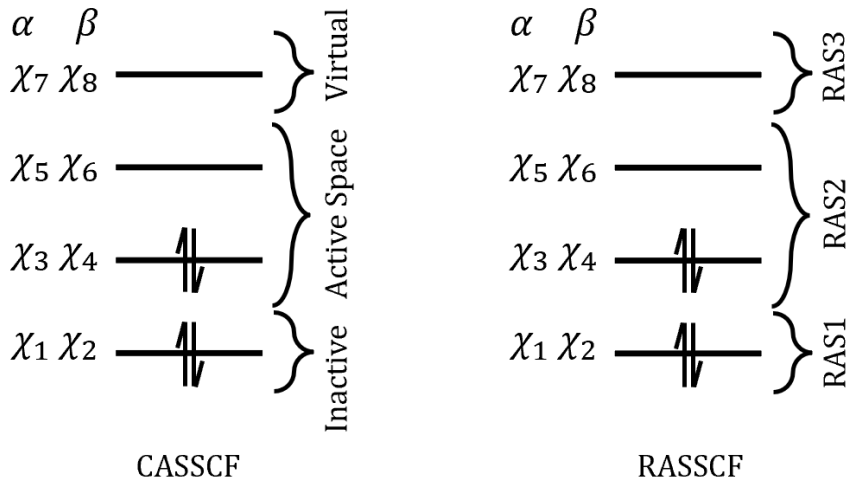

Figure 2.4: Example of possible CASSCF and RASSCF active spaces for a set of eight spin orbitals.

RASSCF offers an alternative set-up. Here, the active space is divided into three subspaces called RAS1, RAS2, and RAS3. RAS1 are those orbitals that are doubly occupied in the reference wavefunction, RAS2 contains orbitals that vary in occupation from 0 to 2, and RAS3 spans orbitals that are empty in the reference wavefunction. In RASSCF, RAS2 is subject to a full-CI expansion generating all possible configurations of electrons amongst the RAS2 orbitals. However, an additional set of configurations is generated through a CI expansion of electrons amongst the RAS1 and RAS3 orbitals, but subject to some user defined restrictions. These restrictions involve setting a maximum number of holes for the RAS1 orbital space, and a maximum number of electrons for the RAS3 orbitals. Given these constraints, all additional configurations from a CI expansion of RAS1 with RAS3 is performed. The two sets of configurations are combined to give the total RASSCF (truncated) CI expansion. Just as in CASSCF, this RASSCF wavefunction is then variationally minimised through optimisation of the orbital and expansion coefficients in a MCSCF step.

The differences in the two approaches can be examined through an example presented in fig. 2.4. In fig. 2.4, the active space for the CASSCF calculation can be defined

to span the spin orbitals $\{\chi_3, \chi_4, \chi_5, \chi_6\}$. The expansion of this CAS active space is performed using eq. (2.134) and changing the summations to a more convenient, $\sum_{i<j} = \sum_i^{n-1} \sum_{j=i+1}^{n}$ form, the multiconfigurational CAS wavefunction $\left|\Phi^{\mathrm{CAS}}\right\rangle$ can then be expressed as

$$\left|\Phi^{\mathrm{CAS}}\right\rangle = C_0 \left|\Psi_0\right\rangle + \sum_i \sum_a C_i^a \left|\Psi_i^a\right\rangle + \sum_{i<j} \sum_{a<b} C_{ij}^{ab} \left|\Psi_{ij}^{ab}\right\rangle \tag{2.149}$$

$$= C_0 \left|\Psi_0\right\rangle + \sum_{i=\{3,4\}} \sum_{i=\{5,6\}} C_i^a \left|\Psi_i^a\right\rangle + \sum_{i=3}^{3} \sum_{j=4}^{4} \left(\sum_{a=5}^{5} \sum_{b=6}^{6} C_{ij} \left|\Psi_{ab}\right\rangle \right) \tag{2.150}$$

$$= \underbrace{C_0 \left|\Psi_0\right\rangle + C_3^5 \left|\Psi_3^5\right\rangle + C_3^6 \left|\Psi_3^6\right\rangle + C_4^5 \left|\Psi_4^5\right\rangle + C_4^6 \left|\Psi_4^6\right\rangle + C_{34}^{56} \left|\Psi_{34}^{56}\right\rangle}_{\text{CI Exapnsion of Active Space}} \tag{2.151}$$

Each configuration ${}^{2S+1}\left|\Psi\right\rangle$, can be expressed as their determinants where $2S+1$ signifies if a configuration is a singlet $(2s+1=1)$ or triplet $(2s+1=3)$ state.

$$\begin{aligned}
{}^1\left|\Psi_0\right\rangle &= \left|\chi_1\chi_2\chi_3\chi_4\right\rangle \\
{}^1\left|\Psi_3^5\right\rangle &= \left|\chi_1\chi_2\chi_4\chi_5\right\rangle \\
{}^3\left|\Psi_3^6\right\rangle &= \left|\chi_1\chi_2\chi_4\chi_6\right\rangle \\
{}^3\left|\Psi_4^5\right\rangle &= \left|\chi_1\chi_2\chi_3\chi_5\right\rangle \\
{}^1\left|\Psi_4^6\right\rangle &= \left|\chi_1\chi_2\chi_3\chi_6\right\rangle \\
{}^1\left|\Psi_{34}^{56}\right\rangle &= \left|\chi_1\chi_2\chi_5\chi_6\right\rangle
\end{aligned} \tag{2.152}$$

Notice that amongst the determinants, the inactive orbitals $\{\chi_1\chi_2\}$ remain unchanged within the determinants and are thus fully occupied throughout. Once the CAS CI expansion is generated eq. (2.149), a MCSCF step is performed to optimise the orbital and expansion coefficients. The CASSCF expansion can be reduced if a state of particular spin multiplicity (singlet or triplet) is of particular interest. Suppose the desired ground-state is a singlet, then the triplet determinants can be eliminated since they do not contribute and therefore the CAS expansion is reduced to

$${}^1\left|\Phi^{\mathrm{CAS}}\right\rangle = C_0 \left|\Psi_0\right\rangle + C_3^5 \left|\Psi_3^5\right\rangle + C_4^6 \left|\Psi_4^6\right\rangle + C_{34}^{56} \left|\Psi_{34}^{56}\right\rangle \tag{2.153}$$

Further reductions can also be made by invoking symmetry. If a state of gerade (g) symmetry is desired, then only determinants with gerade symmetry will contribute to the expansion, further reducing the expansion. The RASSCF expansion is considered next.

In this particular (user defined) case, RAS1 has a maximum of 1 hole and RAS3 contains a maximum of 1 electron. From these constraints, the possible configurations are the full CI set of RAS2 plus the CI set from RAS1 and RAS3. This gives a RASSCF CI expansion of

$$\underbrace{\left|\Phi^{\mathrm{RAS}}\right\rangle = C_0\left|\Psi_0\right\rangle + \sum_{i=\{3,4\}}\sum_{i=\{5,6\}} C_i^a\left|\Psi_i^a\right\rangle + \sum_{i=3}^{3}\sum_{j=4}^{4}\left(\sum_{a=5}^{5}\sum_{b=6}^{6} C_{ij}\left|\Psi_{ab}\right\rangle\right)}_{\text{CI Expansion of RAS2}} + \underbrace{\sum_{i=\{1,2\}}\sum_{i=\{7,8\}} C_i^a\left|\Psi_i^a\right\rangle\left|\Phi\right\rangle}_{\text{CI Expansion of RAS1 + RAS3}} \tag{2.154}$$

$$\left|\Phi^{\mathrm{RAS}}\right\rangle = \underbrace{C_0\left|\Psi_0\right\rangle + C_3^5\left|\Psi_3^5\right\rangle + C_3^6\left|\Psi_3^6\right\rangle + C_4^5\left|\Psi_4^5\right\rangle + C_4^6\left|\Psi_4^6\right\rangle + C_{34}^{56}\left|\Psi_{34}^{56}\right\rangle}_{\text{CI Expansion of RAS2}} + \underbrace{C_1^7\left|\Psi_1^7\right\rangle + C_1^8\left|\Psi_1^8\right\rangle + C_2^7\left|\Psi_2^7\right\rangle + C_2^8\left|\Psi_2^8\right\rangle}_{\text{CI Expansion of RAS1 + RAS3}} \tag{2.155}$$

Notice that since the RASSCF calculation uses the same RAS2 space as that for the CAS active space, the CI expansion of RAS2 contains the same configurations. The key difference between the approaches comes in the additional configurations introduced by considering the RAS1 and RAS3 space. Once the RASSCF wavefunction is formed, a MCSCF step is performed. The same symmetry and spin multiplicity principles apply to the RASSCF wavefunction and now the singlet state obtained using RASSCF can be written as

$$^1\left|\Phi^{\mathrm{RAS}}\right\rangle = C_0\left|\Psi_0\right\rangle + C_3^5\left|\Psi_3^5\right\rangle + C_4^6\left|\Psi_4^6\right\rangle + C_{34}^{56}\left|\Psi_{34}^{56}\right\rangle + C_1^7\left|\Psi_1^7\right\rangle + C_2^8\left|\Psi_2^8\right\rangle \tag{2.156}$$

which is identical to the CASSCF singlet state (eq. (2.153)) but with additional RAS excited determinants.

As demonstrated, a key benefit of the RASSCF approach is the ability to introduce additional (specifically chosen) configurations to the total CI expansion in order to improve the description of the wavefunction. For an appropriately sized active space that is well

constructed, both the CAS and RAS approaches are capable of capturing the majority of the static correlation for the system. A further benefit of RASSCF is that the additional configurations introduce greater flexibility into the many body wavefunction and therefore more electron correlation can be captured compared with CASSCF (depending on the set-up). However, neither approach enables a sufficiently large enough CI expansion to capture dynamical correlation. To correct the total CAS and RAS energies for this missing dynamical correlation, perturbation theory approaches can be utilised.

2.7 Many-Body Perturbation Theory

2.7.1 Rayleigh-Schrödinger Perturbation Theory

In many-body time independent non-degenerate perturbation theory the Hamiltonian is partition into a zeroth-order Hamiltonian, which has known eigenfunctions and eigenvalues, and an unknown perturbation. This enables the total and exact energy of a system to be written as an infinite sum (Taylor series) of increasingly more complex contributions which can be grouped using an ordering parameter λ into zeroth, first, second and the n^{th} order corrections

$$\hat{H} = \hat{H}^{(0)} + \lambda\hat{H}^{(1)} + \lambda^2\hat{H}^{(2)} + \cdots \tag{2.157}$$

$$|\Phi\rangle = \left|\Psi^{(0)}\right\rangle + \lambda\left|\Psi^{(1)}\right\rangle + \lambda^2\left|\Psi^{(2)}\right\rangle + \cdots \tag{2.158}$$

$$\varepsilon = E^{(0)} + \lambda E^{(1)} + \lambda^2 E^{(2)} + \cdots \tag{2.159}$$

If the zeroth order Hamiltonian is already a good approximation of the exact Hamiltonian, the perturbative correction will be small, and the perturbation expansion will converge quickly to the exact answer. In practice only a finite expansion can be taken, but the majority of the perturbative correction will be captured in the first few terms of the series. This is the case for correlation corrections such as Møller-Plesset and CASPT2 methods which utilise second order corrections to the total energy to account for dynamical correlation. Both these approaches use the general results of Rayleigh-Schrödinger (RS) perturbation theory in their methods, and therefore a general introduction is given here.

The Schrödinger equation can be written as

$$\hat{H}\,|\Phi_i\rangle = \varepsilon_i\,|\Phi_i\rangle \quad \text{where } i = 0, 1, 2, \cdots \infty \tag{2.160}$$

where i represents each eigenfunction ($i > 0$ excited-states) and eigenvalue (state energies) of $\hat{H}$. The Hamiltonian is partitioned to include a perturbation $\hat{V}$ to the known $\hat{H}^{(0)}$ Hamiltonian and then substituted into the Schrödinger equation

$$\hat{H} = \hat{H}^{(0)} + \hat{V} \tag{2.161}$$

$$\left(\hat{H}^{(0)} + \hat{V}\right) |\Phi_i\rangle = \epsilon |\Phi_i\rangle \tag{2.162}$$

where $\hat{H}^{(0)}$ has known eigenfunctions and eigenvalues and constitutes the zeroth-order (unperturbed) Shrödinger equation

$$\hat{H}^{(0)} \left|\Psi_i^{(0)}\right\rangle = E_i^{(0)} \left|\Psi_i^{(0)}\right\rangle \tag{2.163}$$

The perturbation expansion eq. (2.157) of the wavefunction and state energies are substituted into eq. (2.163)

$$\begin{aligned}\left(\hat{H}^{(0)} + \hat{V}\right)&\left[\left|\Psi_i^{(0)}\right\rangle + \lambda\left|\Psi_i^{(1)}\right\rangle + \lambda^2\left|\Psi_i^{(2)}\right\rangle + \cdots\right] \\ &= \underbrace{\left(E_i^{(0)} + E_i^{(1)} + E_i^{(2)} + \cdots\right)}_{\text{Perturbation expansion of } \varepsilon} \underbrace{\left[\left|\Psi_i^{(0)}\right\rangle + \lambda\left|\Psi_i^{(1)}\right\rangle + \lambda^2\left|\Psi_i^{(2)}\right\rangle + \cdots\right]}_{\text{Perturbation expansion of } \left|\Phi_i^{(0)}\right\rangle}\end{aligned} \tag{2.164}$$

Assuming the wavefunctions of $\hat{H}_0$ are themselves normalised and using intermediate normalisation such that $\langle\Psi_0|\Phi_0\rangle = 1$, the substituted expansion eq. (2.164) yields a set of perturbation equations which are grouped by their λ^n coefficients to give the zeroth-, first-, second-, and n$^{\text{th}}$-order perturbation equations, respectively

$$\lambda^0: \quad \hat{H}_0 \left|\Psi_i^{(0)}\right\rangle = E_i^0 \left|\Psi_i^{(0)}\right\rangle \tag{2.165}$$

$$\lambda^1: \quad \hat{H}_0 \left|\Psi_i^{(1)}\right\rangle + \hat{V} \left|\Psi_i^{(0)}\right\rangle = E_i^{(0)} \left|\Psi_i^{(1)}\right\rangle + E_i^{(1)} \left|\Psi_i^{(0)}\right\rangle \tag{2.166}$$

$$\lambda^2: \quad \hat{H}_0 \left|\Psi_i^{(2)}\right\rangle + \hat{V} \left|\Psi_i^{(1)}\right\rangle = E_i^{(0)} \left|\Psi_i^{(2)}\right\rangle + E_i^{(1)} \left|\Psi_i^{(1)}\right\rangle + E_i^{(2)} \left|\Psi_i^{(0)}\right\rangle \tag{2.167}$$

$$\vdots \tag{2.168}$$

Multiplying each of the expressions above by $\left\langle\Psi_i^{(0)}\right|$, and using orthogonality constraints,

the following n^{th}-order energies are obtained

$$E_i^{(0)} = \left\langle \Psi_i^{(0)} \right| \hat{H}_0 \left| \Psi_i^{(0)} \right\rangle \tag{2.169}$$

$$E_i^{(1)} = \left\langle \Psi_i^{(0)} \right| \hat{V} \left| \Psi_i^{(0)} \right\rangle \tag{2.170}$$

$$E_i^{(2)} = \left\langle \Psi_i^{(0)} \right| \hat{V} \left| \Psi_i^{(1)} \right\rangle \tag{2.171}$$

$$\vdots \tag{2.172}$$

The zeroth-order energy correction $E_i^{(0)}$ is simply the energy of the unperturbed system which is already known. The first order energy correction $E_i^{(0)}$ is the expectation value of the perturbation Hamiltonian when the system is in the unperturbed state. This can be interpreted as the unperturbed states average energy being shifted by $E_i^{(1)}$. The first correction involving a perturbed wavefunction $\left|\Psi_i^{(1)}\right\rangle$ comes from the second order correction. So far, the zeroth and first order corrections are in terms of the known eigenfunctions and can be calculated once the form of the perturbed Hamiltonian $\hat{V}$ is constructed for the problem at hand. However, the second order correction include an unknown $\left|\Psi_i^{(1)}\right\rangle$ term. From here, additional mathematical steps are taken to solve and write the second order energy correction solely in terms of the perturbed Hamiltonian $\hat{V}$ and the known set of wavefunctions $\left|\Psi_n^{(0)}\right\rangle$. This involves using the first order perturbation equation and writing $\left|\Psi_i^{(0)}\right\rangle$ in terms of linear combination of known eigenfunctions $\left|\Psi_n^{(0)}\right\rangle$. The end result is a second order correction expression for the energy

$$E_i^{(2)} = \sum_{n \neq i} \frac{|\left\langle \Psi_i^{(0)} \right| \hat{V} \left| \Psi_n^{(0)} \right\rangle|^2}{E_i^{(0)} - E_n^{(0)}} \tag{2.173}$$

Therefore, the original problem

$$\hat{H} \left|\Phi_i\right\rangle = \varepsilon_i \left|\Phi_i\right\rangle \quad \text{where } i = 0, 1, 2, \cdots \infty \tag{2.174}$$

is solved using second-order perturbation theory, with the energy ε_i for a given state approximated to second-order as

$$\varepsilon = E^{(0)} + \lambda E^{(1)} + \lambda^2 E^{(2)} \tag{2.175}$$

$$\varepsilon_i = E_i^{(0)} + \lambda \left\langle \Psi_i^{(0)} \right| \hat{V} \left|\Psi_i^0\right\rangle + \lambda^2 \sum_{n \neq i} \frac{|\left\langle \Psi_i^{(0)} \right| \hat{V} \left| \Psi_n^{(0)} \right\rangle|^2}{E_i^{(0)} - E_n^{(0)}} \tag{2.176}$$

where λ will set the strength of the perturbation correction.

2.7.2 Møller-Plesset Perturbation Theory

Møller-Plesset (MP) perturbation theory makes use of Rayleigh-Schrödinger (RS) perturbation theory to correct the total energy from a single determinant approach to include the missing correlation energy. For instance, the Hartree-Fock energy for an N-electron system can be improved by obtaining a perturbation expansion for the correlation energy.[32] The ultimate goal is to solve the Scrödinger equation using the electronic Hamiltonian to obtain both the ground-state wavefunction and energy which includes electron correlation

$$\hat{H} \left|\Psi_0\right\rangle = E_0 \left|\Psi_0\right\rangle \tag{2.177}$$

Instead, RS perturbation theory can be used to obtain an approximate solution to second order. Similar to RS perturbation theory, the electronic Hamiltonian is partitioned to include a perturbation operator $\hat{V}$

$$\hat{H} = \hat{H}_0 + \hat{V} \tag{2.178}$$

where $\hat{H}_0$ is the Hartree-Fock Hamiltonian written as a sum over all electrons for the one-electron Fock operator $f(i)$

$$\hat{H}_0 = \sum_i f(i) = \sum_i [h(i) + v^{\mathrm{HF}}(i)] \tag{2.179}$$

and $\hat{V}$ is given as

$$\hat{V} = \sum_{i<j} r_{ij}^{-1} - \sum_i v^{HF}(i) \tag{2.180}$$

Using the Rayleigh-Schrödinger perturbation theory solutions from the previous section, the zeroth order perturbation to the Hartree-Fock wavefunction $\left|\Psi_0^{(0)}\right\rangle$ is an eigenfunction of $\hat{H}_0$ forming the eigenvalue equation

$$\hat{H}_0 \left|\Psi_0^{(0)}\right\rangle = E_0^{(0)} \left|\Psi_0^{(0)}\right\rangle \tag{2.181}$$

with eigenvalue

$$E_0^{(0)} = \sum_a \varepsilon_a \tag{2.182}$$

which is the sum over orbital energies and the zeroth-order perturbation energy. The first-order energy involves the perturbed Hamiltonian $\hat{V}$

$$E_0^{(1)} = \left\langle \Psi_0^{(0)} \middle| \hat{V} \middle| \Psi_0^{(0)} \right\rangle = -\frac{1}{2} \sum_{ab} \langle ab||ab\rangle \tag{2.183}$$

Taking the zeroth- and first-order corrections together, first order MP1 simply returns the Hartree-Fock energy

$$E(\text{MP1}) = E^{\text{HF}} = E_0 = (E_0^{(0)} + E_0^{(1)}) = \sum_a \varepsilon_a - \frac{1}{2} \sum_{ab} \langle ab||ab\rangle \tag{2.184}$$

The second-order correction for the ground-state takes the general form

$$E_0^{(1)} = \sum_{i \neq n} \frac{\left| \left\langle \Psi_0^{(0)} \middle| \hat{V} \middle| \Psi_n^{(0)} \right\rangle \right|^2}{E_0^{(0)} - E_n^{(0)}} \tag{2.185}$$

here, $\left|\Psi_n^{(0)}\right\rangle$ are the doubly excited determinants of the form$|\Psi_{ab}^{rs}\rangle$. Accounting for the orbital energies ε_a, ε_b, ε_r, ε_s, introduced by the double excitations and with some additional work the second-order correction can be written in terms of the two-electron integrals in two forms

$$E_0^{(2)} = \sum_{\substack{a<b \\ r<s}} \frac{|\langle ab||rs\rangle|^2}{\varepsilon_a + \varepsilon_b - \varepsilon_r - \varepsilon_s} = \frac{1}{4} \sum_{abrs} \frac{|\langle ab||rs\rangle|^2}{\varepsilon_a + \varepsilon_b - \varepsilon_r - \varepsilon_s} \tag{2.186}$$

The Møller-Plesset second order (MP2) energy can be written as

$$E(\text{MP2}) = E(\text{HF}) + \frac{1}{4} \sum_{abrs} \frac{|\langle ab||rs\rangle|^2}{\varepsilon_a + \varepsilon_b - \varepsilon_r - \varepsilon_s} \tag{2.187}$$

and accounts for a portion of the missing correlation energy in Hartree-Fock theory.

2.7.3 Complete Active Space 2nd Order Perturbation Theory: CASPT2

The Rayleigh schrödinger perturbation theory and its application to MP2 also forms the foundations of perturbation applied to multiconfigurational wavefunctions. In Molcas, both Complete Active Space 2nd Perturbation Theory (CASPT2) and its RASPT2 variant are implemented,[33] and additional details can be found in the separate papers of Pulay[34] and Battaglia.[35, 36]

In CASPT2, the CASSCF wavefunction is the zeroth order reference wavefunction in which the perturbation energies are calculated. Since perturbation applies best (less prone

to diverge) when the perturbation is weak, the better the CASSCF reference at capturing correlation, the less "work" is required from perturbation theory to capture the remaining correlation. The approach can also be applied to RASSCF wavefunctions in the form of RASPT2. CASPT2 can be viewed as a modification of MP2 for multiconfigurational wavefunctions and CASPT2 should reduce to the MP2 formalism in the case CASSCF CI is reduced to a single determinant. The problem is formulated in the familiar way by partitioning the Hamiltonian

$$\hat{H} = \hat{H}^{(0)} + \hat{V} \tag{2.188}$$

The reference wavefunction $|\Psi_0\rangle$ is the CASSCF wavefunction and is an eigenfunction of $\hat{H}^{(0)}$ with an associated energy $E_0^{(0)}$. However, it is important to note the $E_0^{(0)}$ does not correspond to the CASSCF energy but the eigenvalue of a generalised Fock operator in the same way the MP2 zeroth-order energy is not equal to the HF energy. The first-order interacting space is spanned by an additional set of eigenfunctions $\left|\Phi_i^{(0)}\right\rangle$ of $\hat{H}^{(0)}$, satisfying the eigenvalue equation

$$\hat{H}^{(0)}\left|\Phi_i^{(0)}\right\rangle = \varepsilon_i\left|\Phi_i^{(0)}\right\rangle \quad i = 1, \cdots, M \tag{2.189}$$

which takes the form of the first order equation from RS perturbation theory. In CASPT2 the functions $\left|\Phi_i^{(0)}\right\rangle$ form the excited configurations of the first order interacting space (which defines which excited configurations are available) and are generated by the application of excitation operators to the CASSCF reference wavefunction. ε_i represents the zeroth-order energy associated with a state Φ_i. The second order correction takes the general form

$$E^{(2)} = \sum_{i=1}^{M} \frac{|\left\langle\Phi_i^{(0)}\right|\hat{V}\left|\Psi_0^{(0)}\right\rangle|^2}{\varepsilon_i - E_0^{(0)}} \tag{2.190}$$

but with the CASSCF reference wavefunction and set of excited configurations. One of the issues that arise in CASPT2 (and similarly RASPT2) is the occurrence of intruder states that enter the equations and cause the denominator to vanish. This can lead to a divergence of the perturbation series or artificially high correction energies. This arises due to a degeneracy between a state Φ_i and the reference state Ψ_0. In both cases, any such states that are in near degeneracy with the reference wavefunction are classed as

intruder states. A simple solution may be to include the state in question, Φ_i, as a possible configuration in the reference state Ψ_0, so that it is explicitly accounted for in the CASSCF step. However, this can either be impractical or simply lead to even further intruder state issues in the next round. Instead, energy shifts can be included within the denominator to avoid near-degeneracy. This can be done with a real parameter called a level shift (κ) or an imaginary shift ($i\kappa$), which in practice only the real part is taken resulting in a $\frac{\kappa^2}{\Delta_i}$ term. The second order energy corrections, where $\Delta_i = \varepsilon_i - E_0^{(0)}$, then become

$$E^{(2)} = \sum_{i=1}^{M} \frac{|\left\langle \Phi_i^{(0)} \right| \hat{V} \left| \Psi_0^{(0)} \right\rangle|^2}{\Delta_i + \kappa} \qquad E^{(2)} = \sum_{i=1}^{M} \frac{|\left\langle \Phi_i^{(0)} \right| \hat{V} \left| \Psi_0^{(0)} \right\rangle|^2}{\Delta_i + (\kappa^2/\Delta_i)} \tag{2.191}$$

In the real level-shift approach, a singularity in the equation can still occur if a state enters the equation with an energy less than the reference. Furthermore, since κ is applied uniformly, it affects the contributions to the energy for states that are dominating and therefore the energy correction $E^{(2)}$ is strongly dependent on the value of κ. In the imaginary shift approach, no singularities can form, and due to the $1/\Delta_i$ dependence, κ only dominates in the expression when Δ_i is small. This corresponds to cases in which an intruder enters the equation and therefore the use of an imaginary shift has less impact on the $E^{(2)}$ correction when there is limited intruder states.

2.8 Relativistic Effects in Molcas

2.8.1 Scalar-Relativistic Effects

For the actinide systems simulated in this thesis, relativistic effects are important. These can be included in Molcas for multiconfigurational wavefunctions. The relativistic effects of the Dirac equation can be incorporated into calculations through the Douglas-Kroll-Hess (DKH) Hamiltonian. The one-electron time-independent Dirac equation is given by

$$\underbrace{[c\alpha \cdot \hat{P} + c^2\beta + V]}_{\text{Dirac Hamiltonian } \hat{H}_\text{D}} \Psi = E\Psi \tag{2.192}$$

where the Dirac Hamiltonian $\hat{H}_\text{D}$ is composed of four-dimensional operators, where $\hat{P}$ is the momentum operator, V is a potential and c is the speed of light. The α and β terms

are four component matrices defined below

$$\alpha_{\mathbf{x,y,z}} = \begin{pmatrix} 0 & \sigma_{\mathbf{x,y,z}} \\ \sigma_{\mathbf{x,y,z}} & 0 \end{pmatrix} \qquad \beta = \begin{pmatrix} \mathbf{I} & 0 \\ 0 & \mathbf{I} \end{pmatrix} \tag{2.193}$$

where $\mathbf{I}$ is the identity matrix and $\sigma_{x,y,z}$ are the three Pauli matrices.

The Dirac spinors Ψ take the form

$$\mathbf{\Psi} = \begin{pmatrix} \mathbf{\Psi}^{\mathrm{L}} \\ \mathbf{\Psi}^{\mathrm{S}} \end{pmatrix} \tag{2.194}$$

and consist of two components, a large $\mathbf{\Psi}^{\mathrm{L}}$ and a small $\mathbf{\Psi}^{\mathrm{S}}$ component. The small components represent the positrons, the anti-matter pair to the electron which are represented by the large component. It is desirable to obtain a representation for the relativistic electronic Hamiltonian which remains accurate but is easy to implement with the conventional non-relativistic methods. To do this, Molcas implements the Douglas-Kroll-Hess Hamiltonian and involves a unitary transformation of the Dirac Hamiltonian to eliminate the small component of the spinors, which further eliminates unwanted negative energy states associated with the positrons.[31] This reduces the Dirac Hamiltonian to a two-component electronic Hamiltonian which can be implemented with conventional non-relativistic approaches.[37, 38] The Douglas-Kroll-Hess Hamiltonian is expanded in a series of operators each obtaining more accuracy but incurring increasing computational expense. DKH to second order tends to offer a reasonable balance between accuracy and cost, and is the approach used in this thesis. Relativistic basis sets are paired with DKH, with the ANO-RCC basis set used throughout this thesis and are described in section 2.2.2.3.

2.8.2 Spin-Orbit Coupling

To account for spin-orbit coupling, the SO-RASSI formalism in Molcas is utilised. The Restricted Active Space State-Interaction (RASSI) program is utilised in general to evaluate properties between two states, such as overlaps, transition dipole moments and strengths, or in this case spin-orbit coupling. Molcas makes use of a Graphical Unitary Group Approach (GUGA) meaning a spin-free formalism is implemented, and RASSCF/CASSCF wavefunctions reflect this. [39] In a spin-free representation the $\mathrm{M_s}$

quantum number is not defined, meaning the CAS and RAS wavefunctions are effectively spinless, but they can be constrained to a specific total spin-multiplicity. One of the main problems that arises in state-interaction approaches using MCSCF wavefunctions is that two states may have differently optimised orbital bases. RASSI was built to enable two mutliconfigurational (spin-free) wavefunctions optimised in separate orbital bases to interact through transformation of pairs of orbital sets to a biorthonormal basis.[40] This enables the equations in RASSI to treat the two wavefunctions as if the orbitals were the same. For spin-orbit coupling, sets of spin-free states are coupled under the influence of SO coupling by an effective one-electron Fock-type SO Hamiltonian suggested by Hess and co-workers,[41] and Wigner-Eckart theory is used to produce matrix elements over individual spin states.[39, 40] RASPT2 energy corrections can be included by shifting the diagonal SO Hamiltonian elements, whilst pairing RASSI calculations with atomic mean-field integrals simplifies the calculations substantially and reduces the computational cost.[33, 42, 43]

References

[1] A. Szabó and N. S. Ostlund, *Modern quantum chemistry : introduction to advanced electronic structure theory*, Dover Publications, Incorporated, New York, UNITED STATES, 1982.

[2] T. Helgaker, P. Jørgensen and J. Olsen, *Molecular Electronic-Structure Theory*, John Wiley & Sons, Ltd, 2000.

[3] M. P. Jensen and A. H. Bond, *Journal of the American Chemical Society*, 2002, **124**, 9870–9877, DOI: 10.1021/ja0178620.

[4] C. J. Cramer, *Essentials of Computational Chemistry : Theories and Models*, John Wiley & Sons, Incorporated, New York, UNITED KINGDOM, 2004.

[5] B. P. Pritchard, D. Altarawy, B. Didier, T. D. Gibson and T. L. Windus, *Journal of Chemical Information and Modeling*, 2019, **59**, 4814–4820, DOI: 10.1021/acs.jcim.9b00725.

[6] *The Journal of Physical Chemistry A*, 2004, **108**, 2851–2858, DOI: 10.1021/jp031064+.

[7] B. O. Roos, R. Lindh, P.-Å. Malmqvist, V. Veryazov and P.-O. Widmark, *The Journal of Physical Chemistry A*, 2005, **109**, 6575–6579, DOI: 10.1021/jp0581126.

[8] B. O. Roos, R. Lindh, P.-Å. Malmqvist, V. Veryazov and P.-O. Widmark, *Chemical Physics Letters*, 2005, **409**, 295–299, DOI: 10.1016/j.cplett.2005.05.011.

[9] J. P. Zobel, P.-O. Widmark and V. Veryazov, *Journal of Chemical Theory and Computation*, 2020, **16**, 278–294, DOI: 10.1021/acs.jctc.9b00873.

[10] C. C. J. Roothaan, *Rev. Mod. Phys.*, 1951, **23**, 69–89, DOI: 10.1103/RevModPhys.23.69.

[11] G. G. Hall and J. E. Lennard-Jones, *Proceedings of the Royal Society of London. Series A. Mathematical and Physical Sciences*, 1951, **205**, 541–552, DOI: 10.1098/rspa.1951.0048.

[12] A. D. Becke, *The Journal of Chemical Physics*, 2014, **140**, 18A301, DOI: 10.1063/1.4869598.

[13] J. P. Perdew, A. Ruzsinszky, J. Tao, V. N. Staroverov, G. E. Scuseria and G. I. Csonka, *The Journal of Chemical Physics*, 2005, **123**, 062201, DOI: 10.1063/1.1904565.

[14] J. P. Perdew and K. Schmidt, *AIP Conference Proceedings*, 2001, **577**, 1–20, DOI: 10.1063/1.1390175.

[15] F. Jensen, *Introduction to Computational Chemistry*, John Wiley & Sons, Incorporated, Newark, UNITED STATES, 2017.

[16] P. Hohenberg and W. Kohn, *Phys. Rev.*, 1964, **136**, B864–B871, DOI: 10.1103/PhysRev.136.B864.

[17] W. Kohn and L. J. Sham, *Phys. Rev.*, 1965, **140**, A1133–A1138, DOI: 10.1103/PhysRev.140.A1133.

[18] A. D. Becke, *The Journal of Chemical Physics*, 1993, **98**, 1372–1377, DOI: 10.1063/1.464304.

[19] A. D. Becke, *Phys. Rev. A*, 1988, **38**, 3098–3100, DOI: 10.1103/PhysRevA.38.3098.

[20] C. Lee, W. Yang and R. G. Parr, *Phys. Rev. B*, 1988, **37**, 785–789, DOI: 10.1103/PhysRevB.37.785.

[21] J. P. Perdew, K. Burke and M. Ernzerhof, *Phys. Rev. Lett.*, 1996, **77**, 3865–3868, DOI: 10.1103/PhysRevLett.77.3865.

[22] J. Sun, A. Ruzsinszky and J. P. Perdew, *Phys. Rev. Lett.*, 2015, **115**, 036402, DOI: 10.1103/PhysRevLett.115.036402.

[23] D. J. Tozer and M. J. G. Peach, *Molecular Physics*, 2018, **116**, 1504–1511, DOI: 10.1080/00268976.2018.1453094.

[24] P. J. Stephens, F. J. Devlin, C. F. Chabalowski and M. J. Frisch, *The Journal of Physical Chemistry*, 1994, **98**, 11623–11627, DOI: 10.1021/j100096a001.

[25] A. D. Becke, *The Journal of Chemical Physics*, 1996, **104**, 1040–1046, DOI: 10.1063/1.470829.

[26] A. D. Becke, *The Journal of Chemical Physics*, 1993, **98**, 5648–5652, DOI: 10.1063/1.464913.

[27] A. D. Becke, *The Journal of Chemical Physics*, 1992, **97**, 9173–9177, DOI: 10.1063/1.463343.

[28] A. D. Becke, *The Journal of Chemical Physics*, 1992, **96**, 2155–2160, DOI: 10.1063/1.462066.

[29] R. Van Noorden, B. Maher and R. Nuzzo, *The top 100 papers*, https://www.nature.com/news/the-top-100-papers-1.16224 (visited on 09/24/2024).

[30] C. Adamo and V. Barone, *The Journal of Chemical Physics*, 1999, **110**, 6158–6170, DOI: 10.1063/1.478522.

[31] F. Aquilante, J. Autschbach, R. K. Carlson, L. F. Chibotaru, M. G. Delcey, L. D. Vico, I. F. Galván, N. Ferré, L. M. Frutos, L. Gagliardi, M. Garavelli, A. Giussani, C. E. Hoyer, G. L. Manni, H. Lischka, D. Ma, P. Å. Malmqvist, T. Müller, A. Nenov, M. Olivucci, T. B. Pedersen, D. Peng, F. Plasser, B. Pritchard, M. Reiher, I. Rivalta, I. Schapiro, J. Segarra-Martí, M. Stenrup, D. G. Truhlar, L. Ungur, A. Valentini, S. Vancoillie, V. Veryazov, V. P. Vysotskiy, O. Weingart, F. Zapata and R. Lindh,

Journal of Computational Chemistry, 2016, **37**, 506–541, DOI: 10.1002/jcc.24221.

[32] D. Cremer, *WIREs Computational Molecular Science*, 2011, **1**, 509–530, DOI: https://doi.org/10.1002/wcms.58.

[33] F. Aquilante, J. Autschbach, A. Baiardi, S. Battaglia, V. A. Borin, L. F. Chibotaru, I. Conti, L. D. Vico, M. Delcey, I. F. Galván, N. Ferré, L. Freitag, M. Garavelli, X. Gong, S. Knecht, E. D. Larsson, R. Lindh, M. Lundberg, P. Å. Malmqvist, A. Nenov, J. Norell, M. Odelius, M. Olivucci, T. B. Pedersen, L. Pedraza-González, Q. M. Phung, K. Pierloot, M. Reiher, I. Schapiro, J. Segarra-Martí, F. Segatta, L. Seijo, S. Sen, D.-C. Sergentu, C. J. Stein, L. Ungur, M. Vacher, A. Valentini and V. Veryazov, *The Journal of Chemical Physics*, 2020, **152**, 214117, DOI: 10.1063/5.0004835.

[34] P. Pulay, *International Journal of Quantum Chemistry*, 2011, **111**, 3273–3279, DOI: https://doi.org/10.1002/qua.23052.

[35] S. Battaglia, L. Fransén, I. Fdez. Galván and R. Lindh, *Journal of Chemical Theory and Computation*, 2022, **18**, 4814–4825, DOI: 10.1021/acs.jctc.2c00368.

[36] S. Battaglia, I. Fdez. Galván and R. Lindh, in *Theoretical and Computational Photochemistry*, Elsevier, 2023, pp. 135–162, DOI: 10.1016/b978-0-323-91738-4.00016-6.

[37] A. L. Wysocki and K. Park, *The Journal of Chemical Physics*, 2024, **160**, 224102, DOI: 10.1063/5.0208851.

[38] T. Nakajima and K. Hirao, *Chemical Reviews*, 2012, **112**, 385–402, DOI: 10.1021/cr200040s.

[39] P. Å. Malmqvist, B. O. Roos and B. Schimmelpfennig, *Chemical Physics Letters*, 2002, **357**, 230–240, DOI: 10.1016/S0009-2614(02)00498-0.

[40] I. Fdez. Galván, M. Vacher, A. Alavi, C. Angeli, F. Aquilante, J. Autschbach, J. J. Bao, S. I. Bokarev, N. A. Bogdanov, R. K. Carlson, L. F. Chibotaru, J. Creutzberg, N. Dattani, M. G. Delcey, S. S. Dong, A. Dreuw, L. Freitag, L. M. Frutos, L. Gagliardi, F. Gendron, A. Giussani, L. González, G. Grell, M. Guo, C. E.

Hoyer, M. Johansson, S. Keller, S. Knecht, G. Kovačević, E. Källman, G. Li Manni, M. Lundberg, Y. Ma, S. Mai, J. P. Malhado, P. Å. Malmqvist, P. Marquetand, S. A. Mewes, J. Norell, M. Olivucci, M. Oppel, Q. M. Phung, K. Pierloot, F. Plasser, M. Reiher, A. M. Sand, I. Schapiro, P. Sharma, C. J. Stein, L. K. Sørensen, D. G. Truhlar, M. Ugandi, L. Ungur, A. Valentini, S. Vancoillie, V. Veryazov, O. Weser, T. A. Wesołowski, P.-O. Widmark, S. Wouters, A. Zech, J. P. Zobel and R. Lindh, *Journal of Chemical Theory and Computation*, 2019, **15**, 5925–5964, DOI: 10.1021/acs.jctc.9b00532.

[41] B. A. Hess, C. M. Marian, U. Wahlgren and O. Gropen, *Chemical Physics Letters*, 1996, **251**, 365–371, DOI: 10.1016/0009-2614(96)00119-4.

[42] F. Gendron, D. Páez-Hernández, F.-P. Notter, B. Pritchard, H. Bolvin and J. Autschbach, *Chemistry – A European Journal*, 2014, **20**, 7994–8011, DOI: https://doi.org/10.1002/chem.201305039.

[43] G. Li Manni, I. Fdez. Galván, A. Alavi, F. Aleotti, F. Aquilante, J. Autschbach, D. Avagliano, A. Baiardi, J. J. Bao, S. Battaglia, L. Birnoschi, A. Blanco-González, S. I. Bokarev, R. Broer, R. Cacciari, P. B. Calio, R. K. Carlson, R. Carvalho Couto, L. Cerdán, L. F. Chibotaru, N. F. Chilton, J. R. Church, I. Conti, S. Coriani, J. Cuéllar-Zuquin, R. E. Daoud, N. Dattani, P. Decleva, C. de Graaf, M. G. Delcey, L. De Vico, W. Dobrautz, S. S. Dong, R. Feng, N. Ferré, M. Filatov(Gulak), L. Gagliardi, M. Garavelli, L. González, Y. Guan, M. Guo, M. R. Hennefarth, M. R. Hermes, C. E. Hoyer, M. Huix-Rotllant, V. K. Jaiswal, A. Kaiser, D. S. Kaliakin, M. Khamesian, D. S. King, V. Kochetov, M. Krośnicki, A. A. Kumaar, E. D. Larsson, S. Lehtola, M.-B. Lepetit, H. Lischka, P. López Ríos, M. Lundberg, D. Ma, S. Mai, P. Marquetand, I. C. D. Merritt, F. Montorsi, M. Mörchen, A. Nenov, V. H. A. Nguyen, Y. Nishimoto, M. S. Oakley, M. Olivucci, M. Oppel, D. Padula, R. Pandharkar, Q. M. Phung, F. Plasser, G. Raggi, E. Rebolini, M. Reiher, I. Rivalta, D. Roca-Sanjuán, T. Romig, A. A. Safari, A. Sánchez-Mansilla, A. M. Sand, I. Schapiro, T. R. Scott, J. Segarra-Martí, F. Segatta, D.-C. Sergentu, P. Sharma, R. Shepard, Y. Shu, J. K. Staab, T. P. Straatsma, L. K. Sørensen, B. N. C. Tenorio, D. G. Truhlar, L. Ungur, M. Vacher, V. Veryazov, T. A. Voß, O. Weser, D. Wu,

X. Yang, D. Yarkony, C. Zhou, J. P. Zobel and R. Lindh, *Journal of Chemical Theory and Computation*, 2023, **19**, 6933–6991, DOI: 10.1021/acs.jctc.3c00182.

Chapter 3

Quantifying Covalency and Environmental Effects in Uranyl O K-edge XANES Simulations

In this chapter, a RASSCF approach for simulating the O K-edge XANES spectrum of three different uranyl models is presented. Simulations successfully reproduce the three peak profile and corresponding peak assignments reported by Denning for the experimental XAS spectrum. The $[UO_2Cl_4]^{2-}$ *model was found to give the best overall prediction for peak positions (to within 1eV) and relative peak separations. Simulated XANES peaks can be attributed to a number of transitions which consist of highly multiconfigurational states, the combination of which complicates the relationship between peak intensity and the specific oxygen character of an anti-bonding orbital in a specific transition. Results in this chapter show that the relationship between the oxygen character in the anti-bonding orbital and the strength of the associated transition breaks down when using a variety of orbital composition approaches for the high energy* $1s \rightarrow \pi_g^*$ *peak. Regardless of the uranyl model, orbital composition analysis of the bonding orbitals in the ground- and core-excited states reveals a reduced U% contribution in the latter. The differences in O% contributions are found to vary depending on the model and peak analysed. QTAIM analysis reveals a strong dependence between U-O bonding and the inclusion of equatorial ligands in both the ground- and core-excited states, with results pointing to lower U-O covalency in the*

latter. Inclusion of caesium point charges to the uranyl tetrachloride model had little impact on QTAIM metrics. Overall, models that better represent the crystal environment provide core-excited state electronic structures and bonding orbital compositions that better represent the ground-state.

3.1 Introduction

X-ray absorption Near-Edge Spectroscopy (XANES) when paired with theoretical simulations has emerged as a powerful tool for probing actinide-ligand covalency.[1–14] Hence, there is a need for robust and reliable theoretical approaches to simulate XANES in order to aid interpretation of experimental spectra in terms of ground-state (GS) covalency, and for understanding the limitations of the technique. Simulating XANES spectra is challenging for actinide systems, which present strong electron correlation, pronounced relativistic effects and substantial multiconfigurational character. Theoretical approaches need to be robust enough to capture these features of actinide systems but also any changes in electronic structures between the GS and core-excited states (CESs) due to core-hole relaxation effects. Capturing orbital relaxation due to the core-hole is crucial for approaches to be truly predictive, accounting for as much as ∼20 eV of predictive error when using TD-DFT to simulate uranyl O K-edge XANES.[15] RASSCF theory [16–19] calculations are able to meet the outlined criteria and have been successfully implemented to simulate XANES in a variety of actinide systems.[7–11, 13]

In this chapter, a RASSCF approach is outlined and applied to simulate the O K-edge XANES spectrum of uranyl. The uranyl dication ($[UO_2]^{2+}$) is the form uranium takes in its most stable +6 oxidation state under ambient conditions, and is therefore a widespread moiety across hexavalent uranium complexes, making it a key system for understanding actinide covalency in general.[20] The covalency of uranyl is well established and is characterised by short, strong and chemically inert U=O bonds.[6, 15, 20–26] Understanding the covalency of uranyl is important for applications in spent nuclear fuel separations, which holds promise for safer long term storage of waste, making nuclear energy generation a more viable alternative to fossil fuel intensive power generation. [27, 28] For instance, the separation and extraction of uranyl ions from high-level liquid waste relies on the design of highly selective ligands, such as trialkyl phosphine oxide (TRPO),

in order to recover uranyl from other actinides in the waste.[29, 30] To this end, O K-edge XANES has proven useful in probing uranyl covalency.

For simulations of uranyl concerned with covalency, care must be taken to carefully consider the models used, since a variety of equatorial ligands can bond to uranyl and directly impact U=O covalency.[25, 26, 31–33] For example, the longer and therefore weaker U-O bond in $[UO_2F_4]^{2-}$ compared to $[UO_2Cl_4]^{2-}$, is explained by the greater electrostatic repulsion between U and O in the presence of the fluoride ligands, which form shorter bonds with uranium compared to chloride.[26, 31] Studies have also pointed to the impact of equatorial chloride ligands on electronic spectra calculations of uranyl. This was highlighted by Pierloot et al.[34, 35] who showed that the presence of the chloride ligands blue-shifted excited states and changed the character of the luminescent state compared to the uranyl dication. The chloride ligands appear to be the main influence on U-O covalency, since Gomes et al.[36] later showed that capturing the $Cs_2UO_2Cl_4$ crystal environment more completely through the incorporation of the Cs counter-ions led to only a small improvement in predicting excited states. The ligands can also directly influence the XANES spectra, as shown by Fillaux et al.,[15] the equatorial ligands in $[UO_2(py)_3I_2]$ and $[UO_2(CN)_5][NEt_4]^3$ species have a measurable effect on the features of the uranyl spectrum. Using a combination of TD-DFT simulations and experimental O K-edge XANES, the study found an additional peak generated in the cyanide systems due to a π-interaction between the ligand and uranyl π_g^* orbitals which does not occur in the pyridine system.

In 2002, the O K-edge XANES spectrum of uranyl was reported by Denning et al.[6] for the $Cs_2UO_2Cl_4$ crystal. Recently, Misael et al.[37] presented 4c-DR-TD-DFT simulations of uranyl O K-edge XANES for the $Cs_2UO_2Cl_4$ crystal. Here, it was shown that the relative peak positions are better predicted with respect to experiment by the inclusion of equatorial chloride ligands, while modelling counter-ions as an embedding potential had little impact on the predictions. This study, once again, points to the importance of considering the models used in XANES simulations. Before the publication of results from this chapter, a comprehensive RASSCF study simulating O K-edge XANES for uranyl was absent from the literature.[38] In this chapter, a RAS(S), RAS(SD), and RAS(SDT) approach to simulating O K-edge XANES of uranyl using three models that progressively

better represent the local $Cs_2UO_2Cl_4$ environment is reported. The aim of this study is to establish a RASSCF methodology capable of reproducing the experimental spectrum and to analyse the electronic structure of states to assess if XANES is a valid probe of GS covalency. The chapter is split into two main areas: First the ability of the RAS approach to reproduce the experimental XANES spectrum reported by Denning[6] is considered and the process for characterising the peaks is outlined. Secondly, the chapter turns to address the assumptions inherent in interpreting XANES as a GS covalency probe, using a variety of analysis approaches to examine differences in electronic structure between the GS and CESs.

3.2 Computational Method

3.2.1 Multiconfigurational XANES simulations

Scalar relativistic multiconfigurational calculations were performed using version 21.02 of Openmolcas.[19, 39–41] All-electron relativistic ANO-RCC TZVP quality basis sets of Roos et al.[42–44]were employed for U (9s8p6d4f2g), O (4s3p2d1f) and Cl (5s4p2d1f). For uranium, higher angular moment h-functions were removed to enable comparability with visualisation and analysis software, which do not support h-functions. Scalar relativistic effects were modelled using the second order Douglas-Kroll-Hess Hamiltonian and Cholesky decomposition was utilized throughout to speed-up integral calculations.[45–49]

3.2.2 Uranyl Models

Three idealised models of the $Cs_2UO_2Cl_4$ crystal were utilised in this study, and are shown in fig. 3.1. The three models aim to progressively capture environmental aspects of the $Cs_2UO_2Cl_4$ crystal utilised in the XAS experiments reported by Denning et al.[6] Simulations made use of the highest abelian point-group D_{2h} with $[UO_2]^{2+}$ and $[UO_2Cl_4]^{2-}$ models adopting the experimental bond lengths of 1.77 and 2.67Å for U-O and U-Cl bond, respectively.[6, 50] By utilising the highest possible symmetry point group available in Molcas (D_{2h}), the cost savings through symmetry considerations are maximised. The idealised D_{2h} model of $Cs_2UO_2Cl_4$ consists of a $[UO_2Cl_4]^{2-}$ sub-unit with atomic centres modelled with all-electron basis sets, and an array of eight point-charges representing the

caesium counter-ions. Each point-charge has a fractional charge $+\frac{1}{4}$ a.u., to ensure charge neutrality of the system overall. The position of the point-charges around the $[UO_2Cl_4]^{2-}$ sub-unit reflect those of the XRD structure,[50] however, some minimal adjustments were required to retain a D_{2h} system. While only minor corrections were needed to arrange the Cs point-charges in a perfect hexagonal arrangement around the sub-unit, a more significant angle adjustment was required for a pair of Cs point-charges relative to the experimental structure as shown in fig. 3.2.

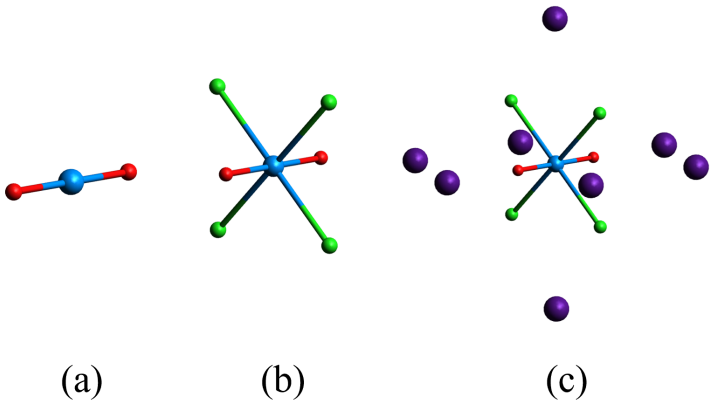

Figure 3.1: (a) $[UO_2]^{2+}$, (b) $[UO_2Cl_4]^{2-}$ and (c) $Cs_2UO_2Cl_4$ uranyl models utilized in O K-edge XANES simulations. The $Cs_2UO_2Cl_4$ model aims to account for the local crystal enviroment and is constructed as a $[UO_2Cl_4]^{2-}$ system plus eight caesium points charges, each with fractional charge $+\frac{1}{4}$ a.u. to ensure charge neutrality.

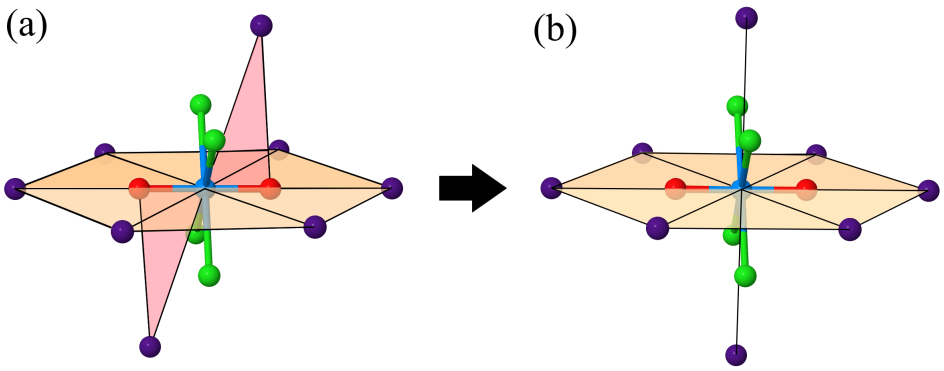

Figure 3.2: (a) XRD local crystal structure utilized in Denning O K-edge XAS experiment.[6, 50] (b) Theoretical local crystal structure used in O K-edge simulations altered to realise the D_{2h} point-group.

3.2.3 RASSCF Set-Up

A RASSCF active-space was constructed to simulate the O K-edge XANES of uranyl, as shown in fig. 3.3. To generate the GS and CESs required for uranyl O K-edge simulations, the two linear combinations of oxygen 1s orbitals (1s-σ_g and 1s-σ_u) span RAS1, the six bonding orbitals ($2\times\pi_g, 2\times\pi_u, \sigma_g, \sigma_u$) span RAS2, and six anti-bonding orbitals ($2\times\pi_g^*, 2\times\pi_u^*, \sigma_g^*, \sigma_u^*$) span RAS3. The four empty non-bonding 5f orbitals ($2\times 5f_\delta$ and $2\times 5f_\phi$) were also included within RAS3. Core-excited states were generated by allowing up to a total

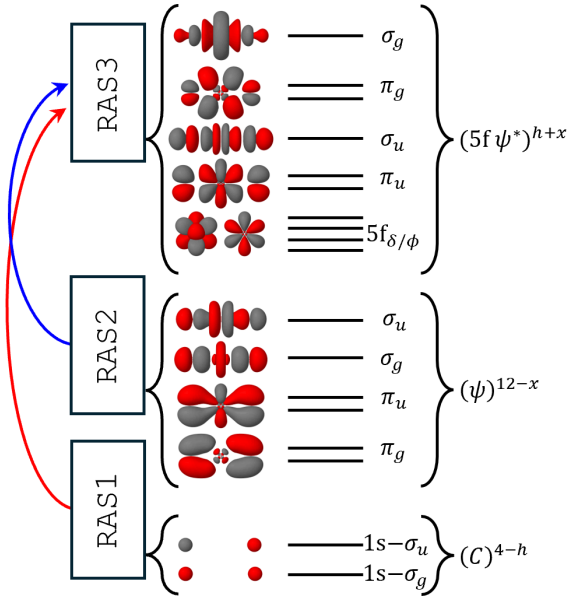

Figure 3.3: Active space utilized in RASSCF O K-edge XANES simulations. Arrows indicate which RAS spaces electrons can populate subject to the active-space constraints. The variables h and x are defined by the level of RAS calculation being performed, RAS(S) or RAS(SD), and define the number of holes and number of electron allowed to move out of RAS2 into RAS3, respectively.

of one, two or three electrons to enter RAS3, and enforcing a single core-hole across RAS1. Using Sauri notation RAS(n,m,l;i,j,k):[51] RAS(S), RAS(SD) and RAS(SDT) correspond to RAS(16,1,1;2,6,10), RAS(16,1,2;2,6,10), and RAS(16,1,3;2,6,10), respectively. Here, n is the total number of active electrons across RAS1+2+3, m is the total number of holes in RAS1, l is the total number of electrons allowed within RAS3, i, j, and k are the total number of orbitals in RAS1, RAS2, and RAS3. In the context of uranyl O K-edge simulations, the notation can be adapted for CESs are follows: RAS(16, h, x; 2, 6, 10)

where the variables h and x are defined by the level of RAS calculation being performed, RAS(S), RAS(SD), RAS(SDT), and define the number of holes (h) and number of electrons (x) allowed to move out of RAS2 into RAS3, respectively. For RAS(S), RAS(SD) and RAS(SDT) calculations, x is 0, 1 and 2, respectively, while h remains set to 1. At the RAS(S) level only electrons from RAS1 can enter RAS3. At higher RAS truncation levels, electrons from RAS2 can also enter RAS3, giving higher quality wavefunctions capable of capturing more electron correlation across the active space orbitals. To ensure that oxygen 1s-orbitals did not rotate out of the active space during the SCF procedure, the orbitals were reclassified with their own separate irreducible representation label using built-in supersymmetry designations of Openmolcas. By imposing the Laporte selection rule, only CESs of ungerade (u) symmetry and a single GS of gerade (g) symmetry were required for state-interaction, introducing a cost saving. The GS was obtained by removing the RAS1 core-hole constraint, corresponding to $h = 0$ in terms of the RAS(16, h, x; 2, 6, 10) notation, and taking the first root of a state-average singlet A_g calculation, with state-averaging found to stabilise the non-bonding 5f orbitals within the active-space. Both singlet and triplet multiplicities are possible within the uranyl electronic structure depending on the spin-alignment of electrons in the core-excited state. The required states of both multiplicities were obtained by performing the appropriate state-average calculations across the odd-parity irreps. The total number of possible core-excited states are reported in table 3.1, states are labelled in the form of ^{2S+1}X, where $2S + 1$ is the multiplicity and X is the irreducible representation of a group. State-specific 2^{nd} order RAS perturbation theory (RASPT2) was applied to all RASSCF states in order to obtain quantitatively meaningful state energies that recover dynamical correlation.[52, 53] These calculations made use of a default IPEA shift[54] of 0.25 a.u. and an imaginary shift[55] of 0.5 a.u. which offered a reasonable compromise between converging intruder free solutions without significantly affecting RASPT2 state energies and is comparable with values used in related studies.[8, 9, 11, 13]

Table 3.1: Total number of possible core-excited (u-irrep) states that can be calculated for uranyl O K-edge XANES simulations.

	^1A_u	$^1B_{1u}$	$^1B_{2u}$	$^1B_{3u}$	^3A_u	$^3B_{1u}$	$^3B_{2u}$	$^3B_{3u}$
RAS(S)	1	3	3	3	1	3	3	3
RAS(SD)	145	155	155	155	217	221	221	221
RAS(SDT)	3553	3579	3579	3579	5968	5954	5954	5954

Table 3.2: Total number of ground- (^1A_g) and core-excited states (u-irreps) that were used in state-interaction calculations for uranyl O K-edge XANES simulations.

	^1A_g	^1A_u	$^1B_{1u}$	$^1B_{2u}$	$^1B_{3u}$	^3A_u	$^3B_{1u}$	$^3B_{2u}$	$^3B_{3u}$
RAS(S)	1	1	3	3	3	1	3	3	3
RAS(SD)	1	62	63	68	68	93	90	95	95
RAS(SDT)	1	198	198	197	197	199	200	200	200

3.2.4 RASSI Calculations

3.2.4.1 Spin-Orbit Coupling

Spin-orbit coupling is pronounced in actinide species and is required in XANES simulations in order to obtain good agreement with experiment. Ground- and core-excited states were spin-orbit coupled *post hoc via* state-interaction of the scalar relativistic RASSCF states with a mean-field spin-orbit operator, making use of atomic mean-field integrals, in the Restricted Active Space State-Interaction (RASSI) formalism.[49, 56] The diagonal energies of the Hamiltonian matrix computed by RASSI take RASSCF state energies by default and were instead replaced by RASPT2 state energies. The cost of RASSI calculations increases with the number of configuration state functions and with the total number of states provided for state-interaction. To reduce the cost of RASSI calculations, the number of states at higher RAS truncation levels was kept as minimal as possible using

a 545 eV energy cutoff, meaning state-interaction was performed on a smaller set of states than the total possible number. These details are reported in table 3.2. The application of the Laporte selection rule also aids in reducing the cost of RASSI calculations by reducing the number of state considered, since any possible CESs belonging to the four gerade irreps were disregarded from state-interaction under this assumption.

To summarize, the criteria used to reduce the number of states calculated using SA-RASSCF and supplied to RASSI calculations is as follows:

1. Implementation of the Lapotre selection rule for SA-RASSCF calculations such that only CESs of ungerade and a single GS of gerade symmetry are calculated.

2. Only CESs which give excitation energies equal to or below 545 eV were included in RASSI calculations since only peaks within this range are of interest.

3.2.4.2 Generating Simulated XANES Plots

RASSI calculations provided spin-orbit coupled state energies and oscillator strengths between the GS and CESs, which were used to generate transition stick spectra. To generate XANES profiles akin to experiment, all transition sticks were broadened by fitting Lorentzian functions to all transitions with a shared full-width at half-maximum (FWHM) value of 0.8 eV. The choice of FWHM is considered somewhat arbitrary since the peak maxima are found to remain the same regardless of the value chosen, but values were chosen to offer good visual comparison with the available experimental references. Once the spectrum was obtained, key transitions were identified, and an additional set of RASSI calculations were performed requesting the calculation of spin-orbit natural orbitals (SONOs) for key states.[9, 57, 58]

3.2.5 Analysis Tools

SONOs produced by RASSI calculations enable the spin-orbit coupled states to be characterised with various software packages. SONOs are provided as raw SOOrb files which contain orbital coefficients and populations. These files were converted to more useful MOLDEN file formats using a custom python3 code, which has been made freely available.[59] The MOLDEN file format enables visual analysis of the SONOs and their

populations using Jmol and Multiwfn software packages.[60, 61] Assignment of the peaks is made by analysing the natural population of the orbitals for important CESs responsible for intense transitions in the XANES spectrum. Additional file formats useful for various analysis software programs were obtained using the MOLDEN2AIM package.[62] Using SONOs to represent the electron density, Quantum Theory of Atoms in Molecules (QTAIM) analysis was performed using version 19.02.13 of AIMALL,[63] and various orbital composition schemes were employed using version 3.8 of Multiwfn.[61]

3.3 Results & Discussion

3.3.1 Simulating O K-edge XANES

The experimental O K-edge X-ray Absorption Spectrum (XAS) of uranyl shown in figure 3.4 was reported by Denning et al,[6] and consists of three main peaks at 531.4 eV, 534.1 eV and 536.5 eV., and correspond to core-excitations from oxygen 1s-orbitals into the π_u^*, σ_u^*, and π_g^* orbitals, respectively. The experiment captures the XAS spectrum when the incident linearly polarised X-ray beam is (near) parallel and perpendicular to the O-U-O axis. A misalignment in the orientation of the crystal with respect to the experimental instruments and a small depolarisation error at the X-ray source, means a substantial degree of polarisation mixing is inherent in the recorded XAS for the sample. As calculated by Denning et al.,[6] it can be expected that 9.6% of the intensity of a linearly polarised transition should appear in one orientation and 90.4% in the other. The polarisation mixing in experiment means peak intensities offer only qualitative information, and given that simulations capture the overall XANES spectrum regardless of the polarisation of the incident X-ray photon, no attempt is made to directly compare intensities between experiment and theory. Instead, focus is turned to examining the relationship between peak intensity and covalency as well as the general ability of the RAS-approach to predict peak positions in agreement with experiment.

3.3.1.1 $[UO_2]^{2+}$ O K-edge XANES

Figure 3.5 presents the spin-orbit coupled O K-edge XANES spectra simulated at three levels of RAS truncation, RAS(S), RAS(SD), and RAS(SDT), for the free uranyl dication

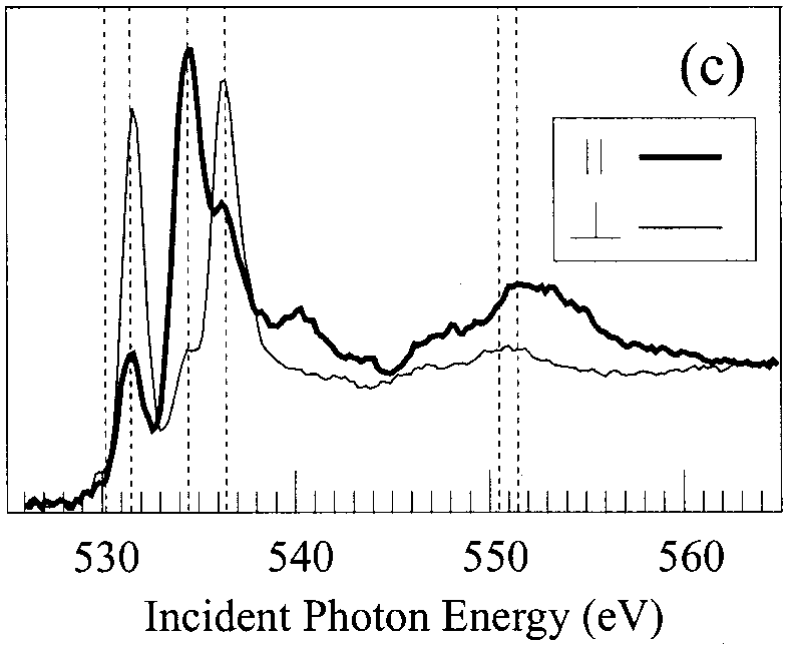

Figure 3.4: Experimental oxygen K-edge XAS spectrum taken from Ref. [6]. Spectrum was recorded using linear polarized X-rays approximately parallel and perpendicular to the O-U-O molecular axis. Dashed lines indicate peak positions. Reprinted from R. G. Denning, J. C. Green, T. E. Hutchings, C. Dallera, A. Tagliaferri, K. Giarda, N. B. Brookes and L. Braicovich, *The Journal of Chemical Physics*, 2002, **117**, 8008–8020., with permission of AIP Publishing.

model ($[UO_2]^{2+}$). The simulated spectra present a similar three peak profile (peaks labelled 1-3) in the 525-545 eV region as found in experiment.[6] Two additional features are also captured by simulations. These include a small shoulder on the first peak at ∼530 eV and an additional feature above the 550 eV mark, best viewed in figures 3.7 and 3.8 which are discussed later in the chapter. Discussion is restricted to peaks 1-3, which are the primary experimental features discussed by Denning. Peak 1 remains well resolved across all three levels of RAS truncation and are characterised by two strong transitions. Peaks 2 and 3 comprise a larger number of transitions as the level of RAS truncation is increased, resulting in broader and overall less intense peaks. These peaks eventually merge at the RAS(SDT) level. As the number of transitions associated with peaks 2 and 3 increase at higher levels of RAS truncation, the relative intensity of peak 2 with respect to peak 3 decreases. Peak 1 remains the most intense feature across the RAS simulations.

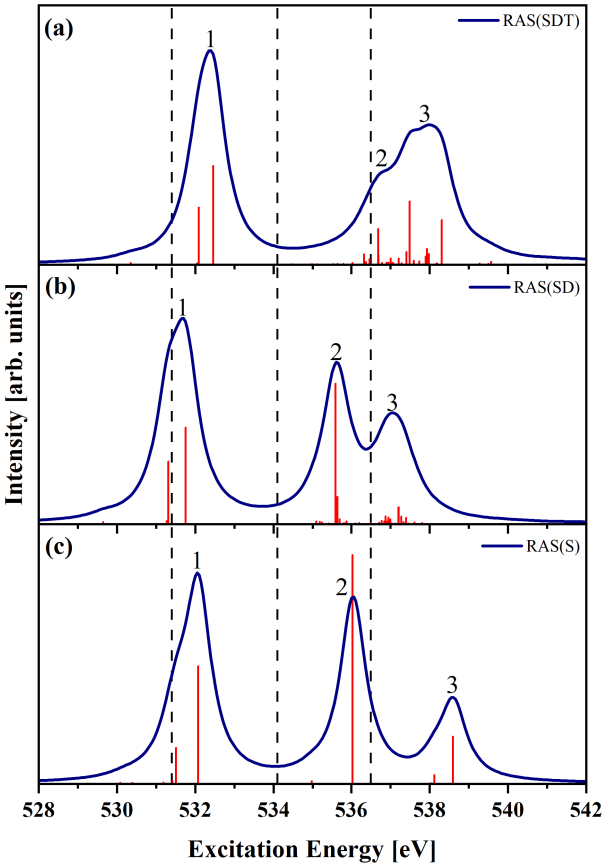

Figure 3.5: Spin-orbit coupled (a) RAS(S), (b) RAS(SD) and (c) RAS(SDT) $[UO_2]^{2+}$ O K-edge XANES simulations. Individual transitions are plotted as red sticks. Experimental positions taken from ref. [6] are indicated by black vertical dashed lines.

To assess the ability of the RAS truncation approach to better capture static correlation, the O K-edge XANES spectra for $[UO_2]^{2+}$ in the absence of RASP2 corrections are plotted in fig. 3.6, still including spin-orbit coupling. Comparing the three spectra in fig. 3.6 with the first experimentally reported peak position (531.4 eV dashed line), it is clear that the RAS truncation approach has the desired effect of predicting XAS spectra in closer energy agreement to experiment at higher RAS levels.

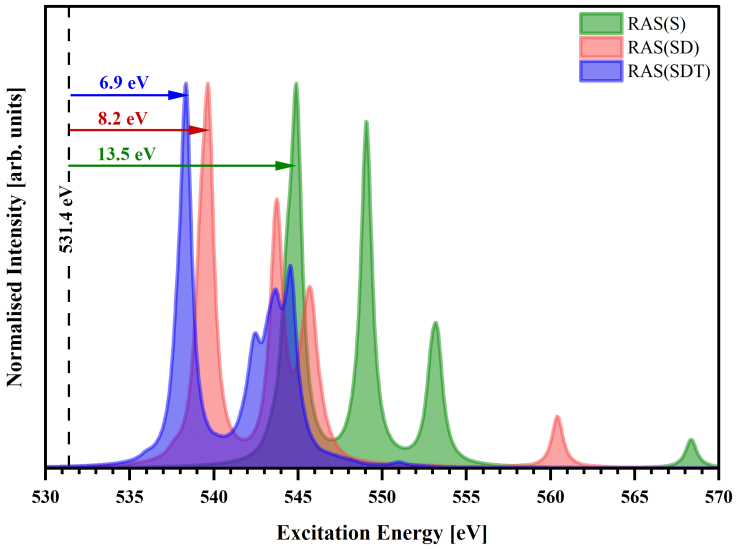

Figure 3.6: Spin-orbit coupled $[UO_2]^{2+}$ RAS(S), RAS(SD) and RAS(SDT) O K-edge XANES simulations without RASPT2 corrections. The first simulated peak is compared to the energy position of the first experimental peak.[6]

Table 3.3: Table of $[UO_2]^{2+}$ O K-edge XANES peak energy positions and the discrepancy (Δ) with respect to experiment when using the RAS-truncation approach. All values reported in eV.

	Peak 1	**Δ**	**Peak 2**	**Δ**	**Peak 3**	**Δ**
Expt. [6]	531.4		534.1		536.5	
RAS(S)	532.1	+0.7	536.1	+2.0	538.6	+2.1
RAS(SD)	531.7	+0.3	535.6	+1.5	537.1	+0.6
RAS(SDT)	532.4	+1.0	536.7	+2.6	537.8	+1.3

Table 3.3 reports the energy positions of peaks in fig. 3.5. The first peak in the spectrum establishes the energy region in which the core-excitations into the anti-bonding orbital occurs and is a good initial indicator of simulation quality. The RAS(SD) simulation offers the best energy prediction for the position of peak 1, followed by RAS(S) and then RAS(SDT). This order extends to the peaks across the spectra as a whole, with RAS(SD)

predicting peak positions with the lowest energy discrepancy with respect to experimental positions. This may be counter-intuitive since at the variational level, RAS(SDT) provides closest agreement between XANES and experiment in fig. 3.6. Including RASPT2 state energies in state-interaction calculations, shifts the first predicted peak for RAS(S), RAS(SD), and RAS(SDT) by 12.5 eV, 7.9 eV and 6.2 eV, respectively. The measured peak positions in table 3.3 and comparison to the spectra without RASPT2 corrections, highlights that a higher RAS truncation level when paired with RASPT2 corrections does not automatically guarantee better energetic agreement with experiment. However, since RASPT2 calculations are only utilized as an energy correction, the underlying core-excited states generated via RAS(SDT) would be expected to be of higher quality than RAS(SD). Overall, considering both the quality of CESs and the ability of simulation to predict absolute peak positions, RAS(SD) offers the best balance between quality, accuracy and simulation cost.

Table 3.4: Table of $[UO_2]^{2+}$ O K-edge XANES relative peak energy positions using the RAS-truncation approach and the discrepancy (Δ) with respect to relative separations in the experimental spectrum. All values reported in eV.

	$\mathbf{P_{21}}$	$\mathbf{\Delta}$	$\mathbf{P_{32}}$	$\mathbf{\Delta}$	$\mathbf{P_{31}}$	$\mathbf{\Delta}$
Expt. [6]	2.7		2.4		5.1	
RAS(S)	4.0	+1.3	2.5	+0.1	6.5	+1.4
RAS(SD)	3.9	+1.2	1.5	-0.9	5.4	+0.3
RAS(SDT)	4.3	+1.6	1.1	-1.3	5.4	+0.3

Table 3.4 reports the relative separations between peaks in fig. 3.5. The separation between peaks 1 and 2 is on the order of 4 eV across the three RAS simulations , with a discrepancy of $\sim$1 eV from experiment. Both RAS(SD) and RAS(SDT) simulations improve the predicted separation between peaks 1 and 3, in both cases predicting 5.4 eV compared to the experimental value of 5.1 eV. RAS(S) gives the best prediction for the relative separation between peaks 3 and 2, differing by 0.1 eV from experiment, but at the cost of predicting other separations over 1 eV greater than experiment. As the RAS

truncation level increases, the predicted separation between peaks 2 and 3 decreases, with RAS(SDT) giving the largest discrepancy compared to experiment. Overall, the values in table 3.4 point to a difficulty in the ability of higher RAS-level simulations to predict the correct position of the second peak relative to the others. Taking the relative separations predicted by all three simulations into consideration, separations are found to be best predicted by the RAS(SD) simulation, and supports its use in additional simulations on crystal structure models.

3.3.1.2 $[UO_2]^{2+}$ XANES Assignments

Core-excitations in uranyl O K-edge XANES occur primarily between the oxygen 1s orbitals in RAS1, into the empty valence orbitals in RAS3, as shown in fig. 3.3. All transitions plotted in the spectra represent a core-excitation between the GS and a unique CES. Due to the set-up of the active space, from a practical standpoint, a full characterisation of the core-excitation can be made solely by examining the RAS3 orbitals of the CES. Assignment of peaks to a particular core-excitation is therefore performed by examining the natural populations of the SONOs for a selection of intense transitions associated with each peak. This section outlines the process of peak assignment whereby key transitions are selected, natural populations of the RAS3 orbitals are analysed for the CESs associated with these transitions, and then an overall core-excitation is assigned to the peak. The three main core-excitations identified by Denning et al.[6] for peaks 1-3 correspond to core-excitations into the the π_u^*, σ_u^*, and π_g^* orbitals, respectively. In all cases, assignments are best informed by examining the results of RAS(S) simulations first, since the active-space constraints at this level ensures that the electron that populates RAS3 in the CES comes from an oxygen 1s orbital. Furthermore, at the RAS(S) level, the set of electronic configurations is highly limited, therefore, CESs tend to be characterised by low multiconfigurational character compared to their RAS(SD) and higher counterparts. This means orbital populations in the CESs tend to be more interpretable and align with the idea of an electron being excited into a single orbital.

Figure 3.7 presents the RAS(S) O K-edge XANES spectrum of $[UO_2]^{2+}$ with four peaks labelled 1-4. For each peak, transition sticks corresponding to key core-excitations are selected and labelled in the form $p.t$, where p is the peak number and t is the transition

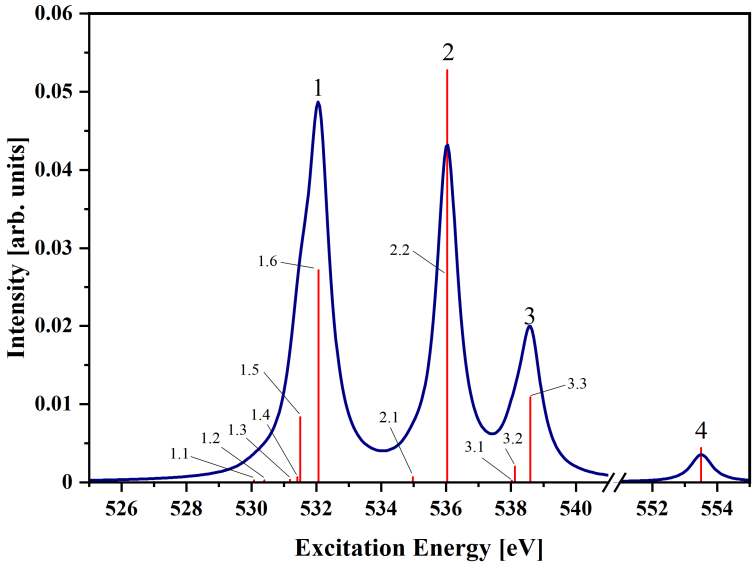

Figure 3.7: Peak and transition stick assignments for the $[UO_2]^{2+}$ spin-orbit coupled RAS(S) O K-edge XANES spectrum.

number associated with the peak. Transitions identified in fig. 3.7 are recorded in table 3.5, along with the natural populations of the RAS3 SONOs for the CES. The GS RAS3 SONO occupations are also reported for comparison. Examining the natural populations of the CESs enables the following characterisation of the RAS(S) spectrum: Peak 1, consists primarily of two intense transitions (1.5/1.6) into to the π_u^* orbitals. The origin of the shoulder feature on peak 1 at ∼530 eV is found to arise from weak transitions into the non-bonding $5f_{\delta/\phi}$ orbitals, confirming these orbitals to be the lowest energy in uranyl. Peak 2 is characterised by a single intense transition (2.2), involving a core-excitation into the σ_u^* orbital. Peak 3 is attributed to transitions (3.2/3.3) into the π_g^* orbitals, while a peak at ∼553 eV is attributable to the σ_g^* orbital. These RAS(S) peak assignments are useful in informing the assignment of higher RAS truncated simulations which give rise to CESs with populations that make peak assignments more ambiguous.

Figure 3.8 presents the RAS(SD) XANES spectrum of uranyl at two different scales to enable ease of assignment. Natural populations for selected transitions are reported in table 3.6. In the RAS(SD) simulation, a much greater density of transitions, particularly for the third peak at higher excitation energy, is observed. This makes assignment less straightforward in comparison to RAS(S), since a larger number of transitions are associated with each peak and contribute to some degree to the overall peak intensity.

Table 3.5: RAS(S) $[UO_2]^{2+}$ O K-edge XANES GS and CES populations for key transitions identified in the spectrum.

Transition	**1s-σ_g**	**1s-σ_u**	**5f$_{\delta/\phi}$**	**π_u^***	**σ_u^***	**π_g^***	**σ_g^***
GS	2.00	2.00	0.00	0.03	0.01	0.00	0.00
1.1	1.00	2.00	1.00	0.00	0.00	0.00	0.00
1.2	1.00	2.00	1.00	0.00	0.00	0.00	0.00
1.3	1.00	2.00	1.00	0.00	0.00	0.00	0.00
1.4	1.10	1.90	0.00	0.88	0.01	0.10	0.00
1.5	1.10	1.90	0.00	0.87	0.03	0.10	0.00
1.6	1.09	1.91	0.05	0.86	0.00	0.09	0.00
2.1	1.05	1.95	0.00	0.02	0.93	0.00	0.05
2.2	0.05	1.95	0.00	0.00	0.95	0.00	0.04
3.1	1.88	1.12	0.00	0.12	0.00	0.88	0.00
3.2	1.89	1.11	0.00	0.10	0.00	0.90	0.00
3.3	1.91	1.09	0.00	0.10	0.00	0.90	0.00
4	1.96	1.04	0.00	0.00	0.04	0.00	0.96

Despite the large number of transitions, peak 1 remains characterised by two intense transitions into the the π_u^* orbital and peak 2 retains its single strong transition into the σ_u^* orbital. The CESs involved in transitions associated with peak 1 show clear π_u^* occupancy, but with additional electron population in both the π_g^* and σ_u^* orbitals. Similarly, transition 2.5 shows high σ_u^* occupancy of 0.68, but coincides with significant population of the non-bonding 5f$_{\delta/\phi}$, π_u^* and π_g^* orbitals at populations of 0.64, 0.16 and 0.08, respectively. This spread of partial electron populations across RAS3 orbitals indicates an increased multiconfigurational character for the CESs at the RAS(SD) level in contrast to RAS(S). This is a direct result of the increased flexibility enabled by the RAS(SD) active-space set-up, which makes it possible to capture more of the possible CES configuration space

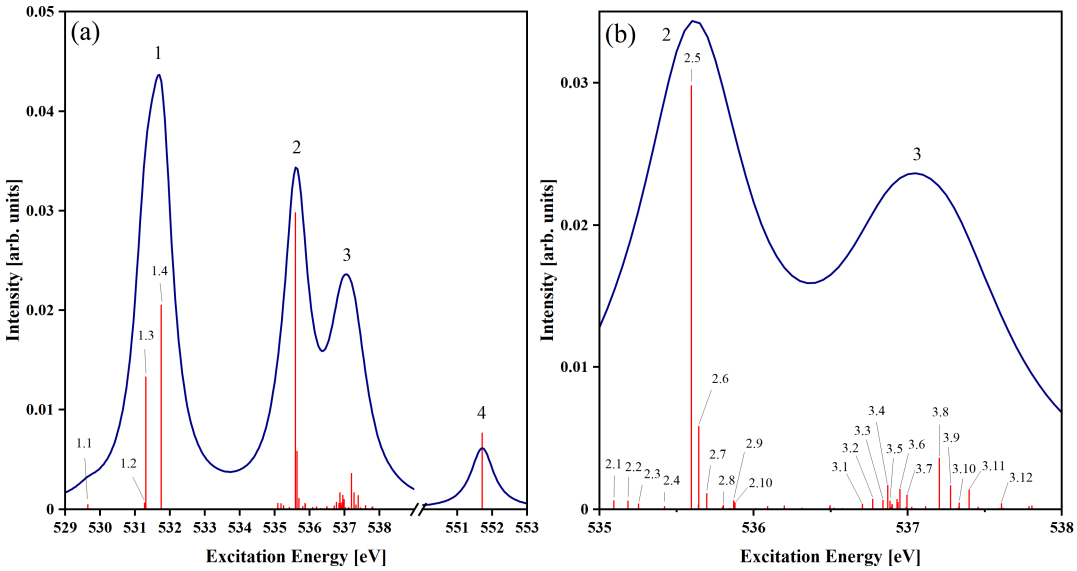

Figure 3.8: Peak and transition stick assignments for the $[UO_2]^{2+}$ spin-orbit coupled RAS(SD) O K-edge XANES spectrum at two energy ranges of (a) 529 - 553 eV and (b) 535 - 538 eV.

in the optimisation of the RASSCF wavefunctions. In contrast to RAS(S), peak 3 at the RAS(SD) level is difficult to assign since it is both characterised by a large number of weak transitions spread across a wide energy range, and involves CESs with highly multiconfigurational character. Despite these complications, transitions associated with peak 3 present CESs with π_g^* populations that are amongst the highest across all the states sampled. Transitions 3.8 and 3.10 both involved CESs with π_g^* orbital populations of 0.26. Between the two transitions, 3.8 has the highest transition strength and is therefore chosen to represent peak 3, and its CES is utilised in later sections for covalency analysis.

Table 3.6: RAS(SD) $[UO_2]^{2+}$ O K-edge XANES GS and CES populations for key transitions identified in the spectrum.

Transition	**1s-σ_g**	**1s-σ_u**	**5f$_{\delta/\phi}$**	**π_u^***	**σ_u^***	**π_g^***	**σ_g^***
GS	2.00	2.00	0.01	0.08	0.05	0.05	0.01

Continued on next page

Table 3.6: (continued)

Transition	**1s-σ_g**	**1s-σ_u**	**5f$_{\delta/\phi}$**	**π_u^***	**σ_u^***	**π_g^***	**σ_g^***
1.1	1.24	1.76	0.96	0.12	0.08	0.10	0.00
1.2	1.27	1.73	0.02	1.00	0.09	0.18	0.00
1.3	1.27	1.73	0.02	1.00	0.09	0.16	0.00
1.4	1.27	1.73	0.04	0.99	0.08	0.16	0.00
2.1	1.36	1.64	0.90	0.19	0.50	0.08	0.01
2.2	1.46	1.54	1.72	0.20	0.03	0.02	0.00
2.3	1.42	1.58	1.86	0.12	0.01	0.00	0.00
2.4	1.43	1.57	1.77	0.22	0.01	0.00	0.00
2.5	1.32	1.68	0.64	0.16	0.68	0.08	0.01
2.6	1.44	1.56	1.57	0.18	0.13	0.04	0.00
2.7	1.44	1.56	1.68	0.25	0.04	0.02	0.00
2.8	1.44	1.56	1.71	0.28	0.01	0.02	0.00
2.9	1.46	1.54	1.82	0.12	0.02	0.02	0.00
2.10	1.47	1.53	1.82	0.12	0.02	0.02	0.00
3.1	1.45	1.55	1.14	0.77	0.03	0.04	0.00
3.2	1.47	1.53	1.05	1.14	0.03	0.07	0.00
3.3	1.47	1.53	1.06	0.75	0.04	0.11	0.00
3.4	1.49	1.51	1.10	0.64	0.04	0.16	0.00
3.5	1.46	1.54	1.10	0.83	0.03	0.04	0.00
3.6	1.49	1.51	1.00	0.80	0.04	0.12	0.00
3.7	1.48	1.52	1.01	0.74	0.04	0.15	0.00
3.8	1.52	1.48	1.02	0.54	0.05	0.26	0.00

Continued on next page

Table 3.6: (continued)

Transition	**1s-σ_g**	**1s-σ_u**	**5f$_{\delta/\phi}$**	**π_u^***	**σ_u^***	**π_g^***	**σ_g^***
3.9	1.49	1.51	1.19	0.62	0.03	0.11	0.00
3.10	1.48	1.52	1.08	0.48	0.05	0.26	0.00
3.11	1.49	1.51	1.05	0.75	0.02	0.12	0.00
3.12	1.46	1.54	1.09	0.73	0.05	0.09	0.00
4	1.74	1.26	0.00	0.22	0.13	0.08	0.97

Electron populations recorded in table 3.6 point to an increasing multiconfigurational character for states as the excitation energy increases from peaks 1 to 3. This character manifests as increased partial occupation of RAS3 orbitals by an electron excited from the 1s core-orbitals as well as by electrons depleted from RAS2. For example, the CES associated with transition 3.8, contains a total electron population of 1.87 across RAS3 orbitals, with 0.87 of this coming from the depletion of RAS2 orbitals. Given that electron redistribution between RAS2 and RAS3 is more prevalent in higher energy CESs, suggests that this redistribution is an effective route for RASSCF to optimise the higher energy states. As to whether this is a real feature of the CESs or simply a feature of the simulation approach, is still an open question.

For completeness, this section finishes by presenting the assignments of the RAS(SDT) spectrum in fig. 3.9 for uranyl. Peak characterisation is performed in the same manner to that of RAS(SD), and the resulting CES populations associated with selected transitions are given in table 3.7. The partial occupation of all the RAS3 orbitals and electron redistribution from RAS2 to RAS3, gives rise to even greater multiconfigurational states at the RAS(SDT) level, making assignments more ambiguous than those before it. A similar trend to that of RAS(SD) persists in that the multiconfigurational nature of the states becomes greater as the energy increases from peaks 1 to 3. However, making similar deductions to those made in RAS(SD) assignments and with reference to RAS(S) simulations as support, leads to the same overall conclusion on the peak assignments.

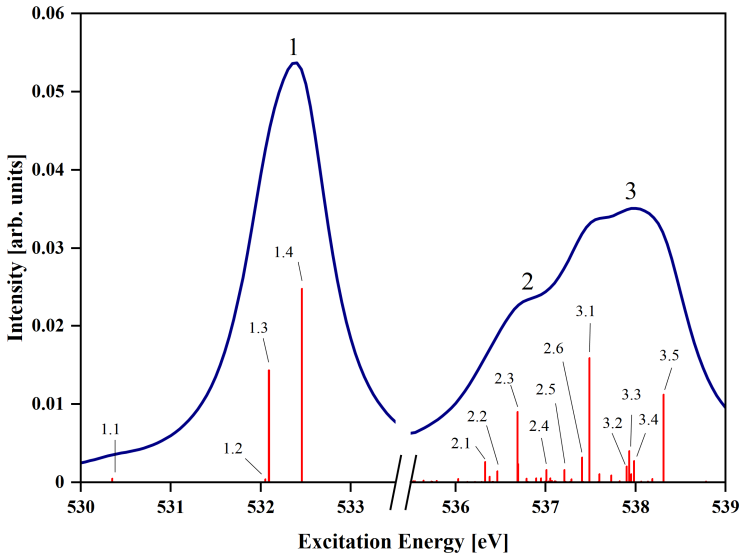

Figure 3.9: Peak and transition stick assignments for the $[UO_2]^{2+}$ spin-orbit coupled RAS(SDT) O K-edge XANES spectrum.

Overall, the outlined characterisation of peaks at all RAS levels supports the assignments made by Denning and others,[6, 20, 37] and suggests an energetic ordering of the empty valence orbitals in uranyl as follows: $5f_{\delta/\phi} < \pi_u^* < \sigma_u^* < \pi_g^* < \sigma_g^*$.

Table 3.7: RAS(SDT) $[UO_2]^{2+}$ O K-edge XANES GS and CES populations for key transitions identified in the spectrum.

Transition	**1s-σ_g**	**1s-σ_u**	**$5f_{\delta/\phi}$**	**π_u^***	**σ_u^***	**π_g^***	**σ_g^***
GS	2.00	2.00	0.02	0.13	0.06	0.06	0.01
1.1	1.28	1.72	0.98	0.18	0.12	0.13	0.00
1.2	1.30	1.70	0.07	1.05	0.12	0.18	0.00
1.3	1.30	1.70	0.07	1.05	0.12	0.18	0.00
1.4	1.30	1.70	0.10	1.05	0.11	0.17	0.00
2.1	1.44	1.56	1.57	0.39	0.09	0.08	0.00

Continued on next page

Table 3.7: (continued)

Transition	1s-σ_g	1s-σ_u	5f$_{\delta/\phi}$	π_u^*	σ_u^*	π_g^*	σ_g^*
2.2	1.47	1.53	1.57	0.41	0.08	0.06	0.00
2.3	1.42	1.58	1.07	0.65	0.23	0.09	0.00
2.4	1.42	1.58	1.16	0.82	0.08	0.09	0.00
2.5	1.41	1.59	0.87	1.09	0.09	0.10	0.00
2.6	1.43	1.57	0.90	0.98	0.13	0.10	0.00
3.1	1.41	1.59	0.64	0.71	0.43	0.13	0.01
3.2	1.50	1.50	0.96	0.73	0.13	0.22	0.00
3.3	1.54	1.46	0.77	0.66	0.12	0.42	0.00
3.4	1.47	1.53	0.66	1.16	0.09	0.20	0.00
3.5	1.61	1.39	0.36	0.51	0.15	0.76	0.00

3.3.2 Considering the Crystal Environment

In the previous sections, the RAS methodology was shown to be successful in simulating the O K-edge XANES of uranyl to within 1.5 eV of experiment when utilizing a simple $[UO_2]^{2+}$ model. In this section, the importance of including aspects of the local crystal environment within uranyl models is assessed. Three different uranyl models were considered, including the $[UO_2]^{2+}$ model discussed in detail within the preceding sections, as well as the $[UO_2Cl_4]^{2-}$ and $Cs_2UO_2Cl_4$ models, both presented in fig. 3.10. The RAS(SD) O K-edge XANES spectra for the three uranyl models is shown in fig. 3.11. All three uranyl simulations generate a three peak spectral profile within the 525 - 545 eV region, consistent with experiment. Peaks 1-3 are assigned to the same core-excitations as those detailed in the previous section for $[UO_2]^{2+}$ and in accordance with those proposed by Denning and others.[6, 20, 37] Assignments for the $[UO_2Cl_4]^{2-}$ and $Cs_2UO_2Cl_4$ models are discussed in some detail within section 3.3.2.2.

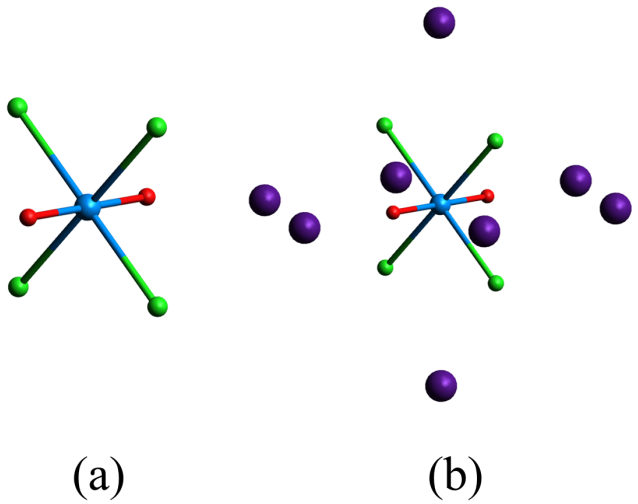

Figure 3.10: (a) $[UO_2Cl_4]^{2-}$ and (b) $Cs_2UO_2Cl_4$ uranyl models utilized in O K-edge XANES simulations.

3.3.2.1 O K-edge Simulations

Results of RAS(SD) O K-edge XANES simulations using three different uranyl models are presented in fig. 3.11. In all three simulations, the intensity profile of peak 3 is attributed to a large number of relatively low intensity transitions spread across a wide energy range compared with other peaks. Additionally, the transitions appear to further spread in energy and decrease in transition strength from $[UO_2]^{2+}$ to $Cs_2UO_2Cl_4$, broadening and decreasing the intensity of peak 3 as models better represent the local crystal environment. Peak positions for all three simulations are predicted to within 1.5 eV of experiment as reported in table 3.8. The $[UO_2]^{2+}$ simulation has the best prediction for the position of peak 1, with a discrepancy of +0.3 eV. Peak 3 is also well predicted with a discrepancy of +0.6 eV. However, Peak 2 is predicted at 535.6 eV compared to an experimental position of 534.1 eV ($\Delta = +1.5$ eV), representing the largest predicted error of any peak across the simulated models. Addition of the equatorial chloride ligands in the $[UO_2Cl_4]^{2-}$ model has a stabilising effect on all the CESs relative to the GS, resulting in a redshift of all the peaks in the spectrum compared to the $[UO_2]^{2+}$. The state stabilisation also reflects a redshift with respect to the experimental peak positions, with peak 1 predicted 0.8 eV below the first experimental peak position. Including the equatorial chloride ligands mitigates the

large discrepancy for peak 2 found in the $[UO_2]^{2+}$ simulation, reduced to -0.3 eV for $[UO_2Cl_4]^{2-}$, predicting peak 2 at 533.8 eV compared with the experimental position of 536.7 eV. The improved peak 2 prediction comes at the apparent cost of predicting peaks 1 ($\Delta = -0.8$ eV) and 3 ($\Delta = -0.9$ eV), with larger magnitude discrepancies in comparison to $[UO_2]^{2+}$. The simulation utilizing the $Cs_2UO_2Cl_4$ model, which introduces caesium counter-ions as point charges, predicts peaks 1 to 3 at 530.7 eV ($\Delta = -0.7$ eV), 535.5 eV ($\Delta = -0.6$ eV) and 537.0 eV ($\Delta = +0.5$ eV), respectively. Predictions for peaks 1 and 2 are consistent in value and in close agreement with experiment, but the relative separations involving peak 3 are negatively impacted by the inclusion of the counter-ions as compared with the $[UO_2Cl_4]^{2-}$ model simulation.

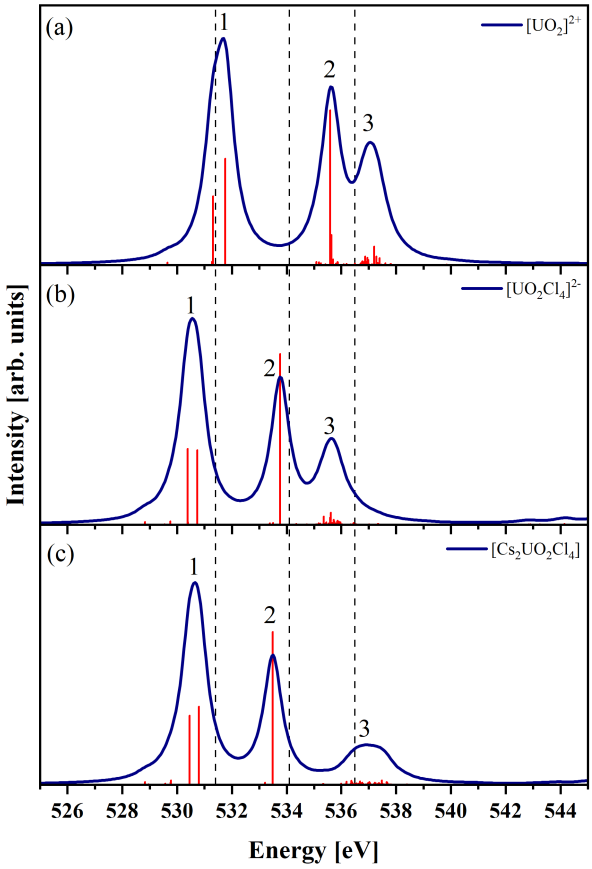

Figure 3.11: Spin-orbit coupled RAS(SD) (a) $[UO_2]^{2+}$, (b) $[UO_2Cl_4]^{2-}$, and (c) $Cs_2UO_2Cl_4$ O K-edge XANES simulations. Individual transitions are plotted as red sticks. Experimental positions taken from ref. [6] are indicated by black vertical dashed lines.

Table 3.8: Simulated RAS(SD) $[UO_2]^{2+}$, $[UO_2Cl_4]^{2-}$ and $Cs_2UO_2Cl_4$ peak energies compared with literature and experimental values. Δ values are the discrepancy with respect to experiment. No energy shift was applied to the reported data and all values are reported in eV.

	Peak 1	**Δ**	**Peak 2**	**Δ**	**Peak 3**	**Δ**
Expt.[6]	531.4		534.1		536.5	
$[UO_2]^{2+}$ ΔSCF [6, 15]	531.8	+0.4	536.7	+2.6	537.3	+0.8
$[UO_2]^{2+}$ TDDFT [15]	510.0	-21.4	515.6	-18.5	516.9	-19.6
$[UO_2Cl_4]^{2-}$ 4c-DR-TDDFT [37]	518.5	-12.9	521.4	-12.7	522.7	-13.8
$[UO_2]^{2+}$ RAS(SD)	531.7	+0.3	535.6	+1.5	537.1	+0.6
$[UO_2Cl_4]^{2-}$ RAS(SD)	530.6	-0.8	533.8	-0.3	535.6	-0.9
$Cs_2UO_2Cl_4$ RAS(SD)	530.7	-0.7	533.5	-0.6	537.0	+0.5

Peak predictions from previous studies are also included in table 3.8. The reported literature energies for ΔSCF and TD-DFT simulations were obtained using free $[UO_2]^{2+}$ dication models. The TD-DFT calculations predict the XANES spectrum at ∼20 eV above the experimental region, which is substantial in comparison with the ΔSCF and RAS(SD) results in table 3.8, which predict peaks to within 2.6 and 1.5 eV of experiment, respectively. Both the ΔSCF and RASSCF simulations capture orbital relaxation effects between the GS and CESs. TD-DFT does not capture such orbital relaxations, and this accounts for the majority of the error in calculating the correct XANES energy region.

Published 4c-DR-TD-DFT calculations performed by Miseal et al show a substantial improvement in peak predictions over the TD-DFT results reported for $[UO_2]^{2+}$ in table 3.8. In these simulations, a $[UO_2Cl_4]^{2-}$ model was utilized and improved peak positions by up to ∼14 eV. The ΔSCF, TD-DFT and more recent 4c-DR-TD-DFT results reported by others[6, 15, 37] for uranyl O K-edge XANES, points to the need for considering both the method used and the models simulated. Both the RAS(SD) simulations from this chapter and the literature ΔSCF simulations offer good predictions for peaks 1 and 3,

but exhibit similar difficulties in predicting the position of peak 2. Both methods predict peak 2 with similar discrepancies of +2.6 eV and +1.5 eV for the ΔSCF and RAS(SD) approaches, respectively. The key finding of this section, is that the addition of chloride ligands in the $[UO_2Cl_4]^{2-}$ model, corrects this discrepancy with substantial improvement. Peak 2 is now predicted to within 0.3 eV of experiment in the $[UO_2Cl_4]^{2-}$ simulation, without significant detriment to other peak predictions.

To facilitate inspection of relative peak predictions, fig. 3.12 presents the same O K-edge XANES spectra for the three models but individually shifted by -0.3, +0.8 and +0.7 eV to align the first simulated peak with the first experimental peak. The measured separations between peaks are reported in table 3.9. The relative separation between peaks 1 and 3 predicted from both $[UO_2]^{2+}$ and $[UO_2Cl_4]^{2-}$ simulations are in good agreement with those found in experiment. The $[UO_2Cl_4]^{2-}$ simulation gives the best predicted separation between peaks 1 and 3, at a value of 5.0 eV, compared with the experimental value of 5.1 eV. The sensitivity of peak 2 to the uranyl crystal environment is made clear in fig. 3.12, with peak 2 moving closer to peak 1, which better aligns prediction with experiment as the models progress from $[UO_2]^{2+}$ to $Cs_2UO_2Cl_4$. The desirable improvement in peak separation between peaks 1 and 2 is offset by the undesirable increase in peak 2 and 3 separation when moving from $[UO_2Cl_4]^{2-}$ to $Cs_2UO_2Cl_4$. This occurs due to the spread of transitions associated with peak 3 across a wider range of energy for the $Cs_2UO_2Cl_4$ simulation, which shifts the overall peak maxima to higher excitation energy. Overall, the results in this chapter point to a particular sensitivity in the position of peak 2 to the equatorial environment. Studies at the An $M_{4/5}$-edge have pointed to a sensitivity of the σ_u^* peak to the crystal environment,[4, 64, 65] and it would appear this may also be the case for O K-edge as well. By considering both the relative peak separations and raw peak predictions, the $[UO_2Cl_4]^{2-}$ model is found to offer the best agreement with experiment out of the three models used to simulate O K-edge XANES.

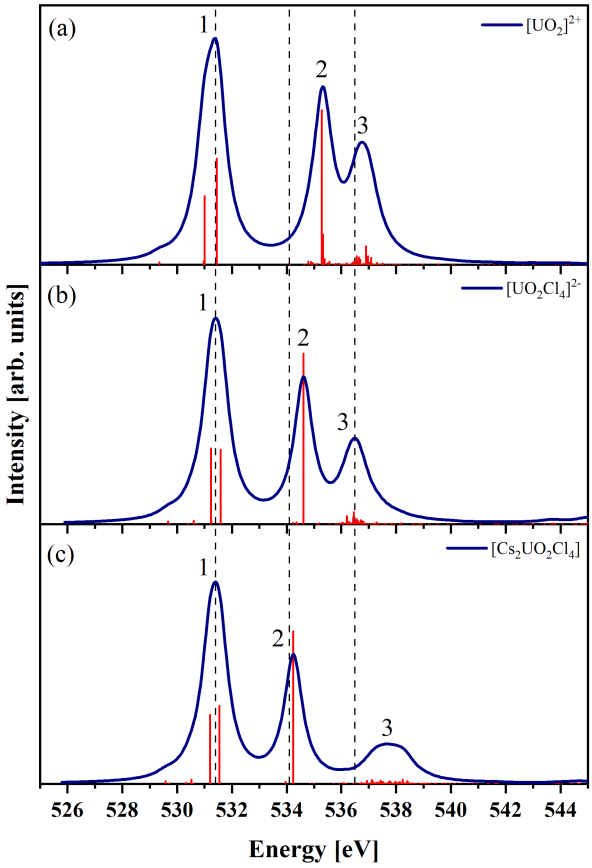

Figure 3.12: Energy shifted spin-orbit coupled RAS(SD) (a) $[UO_2]^{2+}$, (b) $[UO_2Cl_4]^{2-}$, and (c) $Cs_2UO_2Cl_4$ O K-edge XANES simulations. Simulated spectra shifted by (a) -0.3, (b) +0.8 and (c) +0.7 eV to align the first predicted and experimental peaks. Individual transitions are plotted as red sticks. Experimental positions taken from ref. [6] are indicated by black vertical dashed lines.

3.3.2.2 XANES Assignments

The process of assigning peaks to core-excitations was outlined in detail for $[UO_2]^{2+}$ simulations in section 3.3.1.2, and a similar process was repeated for the $[UO_2Cl_4]^{2-}$ and $Cs_2UO_2Cl_4$ simulation results. The full assignment details are not covered in the same detail as those for $[UO_2]^{2+}$, instead this section offers a general overview of the assignments for XANES spectra presented in 3.11 for all three model systems. Key core-excited states associated with intense transitions in fig. 3.11 are reported in table 3.10. In all three model simulations, the first peak is attributed to two intense transitions into the π_u^* orbitals

Table 3.9: RAS(SD) O K-edge relative peak separations for $[UO_2]^{2+}$, $[UO_2Cl_4]^{2-}$ and $Cs_2UO_2Cl_4$. The separation between peaks A and B is given by P_{AB}, and correspond to peak separations as shown in Figure 3.12. Discrepancy with respect to experimental separations is given by Δ.[6] All values reported in eV.

	$\mathbf{P_{21}}$	**Δ**	$\mathbf{P_{32}}$	**Δ**	$\mathbf{P_{31}}$	**Δ**
Expt. [6]	2.7		2.4		5.1	
$[UO_2]^{2+}$	3.9	+1.2	1.5	-0.9	5.4	+0.3
$[UO_2Cl_4]^{2-}$	3.2	+0.5	1.8	-0.6	5.0	-0.1
$Cs_2UO_2Cl_4$	2.8	+0.1	3.5	+1.1	6.3	+1.2

Table 3.10: RAS(SD) $[UO_2]^{2+}$, $[UO_2Cl_4]^{2-}$ and $Cs_2UO_2Cl_4$ O K-edge SONO populations of RAS3 orbitals for CESs associated with key transitions responsible for peaks in figure 3.11.

Model	**Peak**	$\mathbf{5f_{\delta/\phi}}$	$\boldsymbol{\pi_u^*}$	$\boldsymbol{\sigma_u^*}$	$\boldsymbol{\pi_g^*}$	$\boldsymbol{\sigma_g^*}$
$[UO_2]^{2+}$	1	0.04	0.99	0.08	0.16	0.00
	2	0.64	0.16	0.68	0.08	0.01
	3	1.02	0.54	0.05	0.26	0.00
$[UO_2Cl_4]^{2-}$	1	0.02	1.00	0.09	0.17	0.00
	2	0.10	0.17	0.95	0.13	0.00
	3	0.97	0.69	0.04	0.20	0.00
$Cs_2UO_2Cl_4$	1	0.06	0.96	0.06	0.18	0.00
	2	0.07	0.14	0.97	0.14	0.00
	3	1.21	0.42	0.04	0.22	0.00

and peak 2 is attributed to a single intense transition into the σ_u^* orbitals. Peak 3 in both the $[UO_2Cl_4]^{2-}$ and $Cs_2UO_2Cl_4$ simulations is attributed to a large number of weak transitions, offering a similar challenge to that of $[UO_2]^{2+}$ in ascribing a single transition to represent the peak overall. Further ambiguity is introduced by the multiconfigurational nature of the states themselves, with substantial population of all the RAS3 orbitals for the associated states. Despite this, states present electron populations that range between 0.20 and 0.26 across all three models for the π_g^* orbitals. Although these values are low, they are above the level in which these orbitals are populated in other states, and combined with RAS(S) assignments as support, point to peak 3 being attributed to a 1s to π_g^* (1s $\rightarrow \pi_g^*$) excitation overall. Similar to the $[UO_2]^{2+}$ case, the multiconfigurational nature of the states increases from peaks 1 to 3 as the excitation energy increases. This manifests as increased RAS2-RAS3 electron redistribution with electrons spread across all RAS3 orbitals as shown in table 3.10. By evaluating the total number of RAS3 electrons the amount of redistribution is made clear, for example $Cs_2UO_2Cl_4$ RAS3 populations total 1.26, 1.32 and 1.89 for core-states across peaks 1 to 3, with population above 1.00 accounted for by depletion of bonding orbitals. Electrons in the CESs tend to favour populating the $5f_{\delta/\phi}$ and π_u^* orbitals, suggesting that the partial occupation of these lower energy orbitals is an energetically favourable route to optimising the CESs. All three model simulations predict a shoulder at ~530 eV on the first peak, corresponding to core-excitation into the non-bonding $5f_{\delta/\phi}$ orbitals. An additional peak in the post 545 eV region corresponds to a core-excitation into the σ_g^* orbital for $[UO_2Cl_4]^{2-}$, while for $Cs_2UO_2Cl_4$, the same feature does not include substantial σ_g^* occupancy but instead electrons populate all other RAS3 orbitals to various degrees.

3.3.3 XANES as a Covalency probe

3.3.3.1 QTAIM Analysis

The ground- and core-excited states are investigated using Quantum Theory of Atoms in Molecules (QTAIM) of Bader et al.[66, 67] to better understand how the overall covalency differs in the states after core-excitation. Within QTAIM, the molecular space can be be split into atomic basins as shown in fig. 3.13, with red, blue, and green regions representing the oxygen Ω_O, uranium Ω_U, and chlorine Ω_{Cl} electron density basins, respectively. Two

metrics of covalency can be calculated for uranyl by considering the relationship between atomic basins. The first metric considered is the electron density at the point along the bond path where the two basin boundaries meet, known as the bond critical point (BCP), and is clearly visible in fig. 3.13 (gold spheres). The electron density $\rho_{\mathrm{BCP}}(\mathrm{U,O})$ at the BCP between the uranium and oxygen basins gives a quantitative measure of the electron density build-up in the bonding region, with higher values of $\rho_{\mathrm{BCP}}(\mathrm{U,O})$ indicating greater covalency. Given that this metric measures a single point along the bond path, the metric is limited to measuring the charge accumulation due to σ-type bonding interactions only. A complimentary measure of covalency is the delocalisation index, $\delta(\mathrm{U,X})$, which quantifies the number of electrons shared between two atomic basins (U and X), and in the absence of bond polarisation can be considered a measure of bond order. This metric is influenced by all orbital interactions, capturing both σ- and π-type bonding interactions, and can be large in the absence of charge accumulation. The localisation index λ is also a useful quantity to track between states offering complimentary information to δ, and measures the number of electrons localised in an atomic basin.

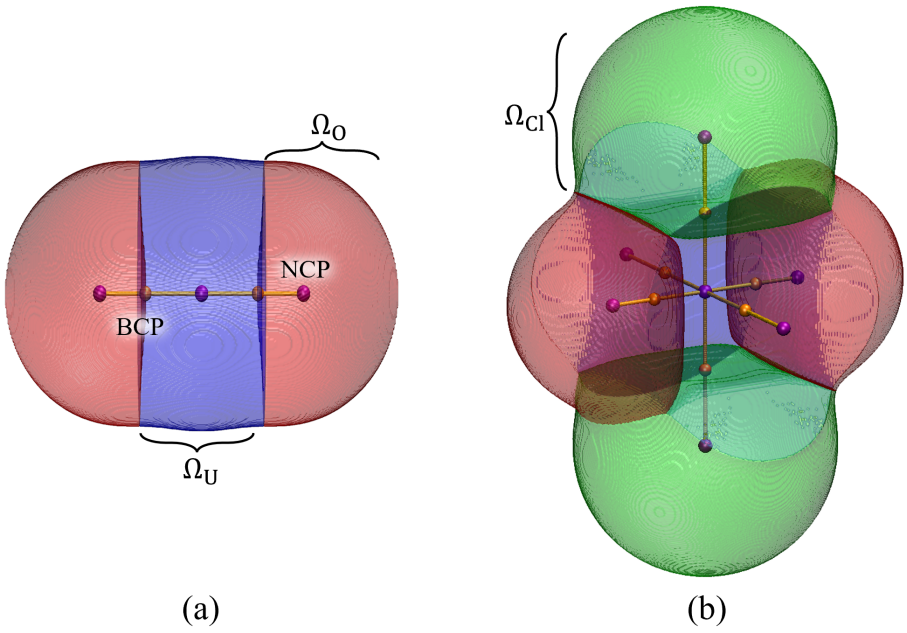

Figure 3.13: Atomic basins for (a) $[UO_2]^{2+}$ and (b) $[UO_2Cl_4]^{2-}$. Blue, red and green regions correspond to the uranium, oxygen and chlorine basins, respectively.

The ground-states of $[UO_2]^{2+}$, $[UO_2Cl_4]^{2-}$ and $Cs_2UO_2Cl_4$ share similar $\rho_{BCP}(U,O)$ values of 0.33, 0.31 and 0.32 a.u., respectively. Given the similarity in values for all three systems, the addition of chloride ligands in the equatorial positions appear not to have a significant impact on the U-O covalency as measured by ρ_{BCP}. Equatorial ligands are thought to from weak bonding interactions with uranium in the uranyl and GS $\rho_{BCP}(U,Cl)$ values of 0.06 a.u. for both chloride models reflect this picture.[20, 68] Upon core-excitation, changes in $\rho_{BCP}(U,O)$ between the ground- and core-excited states is minor, changing by no more than 0.06 a.u. Limited change in $\rho_{BCP}(U,O)$ values upon core-excitation was expected since the bonding orbitals are not substantially depleted, and the population of anti-bonding orbitals was expected to contribute only minimally. The largest change in $\rho_{BCP}(U,O)$ values from the GS was for the $1s \rightarrow \pi_g^*$ CESs. These states exhibit the greatest amount of RAS2-RAS3 electron redistribution and thus the largest depletion of electrons from bonding orbitals, accounting for the relatively larger changes in ρ_{BCP} values. For U-Cl bonds, the ρ_{BCP} values are unchanged upon excitation and this holds largely true for the delocalisation indices as well, indicating that U-Cl bonding interactions on the whole are unchanged due to core-excitation.

The delocalisation indices for the relevant ground-states for all three models are reported in table 3.11. The ground-state $\delta(U,O)$ value is 1.85 for $[UO_2]^{2+}$, decreasing to 1.53 ($\Delta = -0.32$) when equatorial chloride ligands are present in the $[UO_2Cl_4]^{2-}$ model. The localisation indices for the two systems also change between $[UO_2]^{2+}$ and $[UO_2Cl_4]^{2-}$, from 7.70 to 8.03 ($\Delta = +0.33$) on oxygen and from 86.85 to 86.37 ($\Delta = -0.48$) on uranium, respectively. The lower $\delta(U,O)$ values indicates a reduction in electrons shared in the U-O bond between $[UO_2]^{2+}$ and $[UO_2Cl_4]^{2-}$, while $\lambda(U)$ and $\lambda(O)$ values indicate an electron depleted uranium centre and more electron rich oxygen centres from the former to the latter system. The combination of these changes point to an enhancement of U-O ionic character upon addition of electron withdrawing chloride ligands. Similar changes in U-O bonding interactions are also reflected when comparing $[UO_2]^{2+}$ and $Cs_2UO_2Cl_4$ ground-states, finding that the caesium counter-ions have only minor impact on the QTAIM values in comparison to $[UO_2Cl_4]^{2-}$.

Compared to $\rho_{BCP}(U,O)$, the delocalisation index $\delta(U,O)$ for U-O bonds is found to be more sensitive to covalency changes between the ground- and core-excited states.

Table 3.11: GS and CES QTAIM metrics for the different uranyl models. Each core-excited state is represented by the core-excitation that generates it: 1s $\rightarrow \psi^*$. Table reports the delocalisation index δ(U, O) as well as uranium and oxygen localisation indexes λ(U) and λ(O). Analysis is performed on RAS(SD) electron densities.

Model	**Property**	**GS**	**1s** $\rightarrow \boldsymbol{\pi_u^*}$	**1s** $\rightarrow \boldsymbol{\sigma_u^*}$	**1s** $\rightarrow \boldsymbol{\pi_g^*}$
$[UO_2]^{2+}$	ρ(U,O)	0.33	0.31	0.32	0.29
	δ(U,O)	1.85	1.30	1.23	1.17
	λ(U)	86.85	87.56	87.68	87.83
	λ(O)	7.70	7.90	7.91	7.91
$[UO_2Cl_4]^{2-}$	ρ(U,O)	0.31	0.28	0.31	0.26
	δ(U,O)	1.53	1.10	1.10	0.96
	λ(U)	86.37	87.06	87.06	87.36
	λ(O)	8.03	8.12	8.13	8.16
$Cs_2UO_2Cl_4$	ρ(U,O)	0.32	0.28	0.31	0.26
	δ(U,O)	1.52	1.11	1.10	0.97
	λ(U)	86.35	87.04	87.01	87.36
	λ(O)	8.06	8.14	8.15	8.17

Examining changes in both the δ(U, O) and λ(U)/λ(O) metrics gives useful insight into how the electrons re-distribute between atomic centres upon core-excitation. These changes in QTAIM metrics are reported for all three models in table 3.12.

Both δ(U, Cl) and λ(Cl) values for U-Cl bonds remain largely unchanged between the ground and core-excited states, at values of approximately 0.40 and 17.6, respectively. Between the ground- and all core-excited states, δ(U, O) values decrease regardless of the model considered. These decreases in δ(U, O) values were expected since core-excitation leads to the population of anti-bonding orbitals, resulting in a lower U-O bond order. Electrons no longer shared in U-O interactions are instead localised onto both the uranium

Table 3.12: Changes in delocalisation index $\Delta\delta$(U, O) and changes in uranium and oxygen localisation indexes $\Delta\lambda$(U) and $\Delta\lambda$(O), between the GS and CESs in different uranyl models. Each core-excited state is represented by the core-excitation that generates it: 1s $\rightarrow \psi^*$. Analysis is performed on RAS(SD) electron densities.

Model	**Property**	**1s** $\rightarrow \boldsymbol{\pi_u^*}$	**1s** $\rightarrow \boldsymbol{\sigma_u^*}$	**1s** $\rightarrow \boldsymbol{\pi_g^*}$
$[UO_2]^{2+}$	$\Delta\delta$(U,O)	-0.55	-0.62	-0.68
	$\Delta\lambda$(U)	+0.71	+0.83	+0.99
	$\Delta\lambda$(O)	+0.20	+0.22	+0.21
$[UO_2Cl_4]^{2-}$	$\Delta\delta$(U,O)	-0.42	-0.43	-0.57
	$\Delta\lambda$(U)	+0.69	+0.68	+0.98
	$\Delta\lambda$(O)	+0.09	+0.10	+0.13
$Cs_2UO_2Cl_4$	$\Delta\delta$(U,O)	-0.42	-0.42	-0.55
	$\Delta\lambda$(U)	+0.69	+0.66	+1.00
	$\Delta\lambda$(O)	+0.09	+0.10	+0.11

and oxygen centres in the CESs as indicated by increased localisation indices in table 3.12. The increase in localisation indices is greatest for uranium centres over oxygen and is likely a reflection of populating anti-bonding and non-bonding 5f orbitals with predominantly uranium character in the CESs. The increased oxygen localisation in the CESs is rationalised by the increase in the effective nuclear charge of oxygen centres due to the presence of the core-hole, increasing oxygen electronegativity and drawing charge density towards these centres. The degree to which $\delta(\mathrm{U,O})$ values decrease between the ground- and core-excited states for a given model is found to correlate with the greater multiconfigurational nature of states from peak 1 to 3. For instance, in $[UO_2]^{2+}$ the lower energy $1s \rightarrow \pi_u^*$ excitation results in a $\Delta\delta(\mathrm{U,O})$ of -0.55, compared with the higher energy $1s \rightarrow \pi_g^*$ excitation with a $\Delta\delta(\mathrm{U,O})$ of -0.68, where greater multiconfigurational character is found in states associated with the latter excitation. This correlation also holds true for

both $[UO_2Cl_4]^{2-}$ and $Cs_2UO_2Cl_4$. The increase in the multiconfigurational character of states from peaks 1 to 3, coincides with greater electron redistribution into anti-bonding orbitals, which significantly lowers the uranyl bond order, and accounts for the correlation with $\Delta\delta(U,O)$.

The changes in U-O QTAIM metrics between the GS and CESs reported in table 3.12 signify a dependence on the equatorial environment. For example, lower $\delta(U,O)$ values are found for the core-excited states in $[UO_2Cl_4]^{2-}$ simulations compared with $[UO_2]^{2+}$. In $[UO_2Cl_4]^{2-}$, the core-excited state $\delta(U,O)$ values range from 0.96 to 1.10, compared with 1.17 to 1.30 for $[UO_2]^{2+}$. Additionally, the degree to which $\delta(U,O)$ changes between the ground- and core-excited states is influenced by the presence of the chloride ligands. Larger decreases in $\delta(U,O)$ values occur between the ground- and core-excited states in the absence of chloride ligands, with $[UO_2]^{2+}$ $\Delta\delta(U,O)$ values ranging 0.55 to 0.68, and concurrent increases in both $\Delta\lambda(U)$ and $\Delta\lambda(O)$ spanning 0.71-0.99 and 0.20-0.22, respectively. In contrast, upon addition of chloride ligands in the $[UO_2Cl_4]^{2-}$ model, $\Delta\delta(U,O)$ range lower values of 0.42 to 0.57, and $\Delta\lambda(O)$ values are approximately halved, spanning 0.09 to 0.13. The $\Delta\lambda(U)$ values remain comparable to those in $[UO_2]^{2+}$. The smaller $\Delta\delta(U,O)$ values in the chloride systems indicates a greater resistance to a change in U-O covalency when compared to $[UO_2]^{2+}$. This can be rationalised by considering the electron localisation on the oxygen centres. In the ground-state of $[UO_2Cl_4]^{2-}$, the oxygen centres are more electron rich in comparison to $[UO_2]^{2+}$, with $\sim$0.30 more charge localised on each centre. As demonstrated from QTAIM data, upon core-excitation, electrons once shared in U-O bonding interactions are distributed across the three atomic centres. The more electron-rich oxygen centres in the $[UO_2Cl_4]^{2-}$ GS compared to $[UO_2]^{2+}$, introduces a greater energetic cost for removing electrons from bonding interactions and localising them onto the already electron-rich oxygen centres. This argument also extends to $Cs_2UO_2Cl_4$ where the QTAIM results mirror those of $[UO_2Cl_4]^{2-}$, and accounts for the smaller $\Delta\delta(U,O)$ values in the chloride systems compared with $[UO_2]^{2+}$.

3.3.3.2 Orbital Composition Analysis

The degree to which O K-edge XANES is a reliable probe of GS covalency, relies on the bonding orbitals in the GS and CESs being similar. Orbital composition analysis

was performed on the GS and CESs to quantify the changes in orbital mixing and thus the degree to which O K-edge XANES is a valid probe of GS covalency. The RASSCF approach utilized in this chapter facilitates such analysis since the GS and CESs are generated separately, meaning the mixing can be determined in each, and directly compared. Analysis is performed on the bonding SONOs as opposed to the anti-bonding SONOs, since the former remain strongly occupied in the CESs, and thus allows for a more commensurate comparison with GS orbitals. The bonding orbitals are also the key orbitals of interest for covalent interactions. The use of uranyl models that better reflect the local crystal environment allows for further assessment on whether the choice of model has an influence over orbital compositions. A number of orbital composition schemes are available, however, an Atoms In Molecules (AIM) approach was chosen since the composition is determined directly from the electron density associated with atomic basins. The AIM composition scheme has the advantage of being derived from the same QTAIM principals utilized in the preceding section, and keeps all covalency analysis within this study under the same theoretical framework.

For a completely covalent metal-ligand bonding orbital, the maximal metal:ligand mixing would be 50%:50%. The ground-state composition analysis reported in table 3.13 reveals a lower U% contribution to bonding orbitals in the chloride systems, with values deviating to a greater extent from the idealised 50%:50% mixing compared to the GS bonding orbitals in $[UO_2]^{2+}$. This result is consistent with the previous QTAIM findings, since both results point to lower U-O covalency overall in the chloride systems compared to $[UO_2]^{2+}$. For all three models, a trend is identified for the bonding orbitals, finding a decreasing covalency from σ_u to π_g. Compositions reported in tables 3.13 and 3.14 reveal a decreasing U% and increasing O% contribution across the σ_u to π_g bonding orbitals, leading to a greater deviation from maximal covalent mixing. The σ_u orbital reflects a strong covalent mixing across the ground-states of all three models, with U:O mixings of 53.4%:46.6% and 47.8%:50.4% from $[UO_2]^{2+}$ to $Cs_2UO_2Cl_4$, respectively. For the σ_u orbital, the addition of the chloride ligands in the $[UO_2Cl_4]^{2-}$ and $Cs_2UO_2Cl_4$ models do not alter the overall covalent character of the orbital. The presence of the chloride ligands is more impactful in further increasing the ionic character of the two π_u/π_g orbitals, finding that the π_g is most affected with notable shifts from 17.2%:82.8% U:O mixing in $[UO_2]^{2+}$,

Table 3.13: U% AIM orbital compositions for bonding SONOs for the ground- and key core excited-states responsible for peaks in Figure 3.11. Table reports the values from ground- to core excited-states, GS% → CES%, and the overall change given by Δ. Analysis is from RAS(SD) electron densities.

Model	Excitation	SONO	GS% → CES%	Δ
$[UO_2]^{2+}$ [38]	$1s \rightarrow \pi_u^*$	π_u	25.2% → 15.2%	-10.0%
	$1s \rightarrow \sigma_u^*$	σ_u	53.4% → 46.2%	-7.2%
	$1s \rightarrow \pi_g^*$	π_g	17.2% → 9.4%	-7.8%
$[UO_2Cl_4]^{2-}$	$1s \rightarrow \pi_u^*$	π_u	19.9% → 13.2%	-6.7%
	$1s \rightarrow \sigma_u^*$	σ_u	48.3% → 41.4%	-6.9%
	$1s \rightarrow \pi_g^*$	π_g	12.1% → 6.9%	-5.2%
$Cs_2UO_2Cl_4$	$1s \rightarrow \pi_u^*$	π_u	19.2% → 12.6%	-6.6%
	$1s \rightarrow \sigma_u^*$	σ_u	47.8% → 41.1%	-6.7%
	$1s \rightarrow \pi_g^*$	π_g	12.2% → 8.1%	-4.1%

to 12.1%:84.4% in $[UO_2Cl_4]^{2-}$, and to 12.2%:85.4% in $Cs_2UO_2Cl_4$. Note that the omitted chloride percentages are reported in 3.15, and are required to recover compositions of 100% in chloride systems.

Table 3.13 reports the uranium contributions to bonding orbitals in the GS and CESs. Between the GS and CESs in $[UO_2]^{2+}$, the uranium contributions to bonding are 7-10% lower in the latter states, while oxygen contribution increases by the expected 7-10% as reported in table 3.14. In the two chloride systems a consistent ∼4-7% decrease in U% contributions to the bonding SONOs is found between the GS and CESs. Two effects are thought to account for the reported reduction in U% contributions to bonding orbitals in the CESs:

1. The localisation of charge density in the CES onto uranium is driven by the occupation of non-bonding 5f-orbitals and anti-bonding orbitals with predominately

Table 3.14: O% AIM orbital compositions for bonding SONOs for the ground- and key core excited-states responsible for peaks in Figure 3.11. Table reports the values from ground- to core excited-states, GS% → CES%, and the overall change given by Δ. Analysis is from RAS(SD) electron densities.

Model	Excitation	SONO	GS% → CES%	Δ
$[UO_2]^{2+}$	$1s \rightarrow \pi_u^*$	π_u	74.8% → 84.8%	+10.0%
	$1s \rightarrow \sigma_u^*$	σ_u	46.6% → 53.8%	+7.2%
	$1s \rightarrow \pi_g^*$	π_g	82.8% → 90.6%	+7.8%
$[UO_2Cl_4]^{2-}$	$1s \rightarrow \pi_u^*$	π_u	79.0% → 86.0%	+7.0%
	$1s \rightarrow \sigma_u^*$	σ_u	49.8% → 46.0%	-3.8%
	$1s \rightarrow \pi_g^*$	π_g	84.4% → 90.8%	+6.4%
$Cs_2UO_2Cl_4$	$1s \rightarrow \pi_u^*$	π_u	79.8% → 84.4%	+4.6%
	$1s \rightarrow \sigma_u^*$	σ_u	50.4% → 44.6%	-5.8%
	$1s \rightarrow \pi_g^*$	π_g	85.4% → 86.0%	+0.6%

metal character, which repels density in the bonding orbitals away from the U centre.

2. The increased effective nuclear charge of the oxygen centres due to the generation of the core-hole attracts charge density in the bonding orbitals to the electron deficient oxygen centres.

Point 1 is supported by the observation that the largest λ(U) values are found in the highly multiconfigurational $1s \rightarrow \pi_g^*$ CESs, which have the greatest electron redistribution from the bonding orbitals to the RAS3 orbitals which consist predominately of uranium character. Point 2 is also supported by the QTAIM findings, with increased electron localisation on oxygen centres found after core-excitation within the CESs. Both effects (point 1 and 2) combine to re-distribute charge density in the bonding orbitals toward oxygen and away from uranium, accounting for the lower U% and higher O% character.

Examining the changes in orbital compositions between the GS and CESs finds that

Table 3.15: Cl% AIM orbital compositions for bonding SONOs for the ground- and key core excited-states responsible for peaks in Figure 3.11. Table reports the values from ground- to core excited-states, GS% → CES%, and the overall change given by Δ. Analysis is from RAS(SD) electron densities.

Model	Excitation	SONO	GS% → CES%	Δ
$[UO_2Cl_4]^{2-}$	1s → π_u^*	π_u	1.1% → 0.8%	-0.3%
	1s → σ_u^*	σ_u	1.9% → 12.6%	+10.7%
	1s → π_g^*	π_g	3.5% → 2.3%	-1.2%
$Cs_2UO_2Cl_4$	1s → π_u^*	π_u	1.0% → 3.0%	+2.0%
	1s → σ_u^*	σ_u	1.8% → 14.3%	+12.5%
	1s → π_g^*	π_g	2.4% → 5.9%	+3.5%

the chemical environment has an direct impact on the degree to which the orbitals change. This is evident by examining the changes in U% contributions (Δ) in table 3.13, which finds lower U% changes between the GS and CESs for the chloride containing systems. This is rationalised by examining the nature of the orbitals individually for the different models. For the σ_u orbital, a similar ∼7% decrease in U% contributions was found in all three systems upon core-excitation. The nature of the σ_u orbital in the GS is similar across the three systems, with near 50%:50% U:O mixing in each case, and therefore the energetic cost of distributing charge density toward oxygen centres in the $1s \rightarrow \sigma_u^*$ CESs would be similar for all three models, accounting for the similar ΔU% values. Reduction in U% contributions to the π-bonding orbitals upon-core excitation is less pronounced in the two chloride systems compared with $[UO_2]^{2+}$. In the GS, the π-bonding orbitals in chloride systems are more ionic in nature compared with those in $[UO_2]^{2+}$, with a greater balance of charge density on the oxygen centres in the chloride systems. For instance in $[UO_2Cl_4]^{2-}$ the GS π_u and π_g orbitals have 4.2% and 1.6% greater oxygen character, respectively, compared with the same orbitals in $[UO_2]^{2+}$. Upon-core excitation in the chloride systems, there is a greater energetic cost associated with distributing charge

density within π-orbitals towards the oxygen centres compared with $[UO_2]^{2+}$, since a greater charge density already resides on oxygen centres in the GS for chloride systems. The increased energetic costs associated with this redistribution in the chloride systems compared with $[UO_2]^{2+}$ accounts for the lower ΔU% values.

In the chloride systems, the oxygen ligands are no longer the sole atomic centres that can facilitate charge redistribution from uranium centres in the CES bonding orbitals. Chloride ligands offer an additional route for charge redistribution and their presence is found to influence the bonding orbital compositions directly as shown by compositional changes (Δ) in table 3.15. The most prominent example of direct Cl-involvement is for the σ_u orbital in $1s \rightarrow \sigma_u^*$ CESs. In $[UO_2]^{2+}$, a U% reduction of 7.1% is completely accounted for by a necessitated equal increase in O%. This changes for $[UO_2Cl_4]^{2-}$ and $Cs_2UO_2Cl_4$, with the 6.9% and 6.7% reductions in U% contributions to σ_u followed by further decreases in O% contributions of 3.8% and 5.8%, respectively. In these cases, the reductions in both U% and O% contributions is primarily accounted for through large 11.0% and 12.8% increases in Cl% character in $[UO_2Cl_4]^{2-}$ and $Cs_2UO_2Cl_4$, respectively. An additional example involves the π_g orbitals in the $1s \rightarrow \pi_g^*$ CES of $Cs_2UO_2Cl_4$, where a 4.1% reduction in U% is largely compensated for by a 3.5% increase in Cl%. The contribution from oxygen centres remains mostly the same, with only a minor 0.6% increase in contribution to the CES. For other core-excitations not mentioned here within the text, all present a U% reduction which is compensated by a combination of changes to O% and Cl% as reported in tables 3.13 to 3.15.

3.3.3.3 Considering Transition Strength

Peaks in O K-edge XANES spectra correspond to unique core-excitations from oxygen 1s orbitals into valence anti-bonding orbitals. The established interpretation is that O K-edge XANES peaks are driven by the degree of oxygen-2p character in the anti-bonding orbitals, so it is informative to examine if this holds for the theoretical O K-edge XANES spectrum of uranyl. In this section, RAS(S) and RAS(SD) O K-edge XANES spectra for $[UO_2]^{2+}$ are examined to establish whether a link between oxygen character in the anti-bonding orbital can be related to the magnitude of oscillator strength for a given transition. A variety of orbital composition approaches were used, and with the exception

of Mulliken analysis, all give comparable trends in the orbital compositions.

The resulting profiles from all three uranyl O K-edge XANES simulations are similar for peaks 1 and 2 in fig. 3.11, however, peak 3 is most easily ascribed to a single intense transition in the $[UO_2]^{2+}$ simulation. Therefore, analysis was performed on the $[UO_2]^{2+}$ model. In experiment, two XAS are obtained using linearly polarised X-rays incident parallel or perpendicular to the uranyl molecule. Additionally, an imperfect crystal alignment with the incident X-ray beams resulted in polarisation mixing, meaning the measured intensities, as highlighted by Denning, are only qualitative in nature. The spin-orbit coupled RASSCF simulations give the O K-edge XANES obtained when the incident X-rays are averaged over all orientations of the uranyl molecule. Therefore, the simulated and experimental spectra are not directly comparable. Given the outlined considerations, no attempt was made to compare either the transition strengths or the intensity of the overall Lorentzian peak to the experimental O K-edge uranyl spectrum reported by Denning.

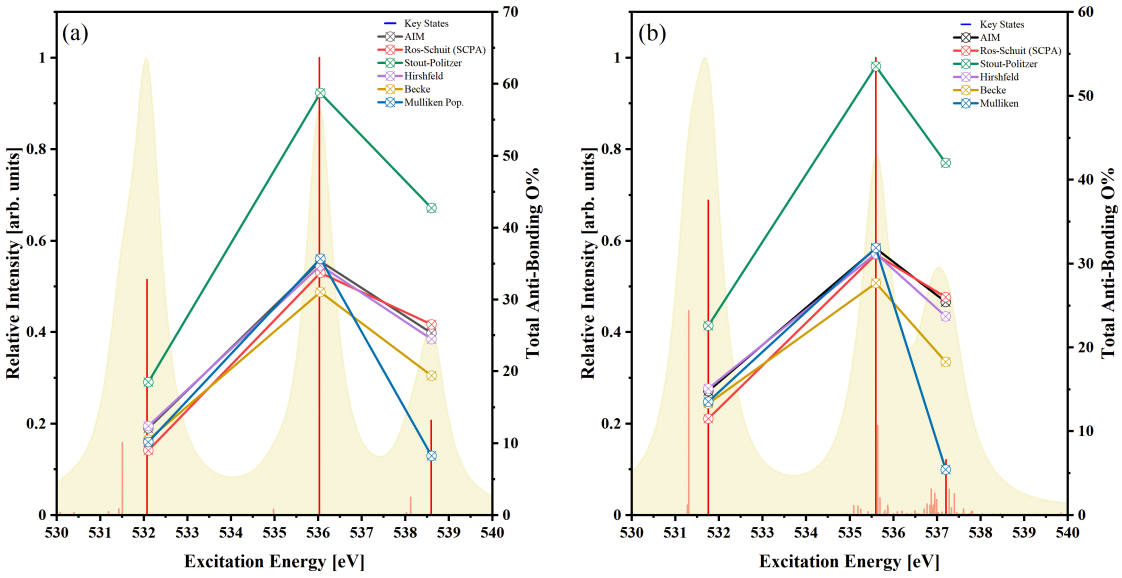

Figure 3.14: Plot showing the total oxygen percentage to anti-bonding orbitals for key intense transitions assigned to peaks 1-3 in (a) RAS(S) and (b) RAS(SD) $[UO_2]^{2+}$ simulations. Both the profile and transition stick intensities have been normalised with respect to the global value.

Orbital composition analysis was performed for key transitions from $[UO_2]^{2+}$ RAS(S)

and RAS(SD) simulated spectra, those assigned in tables 3.5 and 3.6. The O% contributions to the π_u^*, σ_u^*, and π_g^* anti-bonding orbitals for the key transitions assigned to peaks 1, 2 and 3, respectively were obtained using a number of different composition schemes. Mulliken-like methods enable the break-down of total O% into the specific amount of p-character, however, this is not possible using the AIM, Becke, and Hirshfeld approaches. To keep analysis consistent across the methods, only the total O% is considered and the assumption is made that the total O% contribution to the anti-bonding orbital is representative of the oxygen 2p-character. Oxygen character is plotted in fig. 3.14 along with the normalised magnitudes of individual transition oscillator strengths and peak intensities with respect to the global maximum value. This enables the trends in oxygen contributions to be compared with the relative strength of the transitions.

Given the established interpretation that O K-edge peak intensity is driven by O 2p-character, it was expected that the transitions with the greatest oscillator strengths, would correspond to CESs with the greatest amount of oxygen character in the anti-bonding orbitals associated with the transition. Going from highest to lowest oscillator strength, the largest oxygen character would be expected for the $1s \rightarrow \sigma_u^*$ transition, followed by $1s \rightarrow \pi_u^*$ and then $1s \rightarrow \pi_g^*$. Figure 3.14 shows the oscillator strengths for key transitions along with the calculated oxygen character in the anti-bonding orbital associated with the transition using a variety of composition schemes. Figure 3.14(a) corresponds to the RAS(S) and (b) to the RAS(SD) simulated plots, respectively. The expected high oxygen contribution to the σ_u^* orbital compared to π_u^* is found, aligning with the lower transition strength for the latter. Similarly, all methods predict a lower oxygen contribution in the π_g^* orbitals compared to σ_u^*, with a lower transition strength for the former. With the exception of Mulliken analysis, all other methods predict a greater oxygen contribution to the π_g^* orbitals compared to π_u^*, despite the transition strength being much greater in the latter. This finding breaks the established relationship between high oxygen character in the anti-bonding orbitals and the relative transition strength. The outlined trends apply to both the RAS(S) and RAS(SD) simulated plots, and given that at the RAS(S) level only the π_g^* are strongly occupied, this suggests that the breaking of the relationship is not caused by the more multiconfigurational nature of states at the RAS(SD) level. The Mulliken method is found to predict the correct trends between transition intensity

and anti-bonding O% character. However, with all other methods pointing to a larger than expected oxygen character in the π_g^* orbitals for the $1s \rightarrow \pi_g^*$ transition despite the low transition strength, the Mulliken O% composition for this transition is viewed as anomalous.

In the preceding section, it has been demonstrated by QTAIM results that substantial changes in the overall covalency occurs between the GS and CESs in $[UO_2]^{2+}$. Furthermore, direct analysis of the bonding orbitals has found that compositions between the GS and CESs can differ by as much as ∼10%. Given the notable changes in electronic structures between the ground- and core-excited states, the results in this section demonstrates that while the transition strengths may be strongly influenced by the specific oxygen character in a CES anti-bonding orbital, they have a strong dependence on the additional and more complex changes in overall electronic structure between the GS and CES. Therefore, analysing the oxygen character soley within the π_g^* orbital is not adequate for capturing the overall changes between the GS and CES, and by extension the magnitude of the oscillator strength for the associated transition.

3.4 Conclusions

In this chapter a RASSCF approach was utilized to simulate the O K-edge XANES of uranyl. Overall, the RAS(SD) level of RAS truncation was identified as the most appropriate approach for providing accurate prediction of XANES peaks with respect to experiment, whilst balancing the computational cost to run simulations. Three different uranyl models were implemented that progressively capture larger aspects of the local $Cs_2UO_2Cl_4$ crystal environment. RAS(SD) simulations reproduced the three peak profile found in the experimental XAS spectrum reported by Denning et al.[6], as well as additional features such as a shoulder on the first peak and peak structure in the post 545 eV region. The three main peaks in all simulations were assigned to the same core-excitations as those proposed by Denning et al. and highlight an energy ordering to the empty valence orbitals in uranyl as follows: $5f_{\delta/\phi} < \pi_u^* < \sigma_u^* < \pi_g^* < \sigma_g^*$.

O K-edge simulations using the $[UO_2]^{2+}$ model predicted all peaks to within 1.5 eV of experiment. This was improved further to 1 eV by including equatorial chloride ligands in the $[UO_2Cl_4]^{2-}$ model, which also gave relative peak separations in best agreement with

experimental separations. Incorporating caesium point charges in the $Cs_2UO_2Cl_4$ model did not generally improve the predictions. In fact, for peak 3, the spread of transitions across a wider energy range led to a broader and less intense peak with a maxima pushed to higher excitation energy. Overall this had the adverse effect of increasing the relative peak separation between 3 and other peaks.

All uranyl simulations highlight that O K-edge XANES peaks can comprise multiple transitions, and while strong transitions can be identified for peaks 1 and 2 in fig. 3.11, the CESs themselves exhibit multiconfigurational character, which manifests as partial population of all RAS3 orbitals to some degree. The degree to which the transition strength can be linked to the greater oxygen character in the anti-bonding orbitals was assessed using a variety of composition approaches. The results showed that the expected trends break down for the final peak, with composition schemes predicting greater oxygen contributions to the π_g^* orbitals compared to π_u^*, even though the oscillator strength is greater for the transition associated with the latter orbital. These results point to the oscillator strength being dependent on the larger overall changes in electronic structure between the ground- and core-excited state, and not just solely dependent on the oxygen character in a single anti-bonding orbital.

The main assumption that enables XANES spectra to be interpreted in terms of GS covalency is that the orbitals in the GS and CESs do not differ significantly from one another. This chapter aimed to investigate this by examining the overall change in covalency between the electronic structures of the GS and CES, as well as through direct analysis of the orbital compositions. QTAIM analysis was performed on ground- and core-excited states for each of the three uranyl models. All three model simulations found a reduction in the $\delta(\mathrm{U,O})$ values in the CESs, indicating a reduction in U-O electron sharing upon core-excitation. This was to be expected, since core-excitation leads to the population of anti-bonding orbitals which acts to reduce the uranyl bond order. The largest $\delta(\mathrm{U,O})$ reductions across any model are for the highly multiconfigurational $1s \rightarrow \pi_g^*$ CESs, which exhibit the most electron redistribution of electrons from bonding to anti-bonding orbitals. The inclusion of caesium point charges in the $Cs_2UO_2Cl_4$ model had little impact on the overall QTAIM metrics with respect to $[UO_2Cl_4]^{2-}$, meaning any trends identified for the latter model are representative of those in the point-charge model. This

has been identified in the literature before, with limited influence on the QTAIM metrics found between $[UO_2Cl_4]^{2-}$ and $Cs_2UO_2Cl_4$ models that include larger crystal environment effects.[32]

The equatorial chloride ligands are found to have an impact on the uranyl covalency in both the GS and CESs. In comparison to $[UO_2]^{2+}$, the reduction in U-O electron sharing upon core-excitation is substantially less in the chloride systems. The smaller reduction $\delta(U, O)$ values is attributed to more electron-rich oxygen centres in the GSs of chloride models, meaning distributing electrons from U-O bonding interactions onto oxygen centres in the CES incurs a greater energetic cost in comparison to $[UO_2]^{2+}$. Given this, the QTAIM metrics in the CESs for the chloride systems are found to be more representative of the GS values.

To investigate the extent to which the bonding orbitals differ between the GS and CESs, AIM orbital composition analysis was utilized. For $[UO_2]^{2+}$, a 7-10% lower uranium character was found in the CESs compared to the GS, with reductions in U% accounted for through increases in O%. Similarly, a 4-7% reduction in U% contributions to the bonding orbitals is found in both $[UO_2Cl_4]^{2-}$ and $Cs_2UO_2Cl_4$. However, reductions in U% are no longer compensated by sole changes in O%, rather the chloride centres offer an alternative route for charge redistribution and are found to influence the compositional changes. This is particularly evident for the CESs corresponding to the $1s \rightarrow \sigma_u^*$ excitation, where a reduction in both U% and O% contributions is accounted for by relatively large increases in Cl%. Considering just the U% and O% changes for the uranyl unit in all three models reveals that the orbital compositions come in closer alignment between the CESs and GS as models better reflect the crystal environment. For instance, the smallest overall changes in U% and O% contributions between the GS and CESs is found for the $Cs_2UO_2Cl_4$ model. In $Cs_2UO_2Cl_4$, the chloride ligands offers an alternative route for charge redistribution and caesium counter-ions appear to further encourage charge distribution toward the Cl centres in the CESs.

In conclusion, this study introduces a RASSCF methodology that successfully simulates XANES whilst also enabling some degree of control over the cost of the simulations. Results indicate that both the simulation approach and the models utilized are important considerations when predicting XANES spectra. In particular, the choice

of model used is important when obtaining orbital composition changes between the GS and CESs when assessing the validity of XANES as a GS covalency probe. Overall, this study finds that probing O K-edge XANES in the CES does lead to an underestimation of the U% contribution to the GS bonding orbitals. Furthermore, analysis shows that the degree to which the O% may be under- or overestimated will largely depend on the peak investigated and the model used.

References

[1] S. G. Minasian, J. M. Keith, E. R. Batista, K. S. Boland, D. L. Clark, S. A. Kozimor, R. L. Martin, D. K. Shuh and T. Tyliszczak, *Chemical Science*, 2014, **5**, 351–359, DOI: 10.1039/C3SC52030G.

[2] J. Su, E. R. Batista, K. S. Boland, S. E. Bone, J. A. Bradley, S. K. Cary, D. L. Clark, S. D. Conradson, A. S. Ditter, N. Kaltsoyannis, J. M. Keith, A. Kerridge, S. A. Kozimor, M. W. Löble, R. L. Martin, S. G. Minasian, V. Mocko, H. S. L. Pierre, G. T. Seidler, D. K. Shuh, M. P. Wilkerson, L. E. Wolfsberg and P. Yang, *Journal of the American Chemical Society*, 2018, **140**, 17977–17984, DOI: 10.1021/jacs.8b09436.

[3] S. A. Kozimor, P. Yang, E. R. Batista, K. S. Boland, C. J. Burns, D. L. Clark, S. D. Conradson, R. L. Martin, M. P. Wilkerson and L. E. Wolfsberg, *Journal of the American Chemical Society*, 2009, **131**, 12125–12136, DOI: 10.1021/ja9015759.

[4] T. Vitova, I. Pidchenko, D. Fellhauer, P. S. Bagus, Y. Joly, T. Pruessmann, S. Bahl, E. Gonzalez-Robles, J. Rothe, M. Altmaier, M. A. Denecke and H. Geckeis, *Nature Communications*, 2017, **8**, 16053, DOI: 10.1038/ncomms16053.

[5] S. G. Minasian, J. M. Keith, E. R. Batista, K. S. Boland, D. L. Clark, S. D. Conradson, S. A. Kozimor, R. L. Martin, D. E. Schwarz, D. K. Shuh, G. L. Wagner, M. P. Wilkerson, L. E. Wolfsberg and P. Yang, *Journal of the American Chemical Society*, 2012, **134**, 5586–5597, DOI: 10.1021/ja2105015.

[6] R. G. Denning, J. C. Green, T. E. Hutchings, C. Dallera, A. Tagliaferri, K. Giarda, N. B. Brookes and L. Braicovich, *The Journal of Chemical Physics*, 2002, **117**, 8008–8020, DOI: 10.1063/1.1510445.

[7] Y. Qiao, G. Ganguly, C. H. Booth, J. A. Branson, A. S. Ditter, D. J. Lussier, L. M. Moreau, D. R. Russo, D.-C. Sergentu, D. K. Shuh, T. Sun, J. Autschbach and S. G. Minasian, *Chemical Communications*, 2021, **57**, 9562–9565, DOI: 10.1039/D1CC03414F.

[8] G. Ganguly, D.-C. Sergentu and J. Autschbach, *Chemistry – A European Journal*, 2020, **26**, 1776–1788, DOI: 10.1002/chem.201904166.

[9] D.-C. Sergentu, T. J. Duignan and J. Autschbach, *The Journal of Physical Chemistry Letters*, 2018, **9**, 5583–5591, DOI: 10.1021/acs.jpclett.8b02412.

[10] D.-C. Sergentu and J. Autschbach, *Dalton Transactions*, 2022, **51**, 1754–1764, DOI: 10.1039/D1DT04075H.

[11] R. Polly, B. Schacherl, J. Rothe and T. Vitova, *Inorganic Chemistry*, 2021, **60**, 18764–18776, DOI: 10.1021/acs.inorgchem.1c02364.

[12] L. P. Spencer, P. Yang, S. G. Minasian, R. E. Jilek, E. R. Batista, K. S. Boland, J. M. Boncella, S. D. Conradson, D. L. Clark, T. W. Hayton, S. A. Kozimor, R. L. Martin, M. M. MacInnes, A. C. Olson, B. L. Scott, D. K. Shuh and M. P. Wilkerson, *Journal of the American Chemical Society*, 2013, **135**, 2279–2290, DOI: 10.1021/ja310575j.

[13] D.-C. Sergentu and J. Autschbach, *Chemical Science*, 2022, **13**, 3194–3207, DOI: 10.1039/D1SC06454A.

[14] E. I. Solomon, B. Hedman, K. O. Hodgson, A. Dey and R. K. Szilagyi, *Coordination Chemistry Reviews*, 2005, **249**, 97–129, DOI: 10.1016/j.ccr.2004.03.020.

[15] C. Fillaux, D. Guillaumont, J.-C. Berthet, R. Copping, D. K. Shuh, T. Tyliszczak and C. D. Auwer, *Phys. Chem. Chem. Phys.*, 2010, **12**, 14253–14262, DOI: 10.1039/C0CP00386G.

[16] B. O. Roos, in John Wiley and Sons, Ltd, 1987, pp. 399–445, DOI: 10.1002/9780470142943.ch7.

[17] P. A. Malmqvist, A. Rendell and B. O. Roos, *The Journal of Physical Chemistry*, 1990, **94**, 5477–5482, DOI: 10.1021/j100377a011.

[18] B. O. Roos, P. R. Taylor and P. E. M. Sigbahn, *Chemical Physics*, 1980, **48**, 157–173, DOI: 10.1016/0301-0104(80)80045-0.

[19] J. Olsen, B. O. Roos, P. Jo/rgensen and H. J. A. Jensen, *The Journal of Chemical Physics*, 1988, **89**, 2185–2192, DOI: 10.1063/1.455063.

[20] R. G. Denning, *The Journal of Physical Chemistry A*, 2007, **111**, 4125–4143, DOI: 10.1021/jp071061n.

[21] S. Fortier and T. W. Hayton, *Coordination Chemistry Reviews*, 2010, **254**, Inorganic Reaction Mechanisms, 197–214, DOI: https://doi.org/10.1016/j.ccr.2009.06.003.

[22] J. D. Ward, M. Bowden, C. T. Resch, S. Smith, B. K. McNamara, E. C. Buck, G. C. Eiden and A. M. Duffin, *Geostandards and Geoanalytical Research*, 2016, **40**, 135–148, DOI: https://doi.org/10.1111/j.1751-908X.2015.00337.x.

[23] F. Frati, M. O. J. Y. Hunault and F. M. F. de Groot, *Chemical Reviews*, 2020, **120**, 4056–4110, DOI: 10.1021/acs.chemrev.9b00439.

[24] A. Kerridge, *Chemical Communications*, 2017, **53**, 6685–6695, DOI: 10.1039/C7CC00962C.

[25] V. V. Zhurov, E. A. Zhurova, A. I. Stash and A. A. Pinkerton, *The Journal of Physical Chemistry A*, 2011, **115**, 13016–13023, DOI: 10.1021/jp204965b.

[26] V. Vallet, U. Wahlgren and I. Grenthe, *The Journal of Physical Chemistry A*, 2012, **116**, 12373–12380, DOI: 10.1021/jp3091123.

[27] A. Leoncini, J. Huskens and W. Verboom, *Chem. Soc. Rev.*, 2017, **46**, 7229–7273, DOI: 10.1039/C7CS00574A.

[28] M. S. M. J. N. Mathur and K. L. Nash, *Solvent Extraction and Ion Exchange*, 2001, **19**, 357–390, DOI: 10.1081/SEI-100103276.

[29] Y. Zhang, W. Duan, Y. Yang, T. Jian, Y. Qiao, G. Ren, N. Zhang, L. Zheng, W. Yan, J. Wang, J. Chen, S. G. Minasian and T. Sun, *Inorganic Chemistry*, 2022, **61**, 92–104, DOI: 10.1021/acs.inorgchem.1c02236.

[30] J. Chen, X. He and J. Wang, *Radiochimica Acta*, 2014, **102**, 41–51, DOI: doi:10.1515/ract-2014-2093.

[31] P. D. Dau, J. Su, H.-T. Liu, D.-L. Huang, J. Li and L.-S. Wang, *The Journal of Chemical Physics*, 2012, **137**, 064315, DOI: 10.1063/1.4742062.

[32] J. P. W. Wellington, A. Kerridge and N. Kaltsoyannis, *Polyhedron*, 2016, **116**, 57–63, DOI: 10.1016/j.poly.2016.02.048.

[33] P. D. Pietro and A. Kerridge, *Inorganic Chemistry*, 2016, **55**, 573–583, DOI: 10.1021/acs.inorgchem.5b01219.

[34] K. Pierloot and E. van Besien, *The Journal of Chemical Physics*, 2005, **123**, 204309, DOI: 10.1063/1.2121608.

[35] K. Pierloot, E. van Besien, E. van Lenthe and E. J. Baerends, *The Journal of Chemical Physics*, 2007, **126**, 194311, DOI: 10.1063/1.2735297.

[36] A. S. P. Gomes, C. R. Jacob, F. Réal, L. Visscher and V. Vallet, *Phys. Chem. Chem. Phys.*, 2013, **15**, 15153–15162, DOI: 10.1039/C3CP52090K.

[37] W. A. Misael and A. S. P. Gomes, *Inorganic Chemistry*, 2023, **62**, 11589–11601, DOI: 10.1021/acs.inorgchem.3c01302.

[38] K. Stanistreet-Welsh and A. Kerridge, *Phys. Chem. Chem. Phys.*, 2023, **25**, 23753–23760, DOI: 10.1039/D3CP03149G.

[39] F. Aquilante, J. Autschbach, A. Baiardi, S. Battaglia, V. A. Borin, L. F. Chibotaru, I. Conti, L. D. Vico, M. Delcey, I. F. Galván, N. Ferré, L. Freitag, M. Garavelli, X. Gong, S. Knecht, E. D. Larsson, R. Lindh, M. Lundberg, P. Å. Malmqvist, A. Nenov, J. Norell, M. Odelius, M. Olivucci, T. B. Pedersen, L. Pedraza-González, Q. M. Phung, K. Pierloot, M. Reiher, I. Schapiro, J. Segarra-Martí, F. Segatta, L. Seijo, S. Sen, D.-C. Sergentu, C. J. Stein, L. Ungur, M. Vacher, A. Valentini and V. Veryazov, *The Journal of Chemical Physics*, 2020, **152**, 214117, DOI: 10.1063/5.0004835.

[40] F. Aquilante, L. D. Vico, N. Ferré, G. Ghigo, P.-å. Malmqvist, P. Neogrády, T. B. Pedersen, M. Pitoňák, M. Reiher, B. O. Roos, L. Serrano-Andrés, M. Urban, V. Veryazov and R. Lindh, *Journal of Computational Chemistry*, 2010, **31**, 224–247, DOI: 10.1002/jcc.21318.

[41] F. Aquilante, J. Autschbach, R. K. Carlson, L. F. Chibotaru, M. G. Delcey, L. D. Vico, I. F. Galván, N. Ferré, L. M. Frutos, L. Gagliardi, M. Garavelli, A. Giussani, C. E. Hoyer, G. L. Manni, H. Lischka, D. Ma, P. Å. Malmqvist, T. Müller, A. Nenov, M. Olivucci, T. B. Pedersen, D. Peng, F. Plasser, B. Pritchard, M. Reiher, I. Rivalta, I. Schapiro, J. Segarra-Martí, M. Stenrup, D. G. Truhlar, L. Ungur, A. Valentini, S. Vancoillie, V. Veryazov, V. P. Vysotskiy, O. Weingart, F. Zapata and R. Lindh, *Journal of Computational Chemistry*, 2016, **37**, 506–541, DOI: 10.1002/jcc.24221.

[42] B. O. Roos, R. Lindh, P.-Å. Malmqvist, V. Veryazov and P.-O. Widmark, *The Journal of Physical Chemistry A*, 2005, **109**, 6575–6579, DOI: 10.1021/jp0581126.

[43] B. O. Roos, R. Lindh, P.-Å. Malmqvist, V. Veryazov and P.-O. Widmark, *Chemical Physics Letters*, 2005, **409**, 295–299, DOI: 10.1016/j.cplett.2005.05.011.

[44] *The Journal of Physical Chemistry A*, 2004, **108**, 2851–2858, DOI: 10.1021/jp031064+.

[45] A. Wolf, M. Reiher and B. A. Hess, *The Journal of Chemical Physics*, 2002, **117**, 9215–9226, DOI: 10.1063/1.1515314.

[46] B. A. Hess, *Physical Review A*, 1986, **33**, 3742–3748, DOI: 10.1103/PhysRevA.33.3742.

[47] B. A. Hess, *Physical Review A*, 1985, **32**, 756–763, DOI: 10.1103/PhysRevA.32.756.

[48] M. Douglas and N. M. Kroll, *Annals of Physics*, 1974, **82**, 89–155, DOI: 10.1016/0003-4916(74)90333-9.

[49] B. A. Hess, C. M. Marian, U. Wahlgren and O. Gropen, *Chemical Physics Letters*, 1996, **251**, 365–371, DOI: 10.1016/0009-2614(96)00119-4.

[50] D. Hall, A. D. Rae and T. N. Waters, *Acta Crystallographica*, 1966, **20**, 160–162, DOI: 10.1107/S0365110X66000355.

[51] V. Sauri, L. Serrano-Andrés, A. R. M. Shahi, L. Gagliardi, S. Vancoillie and K. Pierloot, *Journal of Chemical Theory and Computation*, 2011, **7**, 153–168, DOI: 10.1021/ct100478d.

[52] S. Vancoillie, H. Zhao, V. T. Tran, M. F. A. Hendrickx and K. Pierloot, *Journal of Chemical Theory and Computation*, 2011, **7**, 3961–3977, DOI: 10.1021/ct200597h.

[53] J. Finley, P.-Å. Malmqvist, B. O. Roos and L. Serrano-Andrés, *Chemical Physics Letters*, 1998, **288**, 299–306, DOI: 10.1016/S0009-2614(98)00252-8.

[54] J. P. Zobel, J. J. Nogueira and L. González, *Chemical Science*, 2017, **8**, 1482–1499, DOI: 10.1039/C6SC03759C.

[55] N. Forsberg and P.-Å. Malmqvist, *Chemical Physics Letters*, 1997, **274**, 196–204, DOI: 10.1016/S0009-2614(97)00669-6.

[56] P. Å. Malmqvist, B. O. Roos and B. Schimmelpfennig, *Chemical Physics Letters*, 2002, **357**, 230–240, DOI: 10.1016/S0009-2614(02)00498-0.

[57] J. Autschbach, *Comments on Inorganic Chemistry*, 2016, **36**, 215–244, DOI: 10.1080/02603594.2015.1121874.

[58] F. Gendron, B. Pritchard, H. Bolvin and J. Autschbach, *Inorganic Chemistry*, 2014, **53**, 8577–8592, DOI: 10.1021/ic501168a.

[59] K. Stanistreet-Welsh, *Molcas2Molden: Molcas INPORB to MOLDEN Convertor*, https://github.com/k-stanistr-wel/Molcas2Molden, 2023.

[60] J. development team, *Jmol: an open-source Java viewer for chemical structures in 3D*, http://www.jmol.org/, 2023.

[61] T. Lu and F. Chen, *Journal of Computational Chemistry*, 2012, **33**, 580–592, DOI: 10.1002/jcc.22885.

[62] Z. Wenli, *Molden2AIM: A utility program which can be used to create AIM-WFN, AIM-WFX, and NBO-47 files from a Molden file*, https://github.com/zorkzou/Molden2AIM, 2023.

[63] T. A. Keith, *AIMAll*, version 19.02.13, TK Gristmill Software, 2019.

[64] L. Amidani, M. Retegan, A. Volkova, K. Popa, P. M. Martin and K. O. Kvashnina, *Inorganic Chemistry*, 2021, **60**, 16286–16293, DOI: 10.1021/acs.inorgchem.1c02107.

[65] K. O. Kvashnina and S. M. Butorin, *Chem. Commun.*, 2022, **58**, 327–342, DOI: 10.1039/D1CC04851A.

[66] R. F. W. Bader, *Atoms in Molecules: A Quantum Theory*, Oxford University Press, 1990.

[67] R. F. W. Bader, *Chemical Reviews*, 1991, **91**, 893–928, DOI: 10.1021/cr00005a013.

[68] M. L. Neidig, D. L. Clark and R. L. Martin, *Coordination Chemistry Reviews*, 2013, **257**, 394–406, DOI: 10.1016/j.ccr.2012.04.029.

Chapter 4

Bounding Actinyl Covalency by Simulated O K-edge and An M-edge XANES:

RASSCF calculations are applied to simulate the O K-edge and An $M_{4/5}$-edge XANES of uranyl, neptunyl and plutonyl. An $M_{4/5}$-edge XANES simulations offer good agreement with experimental peak separations and spectral profiles. Peak assignments for XANES spectra of both edges are in agreement with theoretical and experimental literature. Analysis of the bonding orbitals in the ground- and core-excited states demonstrates an underestimation of actinide contributions to bonding in the latter for O K-edge simulations. Bonding orbitals are comparable between the ground- and core-excited states for uranyl and the neptunyl $3d \rightarrow \pi_u^*$ state, while for the neptunyl $3d \rightarrow \sigma_u^*$ state, there is a small 2% decrease in actinide contribution relative to the ground-state. In plutonyl, composition analysis of bonding orbitals in the core-excited state demonstrates an overestimation of actinide contribution compared to the ground-state bonding. QTAIM analysis was used to rationalise the reported compositional changes as well as changes in the overall electronic structure. Overall, simulations suggest that bonding probed experimentally via O K-edge would give a lower bound on the actinide contribution to bonding, while An $M_{4/5}$-edge would represent an upper bound, with both techniques offering complementary information and providing a means to bound actinide contributions to bonding.

4.1 Introduction

In this chapter, simulated O K-edge and An $M_{4/5}$-edge XANES spectra of uranyl, neptunyl and plutonyl are reported using the same RASSCF methodology described in detail within chapter 3. To date, experimental O K-edge has only been reported for uranyl,[1] and as such, the simulated O K-edge reported for neptunyl and plutonyl represent theoretical predictions yet to be experimentally verified. The U M_4-edge, Np and Pu M_5-edge XANES simulations in this chapter aim to reproduce the experimentally reported XANES by Vitova et al.[2] In An $M_{4/5}$-edge XANES, peaks are generated by core-excitations from actinide 3d-orbitals into valence orbitals of 5f-character. The splitting of the 3d core-orbitals is substantial under spin-orbit coupling (SOC) yielding states that can be characterised as M_4 and M_5 as shown in fig. 4.1. The inclusion of SOC is therefore a crucial feature to capture within An $M_{4/5}$-edge XANES simulations in order to obtain the energetically separated M_4- and M_5-edges. Analogous to the peak intensities in O K-edge XANES, the An $M_{4/5}$-edge peak intensity is driven by the degree of actinide 5f-character in the acceptor orbital (typically anti-bonding orbitals), which can be related to the degree of 5f-character in the bonding orbitals through orthogonality arguments. Limited orbital relaxation is a requirement for the orbital mixing in the CES bonding orbitals to be representative of those in the GS, and is the key assumption made in the interpretation of XANES in terms of GS covalency. Unlike in the case of ligand K-edge, studies in-practice do not widely utilise An $M_{4/5}$-edge peak intensities as a measure of orbital mixing, instead, studies tend to utilize the energetic separation of the peaks as indicators of covalency. For actinyl systems, the peak ascribed to the $3d \rightarrow \sigma_u^*$ core-excitation in An $M_{4/5}$-edge spectra is well resolved from the highly intense peak primarily attributed to the $3d \rightarrow 5f_{\phi,\delta}$ core-excitation, and can be utilized as an indicator of axial covalency.[2]

The actinyl An $M_{4/5}$-edge XANES spectra, from uranyl to plutonyl, have previously been simulated using a RASSCF approach by Autschbach and co-workers,[5] and successfully reproduced the experimental spectra in terms of spectral profile and peak separations. Analysis of the π-bonding orbitals found limited orbital relaxation between the GS and $3d \rightarrow \pi_u^*$ CESs in the actinyl systems. In uranyl, the σ-bonding orbital is

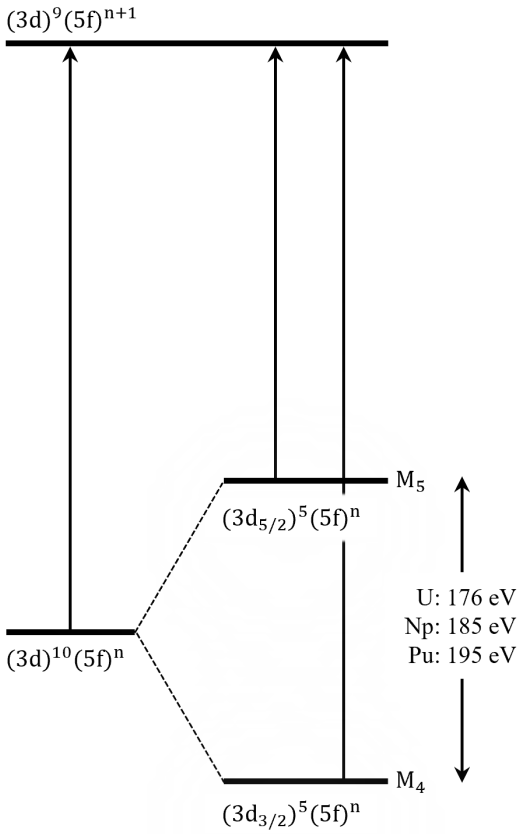

Figure 4.1: Qualitative energy level diagram showing the substantial energy splitting of the 3d-shell due to spin-orbit coupling into J=3/2 and J=5/2 states which can be characterised as M_4 and M_5 states, respectively. Note that the splitting of the 5f shell due to spin-orbit coupling is not shown. Energy values were calculated using transitions energies taken from Kraft et al. [3] and Bearden et al. [4]

similar in composition between the GS and 3d $\rightarrow \sigma_u^*$ CES, while in neptunyl and plutonyl, a 14% and 17% reduction in actinide contribution to the σ_u bonding orbital is reported. In this chapter, orbital composition and QTAIM analysis is utilized to examine the GS and CESs separately in order to assess the degree to which An $M_{4/5}$-edge and O K-edge XANES is a valid probe of GS actinyl covalency. The An $M_{4/5}$-edge RAS simulations reported in this chapter differ from those reported by Autschbach and co-workers,[5] by including the bonding orbitals in the active space of neptunyl and plutonyl simulations, as well as in the application of a consistent set of constraints on the active-space across all three systems and simulations. Additionally, by utilizing the methodology outlined in chapter 3, some

degree of control over the amount of correlation captured and therefore computational cost, is enabled. RAS(SD) level calculations were possible for all three actinyl systems and are presented in this work. Simulations made use of a simplified and idealised $[AnO_2]^{2+}$ model with bond lengths informed by experimentally relevant bond lengths.[1, 2, 6–13] Admittedly, the model does not capture the local environment of the species utilized in experimental references, with the experimental O K-edge being performed on a $Cs_2UO_2Cl_4$ crystal, and experimental An $M_{4/5}$-edge being performed on actinyls in aqueous solution whereby $[AnO_2(H_2O)_5]^{2+}$ complexes form. In chapter 3, it was demonstrated that Cl ligands have a direct impact on the resulting XANES and covalency results for uranyl, and is expected to extend to neptunyl and plutonyl. In contrast, Autschbach and co-workers have demonstrated water ligands have very little impact on the relative separation of peaks in the XANES simulations,[5] but inclusion of these ligands does improve the absolute prediction of the spectrum with respect to experiment. In this chapter, the omission of local environment effects enables comparison of the simulated spectra for both edges without any potential bias from differing equatorial ligands. Furthermore, the use of bare-actinyls with experimental bond lengths is a standard approach taken in a number of published studies.[5, 14–16] The simulations presented in this chapter can therefore be viewed as representative of the XANES spectra obtained for a generic set of actinyl containing complexes.

Simulating the O K-edge and An $M_{4/5}$-edge XANES for open-shell actinyls represents a more significant computational challenge for RASSCF-type approaches compared to the closed shell uranyl systems presented in chapter 3. This is due in-part to the substantial increase in the possible CESs that arise due the presence of unpaired electrons in the non-bonding 5f orbitals. Despite this, high quality XANES spectra are obtained for all three actinyl systems and the results in this chapter showcase the versatility of the RASSCF methodology utilized throughout this thesis.

4.2 Computational Details

Scalar relativistic multiconfigurational XANES simulations were performed using version 21.02 of OpenMolcas.[17–20] All simulations employed the all-electron ANO-RCC basis sets of Roos et al.,[21–23] at the TZP level of quality for oxygen (4s3p2d1f) and actinides

(9s8p6d4f2g) but with higher angular momentum An h-functions removed to enable compatibility with analysis software. Scalar relativistic effects were modelled using the second order Douglas-Kroll-Hess Hamiltonian and Cholesky decomposition was utilized throughout to speed-up integral calculations.[24–28]

4.2.1 Actinyl Models

Simulations were performed utilizing $[AnO_2]^{2+}$ (An= U, Np, Pu) models and using the highest Abelian point-group of D_{2h} with the molecular axis orientated in the z-direction. For O K-edge simulations, solid-state $Cs_2AnO_2Cl_4$ crystals were used to inform the bond lengths,[1, 6–12] to keep neptunyl and plutonyl O K-edge predictions inline with those performed for uranyl in chapter 3 and since the uranyl O K-edge experimental reference made use of a $Cs_2UO_2Cl_4$ single crystal.[1] For An $M_{4/5}$-edge XANES simulations, An-O bond lengths reported in table 4.1 were set to those of the $[AnO_2(H_2O)_5]^{2+}$ systems[13] probed experimentally by Vitova et al.[2]

Table 4.1: Experimental $Cs_2AnO_2Cl_4$[1, 6–12] and $[AnO_2(H_2O)_5]^{2+}$[2, 13] bond lengths (Å) used to inform the An-O bonds in $[AnO_2]^{2+}$ models utilised in for O K-edge and An $M_{4/5}$-edge simulations.

System	Bond Length Å
$Cs_2UO_2Cl_4$	1.770
$Cs_2NpO_2Cl_4$	1.775
$Cs_2PuO_2Cl_4$	1.752
$[UO_2(H_2O)_5]^{2+}$	1.760
$[NpO_2(H_2O)_5]^{2+}$	1.750
$[PuO_2(H_2O)_5]^{2+}$	1.740

Previous simulations by Autschbach and co-workers[5] demonstrated that bare-actinyls set to $[AnO_2(H_2O)_5]^{2+}$ bond lengths were sufficient for simulating the key aspects of experimental An $M_{4/5}$-edge XANES spectra. Furthermore, the inclusion of water

ligands was tested using a $[PuO_2(H_2O)_5]^{2+}$ model, and it was found that the XANES spectrum was largely unaffected in terms of intensity profile and relative peak separations. Including water ligands did improve the absolute energy predictions, reducing the required shift to align with experiment from 27.2 eV for $[PuO_2]^{2+}$ to 10.5 eV for $[PuO_2(H_2O)_5]^{2+}$. [5] However, the experimentally informed $[AnO_2(H_2O)_5]^{2+}$ models come with the disadvantage of C_1 point groups, restricting calculations to a single irreducible representation, and significantly increasing the computational cost in contrast to the higher D_{2h} point-group of $[AnO_2]^{2+}$ models. Given the outlined considerations, free actinyl models with bond lengths reported in table 4.1 were implemented in this study.

4.2.2 RASSCF Set-Up

RASSCF simulations were used to obtain the necessary scalar-relativistic spin-free ground- and core-excited states. The O K-edge active-space and methodology utilized in the chapter 3 for uranyl was adapted for use in this chapter for neptunyl and plutonyl. The active-space is also adapted for An $M_{4/5}$-edge XANES simulations by replacing O(1s) orbitals for An(3d), and removing gerade valence orbitals. The overall construction of the active spaces for XANES simulations follow the same general scheme: with core-orbitals spanning RAS1, occupied bonding orbitals spanning RAS2, non-bonding 5f and anti-bonding orbitals spanning RAS3. The non-bonding orbitals were placed in RAS3 to control the number of possible configurations generated, making calculations involving large numbers of unpaired electrons (particularly plutonyl calculations) more tractable.

Figure 4.2 presents the two different active-space set-ups for O K-edge and An $M_{4/5}$-edge XANES simulations. For O K-edge simulations, RAS1 comprises the gerade (g) and ungerade (u) linear combinations of oxygen 1s-orbitals, meaning transitions are allowed into both u/g-parity empty valence orbitals. For An M-edge simulations, RAS1 comprises the set of five (g) 3d-orbitals, meaning only transitions into the u-parity set of empty valence orbitals is possible under the Laporte selection rule. The active space for M-edge XANES simulations is reduced accordingly so that both RAS2 and RAS3 only contain the necessary u-parity set of valence orbitals. Regardless of the RAS truncation level, RAS(S) or RAS(SD), all simulations concerning neptunyl and plutonyl were set up to contain at least 1 and 2 electrons in RAS3 ($n_3 = 1$ and $n_3 = 2$), respectively, in all

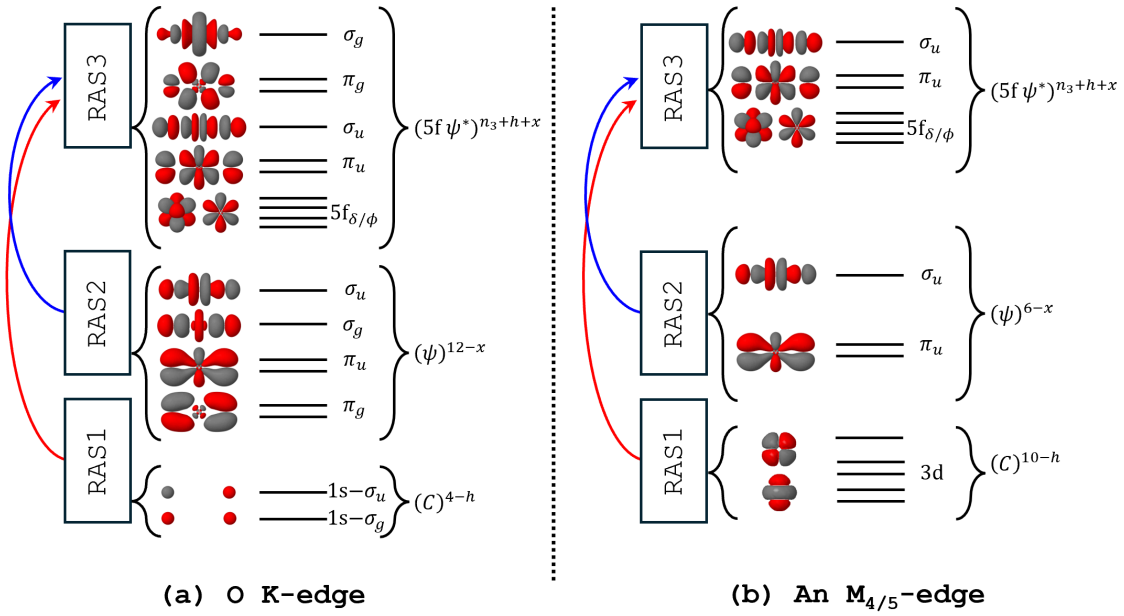

Figure 4.2: Active spaces used in (a) O K-edge and (b) An $M_{4/5}$-edge XANES simulations of the actinyls. Arrows indicate which RAS spaces electrons can move between subject to the the active-space constraints. The terms C, ψ, and (5f ψ^*) represent the core orbitals, bonding orbitals and the set of non-bonding 5f and anti-bonding orbitals, respectively. The variables h, x, and n_3 represent the number of core-holes, the number of electrons depleted from RAS2, and the number of RAS3 electrons in the GS configuration, respectively.

states (both GS and CESs). This was in order to account for the known $5f^1$ and $5f^2$ electronic configurations in the GSs of these systems. This means that in any state generated in the simulations, neptunyl and plutonyl states will always contain at least 1 and 2 electrons in RAS3 orbitals. For all simulations, CESs were generated by enforcing a single core-hole across RAS1 and allowing the core-excited electron (h) to enter RAS3. For RAS(S) level calculations no additional electrons are allowed to enter RAS3 ($x = 0$), while RAS(SD) level calculation allow up to one additional electron to populate the RAS3 space ($x = 1$). For example, this means that RAS(S) and RAS(SD) calculations in uranyl, allows a maximum of 1 and 2 electrons across RAS3, respectively, while plutonyl calculations allow a maximum of 3 and 4, respectively. In Sauri notation[29] the O K-edge RAS(S) and RAS(SD) CES calculations correspond to RAS(16+n_3, 1, 1+n_3; 2, 6, 10) and RAS(16+n_3, 1, 2+n_3; 2, 6, 10), respectively. For M-edge calculations RAS(S) and

RAS(SD) calculations correspond to RAS(16+n_3, 1, 1+n_3; 5, 3, 7) and RAS(16+n_3, 1, 2+n_3; 5, 3, 7), respectively. Depending on the spin-alignment of electrons in the CESs a number of spin-multiplicities are possible. The total number of possible CESs for each spin-multiplicity at the RAS(SD) level are reported in table 4.2, with the Laporte selection rule for centrosymmetric systems being invoked to reduce the number of states that are required for calculation. Supersymmetry designations ensured that the core-orbitals did not rotate out of RAS1 during the SCF procedure. All scalar-relativistic core-excited spin-free states were obtained by taking the appropriate level of state-averaging for RAS(SD) wavefunctions of different spin-multiplicities and irreducible representations as reported in table 4.3.

RAS(S) and RAS(SD) ground-states were obtained by simply removing the RAS1 core-hole constraint ($h = 0$). This converged RAS wavefunctions compatible for state-interaction with CESs, with a fully occupied RAS1 subspace and RAS3 spaces that reflect the expected $5f^0$, $5f^1$, and $5f^2$ GS configurations of uranyl, neptunyl and plutonyl, respectively. For both K- and M-edge RAS(SD) GSs, the first root of a five state-average calculation for the relevant GS irreps and multiplicities were utilized for spin-orbit coupling in RASSI calculations (see table 4.3). State-averaging the states of each ground-state irrep was found to stabilise the non-bonding 5f orbitals within the active-space.

Table 4.2: Total number of possible states that can be obtained via state-average calculations for An $M_{4/5}$-edge and O K-edge RAS(SD) active-space set-ups.

$[UO_2]^{2+}$	U M_4-edge	O K-edge
GS: $^1(A_g)$	73	423
CES: $^1(A_u/B_{1u}/B_{2u}/B_{3u})$	191/193/193/193	145/155/155/155
CES: $^3(A_u/B_{1u}/B_{2u}/B_{3u})$	272/271/271/271	217/221/221/221
$[NpO_2]^{2+}$	Np M_5-edge	O K-edge
GS: $^2(A_u/B_{1u}/B_{2u}/B_{3u})$	313/318/318/318	2976. 2985. 2989. 2989
CES: $^2(A_g/B_{1g}/B_{2g}/B_{3g})$	1031/1033/1033/1033	1192/1196/1196/1196
CES: $^4(A_g/B_{1g}/B_{2g}/B_{3g})$	702/711/711/711	843/874/874/874
$[PuO_2]^{2+}$	Pu M_5-edge	O K-edge
GS: $^1(A_g/B_{1g}/B_{2g}/B_{3g})$	568/534/534/534	7208/7060/7076/7076
GS: $^3(A_g/B_{1g}/B_{2g}/B_{3g})$	741/768/768/768	11274/11410/11386/11386
CES: $^1(A_u/B_{1u}/B_{2u}/B_{3u})$	1658/1664/1664/1664	2793/2809/2809/2809
CES: $^3(A_u/B_{1u}/B_{2u}/B_{3u})$	2625/2625/2625/2625	4653/4629/4629/4629
CES: $^5(A_u/B_{1u}/B_{2u}/B_{3u})$	1096/1093/1093/1093	2172/2136/2136/2136

RAS(S) simulations were utilized solely as an aid for peak assignments as detailed in chapter 3 and are therefore omitted from this discussion, instead, the higher quality RAS(SD) simulation results are presented. Dynamical correlation was included via multiconfigurational 2^{nd} order perturbation theory (RASPT2),[30, 31] with an IPEA shift[32] of 0.25 a.u. and imaginary shift[33] of 0.5 a.u., found to offer a reasonable balance between converging intruder free solutions without significant shifting of the resulting RASPT2 state-energies. These parameters are inline with those used in related studies.[5, 14, 34–36]

Table 4.3: Total number of states obtained via state-average RASSCF which were supplied to RASSI calculations.

$[UO_2]^{2+}$	U M_5-edge	O K-edge
GS: $^1(A_g)$	1	1
CES: $^1(A_u/B_{1u}/B_{2u}/B_{3u})$	137/152/136/136	62/63/68/68
CES: $^3(A_u/B_{1u}/B_{2u}/B_{3u})$	194/215/216/216	93/90/95/95
$[NpO_2]^{2+}$	Np M_5-edge	O K-edge
GS: $^2(A_u/B_{1u}/B_{2u}/B_{3u})$	1/1/1/1	1/1/1/1
CES: $^2(A_g/B_{1g}/B_{2g}/B_{3g})$	597/598/599/599	312/305/303/303
CES: $^4(A_g/B_{1g}/B_{2g}/B_{3g})$	471/474/480/480	234/239/233/233
$[PuO_2]^{2+}$	Pu M_5-edge	O K-edge
GS: $^1(A_g/B_{1g}/B_{2g}/B_{3g})$	1/1/1/1	1/1/1/1
GS: $^3(A_g/B_{1g}/B_{2g}/B_{3g})$	1/1/1/1	1/1/1/1
CES: $^1(A_u/B_{1u}/B_{2u}/B_{3u})$	405/411/384/384	344/345/353/353
CES: $^3(A_u/B_{1u}/B_{2u}/B_{3u})$	595/598/600/600	592/568/573/573
CES: $^5(A_u/B_{1u}/B_{2u}/B_{3u})$	408/411/411/411	317/316/295/295

4.2.3 RASSI Calculations

4.2.3.1 Spin-Orbit Coupling

The appropriate GS and CESs for each system were spin-orbit (SO) coupled *post hoc via* state-interaction of scalar relativistic states with a mean-field SO operator, making use of atomic mean-field integrals (AMFI), in the Restricted Active Space State Interaction (RASSI) formalism.[27, 33] Diagonal energies of the Hamiltonian matrix computed by RASSI were replaced by the calculated RASPT2 energies. The number of GSs and CESs of a given irrep and spin-multiplicity supplied to RASSI calculations is given in table 4.3.

Details on the resulting SO-GSs are discussed in the proceeding results section.

To reduce the cost associated with RASSI calculations, the number of states supplied for state-interaction was reduced using energy cutoffs. For O K-edge XANES calculations, the number of spin-free states supplied to RASSI calculations was restricted to reduce the computational cost of the calculations whilst also ensuring that the final spectrum spanned a 525-545 eV energy range, similar to the procedure undertaken in chapter 3. For the An $M_{4/5}$-edge XANES simulations, determining energy cutoffs is made difficult since SO coupling generates two spectra (M_4 & M_5) at vastly different energy scales. To inform energy cutoffs, first a RAS(S) XANES simulation in the absence of SO coupling is performed to give an initial single spectrum. An energy cutoff is then determined by the point at which the majority of intense transitions contributing to the XANES profile ends in this spin-free RAS(S) spectrum. The energy cutoff is then utilized as a filter to determine which spin-free RAS(SD) RASSCF states are supplied to RASSI calculations. The cutoffs were determined to be 3657, 3773, and 3885 eV for uranyl, neptunyl and plutonyl, respectively.

To summarize, the criteria used to reduce the number of states calculated using SA-RASSCF and supplied to RASSI calculations is as follows:

1. Implementation of the Lapotre selection rule for SA-RASSCF calculations such that a subset of u/g-parity states are required depending on the parity of the GS (see text for details).

2. Out of the total possible states in table 4.2 only a subset were calculated for by SA-RASSCF calculations as reported in table 4.3.

3. To reduce states supplied to RASSI calculations an energy cutoff for states of 545 eV was used for O K-edge simulations.

4. To reduce states supplied to RASSI calculations in An M4/5-edge XANES simulations an energy cutoff for uranyl, neptunyl and plutonyl states of 3657, 3773 and 3885 eV were utilised (see text for details).

4.2.3.2 Generating Simulated XANES plots

RASSI calculations provide SOC state energies and GS → CES electric-dipole transition oscillator strengths, enabling transition sticks to be plotted and broadened using Lorentzian functions to generate the overall XANES curves. A full-width at half-maximum (FWHM) of 1.0 eV was utilized for Lorentzian broadening of all An $M_{4/5}$-edge transitions, and a FWHM of 0.8 eV was utilized for Lorentzian broadening of O K-edge uranyl and neptunyl transitions, while a value of 1.2 eV was used for plutonyl. The choice of FWHM is considered somewhat arbitrary since the peak maxima are found to remain the same regardless of the value chosen, but values were chosen to offer good visual comparison with the available experimental references.

4.2.4 Analysis Tools

RASSI calculations provide spin-orbit natural orbital (SONO) coefficients[34, 37, 38] along with their natural populations and are converted to MOLDEN format using a custom Molcas2Molden package which has been made freely available.[39] SONOs were utilized for peak assignments using JMOL[40] and version 3.8 of Multiwfn.[41] Molden2AIM was utilized for file conversion,[42] enabling QTAIM analysis to be performed using version 19.02.13 of AIMALL[43] and Multifwn. Orbital composition analysis on SONOs was performed using Multiwfn, while Natural Localised Molecular Orbital (NLMO) analysis was performed using NBO6.[44, 45]

4.3 Results and Discussion

4.3.1 $[AnO_2]^{2+}$ O K-edge XANES

4.3.1.1 Spectra & Assignments

The RAS(SD) simulated O K-edge XANES spectra from uranyl to plutonyl are presented in fig. 4.3. The uranyl spectrum is taken from chapter 3 and represented here for convenience. In all three cases, the spectral profiles are similar, presenting three clear peaks labelled 1-3. A small shoulder feature at ∼530 eV generated by weak transitions is identified for uranyl and neptunyl. In both cases, these weak transitions are attributed to

core-excitations into the non-bonding 5f-orbitals. For plutonyl, no such transitions in the vicinity of 530 eV are evident, instead, a weak transition into the non-bonding 5f-orbitals falls under peak 1 closer to 531.4 eV. The simulation set-up restricted the number of states supplied for state-interaction and as such, only transitions in a 525-545 eV energy range were calculated, meaning no post 545 eV region features are reported for neptunyl or plutonyl.

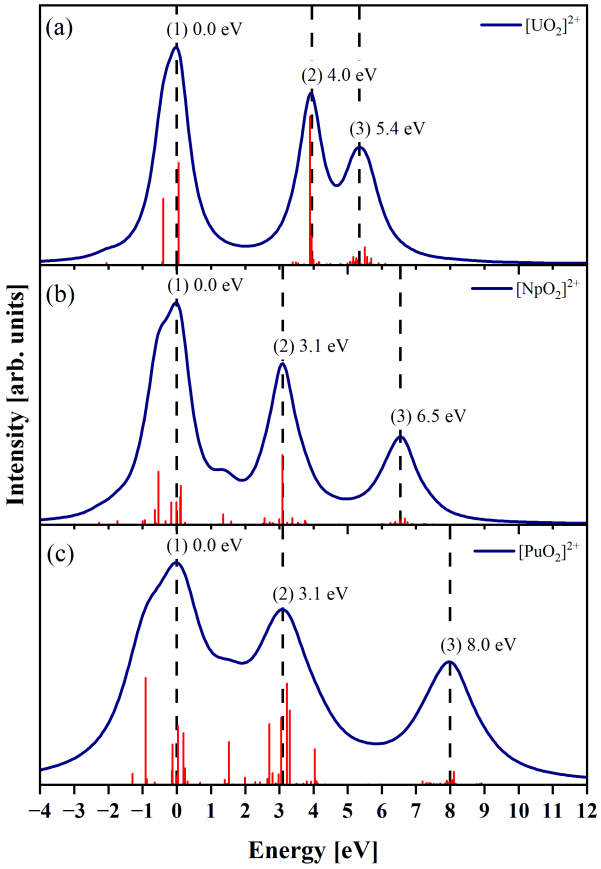

Figure 4.3: RAS(SD) simulated O K-edge XANES for (a) uranyl, (b) neptunyl and (c) plutonyl. All spectra are plotted on a shared relative energy axis by shifting each spectrum so that the energy position of the first predicted peak maxima falls at 0 eV. This corresponded to a shift of 531.7 eV for uranyl and neptunyl and 531.4 eV for plutonyl. Dashed lines indicate the position of the peak maxima on the energy scale. Individual core-excitations that contribute to the overall spectral profile are plotted as red transition sticks.

The number of transitions that contribute to O K-edge peaks is found to increase from uranyl to plutonyl. This was to be expected, since the unpaired electrons in neptunyl and plutonyl expands the possible electronic configuration space compared to uranyl, and this includes the possible number of CESs accessible from the GS. The high density of states, particularly in the third peaks and in general for plutonyl, renders ascribing the intensity of a peak to a single core-excitation difficult. The issue is made more complicated as for cases whereby peaks can be ascribed to a single intense excitation (peak 2 for $[UO_2]^{2+}$) the CESs themselves exhibit substantial multiconfigurational character, and obscures the relationship between peak intensity and the degree of oxygen 2p-character in a specific anti-bonding orbital. Despite the complexities, key intense core-excitations (transition sticks) can be identified and the natural populations of CES SONOs associated with these excitations are reported in table 4.6 along with the GS populations.

Table 4.4: Spin-orbit coupled O K-edge ground-states obtained from RASSI calculations.

System	$\lvert\Psi_{SO}\rangle$	Ω	Term Symbol
$[UO_2]^{2+}$	$1.0\,\lvert{}^1A_g\rangle$	0.0	${}^1\sum^+_{0g}$
$[NpO_2]^{2+}$	$0.45\,\lvert{}^2B_{2u}\rangle + 0.44\,\lvert{}^2B_{3u}\rangle + 0.06\,\lvert{}^2B_{1u}\rangle + 0.06\,\lvert{}^2A_u\rangle$	2.5	${}^2\Phi_{5/2u}$
$[PuO_2]^{2+}$	$0.48\,\lvert{}^3B_{2g}\rangle + 0.48\,\lvert{}^3B_{3g}\rangle + 0.04\,\lvert{}^1B_{1g}\rangle + 0.01\,\lvert{}^3A_g\rangle$	3.9	${}^3H_{4g}$

In the SO-GSs of each system, the expected $5f^0$, $5f^1$, and $5f^2$ GS configurations for uranyl, neptunyl and plutonyl, respectively, are consistent with natural populations reported in table 4.6. In the RASSI formalism, a SO state can be expressed as a linear combination of scalar-relativistic spin-free states. Examining the expansion of the SO-GSs in terms of the spin-free states gives insight into which electronic configurations are most important for describing the SO-state. For each of the systems, the spin-orbit ground-states $|\Psi_{SO}\rangle$ obtained from RASSI calculations are reported in table 4.4. The table also reports the molecular term symbol for the GS, the Ω quantum number, and the expansion of the $|\Psi_{SO}\rangle$ state in terms of a linear combination of spin-free RASSCF states. The Ω quantum number is the projection of the total angular momentum onto the axis of the molecule and is a good quantum number for linear diatomic molecules where the linear

Table 4.5: Key scalar relativistic spin-free RASSCF states that contribute to An $M_{4/5}$-edge SO-GSs reported in table 4.11 and the corresponding highest contributing electronic configuration.

System	State	Configuration
$[UO_2]^{2+}$	^1A_g	$5f^0_\delta 5f^0_\phi$
$[NpO_2]^{2+}$	$^2B_{2u}$,$^2B_{3u}$	$5f^0_\delta 5f^1_\phi$, $5f^0_\delta 5f^1_\phi$
	^2A_u,$^2B_{1u}$	$5f^1_\delta 5f^0_\phi$, $5f^1_\delta 5f^0_\phi$
$[PuO_2]^{2+}$	$^3B_{2g}$,$^3B_{3g}$	$5f^1_\delta 5f^1_\phi$, $5f^1_\delta 5f^1_\phi$
	^3A_g	$5f^0_\delta 5f^1_\phi(\pi^*_u)^1$
	$^1B_{1g}$	$5f^2_\delta 5f^0_\phi$

axis is well defined.

The SO-GS for each of the systems is consistent with findings reported by others.[13, 46] For each of these states, the electronic configurations that contribute most to the GS can be examined further, as shown in table 4.5, to gain greater insight into the electronic structure. For a single RASSCF state, there is a large number of possible electronic configurations that can contribute to the state. Therefore, only those configurations that have the largest contribution are examined. For uranyl, the SO-GS couples solely the spin-free singlet ^1A_g state with a calculated Ω of 0.0. As reported in table 4.5, this ^1A_g spin-free RASSCF state can be characterised as a completely closed shell $5f^0_\delta 5f^0_\phi$ electronic configuration with no electrons occupying the non-bonding orbitals. For the neptunyl SO-GS, the single unpaired electron gives rise to four possible arrangements of an electron in each of the non-bonding orbitals. The SO-GS obtained from the RASSI calculations reflects this in terms of the individual RASSCF states that are coupled, with each RASSCF state reflecting one of the possible arrangements. In neptunyl, the $5f^1$ state can give rise to either a $5f^1_\delta 5f^0_\phi$ configuration which splits under SOC to give a set of $^2\Delta_{3/2u}$ and $^2\Delta_{5/2u}$ SO states, or a $5f^0_\delta 5f^1_\phi$ configuration which splits to give a set of $^2\Phi_{5/2u}$ and $^2\Phi_{7/2u}$ SO states.[46] The calculated Ω of 2.5 points to either the $^2\Delta_{5/2u}$ or $^2\Phi_{5/2u}$

state being the predicted SO-GS. By examining the electronic configurations reported in table 4.5, the two main contributions come from $\left|^2B_{2u}\right\rangle$ and $\left|^2B_{3u}\right\rangle$, and reveals that the $5f_{\delta}^{0}5f_{\phi}^{1}$ configurations dominate the SO-GS. Therefore, considering both the Ω and dominant electronic configurations, the calculated SO-GS corresponds to a set of Kramers doublets with a $^2\Phi_{5/2u}$ molecular term symbol. This is in agreement with the GS reported by Matsika et al.[46] For $[PuO_2]^{2+}$, the SOC GS was captured by including the first root of each irrep in the sets of $^3(A_g, B_{1g}, B_{2g}, B_{3g})$ and $^1(A_g, B_{1g}, B_{2g}, B_{3g})$ to the RASSI calculations. The four highest contributing scalar relativistic RASSCF states to the SO-GS are reported in table 4.4. The $\left|^3B_{2g}\right\rangle$ and $\left|^3B_{3g}\right\rangle$ states are the main contributions, with electronic configurations corresponding to $5f_{\delta}^{1}5f_{\phi}^{1}$. These dominating configurations, alongside a calculated Ω value of approximately 4.0, points to a $^3H_{4g}$ SO-GS, consistent with previous findings.[46]

Having outlined the respective GSs for each system, attention turns to characterising the simulated peaks. Table 4.6 reports the natural populations for the CESs associated with the most intense transitions attributed to XANES peaks. Based on the natural populations, the assignment of peaks 1 to 3 for all three systems correspond to $1s \rightarrow \pi_u^*$, $1s \rightarrow \sigma_u^*$, and $1s \rightarrow \pi_g^*$ core-excitations, respectively. For all three systems, an increase in the multiconfigurational character of the CESs manifests as increased partial occupation of all RAS3 orbitals as the state energies increase from peaks 1 to 3. This is best seen by summing the RAS3 natural populations. For uranyl, summing RAS3 occupations yields values of 1.27, 1.57, and 1.8, for CESs associated with peaks 1-3, respectively. In each case, the population above 1.00 is accounted for by electron redistribution from RAS2 orbitals into RAS3 orbitals. The degree of RAS2-RAS3 electron redistribution is found to increase from uranyl to plutonyl, with the sum of RAS3 populations excluding the 2.00 unpaired 5f-electrons in plutonyl yielding values of 1.31, 1.82, and 1.91 for CESs associated with each peak, respectively. This redistribution of electrons in RAS(SD) states appears to be a principal driver in the recovery of static correlation. Furthermore, as the multiconfigurational character increases from low to higher energy states, energetic optimisation of the states favours the occupation of the lower energy $5f_{\delta/\phi}$ and π_u^* orbitals first, followed by the occupation of higher energy σ_u^* and π_g^* orbitals. For neptunyl and plutonyl, the emergence of a shoulder on the higher energy right-hand side of the first

Table 4.6: Total electron populations of the non-bonding $5f_{\delta/\phi}$ and anti-bonding valence SONOs for the SO-GS and key core-excited states associated with intense core-excitations attributed to peaks in O K-edge RAS(SD) simulated spectra presented in figure 4.3.

Simulation	Peak	$5f_{\delta/\phi}$	π_u^*	σ_u^*	π_g^*	σ_g^*
$[UO_2]^{2+}$ O K-edge	GS	0.00	0.08	0.05	0.04	0.01
	1	0.04	0.99	0.08	0.16	0.00
	2	0.64	0.16	0.68	0.08	0.01
	3	1.02	0.54	0.05	0.26	0.00
$[NpO_2]^{2+}$ O K-edge	GS	1.01	0.16	0.05	0.04	0.01
	1	1.48	0.62	0.08	0.10	0.02
	2	1.32	0.40	0.72	0.06	0.03
	3	1.63	0.79	0.24	0.24	0.01
$[PuO_2]^{2+}$ O K-edge	GS	1.98	0.14	0.05	0.04	0.01
	1	2.06	1.00	0.14	0.10	0.01
	2	2.58	0.82	0.37	0.04	0.01
	3	2.45	0.93	0.29	0.23	0.01

peak (between peaks 1 and 2) is observed. For the shoulder in question, the highest intensity transitions involve CESs with π_u^* occupancy associated with peak 1 and σ_u^* occupancy associated with peak 2, alongside the occupancy of the $5f_{\delta/\phi}$ orbitals. Overall, the peak assignments suggest an energetic ordering to the valence orbitals for the actinyls in agreement with the work of Denning as follows: $5f_{\delta/\phi} < \pi_u^* < \sigma_u^* < \pi_g^* < \sigma_g^*$.[1, 47]

The simulated spectra presented in fig. 4.3 were shifted to align the first peak for each system, enabling a comparison of the relative peak positions. The raw simulated peak positions before application of the shift are reported in table 4.7 for the interested reader. Examining the peaks in fig. 4.3, finds that moving from uranyl to plutonyl, peak 2 is drawn

Table 4.7: Predicted absolute peak energies for RAS(SD) O K-edge XANES simulations.

	Peak 1	Peak 2	Peak 3
$[UO_2]^{2+}$ O K-edge	531.7	535.7	537.1
$[NpO_2]^{2+}$ O K-edge	531.7	534.8	538.2
$[PuO_2]^{2+}$ O K-edge	531.4	534.5	539.4

closer in energy to the first peak, from a separation of 4.0 eV in uranyl to 3.1 eV in both neptunyl and plutonyl. From uranyl to plutonyl, peak 3 is found to separate further from the first, increasing from 5.4 eV in uranyl up to 8.0 eV in plutonyl. Examining the absolute predicted energy positions of peak 1 in table 4.7 reveals a similar ∼531 eV position for the peak in all three systems, and suggests a similar orbital energy position of the π_u^* orbitals across the systems. Assuming this to be the case, the separations between peak 1 and 2, and between 1 and 3, represent the degree to which the σ_u^* and π_g^* orbitals are destabilized relative to the π_u^* orbitals. The increase in separation between peak 1 and 3 from uranyl to plutonyl indicates a destabilisation of the π_g^* orbitals across the systems, which coincides with a stabilisation of the π_g orbitals. This combination of orbital energy changes suggest a stronger π-bonding interaction from uranyl to plutonyl. The reduced separation between peaks 1 and 2 indicates a stabilisation of the σ_u^* orbital from uranyl to plutonyl. Here a stabilisation of the σ_u^* orbital does not necessarily indicate a destabilisation of the σ_u orbitals when considering the influence of the 'pushing from below' (PFB) mechanism. In the PBF mechanism, a filled-filled interaction leads to the destabilisation of both the σ_u and σ_u^* orbitals, and the strengthening of the axial covalency. This interaction has been measured experimentally in An $M_{4/5}$-edge XANES by examining differences between peaks attributed to the $5f_{\delta/\phi}$ and σ_u^* orbitals.[2] Vitova et al.[2] reported a reduction in peak separations and associated this with a reduction in axial covalency from uranyl to plutonyl. Likewise, the same peak separation principal can be applied here for the O K-edge, where a reduction in peak separations is also found from uranyl to plutonyl, and would indicate a reduction in axial covalency across the series. Some caution is required in relating this to GS covalency, since Autschbach and co-workers have demonstrated that the covalency from uranyl to plutonyl increases in the GS, and the reduced axial covalency

only manifests as a weakening σ-interaction in the CESs.[5]

4.3.2 $[AnO_2]^{2+}$ An $M_{4/5}$-edge XANES

4.3.2.1 Spectra

Figure 4.4 presents the RAS(SD) An $M_{4/5}$-edge XANES spectra for uranyl, neptunyl and plutonyl, shifted by 21.9, 21.7 and 26.1 eV, respectively, to align the first simulated peak with experimental positions. The magnitude of these shifts is consistent with two previous studies.[5, 14] Autschbach and co-workers have shown that these shifts can be reduced by moving from a bare-actinyl model to one which includes equatorial water ligands, to better represent the aqueous conditions of the experimental set-up.[5] This was shown for plutonyl, with a $[PuO_2(H_2O)_5]^{2+}$ model reducing the shift required from 27.2 eV to 10.5 eV. In the end, Autschbach and co-workers continued simulations using bare-actinyls since inclusion of the ligands requires a reduction in the operating symmetry from D_{2h} to C_1, which increases the computational cost with no major improvement in spectral profile or peak separations compared to bare-actinyl models. In the An M-edge XANES case, spin-orbit coupling is much more pronounced for the actinide-3d orbitals than it is for oxygen-1s, and therefore the correct position of the M_4- and M_5-edge spectra is highly reliant on the combined ability of RASSCF and RASSI calculations to predict the correct energy positions. An additional source of error comes from the reduced active-spaces for An $M_{4/5}$-edge XANES simulations, since the g-parity valence orbitals are not a requirement for generating XANES peaks and are therefore omitted to reduce computational cost. These orbitals are included in O K-edge simulations. One crucial difference between O K-edge and An M-edge XANES is the appearance of a strong intensity peak in the latter, which is attributed to a core-excitation into the non-bonding $5f_{\delta/\phi}$ orbitals, and is a dominant feature in the spectrum. The choice to place non-bonding $5f_{\delta/\phi}$ orbitals in RAS3 as opposed to RAS2 will impact the quality of correlation captured for interactions associated with the non-bonding 5f electrons, and by extension will impact the energy predictions for processes involving these orbitals.

The simulated U M_4- and Np/Pu M_5-edge spectral profiles in figure 4.4 are in good qualitative agreement with the experimental profiles reported by Vitova et al.[2] RASSI calculations provide both the M_4- and M_5-edges in a single calculation, predicting spin-

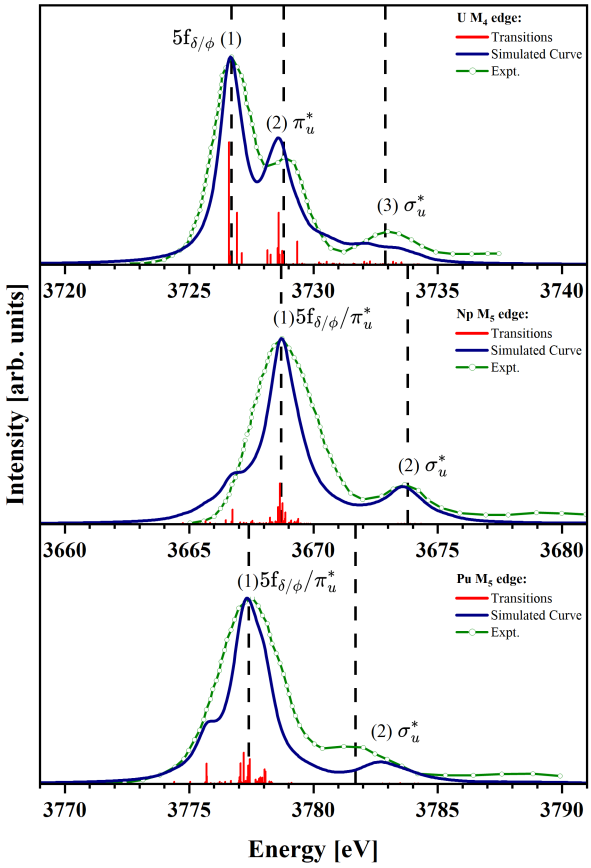

Figure 4.4: The RAS(SD) simulated (top) U M_4-edge of uranyl, (middle) Np M_5-edge of neptunyl and (bottom) Pu M_5-edge of plutonyl. All simulated spectra are shifted to align the energy position of the first predicted peak with the first experimental peak position reported by Vitova et al.[2] This corresponds to a shift of (top) 21.9 eV, (middle) 21.7 eV and (bottom) 26.1 eV for each spectrum. Individual core-excitations that contribute to the overall spectral profile are plotted as red transition sticks. Green dotted line is the digitized experimental XANES spectrum taken with permission from Vitova, T., Pidchenko, I., Fellhauer, D. et al. *Nat Commun*, **8**, 16053 (2017)., Ref [2], under the Creative Commons Attribution 4.0 International License. Dashed lines indicate the reported experimental peak positions.

orbit splittings of 172, 179 and 188 eV for uranyl, neptunyl and plutonyl, respectively. These values are consistent with values of 176, 185, and 195 eV reported experimentally for the splitting of core 3d orbitals in pure U, Np and Pu elements, respectively.[3, 4] Focus

Table 4.8: RAS(SD) An $M_{4/5}$-edge peak positions (eV) for peaks in figure 4.4. Peak positions correspond to those after the application of an energy shift of 21.9, 21.7, and 26.1 eV for uranyl, neptunyl and plutonyl simulated spectra, respectively. The discrepancy Δ with respect to the experimental peak positions is also given.[2]

	Peak 1	Δ	Peak 2	Δ	Peak 3	Δ
U M_4-edge Expt.	3726.7		3728.8		3732.9	
U M_4-edge Sim.	3726.7	+0.0	3728.6	-0.2	3732.2/3733.4	-0.7/+0.5
Np M_5-edge Expt.	3668.7		3673.8		-	-
Np M_5-edge Sim.	3668.7	+0.0	3673.6	-0.2	-	-
Pu M_5-edge Expt.	3777.4		3781.7		-	-
Pu M_5-edge Sim.	3777.4	+0.0	3782.7	+1.0	-	-

in this chapter is restricted to those edges for which Vitova et al. reported experimental XANES data.[2]

The experimental M_4-edge of uranyl consists of three peaks with decreasing relative intensity from peaks 1 to 3, which is replicated by the RAS(SD) simulations. The shifted peaks are in strong agreement with experimental positions as can be seen visually in fig. 4.4 and quantitatively in table 4.8, aligning with experiment to within 1 eV. The relative energy separation between the peaks, reported in table 4.9, is found to be in excellent agreement with experiment, with values also within 1 eV. The separation between peaks 1 and 2 (P_{21}) of ∼2 eV is in good agreement with the two prior U M_4-edge uranyl studies which report similar values when using RASSCF methods.[5, 14] However, the simulations performed in this work grant an improved prediction over the prior studies for the relative separation between peaks 1 and peak 3 (P_{31}) which can be related to the energy separation of the σ_u^* orbital from the non-bonding $5f_{\delta,\phi}$ orbitals. This is considered a key property of interest for determining the axial covalency of actinyl systems and therefore an important feature for simulations to replicate.[2] For peak 3 in the RAS(SD) U M_4-edge presented in fig. 4.4, there is two potential local maxima, and therefore both are reported in table

Table 4.9: RAS(SD) An $M_{4/5}$-edge relative peak separations (eV) between peaks in figure 4.4 and the discrepancy Δ with respect to the experimentally measured peak separations. Note that the P_{31} result of 6.1 eV for uranyl is obtained as follows: $3726.7 - \frac{3732.2+3733.4}{2}$ and represents the difference between the position of peak 1 and the average of two measurements made for peak 2.

	P_{21}	Δ	P_{32}	Δ	P_{31}	Δ
U M_4-edge Expt.	2.1		4.1		6.2	
U M_4-edge Sim.	1.9	-0.2	3.6	-0.5	6.1[a]	-0.1
Np M_5-edge Expt.	5.1		-	-	-	-
Np M_5-edge Sim.	4.9	-0.2	-	-	-	-
Pu M_5-edge Expt.	4.3		-	-	-	-
Pu M_5-edge Sim.	5.3	+1.0	-	-	-	-

4.8. The actual predicted P_{31} relative energy separation therefore falls within the interval $[5.5, 6.7]$ with an average of 6.1 reported in table 4.9. The P_{31} reported in this work improves on the predictions of prior studies which report separations in excess of 7 eV compared to the experimental value of 6.2 eV.[5, 14]

The M_5-edge simulations for neptunyl and plutonyl reflect the spectral profiles found in experiment, presenting a two peak structure with decreasing intensity from peak 1 to 2. Under the broadening scheme utilized, a small shoulder is found both at ∼3667 eV and ∼3776 eV on the low energy side of the first peak in neptunyl and plutonyl spectra, respectively. The relative peak separation was well predicted for neptunyl, but was inaccurate for plutonyl, predicting a P_{21} separation of 5.3 eV compared with 4.3 eV from experiment ($\Delta = 1.0$ eV). The same predicted separation for bare-plutonyl was reported by Autschbach and co-workers,[5] and could indicate that the current active-spaces used in this current study and the work of Autschbach are not sufficiently flexible to capture enough of the correlation effects in plutonyl.

4.3.2.2 Assignments

Peak assignments were performed using the same process outlined in greater detail within chapter 3 (section 3.3.1.2). The SO-GSs are identified by examining the natural populations of the SONOs reported in table 4.10 for each system. Consistent with the SO-GSs from the O K-edge simulations, the population of the non-bonding $5f_{\delta/\phi}$ orbitals are consistent with the expected $5f^0$, $5f^1$, and $5f^2$ states for uranyl to plutonyl, and are given the same $^1\sum^+_{0g}$, $^2\Phi_{5/2u}$, $^3H_{4g}$ molecular term symbols, respectively. These are reported in table 4.11. Each SO-GS reported in table 4.11 can be expanded further as a linear combination of scalar relativistic RASSCF states, which correspond to the same electronic configurations detailed previously in table 4.5 for O K-edge SO-GSs.

Table 4.10: Total electron populations of the non-bonding $5f_{\delta/\phi}$ and anti-bonding valence SONOs for the SO-GS and key core-excited states associated with intense core-excitations attributed to peaks in the An $M_{4/5}$-edge RAS(SD) simulated spectra presented in figure 4.4.

Simulation	Peak	$5f_{\delta/\phi}$	π^*_u	σ^*_u
$[UO_2]^{2+}$ U M_4-edge	GS	0.02	0.08	0.04
	1	1.00	0.04	0.01
	2	0.82	0.65	0.02
	3	1.11	0.74	0.10
$[NpO_2]^{2+}$ Np M_5-edge	GS	1.02	0.10	0.04
	1	1.94	0.42	0.02
	2	1.79	1.01	0.12
$[PuO_2]^{2+}$ Pu M_5-edge	GS	1.99	0.14	0.05
	1	2.45	0.69	0.02
	2	2.84	1.06	0.06

Table 4.11: Spin-orbit coupled An $M_{4/5}$-edge ground-states obtained from RASSI calculations. Table includes the Ω quantum number and the linear combination of the largest contributing spin-free states that constitute the SO GS configuration.

System	$\|\Psi_{SO}\rangle$	Ω	Term Symbol
$[UO_2]^{2+}$	$1.0\left\|^1A_g\right\rangle$	0.0	$^1\sum^+_{0g}$
$[NpO_2]^{2+}$	$0.46\left\|^2B_{2u}\right\rangle + 0.45\left\|^2B_{3u}\right\rangle + 0.05\left\|^2B_{1u}\right\rangle + 0.04\left\|^2A_u\right\rangle$	2.5	$^2\Phi_{5/2u}$
$[PuO_2]^{2+}$	$0.48\left\|^3B_{2g}\right\rangle + 0.48\left\|^3B_{3g}\right\rangle + 0.04\left\|^1B_{1g}\right\rangle + 0.01\left\|^3A_g\right\rangle$	3.9	$^3H_{4g}$

In the experimental work of Vitova et al.,[2] the U M_4-edge spectrum of uranyl comprised three peaks assigned to core-excitations from actinide 3d orbitals into the $5f_{\delta/\phi}$, π^*_u, and σ^*_u orbitals, respectively. The experimental Np/Pu M_5-edge spectra of neptunyl and plutonyl are comprised of two peaks, with the first corresponding to a core-excitation into both the $5f_{\delta/\phi}$ and π^*_u orbitals, while the second corresponds to a core-excitation into the σ^*_u orbital. For the simulated U M_4-edge and Np/Pu M_5-edge XANES spectra, the most intense excitations were identified along with the associated CESs. The natural populations of the anti-bonding and non-bonding $5f_{\delta/\phi}$ SONOs in the CESs are reported in table 4.10, along with the GS SONO populations. Both peaks 1 and 2 in the uranyl U M_4-edge spectrum comprise a number of transitions, with transitions associated with peak 1 involving CESs with clear non-bonding $5f_{\delta/\phi}$ occupancy, while transitions associated with peak 2 involve CESs with clear π^*_u orbital occupancy. Peak 3 has a much greater density of weak intensity transitions involving CESs with substantial multiconfigurational character but present a consistent σ^*_u occupancy above the population level observed for other CESs. The simulated Np/Pu M_5-edge spectrum consists of two peaks comprising a multitude of transitions, with those associated with peak 1 involving CESs with $5f_{\delta/\phi}$ and π^*_u occupancy. Peak 2 in both systems can be attributed to core-excitations into the σ^*_u orbitals. A low energy shoulder on the first peak at ∼3667 eV and ∼3776 eV is identified in neptunyl and plutonyl M_5-edge simulations, respectively. These shoulders correspond predominantly to core-excitations into the non-bonding 5f-orbitals. For neptunyl the CES contains a natural population for $5f_{\delta/\phi}$ and π^*_u orbitals of 1.86 and 0.22, respectively, and

similarly in plutonyl, populations of 2.67 and 0.42, respectively.

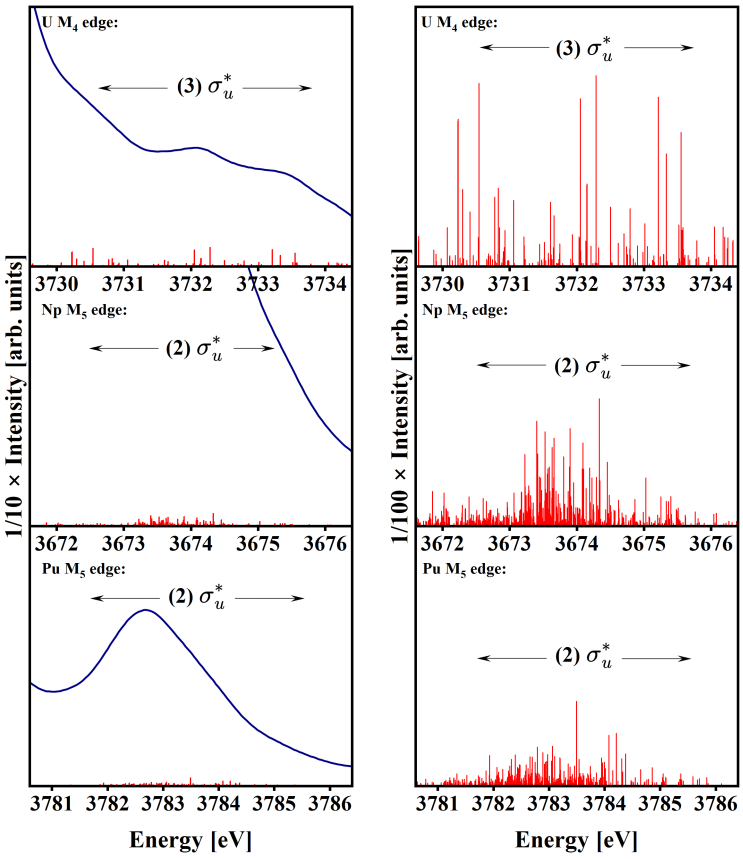

Figure 4.5: Two panels presenting the RAS(SD) simulated (top) U M_4-edge of uranyl, (middle) Np M_5-edge of neptunyl and (bottom) Pu M_5-edge of plutonyl. In both panels, the energy scale is adjusted to only capture part of the final peak in each spectrum characterised by a $1s \rightarrow \sigma_u^*$ excitation. The panels show the same final peak region but at two different intensity magnifications to show the underlying transitions that contribute to the peak. All spectra were taken from fig. 4.4 and share the same shift with respect to the experiment.

In all three actinyls, the final peak (σ^*-satellite) is uniquely generated by a large number of low intensity transitions which are not clearly visible at the scale of the whole spectrum, but can be viewed by magnification in fig. 4.5. The accumulation of broadening each of the low intensity transitions combines to generate the overall peak structure seen at the scale shown in fig. 4.4. Weak transitions associated with the final peak in uranyl U

M_4-edge XANES simulations was also identified by Polly et al.[14]. In the study by Polly et al., a minimal active space consisting of 3d core-orbitals and the empty valence orbitals of uranyl presented relatively strong transitions for the final peak compared to an active space which incorporated the π_u and σ_u bonding orbitals. In the latter calculation, the strength of transitions decreased with the greater active-space flexibility. In the current study discussed in this chapter, strong transitions with CESs containing high σ_u^* occupancy were observed for all three actinyls when simulations were performed at the RAS(S) level. In these calculations, constraints mean that the bonding orbitals remain fully occupied. Simulations performed at the RAS(SD) level of theory presented in fig. 4.4 relax the active-space constraints, leading to CESs associated with the final peak with significant multiconfigurational character arising from substantial electron redistribution from RAS2 bonding orbitals into RAS3 orbitals. The redistributed electrons populate the lower energy $5f_{\delta/\phi}$ and π_u^* first as a means to stabilise the states, and this results in limited σ_u^* population compared to RAS(S) level simulations.

Overall, the peaks comprising the RAS(SD) simulated XANES spectra in fig. 4.4 are assigned to the same core-excitations as those proposed by Vitova et al.[2] As found for O K-edge, the density of transitions, number of accessible CESs, and the degree of multiconfigurational character, all increase when moving from low to high energy XANES peaks in all three actinyl systems. Given that this is a consistent feature of simulations considered in this chapter, it indicates the possibility of this being a feature of RASSCF XANES simulations when the active-space and constraints are sufficiently large and flexible.

4.3.3 Covalency Analysis

To assess the validity of XANES as a GS covalency probe, a number of analysis approaches were used to investigate the changes in covalency between the ground- and core-excited states. In chapter 3, QTAIM analysis was found to give useful insight into the overall changes in electronic structure between the GS and CESs due to core-excitation. QTAIM analysis pointed to a decrease in U-O covalency upon core-excitation, with electrons shared in U-O bonding interactions in the GS localising onto the three atomic centres in the CES. Orbital composition analysis of the GS and CES SONOs found ∼10% lower uranium

contributions to the bonding orbitals in the CESs compared to the GS when simulating O K-edge with a $[UO_2]^{2+}$ model. This underestimation of U% contribution to bonding orbitals was found to persist when using models that better represent the local $Cs_2UO_2Cl_4$ crystal environment, but reduced in value to ∼7%. In this chapter, $[AnO_2]^{2+}$ models are purposely used to ensure that both O K-edge and An $M_{4/5}$-edge states can be compared without influence of additional ligands. The validity of this approach is confirmed in chapter 3: for instance, while the presence of equatorial ligands do change the magnitude of the orbital composition and QTAIM changes between GS and CESs, the overall pattern of trends remains similar between $[AnO_2]^{2+}$ models and others considered. The main conclusion from chapter 3, being that there is a decrease in uranium contributions to bonding orbitals in all cases. These compositional changes can be explained with reference to the QTAIM results, with charge density in the bonding orbitals drawn toward the oxygen centres due to a greater effective nuclear charge upon creation of the ligand core-hole. This is reinforced by repulsion of charge density away from the actinide centre due to the increased electron localisation on uranium through the occupation of RAS3 orbitals with predominantly uranium character. Overall, results from chapter 3 suggest that the extraction of orbital mixing from O K-edge XANES peaks would lead to an underestimation of the uranium contribution to bonding interactions in uranyl. Similar analysis is implemented in this chapter for both the O K-edge and An $M_{4/5}$-edge states for all three actinyl systems, enabling a comprehensive assessment of the validity of XANES as a probe of GS actinyl covalency.

4.3.3.1 QTAIM Analysis

The O K-edge and An $M_{4/5}$ M-edge ground-state QTAIM metrics are reported in table 4.12 for each actinyl system. The ground-states associated with O K-edge and An M-edge simulations differ in their QTAIM metrics since bond lengths differ due to being informed by $Cs_2AnO_2Cl_4$ crystals in the former and $[AnO_2(H_2O)_5]^{2+}$ complexes in the latter simulations. The biggest differences between the two sets of GS come from the delocalisation index values (δ-values), particularly for neptunyl, while ρ_{BCP} values on the whole are largely comparable between the two sets, ranging 0.30 - 0.34 a.u.

Table 4.12: GS and CES QTAIM metrics for different actinyl systems. Table reports the electron density at the bond critical point ρ_{BCP} in atomic units, delocalisation index δ(An, O), as well as actinide and oxygen localisation indexes λ(An) and λ(O). Analysis is performed on RAS(SD) electron densities.

Simulation	Excitation	ρ_{BCP}	δ(An, O)	λ(An)	λ(O)
$[UO_2]^{2+}$ O K-edge	GS	0.33	1.85	86.85	7.70
	$1s \rightarrow \pi_u^*$	0.31	1.30	87.56	7.90
	$1s \rightarrow \sigma_u^*$	0.32	1.23	87.68	7.91
	$1s \rightarrow \pi_g^*$	0.29	1.17	87.83	7.91
$[NpO_2]^{2+}$ O K-edge	GS	0.30	1.73	87.95	7.77
	$1s \rightarrow \pi_u^*$	0.28	1.26	88.55	7.94
	$1s \rightarrow \sigma_u^*$	0.29	1.14	88.72	7.98
	$1s \rightarrow \pi_g^*$	0.27	1.00	88.9	8.03
$[PuO_2]^{2+}$ O K-edge	GS	0.31	1.80	89.04	7.64
	$1s \rightarrow \pi_u^*$	0.29	1.20	89.67	7.94
	$1s \rightarrow \sigma_u^*$	0.29	1.04	89.91	7.99
	$1s \rightarrow \pi_g^*$	0.28	0.98	89.90	8.06
$[UO_2]^{2+}$ U M_4-edge	GS	0.33	1.85	86.67	7.78
	$3d \rightarrow 5f_{\delta/\phi}$	0.34	2.03	86.79	7.51
	$3d \rightarrow \pi_u^*$	0.32	1.65	87.05	7.77
	$3d \rightarrow \sigma_u^*$	0.32	1.48	87.28	7.85
$[NpO_2]^{2+}$ Np M_5-edge	GS	0.34	1.86	87.83	7.69

Continued on next page

Table 4.12: (continued)

Simulation	Excitation	ρ_{BCP}	δ(An, O)	λ(An)	λ(O)
	$3d \rightarrow 5f_{\delta/\phi}/\pi_u^*$	0.34	1.72	88.21	7.61
	$3d \rightarrow \sigma_u^*$	0.33	1.44	88.37	7.85
$[PuO_2]^{2+}$ Pu M_5-edge	GS	0.34	1.85	88.97	7.63
	$3d \rightarrow 5f_{\delta/\phi}/\pi_u^*$	0.35	1.72	89.34	7.55
	$3d \rightarrow \sigma_u^*$	0.33	1.46	89.42	7.78

No direct correlation between either ρ_{BCP} or δ-values with bond lengths can be established, but QTAIM values nonetheless point to some discernible differences in covalency between systems. For instance, in the set of O K-edge GSs, the ρ_{BCP} value of 0.33 is slightly larger than those of 0.30 and 0.31 in neptunyl and plutonyl, suggesting greater overlap driven covalency in the former. The δ-values also mirror this finding, but cannot be specifically identified as originating from either overlap driven or energy degeneracy driven covalency. Both ρ_{BCP} and δ-values for the set of An M-edge GSs are comparable between each system and do not point to a clear covalency trend. Given that O K-edge active-spaces include all the key bonding and anti-bonding orbitals, they are expected to yield higher quality ground-states and thus QTAIM metrics that better represent the covalency trends of the actinyls. The similar magnitude of the QTAIM metrics between the O K-edge and An M-edge GSs is an encouraging sign that the smaller active-space used in the latter is still sufficient to capture the majority of the bonding interactions, but it is ultimately impossible to decouple the QTAIM findings between the two sets of GSs due to the use of different bond lengths.

Upon core-excitation from either O 1s or An 3d orbitals, the ρ_{BCP} values do not differ substantially between the GS and resulting CESs. ρ_{BCP} values differ no more than 0.04 a.u. between O K-edge GSs and CESs for any of the three systems, and no more than 0.01 for An $M_{4/5}$-edge states. The limited change in ρ_{BCP} between the GS and CESs suggests that the electron density accumulation along the bonding axis is not significantly

Table 4.13: Changes in delocalisation index $\Delta\delta$(An, O) and changes in actinide and oxygen localisation indexes $\Delta\lambda$(An) and $\Delta\lambda$(O), between the GS and CESs in different actinyl simulations. Analysis is performed on RAS(SD) electron densities.

Simulation	Excitation	$\Delta\delta$(An, O)	$\Delta\lambda$(An)	$\Delta\lambda$(O)
$[UO_2]^{2+}$ O K-edge	$1s \rightarrow \pi_u^*$	-0.55	+0.71	+0.20
	$1s \rightarrow \sigma_u^*$	-0.62	+0.83	+0.22
	$1s \rightarrow \pi_g^*$	-0.68	+0.99	+0.21
$[NpO_2]^{2+}$ O K-edge	$1s \rightarrow \pi_u^*$	-0.47	+0.60	+0.17
	$1s \rightarrow \sigma_u^*$	-0.58	+0.77	+0.21
	$1s \rightarrow \pi_g^*$	-0.72	+0.96	+0.26
$[PuO_2]^{2+}$ O K-edge	$1s \rightarrow \pi_u^*$	-0.60	+0.63	+0.29
	$1s \rightarrow \sigma_u^*$	-0.76	+0.88	+0.35
	$1s \rightarrow \pi_g^*$	-0.82	+0.86	+0.42
$[UO_2]^{2+}$ U M_4-edge	$3d \rightarrow 5f_{\delta/\phi}$	+0.18	+0.12	-0.27
	$3d \rightarrow \pi_u^*$	-0.19	+0.37	-0.01
	$3d \rightarrow \sigma_u^*$	-0.37	+0.61	+0.07
$[NpO_2]^{2+}$ Np M_5-edge	$3d \rightarrow 5f_{\delta/\phi}/\pi_u^*$	-0.14	+0.38	-0.08
	$3d \rightarrow \sigma_u^*$	-0.42	+0.54	+0.16
$[PuO_2]^{2+}$ Pu M_5-edge	$3d \rightarrow 5f_{\delta/\phi}/\pi_u^*$	-0.13	+0.37	-0.08
	$3d \rightarrow \sigma_u^*$	-0.38	+0.45	+0.15

affected by core-excitation. This result is unsurprising given that core-excitations do not involve substantial depletion of electrons from bonding orbitals, in contrast with valence excitations.

Changes in δ(An, O), λ(An), and λ(O) metrics between the GS and CESs associated

with intense transition in the RAS(SD) simulated O K-edge and An $M_{4/5}$-edge spectra are reported in table 4.13. In both K- and M-edge simulations, δ(An, O) values decrease from the GS to the CESs, with the notable exception of the 3d $\rightarrow$ $5f_{\delta/\phi}$ transition associated with peak 1 in the uranyl U M_4-edge spectrum which is discussed separately. A reduction in δ(An, O) values is expected in CESs regardless of the edge simulated since occupation of anti-bonding orbitals reduces the systems bond order. In O K-edge simulations, a decrease in δ(An, O) values within the CESs (table 4.13), coincides with an increase in λ-values across all three atomic centres. This indicates a decrease in the number of electrons shared within bonding interactions upon core-excitations, and the redistribution of these electrons onto each atomic centre. The share of electron localisation onto the actinide centre is greater than that of oxygen centres in the CESs. However, from uranyl to plutonyl, the share of electrons localising onto oxygen centres increases, with values of λ(O) ranging 0.20 - 0.22 for uranyl CESs to 0.29 - 0.42 in plutonyl CESs. This result can be explained by greater Coulomb repulsion between the excited electrons in anti-bonding orbitals and the $5f_{\delta/\phi}$ electrons that already reside in the RAS3 space of neptunyl ($5f^1_{\delta/\phi}$) and plutonyl ($5f^2_{\delta/\phi}$). In An M-edge simulations, the decrease in δ(An, O) values from the GS to CESs coincides primarily with an increase in λ(An) values (table 4.13). In uranyl, 3d $\rightarrow$ π^*_u and 3d $\rightarrow$ σ^*_u CESs present a limited change of -0.01 and +0.07 in λ(O), respectively. Similarly for 3d $\rightarrow$ $5f_{\delta/\phi}/\pi^*_u$ CESs in neptunyl and plutonyl, a limited -0.08 change in λ(O) occurs, while more substantive changes of +0.16 and +0.15 occur in λ(O) values for the 3d $\rightarrow$ σ^*_u CESs, respectively. These increases in λ(O) values are also attributed to Coulombic repulsion effects between excited electrons in anti-bonding orbitals and $5f_{\delta/\phi}$ electrons. The 'anomalous' result of a +0.18 increase in δ(An, O) within the 3d $\rightarrow$ $5f_{\delta/\phi}$ CES in uranyl coincides with a relatively small +0.12 increase in λ(An), but a more substantial -0.27 decrease in λ(O). Since the core-excitation in this instance involves occupying the non-bonding $5f_{\delta/\phi}$ orbitals rather than the anti-bonding orbitals, a reduction in δ(An, O) due to a change in the uranyl bond order is not necessarily expected. Additionally, the occupation of the actinide non-bonding $5f_{\delta/\phi}$ orbitals by the excited 3d core electron does not completely shield the core-hole, thus the effective nuclear charge of the actinide is greater overall. This promotes the donation of charge density from oxygen centres toward uranium through U-O bonding interactions, and accounts for the observed

QTAIM findings.

The QTAIM results in table 4.13 can largely be explained by the location of the core-hole which increases the effective nuclear charge of the centre it resides within and encourages charge density localisation onto that centre. This accounts for the high localisation of charge density onto oxygen centres in all O K-edge CESs and high actinide localisation in An M-edge CESs. Two additional effects influence charge localisation in the CESs regardless of the edge simulated, these being Coulombic repulsion of electrons in anti-bonding orbitals with $5f_{\delta/\phi}$ electrons and the redistribution of electrons into orbitals of predominately metal character. The former effect increases electron localisation on oxygen centres, while the latter increases electron localisation onto the actinide centre. The former effect accounts for higher λ(O) values for the 3d $\rightarrow \sigma_u^*$ CESs in neptunyl and plutonyl. The latter effect explains why CESs with the greatest multiconfigurational character exhibit the largest λ(An) values, since these states have the greatest electron re-distribution from bonding orbitals of predominantly ligand character into anti-bonding orbitals of predominately actinide character as well as into non-bonding actinide 5f orbitals; driving charge density away from ligands to the actinide centre. In O K-edge and An $M_{4/5}$-edge simulations, these highly multiconfigurational states specifically correspond to the 1s $\rightarrow \pi_g^*$ and 3d $\rightarrow \sigma_u^*$ CESs, respectively. These states also exhibit the greatest decrease in δ(An, O) values since electrons are distributed into anti-bonding orbitals and removed from bonding orbitals, both effects acting to reduce the system bond order.

4.3.3.2 Density Differences

A visual representation of the changes in electronic structure between the GS and CESs can be encompassed in electron density differences plots. In these plots, the difference between the GS and CES RAS(SD) electron densities, CES (ρ_{CES}) and GS (ρ_{GS}), is taken as follows:

$$\Delta\rho(\mathbf{r}) = \rho_{\mathrm{CES}}(\mathbf{r}) - \rho_{\mathrm{GS}}(\mathbf{r}) \tag{4.1}$$

The CES (ρ_{CES}) and GS (ρ_{GS}) electron densities are constructed from the SONOs obtained from RASSI calculations. The resulting density differences $\Delta\rho(\mathbf{r})$ associated with each CES and the GS are presented as contour plots by taking a slice in the XZ-plane of the

actinyl $\Delta\rho(\mathbf{r})$. The dotted blue regions correspond a depletion of electron density, while red lined regions correspond to a build-up of electron density, upon core-excitation. This can also be pictured as the redistribution of electron density from blue regions to red regions due to core-excitation.

The differences in electron density between the GS and three main CESs for $[UO_2]^{2+}$ are plotted in fig. 4.6. This enables visual inspection of the changes to electronic structure due to core-excitation reported in section 3.3.3.1 to be examined. The three density

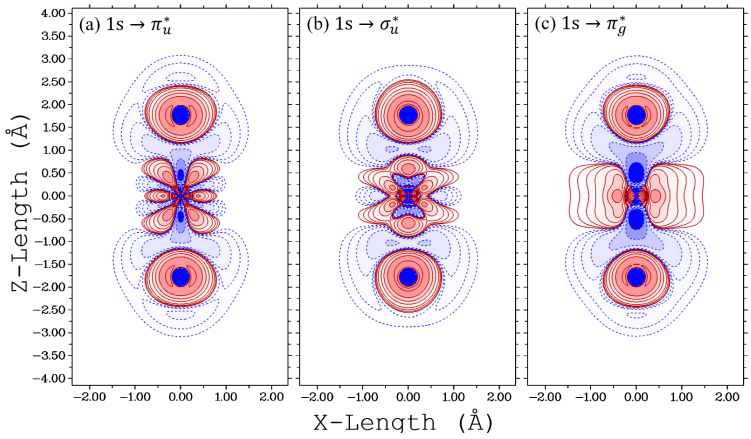

Figure 4.6: Contour plots representing the differences between the (a) 1s $\rightarrow \pi_u^*$, (b) 1s $\rightarrow \sigma_u^*$, and (c) 1s $\rightarrow \pi_g^*$ core-excited state electron densities and the ground-state electron density, $\rho_{\mathrm{CES}}(\mathbf{r}) - \rho_{\mathrm{GS}}(\mathbf{r})$, from RAS(SD) $[UO_2]^{2+}$ simulations. Contour plots were obtained by taking an XZ-slice through the molecule. Red regions indicate areas of electron accumulation, while blue regions indicate electron depletion.

difference plots in fig. 4.6 correspond to the three key core-excitations, namely (a) 1s $\rightarrow \pi_u^*$, (b) 1s $\rightarrow \sigma_u^*$, and (c) 1s $\rightarrow \pi_g^*$. For all three core-excitations, the plots show a depletion of electron density from bonding regions and a reduced electron density surrounding the oxygen centres. Electron density is redistributed towards and highly localised upon the three atomic centres. This aligns with measured QTAIM metrics for the CESs and qualitatively summarises the key findings: higher λ(O) and λ(U) values, and lower ρ_{BCP} and δ(U, O) values in the CES compared with the GS.

Density differences have also been obtained for states in neptunyl and plutonyl RAS(SD) O K-edge simulations and are presented in fig. 4.7. The panels present the changes in electron density for the key core-excitations in (a)-(c) neptunyl and (d) -(f)

plutonyl. In both systems, the density difference plots indicate a reduction in electron density within the An-O bonding region (indicated by dotted blue contours) and a highly localised increase in electron density on each of the three atomic centres. These changes align with the reported decrease in δ(An, O) and increase in both λ(An) and λ(O) values obtained from QTAIM analysis. The density plots presented here for neptunyl and plutonyl also reflect similar changes observed for the states involved in uranyl core-excitations, presented in fig. 4.6.

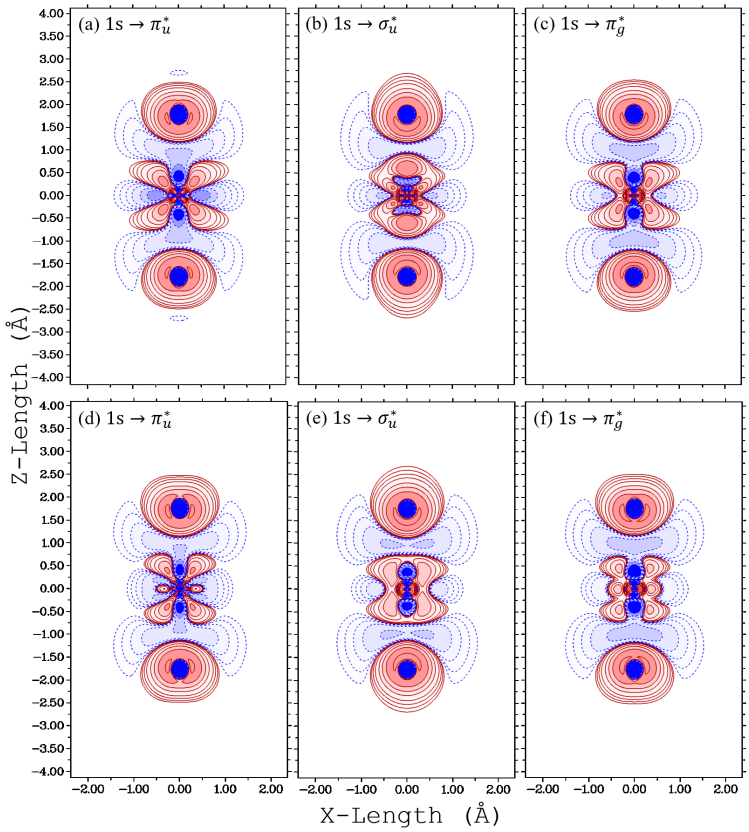

Figure 4.7: Contour plots representing the differences between the (a, d) 1s → π_u^*, (b, e) 1s → σ_u^*, and (c, f) 1s → π_g^* core-excited state electron densities and the ground-state electron density, $\rho_{\mathrm{CES}}(\mathbf{r}) - \rho_{\mathrm{GS}}(\mathbf{r})$, from RAS(SD) (top, a, b, c) $[NpO_2]^{2+}$ and (bottom, d, e, f) $[PuO_2]^{2+}$ simulations. Contour plots were obtained by taking an XZ-slice through the molecule. Red regions indicate areas of electron accumulation, while blue regions indicate electron depletion.

From uranyl to plutonyl, the degree to which electron density is drawn from the

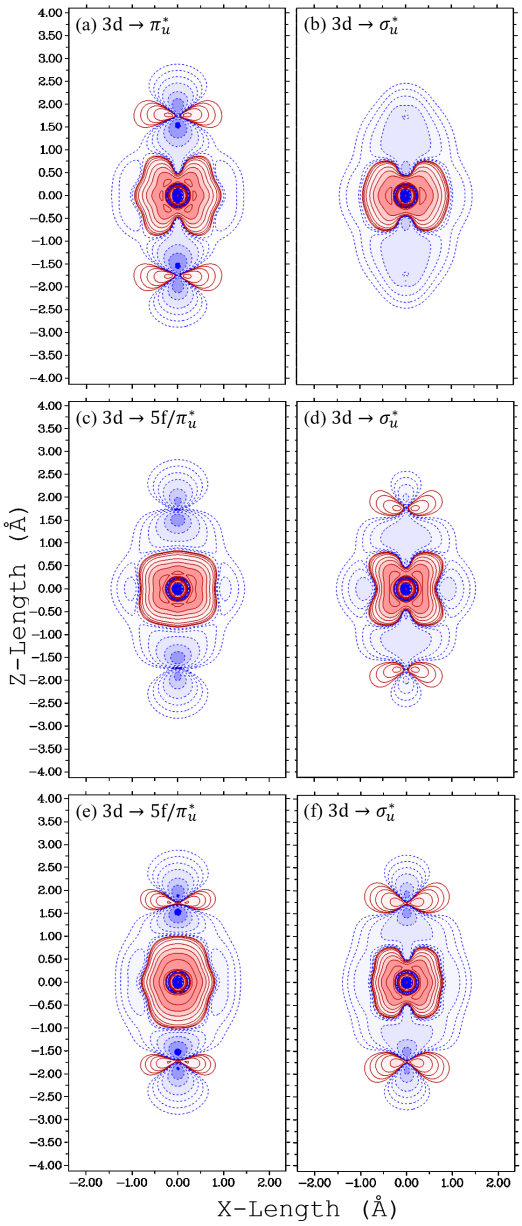

Figure 4.8: Contour plots representing the differences between the (a) 3d $\rightarrow \pi_u^*$, (c, e) 3d $\rightarrow$ 5f/π_u^*, and (b, d, f) 3d $\rightarrow \sigma_u^*$ core-excited state electron densities and the ground-state electron density, $\rho_{\mathrm{CES}}(\mathbf{r}) - \rho_{\mathrm{GS}}(\mathbf{r})$, from RAS(SD) (top, a, b) $[UO_2]^{2+}$, (middle, c, d) $[NpO_2]^{2+}$ and (bottom, e, f) $[PuO_2]^{2+}$ simulations. Contour plots were obtained by taking an XZ-slice through the molecule. Red regions indicate areas of electron accumulation, while blue regions indicate electron depletion.

bonding region as opposed to an area covering both the bonding and oxygen centres is greater. In uranyl, there is a reduction in electron density in the bonding region as well as in the region surrounding the oxygen centres. This is less significant for neptunyl and plutonyl, and the depletion of electron density is largely drawn from the bonding region only.

Figure 4.8 presents the (a)-(b) uranyl, (c)-(d) neptunyl and (e)-(f) plutonyl electron density difference plots between the GS and An $M_{4/5}$-edge CESs. In all plots, it is clear that charge accumulation is highly localised onto the actinide centres after core-excitation. The majority of electron depletion due to core-excitation is found to occur from the bonding region and from the vicinity of the actinide centre.

Overall, the density difference plots visually confirm the findings from QTAIM analysis and clearly show the different nature of electron density redistribution upon core-excitation depending on the location of the generated core-hole.

4.3.3.3 Orbital Compositions

Orbital composition analysis was performed to assess the degree to which the bonding orbitals differ between the GS and CESs associated with intense transitions in the simulated XANES spectra. This enables the validity of XANES as a GS covalency probe in both O K-edge and An $M_{4/5}$-edge to be assessed. RAS(SD) simulations include bonding orbitals within the active spaces to ensure both orbital relaxation and correlation effects associated with these orbitals are accounted for. The changes in AIM orbital compositions for bonding SONOs between the GS and CESs for both O K-edge and An $M_{4/5}$-edge simulations are presented in table 4.14. Only An% contributions are reported since in $[AnO_2]^{2+}$ models O% is simply $100\% - An\%$, and changes in the total oxygen composition to the bonding orbitals between the GS and CESs is simply the reverse sign of $\Delta\%$ values reported in table 4.14.

In O K-edge XANES, AIM analysis reveals An% contributions to the bonding SONOs in the CESs are underestimated by up to 13% with respect to the GS. In uranyl, U% contributions are 7-10% lower in the CESs compared to the GS. In plutonyl, similar decreases between 7-13% are reported in the CESs. In neptunyl, decreases in Np% contribution between the GS and the $1s \rightarrow \pi_u^*$ and $1s \rightarrow \pi_g^*$ CESs of 13% and 6%

Table 4.14: Total AIM-calculated actinide-% contribution to bonding SONOs between the ground- and key core-excited states identified from peaks in RAS(SD) XANES simulations. Table reports the values from the ground to core-excited states, GS%→CES%, and the overall change given by Δ%.

Simulation	Excitation	SONO	GS → CES	Δ%
$[UO_2]^{2+}$ O K-edge	$1s \rightarrow \pi_u^*$	π_u	25% → 15%	-10%
	$1s \rightarrow \sigma_u^*$	σ_u	53% → 46%	-7%
	$1s \rightarrow \pi_g^*$	π_g	17% → 9%	-8%
$[NpO_2]^{2+}$ O K-edge	$1s \rightarrow \pi_u^*$	π_u	28% → 15%	-13%
	$1s \rightarrow \sigma_u^*$	σ_u	55% → 54%	-1%
	$1s \rightarrow \pi_g^*$	π_g	16% → 10%	-6%
$[PuO_2]^{2+}$ O K-edge	$1s \rightarrow \pi_u^*$	π_u	30% → 17%	-13%
	$1s \rightarrow \sigma_u^*$	σ_u	59% → 52%	-7%
	$1s \rightarrow \pi_g^*$	π_g	17% → 9%	-8%
$[UO_2]^{2+}$ U M_4-edge	$3d \rightarrow \pi_u^*$	π_u	26% → 26%	+0%
	$3d \rightarrow \sigma_u^*$	σ_u	56% → 57%	+1%
$[NpO_2]^{2+}$ Np M_5-edge	$3d \rightarrow 5f_{\delta/\phi}/\pi_u^*$	π_u	27% → 28%	+1%
	$3d \rightarrow \sigma_u^*$	σ_u	62% → 60%	-2%
$[PuO_2]^{2+}$ Pu M_5-edge	$3d \rightarrow 5f_{\delta/\phi}/\pi_u^*$	π_u	27% → 32%	+5%
	$3d \rightarrow \sigma_u^*$	σ_u	60% → 64%	+4%

are reported in table 4.14, respectively. For the $1s \rightarrow \sigma_u^*$ CES, the Np% contribution of 54% in the σ_u SONO is comparable with the GS Np% of 55%, a decrease of 1%. This relatively minor compositional change compared with the other O K-edge states has no clear explanation, since the QTAIM results for this state are consistent with those

reported for all other O K-edge states. However, the general trend of a decrease in AIM actinide contribution to the bonding orbitals from the GS to the CESs is clear, and can be qualitatively explained with reference to the QTAIM findings from section 4.3.3.1. An explanation was already outlined in the context of uranyl O K-edge simulations in chapter 3, but is generalisable to CESs in all three actinyl systems examined here. The decrease in An% contributions to bonding SONOs in O K-edge CESs is attributed to two contributing effects:

1. Increased charge density on the An centre driven by the occupation of anti-bonding orbitals of predominantly actinide character in the CESs, which acts to drive electron density in the bonding orbitals away from the An centre.

2. Increased effective nuclear charge on oxygen centres due to the presence of the ligand core-hole which withdraws charge density in bonding orbitals toward O and away from An centres.

Both effects combine to produce the reported decrease in An% contributions to the bonding SONOs in table 4.14 between the GS and CESs.

In comparison with O K-edge CESs, An $M_{4/5}$-edge CESs present bonding SONOs with AIM compositions that are significantly more representative of those in the GS. In the uranyl U M_4-edge 3d $\rightarrow \pi_u^*$ and 3d $\rightarrow \sigma_u^*$ CESs the bonding SONO compositions are comparable to those in the GS, differing by no more than 1%. For CESs in uranyl, any potential decrease in An% contribution to bonding orbitals driven by the occupation of anti-bonding orbitals, is counteracted by the increase in actinide effective nuclear charge due to the core-hole. The effects appear to largely cancel, leaving the bonding orbital compositions similar between the GS and CESs. In the neptunyl M_5-edge 3d $\rightarrow 5f_{\delta/\phi}/\pi_u^*$ CES, the same cancellation largely applies, leading to similar Np% contributions to the π_u bonding SONOs in the GS. For the 3d $\rightarrow \sigma_u^*$ CES in neptunyl, a decrease of 2% in the Np contribution to the σ_u orbital is reported, which although small, does represent a minor deviation from the trend established thus far. The same effects discussed for uranyl are expected to also manifest here, however, QTAIM analysis points to an additional Coulomb repulsion arising between the unpaired $5f^1$ electron and the excited core-electron in σ_u^*, which appears substantial enough to change the electron localisation pattern as

seen in table 4.13. The analogous repulsion does not appear to impact the localisation (λ) pattern of the 3d $\rightarrow$ 5f$_{\delta/\phi}$/π_u^* CES in neptunyl. The relatively small reduction in Np% to the σ_u orbital could potentially arise from this Coulomb repulsion. In plutonyl, the CESs associated with the 3d $\rightarrow$ 5f$_{\delta/\phi}$/π_u^* and 3d $\rightarrow$ σ_u^* transitions both present greater An% contributions to the π_u and σ_u bonding orbitals compared to the GS, with an increase of 5% and 4%, respectively. This is somewhat puzzling since the changes in QTAIM metrics in table 4.13 are similar for both neptunyl and plutonyl CESs, and therefore it was thought similar behaviour in the orbital compositions may manifest in both systems. In particular, if the Coulomb repulsion between the single unpaired 5f^1 electron and the excited core-electron in σ_u^* is responsible for the minor 2% decrease in An% to the σ_u orbital, then given the additional electron in plutonyl, it was expected that an even greater decrease in An% to the σ_u bonding orbital would be found.

Autschbach and co-workers have previously reported An M$_{4/5}$-edge simulations and examined the bonding orbitals between the GS and CESs using Natural localised Molecular Orbital (NLMO) analysis.[5] In the study, compositions of the σ- and π-bonding NLMOs were found to be comparable between the GS and CESs for uranyl, confirming the same findings from the reported AIM compositions in table 4.14. For neptunyl and plutonyl, the π-bonding NLMO compositions were comparable between the GS and 3d $\rightarrow$ π_u^* CESs, while for σ-bonding NLMOs, a substantial decrease of 14% and 17% in Np and Pu contributions, respectively, were found between the GS and 3d $\rightarrow$ σ_u^* CESs. This substantial reduction in covalent mixing for the σ-bonding NLMOs of neptunyl and plutonyl was attributed to a number of potential effects. First, the generation of the core-hole and population of the σ_u^* orbital results in significant orbital relaxation and the reduction in σ-covalency. The generation of a core-hole on the actinide centre is also expected to specifically impact the 'pushing from below' (PFB) mechanism in σ-bonding, as an increase in the effective nuclear charge renders the 6p-orbital more core-like and reduces the PFB contribution to covalency. Lastly, the reduction in σ-covalency was also thought to be enhanced by the presence of Coulomb repulsion between the partially filled non-bonding 5f$_{\delta/\phi}$ orbitals and the anti-bonding orbitals. The changes in AIM compositions for uranyl reported in this chapter find agreement with the NLMO compositions reported by Autschbach. The changes in AIM composition for neptunyl only

tentatively agree with the NLMO findings reported by Autschbach, with only a minor 2% reduction in An% contribution to the σ-bonding orbital found using AIM analysis versus a more substantial 14% reduction reported by Autschbach.[5] The most significant point of disagreement between AIM compositions in this chapter and the reported NLMO compositions by Autschbach is for plutonyl. In this chapter, the AIM analysis finds greater An% contributions to the plutonyl π_u and σ_u bonding orbitals in the CESs and is in strong contrast to the reported 17% reduction in An% contribution to σ-bonding found in the reported NLMO analysis.

To examine the disagreement in orbital compositions between findings reported in this chapter and those of Autschbach, NLMO analysis was performed for the same An M-edge and O K-edge states reported in table 4.14. The resulting An% contributions to the σ- and π-bonding NLMOs are reported in table 4.15. A similar decrease in An% contributions to bonding orbitals in the O K-edge CESs found via AIM composition analysis is reproduced in the NLMO results, and the two contributing effects outlined to explain this reduction in O K-edge states hold here for NLMO compositions. Interestingly, the minor 1% reduction in Np% contribution to the σ_u orbital for the 1s $\rightarrow \sigma_u^*$ CES in neptunyl found using AIM analysis is no longer an outlier compared with other states when using NLMO analysis. NLMO compositions for An M-edge states reported in table 4.15 support the general conclusion drawn from the AIM results, that the bonding orbitals in An M-edge CESs are significantly more comparable with the GS than those in O K-edge CESs. The NLMO compositions for both M-edge CESs in uranyl, as well as the 3d $\rightarrow$ 5f$_{\delta/\phi}/\pi_u^*$ CESs in neptunyl and plutonyl, are comparable with the GS, in agreement with the findings of Autschbach and co-workers.[5] However, the substantial reduction in Np% and Pu% contribution to σ-NLMOs in 3d $\rightarrow \sigma_u^*$ CESs reported by Autschbach are not found for the analogous states in simulations reported in this chapter. Instead, the σ-NLMO composition in the 3d $\rightarrow \sigma_u^*$ CESs are comparable with the GS for neptunyl. While for plutonyl, NLMO compositions for the π- and σ-bonding orbitals in both CESs show an increase in An% contributions compared with the GS bonding orbitals, and support the AIM findings.

Overall, the reported NLMO compositions support the AIM findings. In addition, both the AIM and NLMO compositions do not provide any clear evidence of the Coulomb

Table 4.15: Total actinide-% contribution to σ- and π-bonding NLMOs between the ground- and key core-excited states identified from peaks in RAS(SD) XANES simulations. Table reports the values from the ground- to core excited-states, GS%→CES%, and the overall change given by Δ%.

Simulation	Excitation	NLMO	GS → CES	Δ%
$[UO_2]^{2+}$ O K-edge	$1s \rightarrow \pi_u^*$	π	22% → 13%	-9%
	$1s \rightarrow \sigma_u^*$	σ	35% → 23%	-12%
	$1s \rightarrow \pi_g^*$	π	22% → 9%	-13%
$[NpO_2]^{2+}$ O K-edge	$1s \rightarrow \pi_u^*$	π	24% → 15%	-9%
	$1s \rightarrow \sigma_u^*$	σ	34% → 20%	-15%
	$1s \rightarrow \pi_g^*$	π	24% → 10%	-14%
$[PuO_2]^{2+}$ O K-edge	$1s \rightarrow \pi_u^*$	π	26% → 15%	-11%
	$1s \rightarrow \sigma_u^*$	σ	36% → 19%	-17%
	$1s \rightarrow \pi_g^*$	π	26% → 10%	-16%
$[UO_2]^{2+}$ U M_4-edge	$3d \rightarrow \pi_u^*$	π	21% → 21%	0%
	$3d \rightarrow \sigma_u^*$	σ	34% → 34%	0%
$[NpO_2]^{2+}$ Np M_5-edge	$3d \rightarrow 5f_{\delta/\phi}/\pi_u^*$	π	22% → 22%	0%
	$3d \rightarrow \sigma_u^*$	σ	37% → 37%	0%
$[PuO_2]^{2+}$ Pu M_5-edge	$3d \rightarrow 5f_{\delta/\phi}/\pi_u^*$	π	23% → 24%	+1%
	$3d \rightarrow \sigma_u^*$	σ	38% → 40%	+2%

repulsion between the $5f_{\delta/\phi}$ orbitals and the occupied σ_u^* orbital having a direct impact on the σ-bonding compositions in either neptunyl or plutonyl. Both the AIM and NLMO analysis results show no significant change in the bonding orbital compositions between the GS and An M-edge CESs in uranyl and neptunyl. In these systems, any potential decrease

in An% contribution to bonding orbitals due to the population of valence orbitals with predominant actinide character is counteracted by the increase in effective nuclear charge of the actinide centre due to the core-hole. Both effects largely cancel to leave the bonding orbitals similar between the GS and CESs. In plutonyl, the increase in An% contribution to the bonding orbitals in both the 3d $\rightarrow$ 5f$_{\delta/\phi}$/π_u^* and 3d $\rightarrow$ σ_u^* states could result from an imbalance of the two effects, with the core-hole having greater influence on the attraction of charge density toward the actinide centre in the bonding orbitals. The discrepancy in NLMO findings reported in this chapter and those reported by Autschbach are likely to arise from a combination of differences in active space size and constraints for neptunyl and plutonyl simulations.

4.4 Conclusion

RAS(SD) simulations of O K-edge and An $M_{4/5}$-edge XANES spectra for $[UO_2]^{2+}$, $[NpO_2]^{2+}$, and $[PuO_2]^{2+}$ are reported. The O K-edge of neptunyl and plutonyl are simulated using RAS approaches for the first time and the resulting predictions await experimental verification. For all three actinyl systems, the RAS(SD) O K-edge spectra present similar three peak profiles, labelled peaks 1-3, and assigned to 1s $\rightarrow$ π_u^*, 1s $\rightarrow$ σ_u^*, and 1s $\rightarrow$ π_g^* excitations, respectively. The U M_4-, Np and Pu M_5-edge XANES for the actinyls was also simulated at the RAS(SD) level, and are in good agreement with the experimental work of Vitova et al. [2] in terms of the relative peak separations (within 1 eV of experiment) and spectral profiles.

RASSCF simulations reveal that XANES spectra and their observed peaks are comprised of multiple transitions, and therefore ascribing the intensity of the peak to the specific 5f-character of an orbital in the CES of a single transition is not valid. For peaks which can be ascribed to a small number of intense core-excitations (Peak 2 in uranyl for both O K-edge and U M_4-edge), the CESs themselves can exhibit multiconfigurational character, obscuring the relationship between peak intensity and the degree of O 2p- or An 5f-character in a specific anti-bonding orbital. The density of transitions associated with peaks in both O K-edge and An M-edge simulations increases from uranyl to plutonyl inline with the increasing number of unpaired 5f electrons, which substantially increases the number of possible core-excited states. Multiconfigurational character, as found in

chapter 3, manifests as the partial occupation of all the RAS3 orbitals by RAS2 electrons, and is found to increase substantially for higher energy CESs in both K-edge and M-edge simulations.

XANES is regularly utilized as a probe of GS bonding, and the simulation results presented in this chapter demonstrate the importance of considering the complementary data obtained from both ligand K-edge and An M-edge XANES in concert. By doing so, a more complete picture of bonding can be established, with each edge serving to bound the actinide contributions to bonding orbitals. AIM orbital analysis reveals that CESs probed through O K-edge may underestimate the GS bonding by up to 13%, serving as a lower bound. In contrast, An M-edge XANES provides orbital compositions that are significantly more comparable between the CESs and the GS, particularly for uranyl and neptunyl, with CES actinide contributions remaining within 2% of those in the GS. However, probing the the CESs of plutonyl leads to an overestimation of the actinide contribution to bonding by up to 5%, and can serve as an upper bound. These findings are also supported by NLMO analysis of the same states. Taken together, the use of both ligand K-edge and An $M_{4/5}$-edge, provides an upper and lower bound to the actual actinide contribution to GS bonding orbitals, An_{GS}%, compared to the measured contribution from either edge $An_{M\text{-}/K\text{-edge}}$% as follows: $An_{K\text{-edge}}\% \leq\leq An_{GS}\% \leq An_{M\text{-edge}}\%$.

QTAIM analysis provides insight into the changes in electronic structure between the GS and CESs. Analysis reveals that the ρ_{BCP} values reported for CESs remain within 0.04 a.u. of those in the GS for both O K-edge and An M-edge states. The delocalisation (δ) values, on the other hand, are found to be more sensitive and thus a more useful measure of changes in actinyl bonding due to core-excitation. In both ligand K-edge and actinide M-edge simulations, there is a reduction in δ(An, O) values from the GS to CESs, which is to be expected when occupying anti-bonding orbitals. The 3d $\rightarrow$ $5f_{\delta/\phi}$ CES in uranyl is the only exception to this, with an increase in δ(U, O) resulting from electron donation from the oxygen ligands as indicated by reduced λ(O) values. Here, it is expected that the occupation of the uranium $5f_{\delta/\phi}$ orbitals does not completely shield the 3d core-hole nor diminish the increased effective nuclear charge in the CES compared with the GS, and thus the uranium centre withdraws electron density to its centre to re-balance charge across the system. For all other states, the electrons depleted from bonding interactions

in O K-edge CESs are localised onto all three atomic centres, while in An M-edge CESs, localisation is primarily driven onto actinide centres. In O K-edge CESs, localisation onto the oxygen centres is driven by the increase in effective nuclear charge due to the ligand core-hole, while localisation onto the actinide centre is driven by the occupation of anti-bonding orbitals with predominantly actinide character. In An M-edge states, actinide localisation is again driven by the occupation of anti-bonding orbitals, but also due to the core-hole now residing on the actinide centre. Both effects account for the limited oxygen localisation in An M-edge CESs. Some noteworthy oxygen localisation is found for 3d $\rightarrow \sigma_u^*$ CESs in neptunyl and plutonyl, and is attributed to Coulomb repulsion of the unpaired 5f electrons and the core-electron in the σ_u^* orbital.

Overall, the QTAIM results together enables a qualitative rationalisation for the reported SONO compositions, with two effects thought to impact the reported orbital compositions:

1. The increase of effective nuclear charge on the centre in which the core-hole is localised acts to draw electron density in the bonding orbitals to these centres.

2. The occupation of anti-bonding orbitals with predominantly actinide character acts to drive electron density away from the actinide centre in bonding orbitals.

For O K-edge CESs, the two effects combine to produce the reported decrease in An% contributions to bonding SONOs in all three actinyl systems. In An $M_{4/5}$-edge CESs, the two contributing effects largely cancel for uranyl and neptunyl, leaving the bonding orbital compositions comparable to the GS. In plutonyl, compositional analysis reveals a minor increase in the An% contributions to bonding orbitals in the CESs, meaning the effects do not completely cancel, and is attributed to greater influence on the bonding orbitals from the core-hole.

More generally, the simulations in this chapter demonstrate the ability of the truncated RASSCF methodology to generate the required spectroscopic states needed for XANES simulations in open-shell systems, up to and including RAS(SD) level calculations for $5f^2$ systems. The main source of computational cost in the simulations comes from the vast number of states required for state-interaction in the RASSI formalism. So while RAS(SDT) level RASSCF calculations may be possible to obtain for open shell systems,

the number of states generated would likely render RASSI calculations intractable for the majority of research groups.

References

[1] R. G. Denning, J. C. Green, T. E. Hutchings, C. Dallera, A. Tagliaferri, K. Giarda, N. B. Brookes and L. Braicovich, *The Journal of Chemical Physics*, 2002, **117**, 8008–8020, DOI: 10.1063/1.1510445.

[2] T. Vitova, I. Pidchenko, D. Fellhauer, P. S. Bagus, Y. Joly, T. Pruessmann, S. Bahl, E. Gonzalez-Robles, J. Rothe, M. Altmaier, M. A. Denecke and H. Geckeis, *Nature Communications*, 2017, **8**, 16053, DOI: 10.1038/ncomms16053.

[3] S. Kraft, J. Stümpel, P. Becker and U. Kuetgens, *Review of Scientific Instruments*, 1996, **67**, 681–687, DOI: 10.1063/1.1146657.

[4] J. A. Bearden and A. F. Burr, *Rev. Mod. Phys.*, 1967, **39**, 125–142, DOI: 10.1103/RevModPhys.39.125.

[5] D.-C. Sergentu, T. J. Duignan and J. Autschbach, *The Journal of Physical Chemistry Letters*, 2018, **9**, 5583–5591, DOI: 10.1021/acs.jpclett.8b02412.

[6] D. Hall, A. D. Rae and T. N. Waters, *Acta Crystallographica*, 1966, **20**, 160–162, DOI: 10.1107/S0365110X66000355.

[7] D. J. Watkin, R. G. Denning and K. Prout, *Acta Crystallographica Section C*, 1991, **47**, 2517–2519, DOI: 10.1107/S0108270191006777.

[8] S. M. Cornet, M. P. Redmond, D. Collison, C. A. Sharrad, M. Helliwell and J. Warren, *Comptes Rendus Chimie*, 2010, **13**, 832–838, DOI: 10.1016/j.crci.2010.04.013.

[9] M. P. Wilkerson, C. A. Arrington, J. M. Berg and B. L. Scott, *Journal of Alloys and Compounds*, 2007, **444-445**, 634–639, DOI: 10.1016/j.jallcom.2006.12.011.

[10] J. Su, W. H. E. Schwarz and J. Li, *Inorganic Chemistry*, 2012, **51**, 3231–3238, DOI: 10.1021/ic202712p.

[11] Y. Teterin, K. Maslakov, M. Ryzhkov, A. Teterin, K. Ivanov, S. Kalmykov, V. Petrov and D. Suglobov, *Nuclear Technology and Radiation Protection*, 2015, **30**, 99–112, DOI: 10.2298/NTRP1502099T.

[12] M. P. Wilkerson and B. L. Scott, *Acta Crystallographica Section E*, 2008, **64**, i5, DOI: 10.1107/S1600536807066354.

[13] P. J. Hay, R. L. Martin and G. Schreckenbach, *The Journal of Physical Chemistry A*, 2000, **104**, 6259–6270, DOI: 10.1021/jp000519h.

[14] R. Polly, B. Schacherl, J. Rothe and T. Vitova, *Inorganic Chemistry*, 2021, **60**, 18764–18776, DOI: 10.1021/acs.inorgchem.1c02364.

[15] J. N. Ehrman, K. Shumilov, A. J. Jenkins, J. M. Kasper, T. Vitova, E. R. Batista, P. Yang and X. Li, *JACS Au*, 2024, **4**, 1134–1141, DOI: 10.1021/jacsau.3c00838.

[16] P. S. Bagus, C. J. Nelin, K. M. Rosso, B. Schacherl and T. Vitova, *Inorganic Chemistry*, 2024, **63**, 1793–1802, DOI: 10.1021/acs.inorgchem.3c03158.

[17] J. Olsen, B. O. Roos, P. Jo/rgensen and H. J. A. Jensen, *The Journal of Chemical Physics*, 1988, **89**, 2185–2192, DOI: 10.1063/1.455063.

[18] F. Aquilante, J. Autschbach, A. Baiardi, S. Battaglia, V. A. Borin, L. F. Chibotaru, I. Conti, L. D. Vico, M. Delcey, I. F. Galván, N. Ferré, L. Freitag, M. Garavelli, X. Gong, S. Knecht, E. D. Larsson, R. Lindh, M. Lundberg, P. Å. Malmqvist, A. Nenov, J. Norell, M. Odelius, M. Olivucci, T. B. Pedersen, L. Pedraza-González, Q. M. Phung, K. Pierloot, M. Reiher, I. Schapiro, J. Segarra-Martí, F. Segatta, L. Seijo, S. Sen, D.-C. Sergentu, C. J. Stein, L. Ungur, M. Vacher, A. Valentini and V. Veryazov, *The Journal of Chemical Physics*, 2020, **152**, 214117, DOI: 10.1063/5.0004835.

[19] F. Aquilante, L. D. Vico, N. Ferré, G. Ghigo, P.-å. Malmqvist, P. Neogrády, T. B. Pedersen, M. Pitoňák, M. Reiher, B. O. Roos, L. Serrano-Andrés, M. Urban, V. Veryazov and R. Lindh, *Journal of Computational Chemistry*, 2010, **31**, 224–247, DOI: 10.1002/jcc.21318.

[20] F. Aquilante, J. Autschbach, R. K. Carlson, L. F. Chibotaru, M. G. Delcey, L. D. Vico, I. F. Galván, N. Ferré, L. M. Frutos, L. Gagliardi, M. Garavelli, A. Giussani, C. E. Hoyer, G. L. Manni, H. Lischka, D. Ma, P. Å. Malmqvist, T. Müller, A. Nenov, M. Olivucci, T. B. Pedersen, D. Peng, F. Plasser, B. Pritchard, M. Reiher, I. Rivalta, I. Schapiro, J. Segarra-Martí, M. Stenrup, D. G. Truhlar, L. Ungur, A. Valentini, S. Vancoillie, V. Veryazov, V. P. Vysotskiy, O. Weingart, F. Zapata and R. Lindh,

Journal of Computational Chemistry, 2016, **37**, 506–541, DOI: 10.1002/jcc.24221.

[21] B. O. Roos, R. Lindh, P.-Å. Malmqvist, V. Veryazov and P.-O. Widmark, *The Journal of Physical Chemistry A*, 2005, **109**, 6575–6579, DOI: 10.1021/jp0581126.

[22] B. O. Roos, R. Lindh, P.-Å. Malmqvist, V. Veryazov and P.-O. Widmark, *Chemical Physics Letters*, 2005, **409**, 295–299, DOI: 10.1016/j.cplett.2005.05.011.

[23] *The Journal of Physical Chemistry A*, 2004, **108**, 2851–2858, DOI: 10.1021/jp031064+.

[24] A. Wolf, M. Reiher and B. A. Hess, *The Journal of Chemical Physics*, 2002, **117**, 9215–9226, DOI: 10.1063/1.1515314.

[25] B. A. Hess, *Physical Review A*, 1986, **33**, 3742–3748, DOI: 10.1103/PhysRevA.33.3742.

[26] B. A. Hess, *Physical Review A*, 1985, **32**, 756–763, DOI: 10.1103/PhysRevA.32.756.

[27] M. Douglas and N. M. Kroll, *Annals of Physics*, 1974, **82**, 89–155, DOI: 10.1016/0003-4916(74)90333-9.

[28] B. A. Hess, C. M. Marian, U. Wahlgren and O. Gropen, *Chemical Physics Letters*, 1996, **251**, 365–371, DOI: 10.1016/0009-2614(96)00119-4.

[29] V. Sauri, L. Serrano-Andrés, A. R. M. Shahi, L. Gagliardi, S. Vancoillie and K. Pierloot, *Journal of Chemical Theory and Computation*, 2011, **7**, 153–168, DOI: 10.1021/ct100478d.

[30] S. Vancoillie, H. Zhao, V. T. Tran, M. F. A. Hendrickx and K. Pierloot, *Journal of Chemical Theory and Computation*, 2011, **7**, 3961–3977, DOI: 10.1021/ct200597h.

[31] J. Finley, P.-Å. Malmqvist, B. O. Roos and L. Serrano-Andrés, *Chemical Physics Letters*, 1998, **288**, 299–306, DOI: 10.1016/S0009-2614(98)00252-8.

[32] J. P. Zobel, J. J. Nogueira and L. González, *Chemical Science*, 2017, **8**, 1482–1499, DOI: 10.1039/C6SC03759C.

[33] N. Forsberg and P.-Å. Malmqvist, *Chemical Physics Letters*, 1997, **274**, 196–204, DOI: 10.1016/S0009-2614(97)00669-6.

[34] G. Ganguly, D.-C. Sergentu and J. Autschbach, *Chemistry – A European Journal*, 2020, **26**, 1776–1788, DOI: 10.1002/chem.201904166.

[35] D.-C. Sergentu and J. Autschbach, *Dalton Transactions*, 2022, **51**, 1754–1764, DOI: 10.1039/D1DT04075H.

[36] D.-C. Sergentu and J. Autschbach, *Chemical Science*, 2022, **13**, 3194–3207, DOI: 10.1039/D1SC06454A.

[37] P. Å. Malmqvist, B. O. Roos and B. Schimmelpfennig, *Chemical Physics Letters*, 2002, **357**, 230–240, DOI: 10.1016/S0009-2614(02)00498-0.

[38] J. Autschbach, *Comments on Inorganic Chemistry*, 2016, **36**, 215–244, DOI: 10.1080/02603594.2015.1121874.

[39] K. Stanistreet-Welsh, *Molcas2Molden: Molcas INPORB to MOLDEN Convertor*, https://github.com/k-stanistr-wel/Molcas2Molden, 2023.

[40] J. development team, *Jmol: an open-source Java viewer for chemical structures in 3D*, http://www.jmol.org/, 2023.

[41] T. Lu and F. Chen, *Journal of Computational Chemistry*, 2012, **33**, 580–592, DOI: 10.1002/jcc.22885.

[42] Z. Wenli, *Molden2AIM: A utility program which can be used to create AIM-WFN, AIM-WFX, and NBO-47 files from a Molden file*, https://github.com/zorkzou/Molden2AIM, 2023.

[43] T. A. Keith, *AIMAll*, version 19.02.13, TK Gristmill Software, 2019.

[44] E. D. Glendening, C. R. Landis and F. Weinhold, *Journal of Computational Chemistry*, 2013, **34**, 1429–1437, DOI: https://doi.org/10.1002/jcc.23266.

[45] A. E. Reed and F. Weinhold, *The Journal of Chemical Physics*, 1985, **83**, 1736–1740, DOI: 10.1063/1.449360.

[46] S. Matsika and R. M. Pitzer, *The Journal of Physical Chemistry A*, 2000, **104**, 4064–4068, DOI: 10.1021/jp993767q.

[47] R. G. Denning, *The Journal of Physical Chemistry A*, 2007, **111**, 4125–4143, DOI: 10.1021/jp071061n.

Chapter 5

Probing Covalency in RASSCF An $M_{4/5}$-edge XANES Simulations of Actinyls in Different Oxidation States:

This chapter presents the first application of the RASSCF approach to simulate the $M_{4/5}$-edge XANES of actinyls in the +5 oxidation state. The predicted XANES profiles and assignments align well with experimental data, particularly in demonstrating a red-shift of approximately 2 eV upon reduction from An(VI) to An(V). Though this overestimates the oxidation-state shift, it correctly captures the expected red-shift behaviour. The oxidation-state shifts are explained by the relative stability of the CESs, with the An(VI) CES being less stable than its equivalent in the An(V) system due to an additional and unfavourable Coulomb interactions which raises the states energy. QTAIM analysis revealed increasing covalency across the series for both +5 and +6 oxidation states, while a reduction in covalency was observed upon reduction from An(VI) to An(V). Orbital composition analysis revealed that in actinyl(VI) systems, both the π- and σ-bonding orbitals are largely comparable between the GS and CESs, with the main exception being the π-bonding orbitals in plutonyl(VI). In contrast, for actinyl(V) systems, there is significant differences between the bonding orbitals in the GS and CESs, except for the π-bonding orbitals in

uranyl(V). Various factors influence the extent to which bonding orbitals differ between the GS and CESs, however, connecting changes within a single orbital to the broader electronic structure variations between the GS and CES remains challenging. Results highlight that the validity of XANES as a probe of GS covalency is highly variable and dependent on both the system in question and its oxidation state. The relationship between the separation of the 5f$_{\delta/\phi}$ and 5f-σ_u^* peaks and σ_u orbital covalency in the actinyl(VI) systems was explored, confirming that the shifts in the experimental and simulated 5f-σ_u^* peaks serve as qualitative indicators of covalency in the CES and GS σ_u orbitals, respectively. However, results suggest that the covalency information extracted from shifts reflect changes in σ_u covalency only, and do not necessarily reflect the overall covalency of the actinyl axial bond. No such correlation between 5f-σ_u^* peak shifts and σ_u orbital covalency in the actinyl(V) systems was found.

5.1 Introduction

As demonstrated in the previous chapter, $M_{4/5}$-edge XANES is a powerful tool for probing covalency, but it is also a highly sensitive probe of metal oxidation state. Examples of oxidation state determination on actinide systems using $M_{4/5}$-edge XANES are numerous and presented in greater detail in chapter 1.[1–11] In actinide M-edge XANES, core-excitations occur from 3d core-orbitals into valence orbitals with 5f character.[2] A change in the actinide oxidation state alters the excitation energy required to access the 5f-shell, resulting in a characteristic oxidation-state shift in the XANES spectrum, with higher oxidation states in general leading to greater excitation energies. The resulting spectra (shifted) can be compared to known reference species in order to determine the oxidation state of a system. In the literature, the oxidation-state shift is rationalised in terms of electrostatic effects of core-hole shielding and changes in effective nuclear charge of the actinide.[4, 11–13] When the oxidation state of the actinide is changed through the addition or removal of an electron, the effective nuclear charge is altered. At higher oxidation states, the removal of electrons increases the effective nuclear charge of the actinide centre, drawing the 3d shell closer to the nucleus, binding the 3d electrons more tightly to the actinide, and increasing the energy of excitation.[14] Kubin et al.[15] has proposed a more nuanced explanation for oxidation-state shifts in XAS spectra due to

oxidation state. The study utilized a RASSCF approach to simulate Mn L-edge XANES of a Mn(II) and Mn(III) complex and examined the relative energies of the key states that generate the main absorption edges. Kubin proposed that shifts are primarily attributed to differences in electron affinity between the CESs, with a higher electron affinity in the Mn(III) CES leading to a more stabilised CES in the reduced species. The lowering of the CES energy relative to the GS in the reduced species is more substantial than in the higher oxidation state species due to more favourable Coulomb interactions, and explains the lower excitation energy required to access the CES in the reduced species.

The capability to predict changes to $M_{4/5}$-edge XANES spectra due to oxidation state is also important for probing covalency. Studies utilizing An $M_{4/5}$-edge for determining covalency in actinyls have uncovered an apparent relationship between the energy separation of the 3d→ σ_u^* and 3d→$5f_{\delta/\phi}$ peaks, and the axial An-O bond covalency.[11–13, 16–20] The position of the $5f_{\delta/\phi}$-orbitals are viewed as fixed reference points in which to compare the relative destabilisation of the π_u^* and σ_u^* orbitals in the actinyls under different conditions, the assumption being that the $5f_{\delta/\phi}$-orbitals are less prone to influence from coordinating ligands and adjustments in actinyl bond length. The particular sensitivity of the final 3d→ σ_u^* peak as a measure of axial bond covalency is explained by the 'pushing from below' (PFB) mechanism. The PFB mechanism explains the high energy of the σ_u HOMO, which arises due to repulsive filled-filled interactions between the otherwise An(5f)-O(2p) interaction with a pseudo-core actinide 6p-orbital.[21, 22] The hybridisation of the An 6p-orbital into the σ_u bonding interaction coincides with an increase in An 5f-contribution leading to enhanced axial covalency due to better energy alignment of actinide 5f- and oxygen 2p-orbitals.[13] At the same time, the σ_u^* orbital is 'pushed' to higher energies whereas the non-bonding $5f_{\delta/\phi}$ orbital energy remains unchanged, the combined effect manifesting as a greater energy separation of the 3d→ σ_u^* peak compared to the first 3d→$5f_{\delta/\phi}$ peak.[18] The studies by Kaltsoyannis et al.[22] and Fryer-Kanssen et al.[23] have detailed the impact of the actinide 6p-orbital on the σ_u bonding orbital in terms of its energy stability and the degree to which increased actinide 5f participation aids in strengthening the axial covalency.

Correlation between shorter axial bond lengths and a greater shift in the 5f-σ_u^* peak (relative to the $5f_{\delta/\phi}$ peak) in the actinyls has been demonstrated in a number of studies

due to either changes in the ligand environment or oxidation state.[11–13, 16–20] For instance, 5f-σ_u^* peak shifts are found to be smaller in actinyl(V) systems compared to actinyl(VI) systems, with the former having greater An-O bond lengths and weakened An-O covalency. To date, the most comprehensive experimental study of changes in covalency between the actinyls using $M_{4/5}$-edge XANES comes from the work of Vitova and co-workers, generating XANES for uranyl through to plutonyl.[18] Utilizing 5f-σ_u^* peak shifts as covalency indicators, results suggested that covalency decreased from uranyl to plutonyl, which Vitova et al. found puzzling since bond lengths contract across the series and recent studies report increasing covalency across the actinyl series.[24–26] Increasing 5f-covalency from uranyl to plutonyl was explained by Vitova et al. as an increasing energy degeneracy driven covalency rather than overlap driven covalency. Autschbach and co-workers later simulated the $M_{4/5}$-edge XANES of the actinyls using RAS approaches and examined the claims of Vitova et al.[27] The simulated spectra present relative separations between the $5f_{\delta/\phi}$ and 5f-σ_u^* peaks which align with the experimental trend of decreasing energy shifts from uranyl to plutonyl, which suggests a decreasing covalency across the series. NLMO analysis of the GS orbitals reveals an opposite trend, with covalency increasing across the series. Instead, the covalency trend suggested by 5f-σ_u^* peak shifts better fits the decreasing covalency of the CESs from uranyl to plutonyl. It was concluded that the XANES spectra are not indicators of a decreasing overlap driven covalency in the GS, but rather reflect the covalency of the CESs in going from uranyl to plutonyl.[27]

In this chapter, the work started in chapter 4 is continued, examining the degree to which the $M_{4/5}$-edge spectra represent features of actinyl covalency in the GS. Two features are examined, first the degree to which the GS and CES orbitals differ due to relaxation in the presence of the core-hole, the addition of $5f_{\delta/\phi}$ electrons across the series, and due to oxidation state changes. Second, the validity of $5f_{\delta/\phi}$ peak shifts as indicators of axial bond covalency is examined. This is done for both the +6 and +5 oxidation state actinyls and results are compared and contrasted to the experimental work by Vitova et al. and the theoretical work of Autschbach and co-workers.[18, 27] While Kubin et al. has demonstrated the ability of RAS approaches to simulate the shift in XANES spectra due to oxidation state, to the authors best knowledge, no study has yet attempted to simulate the oxidation-state shift in $M_{4/5}$-edge spectra for actinide species using RAS approaches. This

chapter aims to fill this gap in the literature. The calculations presented in this chapter represent a significant challenge for RASSCF approaches due to the substantial number of states to calculate, but demonstrates how the careful set-up of RASSCF active-spaces can enable accurate XANES predictions for systems with a large numbers of unpaired electrons.

5.2 Computational Details

5.2.1 Density Functional Theory Optimisations

Structural optimisations of $[AnO_2(H_2O)_5]^{2+/+}$ (An= U, Np, Pu) actinyl aquo complexes in the absence of symmetry (C_1 point group) for both the +6 and +5 oxidation states were performed using version 6.6 of TURBOMOLE.[28] Optimisations utilized the PBE0 hybrid GGA exchange-correlation functional[29, 30] paired with Aldrichs def2-TZVP basis set for light elements (H,O) and def-TZVP for actinide centres, along with the associated actinide effective core potential (ECP).[31, 32] This model chemistry has been utilized previously for the accurate optimisation of actinide systems.[33–36] Solvation effects outside of the primary solvation sphere were modelled using a continuum solvation model (COSMO) with dielectric constant set to that of water.[37] Convergence of energetic minima structures was confirmed by vibrational frequency analysis.

5.2.2 Multiconfigurational XANES simulations

Scalar relativistic multiconfigurational calculations were performed using version 21.02 of Openmolcas.[38–41] All-electron relativistic ANO-RCC TZVP quality basis sets of Roos et al.[42–44] were employed, taking the form An(9s8p6d4f2g) and O (4s3p2s1f), with higher angular momentum h-functions removed from actinide centres to enable compatibility with analysis software. Scalar relativistic effects were modelled using the second order Douglas-Kroll-Hess Hamiltonian and Cholesky decomposition was utilized throughout to speed-up integral calculations.[45–49]

5.2.2.1 Actinyl Models

Multiconfigurational simulations were performed on bare actinyl complexes, $[AnO_2]^{2+/+}$ An = (U, Np, Pu), with D_{2h} symmetry and An-O bond lengths set to those derived from PBE0 optimised actinyl aquo complexes.

5.2.2.2 RASSCF Set-Up

RASSCF calculations were used to obtain the ground- and core-excited states following an approach similar to that of chapter 4 for An $M_{4/5}$-edge simulations.

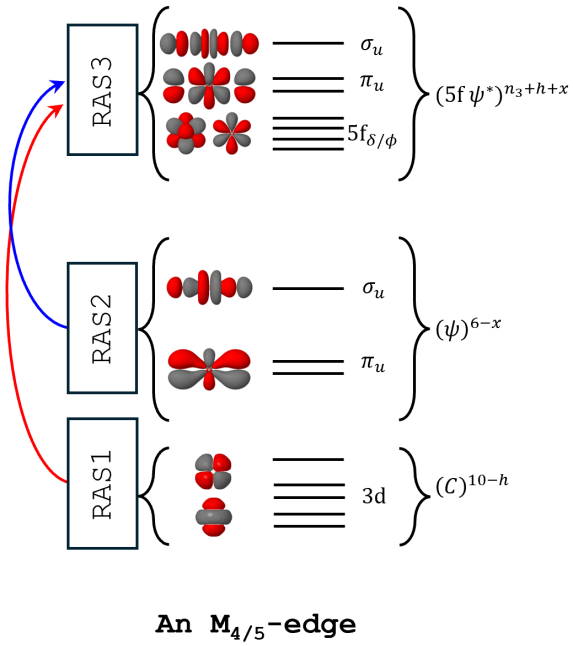

Figure 5.1: Active space used for An $M_{4/5}$-edge XANES simulations of the actinyls in the +5 and +6 oxidation states. Arrows indicate which RAS spaces electrons can move between subject to the the active-space constraints. The terms C, ψ, and (5f ψ^*) represent the core orbitals, bonding orbitals and the set of non-bonding 5f and anti-bonding orbitals, respectively. The variables h, x, and n_3 represent the number of core-holes, the number of electrons depleted from RAS2, and the number of RAS3 electrons in the GS configuration, respectively.

A similar active-space partitioning and set-up used in chapter 4 was used here (figure 5.1), with 3d core-orbitals (5×3d) spanning RAS1, u-parity bonding orbitals ($2\times\pi_u, 1\times\sigma_u$)

spanning RAS2, and u-parity anti-bonding orbitals ($2 \times \pi_u^*, 1 \times \sigma_u^*$) spanning RAS3. Non-bonding $5f_{\delta/\phi}$ orbitals ($2 \times 5f_\delta$, $2 \times 5f_\phi$) are placed in RAS3 to manage calculation cost. M-edge calculations are split into two different levels of quality, RAS(S) and RAS(SD), corresponding to RAS(16+n_3,1,1+n_3;5,3,7) and RAS(16+n_3,1,2+n_3;5,3,7) calculations in Sauri notation,[50] respectively, where n_3 is the number of 5f electrons in the GS electronic configuration of the actinyl. Restrictions to the number of electrons that can enter the RAS3 space is used to control the amount of electronic configurations captured in RASSCF calculations and thus the cost. CESs are generated by allowing up to one or two electrons in addition to the 5f electrons already present in the GS (n_3) of the actinyl species to enter RAS3, and by enforcing a single core-hole across RAS1. Due to the constraints on the active space in RAS(S), in the CES the only electrons populating RAS3 in addition to any 5f electrons already present, comes directly from core-excitation of the 3d orbitals. For this reason, the RAS(S) calculations give CESs with clear orbital populations and are highly useful for peak assignment. The higher quality RAS(SD) simulation results are chosen to be presented in this chapter. Built-in supersymmetry designations of Openmolcas were used to restrict rotation of the 3d core-orbitals out of RAS1 during the SCF procedure. The GSs were obtained by removing the RAS1 core-hole constraint and taking the appropriate state-average calculations of the necessary spin and state symmetries as reported in table 5.1. For the CESs, various state symmetries and multiplicities are possible depending on the number of unpaired electrons. Details on the number of roots obtained via state-average calculations are also reported in table 5.1.

State-specific 2^{nd} order RAS perturbation theory (SS-RASPT2) calculations[51, 52] with a default IPEA sift[53] of 0.25 a.u. and imaginary shift[54] of 0.5 a.u. was performed on RASSCF states to recover dynamical correlation and gain quantitative state energies. The chosen imaginary shift value offered a reasonable balance between converging intruder free solutions without introducing a significant shift bias to RASPT2 energies, and is comparable with values used in other related studies.[27, 55–58]

Table 5.1: Total number of states obtained via state-average calculations and the number of these states that were supplied to RASSI calculations for An $M_{4/5}$-edge simulations.

Simulation	Irrep-set	RASSCF	RASSI
U(VI) M_4	GS: $^1(A_g)$	5	1
	CES: $^1(A_u,B_{1u},B_{2u},B_{3u})$	191,193,193,193	147,147,147,147
	CES: $^3(A_u,B_{1u},B_{2u},B_{3u})$	272,271,271,271	225,218,211,211
Np(VI) M_5	GS: $^2(A_u,B_{1u},B_{2u},B_{3u})$	5,5,5,5	1,1,1,1
	CES: $^2(A_g,B_{1g},B_{2g},B_{3g})$	597,598,599,599	597,598,599,599
	CES: $^4(A_g,B_{1g},B_{2g},B_{3g})$	599,597,596,596	490,493,476,476
Pu(VI) M_5	GS: $^1(A_g,B_{1g},B_{2g},B_{3g})$	5,5,5,5	0,1,0,0
	GS: $^3(A_g,B_{1g},B_{2g},B_{3g})$	5,5,5,5	1,0,1,1
	CES: $^1(A_u,B_{1u},B_{2u},B_{3u})$	600,600,600,600	465,455,462,462
	CES: $^3(A_u,B_{1u},B_{2u},B_{3u})$	594,598,600,600	594,598,600,600
	CES: $^5(A_u,B_{1u},B_{2u},B_{3u})$	597,600,596,596	449,444,462,462
U(V) M_4	GS: $^2(A_u,B_{1u},B_{2u},B_{3u})$	5,5,5,5	1,1,1,1
	CES: $^2(A_g,B_{1g},B_{2g},B_{3g})$	598,597,597,600	463,463,473,473
	CES: $^4(A_g,B_{1g},B_{2g},B_{3g})$	600,600,599,600	365,367,359,365
Np(V) M_5	GS: $^1(A_g,B_{1g},B_{2g},B_{3g})$	5,5,5,5	0,1,0,0
	GS: $^3(A_g,B_{1g},B_{2g},B_{3g})$	5,5,5,5	1,0,1,1
	CES: $^1(A_u,B_{1u},B_{2u},B_{3u})$	600,600,597,597	407,390,404,404
	CES: $^3(A_u,B_{1u},B_{2u},B_{3u})$	600,599,599,593	600,599,599,593
	CES: $^5(A_u,B_{1u},B_{2u},B_{3u})$	600,600,600,600	425,427,424,424
Pu(V) M_5	GS: $^2(A_u,B_{1u},B_{2u},B_{3u})$	5,5,5,5	0,0,0,0
	GS: $^4(A_u,B_{1u},B_{2u},B_{3u})$	5,5,5,5	1,1,1,1
	CES: $^2(A_g,B_{1g},B_{2g},B_{3g})$	599,600,599,599	599,600,599,599
	CES: $^4(A_g,B_{1g},B_{2g},B_{3g})$	600,600,600,600	600,600,600,600
	CES: $^6(A_g,B_{1g},B_{2g},B_{3g})$	600,596,598,598	397,352,345,345

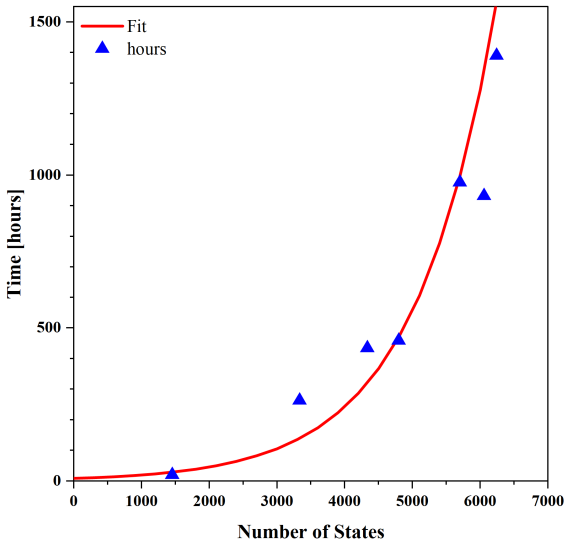

Figure 5.2: Plot shows the high cost dependence of RASSI on the number of spin-free states supplied for state-interaction. An exponential function was fitted to the data to approximate the relationship between number of spin-free states and simulation time in hours.

5.2.2.3 RASSI Calculations

The appropriate RASSCF states labelled as GS and CES in table 5.1 for each system were spin-orbit (SO) coupled *post hoc via* state-interaction of scalar relativistic states with a mean-field SO operator, making use of atomic mean-field integrals (AMFI), in the Restricted Active Space State Interaction (RASSI) formalism.[48, 54] Diagonal energies of the Hamiltonian matrix computed by RASSI were replaced by the calculated RASPT2 energies. The number of GSs and CESs of a given irrep and spin-multiplicity supplied to RASSI calculations is given in table 5.1. Details on the resulting SO-GSs are discussed in the proceeding results section.

Keeping the cost of RASSI calculations reasonable is key to obtaining the spin-orbit coupled XANES spectra of the open-shell Np(V), Pu(V), and Pu(VI) actinyls with a large number of unpaired electrons. The RASSI calculations on the hardware available can be approximated to fit an exponential curve with respect to the number of states supplied for state-interaction, as shown in fig. 5.2. To keep computational cost of RASSI manageable, the number of states must be reduced, and this was achieved in two ways:

(1) by generating the SO-GS with as minimal amount of spin-free states as possible and (2) by using energy cutoffs to limit the number of CESs supplied to RASSI. Even with these two conditions applied to filter out states, the RASSI calculations can be viewed as exponentially expensive (figure 5.2). To reduce the number of CESs supplied to RASSI calculations, the spin-free RAS(S) spectra were used to inform energy cutoffs of 3655, 3771, and 3886 eV for U(VI), Np(VI), and Pu(VI) actinyls, while cutoffs of 3651, 3767, and 3884 eV were applied for U(V), Np(V), and Pu(V) actinyls, respectively. All RASSCF states below the cutoffs were included. This reduced the number of states from those listed under RASSCF in table 5.1 to those listed under the RASSI column.

Table 5.2: Spin-orbit coupled (SOC) ground-states (GS) obtained from RASSI calculations utilizing all the calculated spin-free states that could contribute to the SO-GS. The spin-free states are those under the RASSCF column and labelled as GS irreps in table 5.1. Table includes the total SOC GS energy, the Ω quantum number, and the linear combination of the largest contributing spin-free states that constitute the SO GS configuration.

Simulation	Energy (a.u.)	Ω	Configuration
U(VI)	-28099.5694	0	$1.00\left\vert^1\mathrm{A_g}\right\rangle$
Np(VI)	-28886.6353	5/2	$0.45\left\vert^2\mathrm{B_{2u}}\right\rangle + 0.45\left\vert^2\mathrm{B_{3u}}\right\rangle + 0.05\ \left\vert^2\mathrm{A_u}\right\rangle + 0.05\ \left\vert^2\mathrm{B_{1u}}\right\rangle$
Pu(VI)	-29689.0426	3.9	$0.48\left\vert^3\mathrm{B_{3g}}\right\rangle + 0.48\ \left\vert^3\mathrm{B_{2g}}\right\rangle + 0.04\ \left\vert^1\mathrm{B_{1g}}\right\rangle + 0.01\ \left\vert^3\mathrm{A_g}\right\rangle$
U(V)	-28100.1298	5/2	$0.46\left\vert^2\mathrm{B_{2u}}\right\rangle + 0.46\ \left\vert^2\mathrm{B_{3u}}\right\rangle + 0.04\left\vert^2\mathrm{A_u}\right\rangle + 0.04\ \left\vert^2\mathrm{B_{1u}}\right\rangle$
Np(V)	-28887.2440	3.9	$0.47\ \left\vert^3\mathrm{B_{3g}}\right\rangle + 0.47\ \left\vert^3\mathrm{B_{2g}}\right\rangle + 0.04\ \left\vert^1\mathrm{B_{1g}}\right\rangle + 0.01\left\vert^3\mathrm{A_g}\right\rangle$
Pu(V)	-29689.6380	3/2	$0.26\left\vert^4\mathrm{B_{3u}}\right\rangle + 0.26\left\vert^4\mathrm{B_{2u}}\right\rangle + 0.13\left\vert^4\mathrm{B_{1u}}\right\rangle + 0.13\left\vert^4\mathrm{A_u}\right\rangle + 0.08\left\vert^2\mathrm{A_u}\right\rangle$

In order to determine which minimal number of spin-free RASSCF states are essential for constructing the SO-GSs, two sets of ground-state RASSI calculations were performed. The first RASSI included the first five spin-free states of each irrep and multiplicity possible in each system, which yielded the SO-GSs reported in table 5.2. For example, the first

Pu(V) ground-state RASSI calculation included both the doublet and quartet set of *u*-parity irrep spin-free states to supply a total of 40 states for spin-orbit coupling in RASSI. From examining the linear combination of the highest contributing spin-free RASSCF states to each SO-GS, it is found that in the majority of cases, only the lowest energy spin-free states of four irreps contribute substantially to each SO-GS. An exception to this being an additional $\left|^2\mathrm{A_u}\right\rangle$ spin-free state in Pu(V), which corresponds to one of the possible excited states for this system. Therefore, for the full RASSI calculations used in simulating XANES, reasonable GSs can be obtained by including just four spin-free states. To be confident that this is the case, a second ground-state RASSI calculation was performed including just those four spin-free states that were found to contribute the most to the SO-GSs. This yielded a set of SO-GSs reported in table 5.3.

Table 5.3: Spin-orbit coupled (SOC) ground-states (GS) obtained from RASSI calculations with a conserved number of spin-free states used to construct the GS. Table includes the total SOC GS energy, the Ω quantum number, and the linear combination of the largest contributing spin-free states that constitute the SO GS configuration.

Simulation	Energy (a.u.)	Ω	Configuration
U(VI)	-28099.5694	0	$1.00\left\|^1\mathrm{A_g}\right\rangle$
Np(VI)	-28886.6353	5/2	$0.45\left\|^2\mathrm{B_{2u}}\right\rangle + 0.45\left\|^2\mathrm{B_{3u}}\right\rangle + 0.05\left\|^2\mathrm{A_u}\right\rangle + 0.05\left\|^2\mathrm{B_{1u}}\right\rangle$
Pu(VI)	-29689.0421	3.9	$0.48\left\|^3\mathrm{B_{3g}}\right\rangle + 0.48\left\|^3\mathrm{B_{2g}}\right\rangle + 0.04\left\|^1\mathrm{B_{1g}}\right\rangle + 0.01\left\|^3\mathrm{A_g}\right\rangle$
U(V)	-28100.1297	5/2	$0.46\left\|^2\mathrm{B_{2u}}\right\rangle + 0.46\left\|^2\mathrm{B_{3u}}\right\rangle + 0.04\left\|^2\mathrm{A_u}\right\rangle + 0.04\left\|^2\mathrm{B_{1u}}\right\rangle$
Np(V)	-28887.2436	3.9	$0.47\left\|^3\mathrm{B_{3g}}\right\rangle + 0.47\left\|^3\mathrm{B_{2g}}\right\rangle + 0.04\left\|^1\mathrm{B_{1g}}\right\rangle + 0.01\left\|^3\mathrm{A_g}\right\rangle$
Pu(V)	-29689.6267	3/2	$0.45\left\|^4\mathrm{B_{3u}}\right\rangle + 0.44\left\|^4\mathrm{B_{2u}}\right\rangle + 0.06\left\|^4\mathrm{B_{1u}}\right\rangle + 0.05\left\|^4\mathrm{A_u}\right\rangle$

Comparing the two sets of SO-GSs from both RASSI calculations, finds similar energies and weights between the two, and validates the use of these four spin-free states to obtain the SO-GS in the RASSI calculations used for XANES simulations. The benefit of this approach is that the number of dipole allowed transitions that RASSI must calculate between the GSs and CESs is reduced, introducing a cost saving. For example,

when simulating the XANES for plutonyl(VI), allowed transitions occur between u-parity 'ground' states and g-parity CESs. If the 5 states of each u-parity irrep belonging to doublet and quartet multiplicities were supplied to RASSI, this would introduce at the spin-free level, 40 separate u-parity states which can all engage in various dipole allowed transitions with the set of g-parity CESs. By restricting the number of spin-free states to those required to construct the SO-GS, the 40 states is reduced to 4, and only 4 sets of transitions with the CESs is then required at the spin-free level.

To summarise, the criteria used to reduce the number of states calculated using SA-RASSCF and supplied to RASSI calculations is as follows:

1. Implementation of the Lapotre selection rule for SA-RASSCF calculations such that a subset of u/g-parity states are required depending on the parity of the GS (see text for details).

2. Out of the total states calculated by SA-RASSCF calculations, only a subset were supplied to RASSI calculations as shown in table 5.1.

3. To reduce the cost of RASSI calculations, the spin-orbit GSs were optimised such that only the most dominant scalar relativistic spin-free state required to generate a reasonable description of the SO GSs were supplied in the production level RASSI calculations (see text for details).

4. To reduce states supplied to RASSI calculations in An M4/5-edge XANES simulations an energy cutoffs for uranyl(VI), neptunyl(VI) and plutonyl(VI) states of <3655, <3771 and <3886 eV were utilised. Likewise, energy cutoffs for uranyl(V), neptunyl(V) and plutonyl(V) states of <3651, <3767 and <3884 eV were utilised. Informed by unreported spin-free RAS(S) simulations.

Spin-orbit coupled state energies and oscillator strengths between the GS and CESs were used to generate transition stick spectra. Each individual transition was subsequently broadened by fitting Lorentzian functions with a shared full width at half maximum (FWHM) value of 1.2 eV. The choice of FWHM is considered somewhat arbitrary since the peak maxima are found to remain the same regardless of the value chosen, but values were chosen to offer good visual comparison with the available experimental references.

5.2.2.4 Analysis Tools

RASSI calculations provide spin-orbit natural orbital (SONO) coefficients[55, 59, 60] along with their natural populations and are converted to MOLDEN format using a custom Molcas2Molden package which has been made freely available.[61] SONOs were utilized for peak assignments using JMOL[62] and version 3.8 of Multiwfn.[63] Molden2AIM was utilized for file conversion,[64] enabling QTAIM analysis to be performed using version 19.02.13 of AIMALL[65] and Multifwn. A variety of orbital composition analysis methods were performed on SONOs using Multiwfn,[63, 66–73] while Natual Bond Orbital (NBO) and Natural Localised Molecular Orbital (NLMO) analysis was performed using NBO6.[74, 75]

5.3 Results and Discussion

5.3.1 $[AnO_2(H_2O)_5]^{2+}$ Structure Optimisations

A key aim of this chapter is to predict the change in An $M_{4/5}$-edge spectra due to change in the actinyl oxidation state from +6 to +5. To study such changes, a consistent set of actinyl geometries in each oxidation state is required.

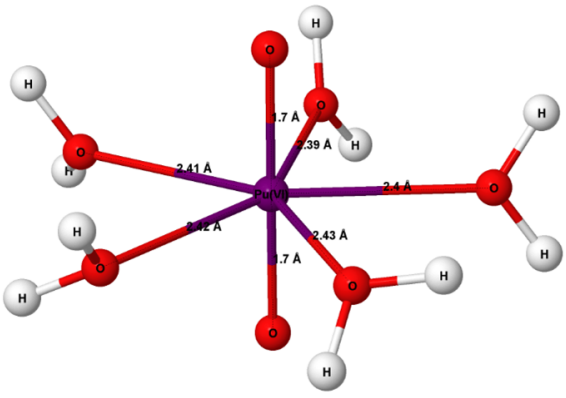

Figure 5.3: PBE0 optimised $[PuO_2(H_2O)_5]^{2+}$ structure of C1 symmetry. Structure is illustrative of other $[AnO_2(H_2O)_5]^{2+/+}$ structures.

In actinyl aquo complexes, the actinyl units are all coordinated by the same weakly bound equatorial water ligands which gives a valuable set of stable actinyl systems for which the electronic structure of the actinyl unit can be investigated with minimal

influence from coordinating ligands.[76] A number of solution EXAFS structures are reported in the literature, giving An-O bond lengths for Np and Pu actinyls in both the +5 and +6 oxidation states, and for U in the +6 oxidation state.[18, 76] In these studies, similar experimental procedures were used in the synthesis. To the authors best knowledge, there is no experimentally reported An-O bond length for $[U^{V}O_2(H_2O)_5]^+$, leaving a gap in the series of +5 actinyl complexes which requires theoretical calculations to address. Even in such a case whereby the U^{V}-O bond length is experimentally available, it may nonetheless be inconsistent in the sense that structures and geometric properties come from experiments with different conditions and methodologies. Therefore, it is advantageous to work with a theoretical set of consistent structures. A number of studies have investigated the electronic structure of actinyl aquo complexes in a variety of oxidation states,[76–78] with theoretical studies coming to a reasonable consensus that five water ligands coordinate with the actinyl unit.[79–82] The PBE0/def2-TZVP COSMO optimisations were performed in the absence of symmetry to enable as much spatial flexibility in the structural optimisation as possible. Previous studies have shown that actinyl aquo complexes can be modelled effectively by including five equatorial water ligands in the primary solvation sphere and further solvation effects through a COSMO model.[76, 78] Therefore the structure optimisations in this chapter followed similar recommendations.

The PBE0 derived plutonyl(VI) structure in fig. 5.3 is representative of all the optimised structures, which are all similar to those reported previously for An(VI) systems,[76–78] distorting from a C_5 structure with primarily a single water molecule bent out of alignment with other water ligands in the equatorial plane. The linearity of the An-O actinyl bond is only minimally impacted by the water equatorial ligands, remaining within $\sim 2^{\circ}$ as reported in table 5.4. Theoretical bond lengths of 1.74, 1.72, and 1.70Å are obtained for An-O actinyl bonds from uranyl(VI) to plutonyl(VI), respectively, and change by a consistent 0.02Å. Similarly, bond lengths in the theoretical actinyl(V) complexes change by 0.02Å between systems also, with bond lengths of 1.81, 1.79, and 1.77Å from uranyl(V) to plutonyl(V), respectively. The consistent change in bond length between the systems is a trend found between the experimentally reported actinyl bond lengths of of 1.76, 1.75, 1.74Å from uranyl to plutonyl, with a consistent 0.01Å change in

Table 5.4: PBE0 optimised $[AnO_2(H_2O)_5]^{2+/+}$ structure paramters. Bond lengths are measured in angstroms (Å) and angles measured in degrees (°).

PBE0 System	Actinyl An-O	Average An-OH_2	Actinyl ∠(O-An-O)
$[UO_2(H_2O)_5]^{2+}$	1.74	2.42	177.9
$[NpO_2(H_2O)_5]^{2+}$	1.72	2.41	178.7
$[PuO_2(H_2O)_5]^{2+}$	1.70	2.41	179.1
$[UO_2(H_2O)_5]^{+}$	1.81	2.53	179.9
$[NpO_2(H_2O)_5]^{+}$	1.79	2.53	178.8
$[PuO_2(H_2O)_5]^{+}$	1.77	2.53	178.9

bond lengths.[18, 76] Differences in theoretical bond lengths between the actinyl(VI) and actinyl(V) systems is 0.07Å and reflects the 0.07-0.08Å changes in bond lengths between neptunyl(V/VI) and plutonyl(V/VI) aquo complexes reported by others.[83–85]

The PBE0 derived actinyl bond lengths from $[AnO_2(H_2O)_5]^{2+}$ complexes were utilized to set bond lengths in the D_{2h} $[AnO_2]^{2+}$ models used for multiconfigurational An $M_{4/5}$-edge XANES simulations.

5.3.2 Actinyl Ground-States

Density functional theory (DFT) calculations for the An(VI) species predict the expected $5f^0$ closed shell singlet state for uranyl with a spin-square expectation value $\langle s^2 \rangle$ of zero,[86] and the expected open-shell $5f^1$ doublet ($\langle s^2 \rangle = 0.756$) and $5f^2$ triplet ($\langle s^2 \rangle = 2.029$) ground-states for neptunyl and plutonyl, respectively.[87] The U(V) and Np(V) actinyls are isoelectric with Np(VI) and Pu(VI) respectively, giving the same doublet ($\langle s^2 \rangle = 0.754$) and triplet ($\langle s^2 \rangle = 2.015$) ground-state multiplicities. The GS of plutonyl(V) is predicted by DFT to be an open-shell $5f^3$ quartet state with a $\langle s^2 \rangle$ of 3.793 compared to the formal value of 3.75 for a pure quartet state. Although this GS presents the largest degree of spin-contamination of the DFT calculations, it is still relatively small and within acceptable margin. These calculated ground-states are consistent with those reported by Hay et al.

in a more extensive DFT study of the actinyls and their ground-state properties.[76]

Table 5.5: Details for the spin-orbit coupled ground-states (GS) obtained in RASSI calculations for An $M_{4/5}$-edge XANES calculations. Table includes term symbols, Ω quantum number, and natural orbital (NO) occupations of the GS spin-orbit natural orbitals (SONOs).

System	Term Symbol	Ω	NO Occupation
$[UO_2]^{2+}$	$^1\sum^+_{0g}$	0	$(5f_\delta)^{0.01}(5f_\phi)^{0.00}(\pi^*_u)^{0.08}(\sigma^*_u)^{0.03}$
$[NpO_2]^{2+}$	$^2\Phi_{5/2u}$	5/2	$(5f_\delta)^{0.12}(5f_\phi)^{0.90}(\pi^*_u)^{0.09}(\sigma^*_u)^{0.03}$
$[PuO_2]^{2+}$	$^3H_{4g}$	3.9	$(5f_\delta)^{1.03}(5f_\phi)^{0.97}(\pi^*_u)^{0.13}(\sigma^*_u)^{0.04}$
$[UO_2]^{+}$	$^2\Phi_{5/2u}$	5/2	$(5f_\delta)^{0.09}(5f_\phi)^{0.92}(\pi^*_u)^{0.05}(\sigma^*_u)^{0.04}$
$[NpO_2]^{+}$	$^3H_{4g}$	3.9	$(5f_\delta)^{1.02}(5f_\phi)^{0.97}(\pi^*_u)^{0.09}(\sigma^*_u)^{0.05}$
$[PuO_2]^{+}$	$^4\Phi_{3/2u}$	3/2	$(5f_\delta)^{1.87}(5f_\phi)^{1.09}(\pi^*_u)^{0.12}(\sigma^*_u)^{0.06}$

More detailed information of the GSs can be extracted from the spin-orbit coupled multiconfigurational calculations performed in this study. The SO-GSs examined here are those obtained from the RASSI calculations used for simulating the An $M_{4/5}$-edge XANES, reported previously in table 5.3. The assigned molecular term symbols, Ω quantum numbers and NO occupations for the SO-GSs are reported in table 5.5. The ground-states can be analysed in terms of the SONO natural populations and the calculated molecular Ω value, which is a good quantum number for linear molecules. The expected $[UO_2]^{2+}$ singlet GS is obtained and according to NO occupations reflects a $5f^0_{\delta/\phi}$ state, and can be assigned the $^1\sum^+_{0g}$ term symbol. The $[NpO_2]^{2+}$ and $[PuO_2]^{2+}$ ground-state electronic configurations, which are isoelectric to $[UO_2]^+$ and $[NpO_2]^+$, respectively, are characterised as $5f^0_\delta 5f^1_\phi$ and $5f^1_\delta 5f^1_\phi$ based on SONO populations in table 5.5. Both $[NpO_2]^{2+}$ and $[UO_2]^+$ give a degenerate pair of Kramers doublets (i.e. 2 generate states) corresponding to $^2\Phi_{5/2u}$ molecular ground-states. The ground-states of $[PuO_2]^{2+}$ and $[NpO_2]^+$ correspond to $^2H_{4g}$ molecular states, with Ω values calculated to be 3.9 as opposed to the formal value of 4.0 for quartet states. A degenerate quartet ground state with a $5f^2_\delta 5f^1_\phi$ electronic configuration is

obtained for $[PuO_2]^+$, and corresponds to a $^4\Phi_{3/2u}$ molecular state. The characterisation of the ground-states outlined here are in good agreement with those proposed by others.[76, 87, 88]

5.3.3 Actinyl An $M_{4/5}$-edge XANES Simulations

5.3.3.1 XANES Spectra and Peak Assignment

The simulated RAS(SD) U M_4-edge, Np and Pu M_5-edge XANES spectra obtained using theoretically derived actinyl stuctures in both the +6 and +5 oxidation states, are presented in fig. 5.5. Since the simulated XANES spectra are not compared directly or quantitatively to experimental spectra, the excitation energies of the spectra are left un-shifted. Both M_4-edge and M_5-edge spectra are obtained in a single RASSI calculation, meaning both are available for each system. In this chapter, only those edges which are of key interest to the community and those which make up the results of experimental studies are presented and discussed. Figure 5.4 presents a number of relevant XANES spectra for comparison.

In fig. 5.5, the top row of XANES spectra belong to the An(VI) species from uranyl (left) to plutonyl (right). The spectral profiles of the actinyl(VI) systems are characteristic of those reported by Vitova et al.,[18] with a three peak profile for uranyl, and a two peak profile for both neptunyl and plutonyl, with peaks decreasing in intensity from low to high excitation energy. The simulated profiles using theoretical actinyl structures are also characteristic of those presented in the previous chapter using actinyls with experimentally informed bond lengths as well as those reported by Autschbach and co-workers.[27]

An $M_{4/5}$-edge XANES experiments on An(V) species is limited. The simulated M_5-edge XANES profile for neptunyl(V) can be compared with a XANES spectrum of an aqueous Np(V) reference sample used in a larger study, and is thought to form pentavalent neptunyl complexes.[89] The experimental $Np(V)_{aq}$ spectrum contains two peaks with the second at lower intensity than the first, and is replicated in the RAS(SD) simulated profile. Additionally, two more experimental studies on crystalline Np(V) species also confirm a two peak M_5-edge profile for neptunyl (V) with a second lower intensity peak. [20, 90] The simulated Pu(V) M_5-edge profile can be compared with an experimental M_5-edge spectrum for $KPu^VO_2CO_3$ compound.[90] The experimental spectrum presents a two peak profile

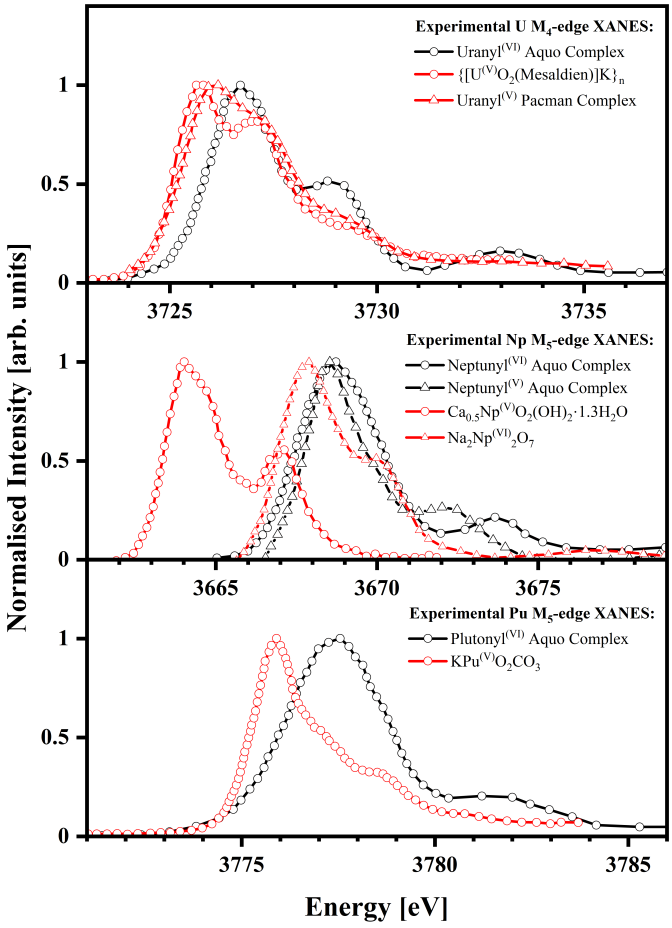

Figure 5.4: Digitized experimental XANES spectra for uranyl$^{(VI)}$ aquo complexes [18], $\{[U^{(V)}O_2(Mesaldien)]K\}_n$ [13], uranyl pacman complex [11], neptunyl$^{(VI)}$ aquo complex [18], neptunyl$^{(V)}$ aquo complex [89], $Ca_{0.5}Np^{(V)}O_2(OH)_2{\cdot}1.3H_2O$ and $Na_2Np_2^{(VI)}O_7$ [20], plutonyl$^{(VI)}$ aquo complex [18], and $KPu^{(VI)}O_2CO_3$ [90]. $Ca_{0.5}Np^{(V)}O_2(OH)_2{\cdot}1.3H_2O$ and $Na_2Np_2^{(VI)}O_7$ data was digitized with permission from T. Vitova, I. Pidchenko, D. Schild, T. Prubmann, V. Montoya, D. Fellhauer, X. Gaona, E. Bohnert, J. Rothe, R. J. Baker and H. Geckeis, *Inorganic Chemistry*, 2020, **59**, 8–22., Copyright 2024 American Chemical Society.[20] All other data was obtained with permission under open-access licenses.

with the second peak appearing as a lower intensity shoulder on the high energy side of the first peak.

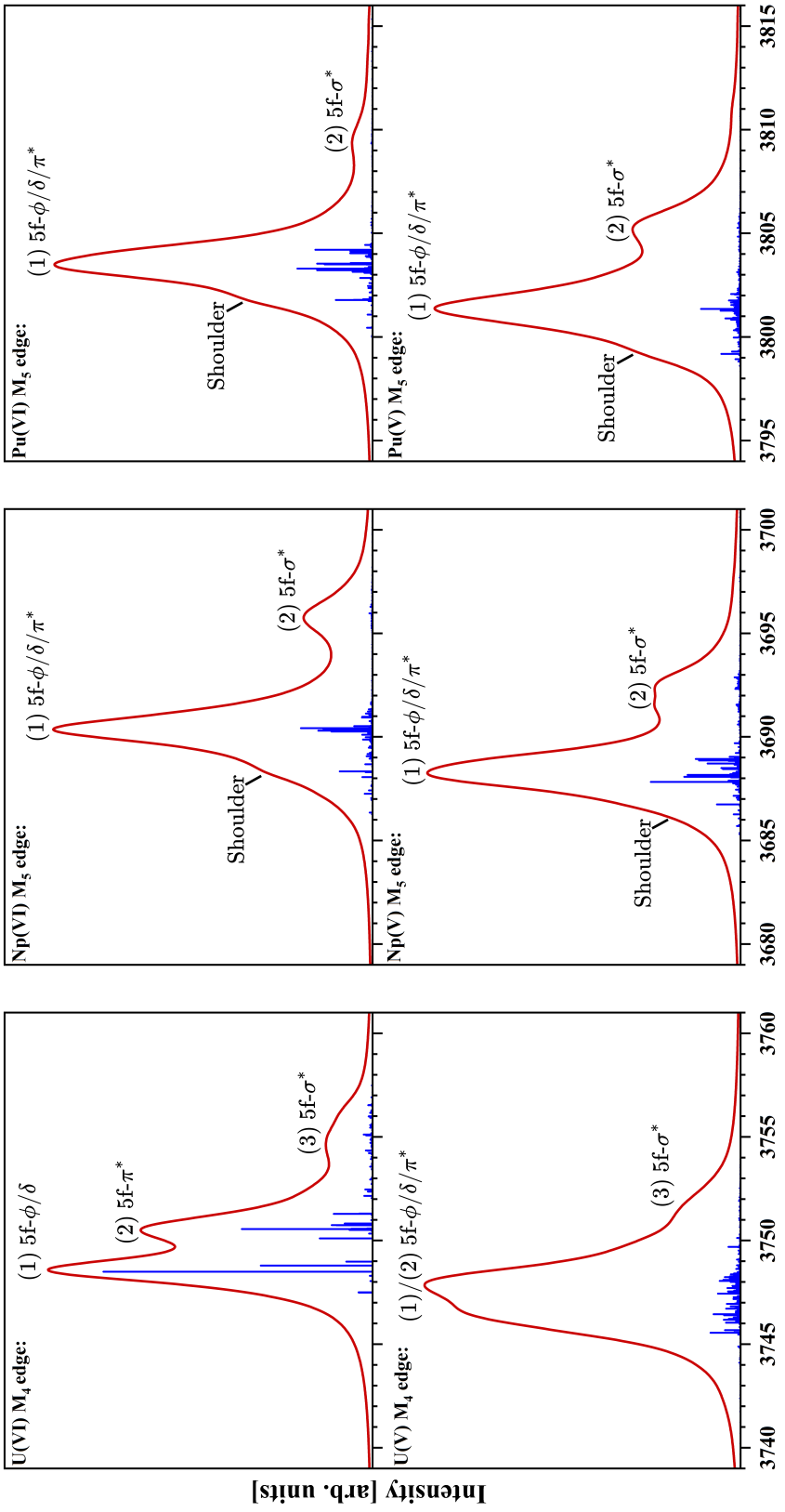

Figure 5.5: An $M_{4/5}$-edge XANES simulated spectra for actinyls in the +5 and +6 oxidation states. Figures present general peak assignments based on orbital populations in table 5.6. Individual core-excitations that contribute to the overall spectral profile are plotted as blue transition sticks. No energy shift is applied to the spectra.

Although no U M_4-edge data for aqueous uranyl(V) complexes exists in which to compare simulation directly with experiment, M_4-edge spectra have been reported for U(V) species in the solid state, with key examples being KUO_3 and $NaUO_3$,[2, 4, 91, 92] and give spectral profiles similar to those simulated in fig. 5.5 for uranyl(V). Additionally, simulation can be compared to molecular systems containing uranyl(V) units.[8, 9, 11, 13] The simulated uranyl(V) spectrum in fig. 5.5 is highly representative of the experimental U M_4-edge of a variety of uranyl(V) species reported by Vitova et al.,[13] and for a uranyl(V) 'Pacman' complex reported by Zegke et al.[11] In both these cases, the spectra for the uranyl(V) complexes contains three peaks that are not well resolved from one another, with peaks 1 and 2 exhibiting much greater intensity than 3. In the experiments, peak 2 is at lower intensity than peak 1, however, for the RAS(SD) simulated spectrum in this chapter the reverse is the case and is a key difference between the experimental and theoretical profiles.

Peak assignments were performed by analysing the natural populations of SONOs reported in table 5.6 in key CESs associated with intense excitations in fig. 5.5. The assignments of the actinyl(VI) systems is in agreement with those made in the previous chapter as well as those proposed by others.[2, 7, 16, 18, 20, 27, 58, 93, 94] These assignments are summarised in fig. 5.5 by labelling each peak with the main acceptor orbital facilitating the core-excitation. Separation of transitions associated with peak 1 in both Np and Pu simulations into distinct excitations into either the π_u^* or $5f_{\delta/\phi}$ orbitals is not feasible due to the significant electron population of both orbitals across the transitions associated with peak 1. A small shoulder feature is identified for both Np and Pu M_5-edge spectra on the low energy side of peak 1, and is generated predominantly by core-excitations into the $5f_{\delta/\phi}$ orbitals. The share of electron population across both the π_u^* and $5f_{\delta/\phi}$ orbitals in the CESs associated with peak 1 is a persistent feature for neptunyl(VI) and plutonyl(VI), appearing also in the unreported RAS(S) level spectra.

Changing the oxidation state from actinyl(VI) to actinyl(V) was not expected to change the overall peak assignments of the spectra since the same types of core-excitations were expected to occur in the same energy order. This assumes that the energy ordering of the valence orbitals in RAS3 remains the same. Indeed, the overall assignments of the two peaks in the Np and Pu M_5-edge spectra are not altered for neptunyl(V) and plutonyl(V)

compared with their An(VI) analogues. The shoulder feature attributed to 3d→5f$_{\delta/\phi}$ excitations remains for the +5 species, but is less resolved from the main peak compared with the +6 species. These assignments align with those made by Vitova et al. for a neptunyl(V) Np M_5-edge XANES spectrum.[20]

The most significant change in spectral profiles arises from uranyl(VI) to uranyl(V), with peaks 1 and 2 in the uranyl(V) M_4-edge spectrum no longer resolved, but are merged to a near single peak. While overall peak 1 in fig. 5.5 is attributed to a 3d→5f$_{\delta/\phi}$/π_u^* excitation, unlike in the Np and Pu M_5-edge case, the individual transitions can be separated into those characterised as 3d→5f$_{\delta/\phi}$ and 3d→π_u^*, with the former transitions coming first in energy and the latter coming toward the higher energy side of the peak. In table 5.6, a clear distinction in electron population levels for the π_u^* and 5f$_{\delta/\phi}$ orbitals is evident for the two 3d→5f$_{\delta/\phi}$ and 3d→π_u^* excitations, and supports the separate classification of these excitations under the same peak. Furthermore, unreported RAS(S) spectra also confirm that the excitations under the main absorption peak labelled 1 in the uranyl(V) spectrum, can be separated into those belonging to distinct 3d→5f$_{\delta/\phi}$ or 3d→π_u^* excitations. These peak assignment for uranyl(V) align with those reported by Zegke et al. for a uranyl(V) complex.[11]

In both sets of An(VI) and An(V) actinyl spectra, peaks assigned to 3d→5f$_{\delta/\phi}$ and 3d→π_u^* excitations are characterised by strong oscillator strength transitions contributing to the peak intensity. Peak intensity associated with 3d→σ_u^* excitations is much lower in comparison, with weak transitions associated with these excitations at the RAS(SD) level. This is not surprising since the intensity is driven largely through the degree of actinide-5f character in the acceptor orbital. The 5f$_{\delta/\phi}$ orbitals have pure 5f-character and π_u^* are dominated by actinide 5f character, hence the high transition strengths for the associated excitations. The σ_u^* orbitals remain largely covalent in their metal-ligand mixing with much lower actinide-5f contributions, and therefore give much weaker transition strengths for core-excitations involving these orbitals. Therefore peaks assigned to 3d→5f$_{\delta/\phi}$ and 3d→π_u^* excitations are characterised by a large number of strong oscillator strength transitions contributing to the overall peak intensity. For peaks assigned to 3d→σ_u^* excitations, the peak intensity comes from a collection of low oscillator strength transitions. This feature of RAS(SD) simulations was also found in chapter 4 for similar simulations,

Table 5.6: Total electron populations of the non-bonding $5f_{\delta/\phi}$ and anti-bonding valence SONOs for the SO-GS and key core-excited states associated with intense core-excitations attributed to peaks in An $M_{4/5}$-edge simulated spectra presented in figure 5.5.

Simulation	**Peak**	Assignment	$\mathbf{5f_{\delta/\phi}}$	$\boldsymbol{\pi_u^*}$	$\boldsymbol{\sigma_u^*}$
U(VI) M_4	1	$3d \rightarrow 5f_{\delta/\phi}$	0.97	0.09	0.01
	2	$3d \rightarrow \pi_u^*$	0.65	0.73	0.02
	3	$3d \rightarrow \sigma_u^*$	0.94	0.78	0.16
Np(VI) M_5	Shldr.	$3d \rightarrow 5f_{\delta/\phi}$	1.87	0.19	0.01
	1	$3d \rightarrow 5f_{\delta/\phi}/\pi_u^*$	1.73	0.55	0.02
	2	$3d \rightarrow \sigma_u^*$	1.77	1.08	0.10
Pu(VI) M_5	Shldr.	$3d \rightarrow 5f_{\delta/\phi}$	2.73	0.35	0.01
	1	$3d \rightarrow 5f_{\delta/\phi}/\pi_u^*$	2.35	0.78	0.01
	2	$3d \rightarrow \sigma_u^*$	2.78	1.08	0.08
U(V) M_4	1	$3d \rightarrow 5f_{\delta/\phi}$	2.00	0.35	0.07
	2	$3d \rightarrow \pi_u^*$	1.55	0.74	0.06
	3	$3d \rightarrow \sigma_u^*$	2.03	0.73	0.14
Np(V) M_5	Shldr.	$3d \rightarrow 5f_{\delta/\phi}$	2.50	0.55	0.04
	1	$3d \rightarrow 5f_{\delta/\phi}/\pi_u^*$	2.21	0.88	0.05
	2	$3d \rightarrow \sigma_u^*$	2.81	0.92	0.12
Pu(V) M_5	Shldr.	$3d \rightarrow 5f_{\delta/\phi}$	3.34	0.73	0.04
	1	$3d \rightarrow 5f_{\delta/\phi}/\pi_u^*$	3.07	1.01	0.04
	2	$3d \rightarrow \sigma_u^*$	3.26	1.34	0.16

with CESs associated with An $M_{4/5}$-edge simulations presenting multiconfigurational character that manifests through electron population of all RAS3 orbitals to varying degrees. Additionally, it was found that higher energy CESs show more pronounced multiconfigurational character and is driven by substantial electron re-distribution from RAS2 to RAS3 orbitals. This multiconfigurational character and behaviour identified in chapter 4, persists in the CESs of systems simulated in this chapter.

Interestingly, between the actinyls, the degree to which electron redistribution occurs from the bonding bonding orbitals that constitute RAS2 into the anti-bonding and non-bonding 5f orbitals that constitute RAS3, is fairly constant. Accounting for the unpaired electrons already present in the RAS3 orbitals, as well as the excited core-electron, gives the number of electrons that redistribute from RAS2 into RAS3 as 0.88 to 0.94 for the 3d→σ_u^* CESs when moving from uranyl(VI) to plutonyl(VI), respectively. While from uranyl(V) to plutonyl(V) the redistribution actually decreases from 0.90 to 0.76 in the 3d→σ_u^* CES, respectively. Therefore, any increased multiconfigurational character in the +5 oxidation state actinyls does not come from increased electron redistribution from bonding orbitals, and instead comes from the increasing number of unpaired electrons as the actinyl series is crossed. Given this, the CESs arising from plutonyl(V) M_5-edge simulations present the most multiconfigurational character simply due to the large number of unpaired electrons already present in the valence space of these states in the GS.

5.3.3.2 Predicting Oxidation-State Shifts in $M_{4/5}$-edge Spectra

Figure 5.6 presents the simulated An $M_{4/5}$-edge XANES spectra for each actinyl species in the +5 and +6 oxidation states. For a decrease in the actinide oxidation state (reduction), the main absorption peaks in the XANES spectra are expected to red shift, and is a key feature identified in experimental XANES spectra. This oxidation-state shift is the principle feature used in XANES experiments for determining a change in actinide oxidation state.[2] Simulations, as shown in fig. 5.6, demonstrate this key feature of experiment with the actinyl(V) species red shifted by ∼2 eV in all cases.

The XANES shifts due to oxidation state are reported in table 5.7. Shifts were measured between the maximum of the first absorption peak in the spectrum of each actinyl as indicated by dashed lines in fig. 5.5. Although an oxidation-state shift of

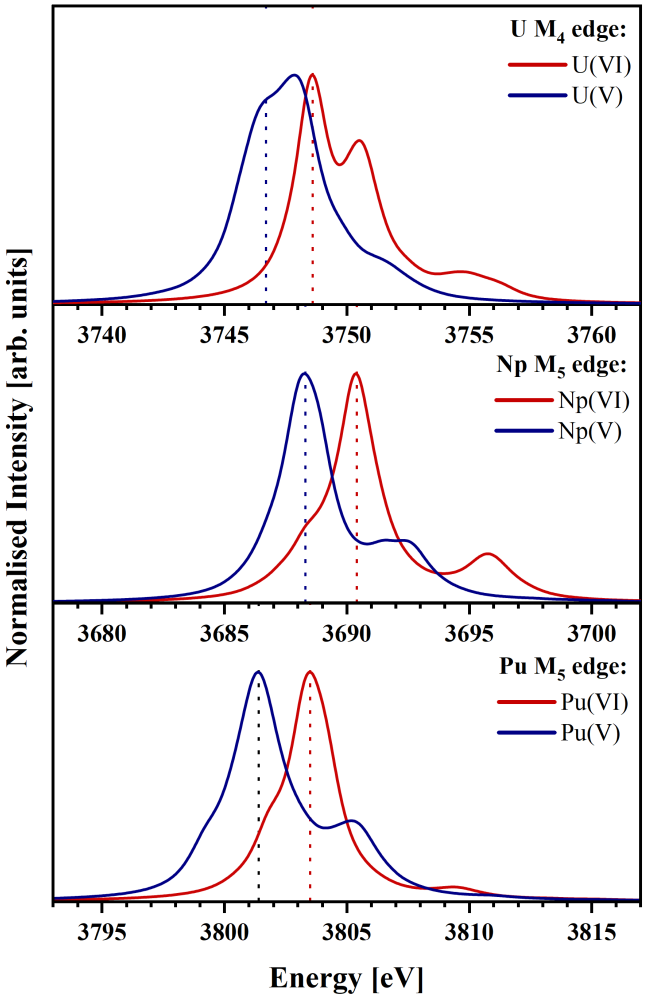

Figure 5.6: Simulated An $M_{4/5}$-edge XANES spectra presenting oxidation-state shifts due to a change in actinide oxidation state from +6 to +5. The first absorption peaks used to calculate the oxidation-state shift are identified with dashed vertical lines. No energy shifts have been applied to spectra.

~2 eV is not unreasonable for a change in oxidation state,[2] shifts from experimentally relevant references for An(VI/V) couples report oxidation-state shifts on the order of 0.4 - 0.6 eV,[11, 20, 91, 92] and indicate an overestimation from theory. For instance, the U(VI)/U(V) oxidation-state shift in the M_4-edge spectrum for uranyl 'Pacman' complexes is reported as 0.6±0.05 eV.[11] The same shift is reported between Np(VI) and Np(V) compounds reported by Vitova et al.[20] Comparing the main absorption peaks of $Pu(VI)_{(aq)}$ at ~3776.5 eV,[95, 96] with that of a $KPu^{V}O_2CO_3$ at 3775.9 eV,[90]

Table 5.7: Predicted absolute peak energies corresponding (dashed) vertical measurement lines in figure 5.6 which correspond to the first absorption edges in An(VI) and An(V) systems. The Chemical shift is the difference in energy for the two absorption edges. All energies are in electron-volts (eV).

Simulation	**An(VI) Abs.**	**An(V) Abs.**	**Oxidation-State Shift**
U(VI)/U(V) M_4	3748.6	3746.7	1.9
Np(VI)/Np(V) M_5	3690.4	3688.3	2.1
Pu(VI)/Pu(V) M_5	3803.5	3801.4	2.1

gives an estimate for a Pu(VI)/Pu(V) oxidation-state shift on the order of 0.6 eV as well. Bond length differences between An(VI) and An(V) species for the experimental references discussed are on the order of ∼0.1 Å,[11, 20] and is comparable to the predicted change in bond lengths for DFT predicted actinyl systems due to oxidation state. This suggests that the discrepancy in the predicted oxidation-state shifts reported in table 5.7 and those reported in experiment, likely does not originate from structural differences in the actinyls.

Accurately predicting the oxidation-state shift between two simulated spectra is expected to be difficult since a number of factors in the simulations can influence the position of the spectra with respect to each other. An accurate prediction of oxidation-state shift relies on the the RAS calculations predicting the exact energy positions at which two systems with differing electronic structures will present their absorption edges, and further relies on an accurate prediction of the relative separation between the GS and first CES, which will established the energy point at which the proceeding excitations between the GS and CESs will fall within each actinyl system. The ability of the RAS method to accurately predict the absorption edges differs between the actinyls, with simulations in chapter 4 on actinyls with experimental bond lengths requiring shifts of 21.9, 21.7 and 26.1 eV from uranyl to plutonyl, respectively, to align with experiment. The differing shifts required highlights how the RAS approach differs in the its capability to predict the absolute position of the absorption edge for different systems.

The key finding from the simulation results in this chapter, is that the RAS

methodology correctly predicts a red-shift of the reduced actinyl spectrum and also predicts a consistent oxidation-state shift value for actinyls across the series, and so too does experiment.

5.3.3.3 Understanding Oxidation-State Shifts in $M_{4/5}$-edge Spectra

The RAS simulations performed in this chapter can give useful insight into the underlying mechanism for oxidation-state shifts that occur in the $M_{4/5}$-edge XANES spectra. Literature explanations most commonly attribute the oxidation-state shift to electrostatic effects such as variations in the screening of the 3d-shell upon the addition or removal of electrons.[2, 4, 11–14] First the electrostatic effects on the actinide centre due to oxidation state is investigated using QTAIM analysis. Some degree of caution is required in such analysis, since changes in charge localisation on the actinide can also be affected by the nature of the ligands, with differences in covalent interactions changing the degree to which electron density is drawn onto or withdrawn from the actinide centre, affecting the position of the absorption edge.[12, 89, 97]

Table 5.8: Actinide localisation index λ(An) and QTAIM atomic charge q(An) for the SO-GSs and CES corresponding to the 3d→5f$_{\delta/\phi}$ excitation responcible for the first absorption peak in figure 5.6 for each actinyl system in the +6 and +5 oxidation state.

	λ(An)		**q(An)**	
Simulation	**GS**	**CES**	**GS**	**CES**
U(VI) M_4	86.64	86.83	3.50	3.15
U(V) M_4	87.30	87.70	3.05	2.78
Np(VI) M_5	87.76	88.15	3.35	3.11
Np(V) M_5	88.41	88.74	2.92	2.73
Pu(VI) M_5	88.89	89.27	3.22	2.99
Pu(V) M_5	89.53	89.80	2.80	2.67

The localisation index, which measures the number of electrons localised on the actinide

centre, and the QTAIM atomic charge, are both useful metrics for understanding the local changes that occur on the actinide centre due to oxidation state. These values are reported in table 5.8 for the +6 and +5 actinyl GSs and the 3d→5f$_{\delta/\phi}$ CES associated with the first peak in the XANES spectra used to calculated the oxidation-state shifts. QTAIM results indicate that a change in oxidation state has a direct effect on actinide electron localisation and atomic charge. The GS localisation indices increase from An(VI) to An(V) as to be expected upon addition of an electron. However, the difference in λ(An) values between the An(VI) and An(V) GSs in table 5.8 is not unity as might be expected from a classical picture of oxidation state change. Nonetheless, an increase in electron localisation on the actinide in the +5 oxidation state occurs, and reduces the effective nuclear charge compared to the An(VI) system, as confirmed by the lowering of local atomic charge from the An(VI) centre to An(V). Zimmermann et al.[14] explains that the "shift of the absorption edge occurs due to the change of the effective charge Z_{eff} of the nucleus" which affects "the binding energy of the core electrons" and hence the "the energy required to promote an electron from a core-level into an empty orbital results in a shift of the absorption edge to higher (oxidation) or lower (reduction) energy". While the QTAIM results presented here do not contradict this electrostatic argument for the observed shift, in the case of the actinyls, the explanation does not consider any potential stabilisation or destabilisation of the sometimes partially occupied 5f$_{\delta/\phi}$ orbitals. In the actinyls, these orbitals are responsible for the main absorption peaks that are used to calculate the oxidation-state shifts in $M_{4/5}$-edge spectra.

A more nuanced explanation for the observed XAS oxidation-state shift was proposed by Kubin et al.[15]. Kubin utilized a RAS approach to simulate the L-edge XAS spectra of Mn(II) and Mn(III) complexes and examined the relative energies of the GSs and the CESs responsible for the oxidation-state shift. It was proposed that shifts can be attributed to differences in electron affinity between the CESs, with greater stabilisation occurring for the CES in the reduced species. The greater stabilisation lowers the CES energy relative to the GS more substantially in the reduced species, making core-excitation more accessible, lowering the absorption edge. The same mechanism is explored to examine if it applies to the M-edge oxidation-state shifts for the actinyls.

Figure 5.7 shows the relative energies for the ground- and 3d→5f$_{\delta/\phi}$ core-excited states

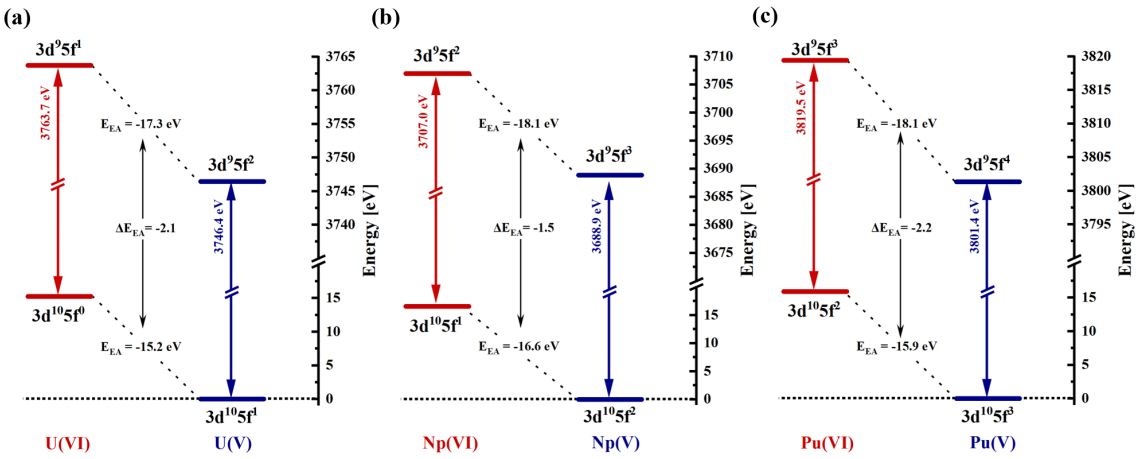

Figure 5.7: Total energy level diagrams (including spin-orbit coupling) of An(VI) and An(V) systems for the initial GS and 3d→5f$_{\delta/\phi}$ CES responsible for the first absorption peak in An M$_{4/5}$-edge XANES spectra. These diagrams were constructed based on those from Ref.[15] with permission from the Royal Society of Chemistry under the Creative Commons Attribution 3.0 Unported Licence.

responsible for the main absorption peak in the XAS spectra of An(VI) and An(V) actinyls. The state energy diagrams are adapted from those reported by Kubin et al.[15] and repurposed for the relevant states in the three actinyls systems. Regardless of the actinyl system, both the GS and CES of the An(V) species is relatively more stabilised compared with the An(VI) species, which come at higher energies. Additionally, in each system, a greater stabilisation occurs for the CESs than for the GSs when changing oxidation state from An(VI) to An(V). For example, in uranyl, the U(V) CES is 17.3 eV lower in energy compared with the U(VI) CES, and this is a much greater difference in energy than the 15.2 eV separating the U(VI) and U(V) GSs. The energy diagrams confirm a greater electron affinity in the An(VI) states, since the addition of electrons leads to a stabilisation of the state energy. Furthermore, the diagrams also confirm that the electron affinity in the An(VI) CES is greater than that of the An(VI) GS, since adding an additional electron to the CES yields a greater stabilisation of the state than it does when added to the GS. Therefore, access to the CES in the An(V) species is more accessible than in the An(VI) species, due to the high electron affinity of the An(VI) CES. This leads to a lower absorption peak in the XANES spectra for the reduced species since the core-excitation

energy is lowered. Taking the relative difference in stabilisation/electron affinity energies E_{EA} shown in fig. 5.7 between the An(VI) and An(V) states gives ΔE_{EA} values of ∼2 eV, which align with the oxidation-state shift values reported in table 5.7 for the simulated XANES. Therefore the mechanism for oxidation-state shifts in the L-edge of Mn complexes proposed by Kubin, also applies to the $M_{4/5}$-edge of the actinyls.[15]

Table 5.9: The number of Coulomb interactions in the GS and in the 3d→$5f_{\delta/\phi}$ CES associated with the first absorption peak assuming high spin configurations throughout. The number of Coulomb interactions between electrons in the $5f_{\delta/\phi}$ orbitals and in the actinide 3d orbitals is given by J_{df}. The number of Coulomb interactions between electrons within the $5f_{\delta/\phi}$ orbitals is given by J_{ff}. Differences in Coulomb interactions between the GS and CES for a given actinyl in the +6 or +5 oxidation state is given by ΔJ.

	GS		CES		Δ(CES - GS)	
	J_{df}	J_{ff}	J_{df}	J_{ff}	ΔJ_{df}	ΔJ_{ff}
U(VI)	0	0	9	0	9	0
U(V)	10	0	18	1	8	1
Np(VI)	10	0	18	1	8	1
Np(V)	20	1	27	3	7	2
Pu(VI)	20	1	27	3	7	2
Pu(V)	30	3	36	6	6	3

Kubin also performed additional analysis to examine the contributions of exchange and Coulomb interactions for electrons within the valence orbitals (3d-3d) and between core-orbitals (2p-3d) in each state of the Mn complexes. It was found that exchange interactions contributed negligibly to the XAS shift. Kubin points out that even if exchange interactions do play some role, the Coulomb interactions are about one order of magnitude larger than the exchange interactions and so the oxidation-state dependent L-edge XAS shift is still dominated by differences in the direct Coulomb interactions in

the final CESs.[15] Accounting for all Coulomb interactions in the GS and CESs, it was found that one additional 2p-3d and one less 3d-3d interaction occurred for the Mn(III) core-excitation. This finding is rationalised in terms of the "$Q-U$ explanation" proposed by van der Laan and Kirkman.[98] The calculated energies of the Slater 2p-3d Coulomb interactions (Q) are larger than the 3d-3d (U) for the Mn(III) core-excitation ($Q-U>0$), and therefore the CES shifts to higher energies in Mn(III) compared to Mn(II).

Assuming that the exchange interactions also contribute negligibly to the shift in actinyl M-edge XAS spectra, the same $Q-U$ explanation also applies. Counting the 3d-5f and 5f-5f Coulomb interactions between the GS and CES (table 5.9), finds that between the An(V) and An(VI) core-excitations (ΔJ_{df}, ΔJ_{ff}) one additional 3d-5f (Q) and one less 5f-5f Coulomb (U) interaction remains. This is the case for core-excitation in all three actinyl systems. Assuming $Q-U>0$ also applies here, the same explanation accounts for the higher An(VI) CES energy compared with An(V) in fig. 5.7 and the shift found for the actinyl M-edge spectra.

5.3.4 Covalency Analysis

5.3.4.1 Actinyl Ground-State Covalency:

Table 5.10 presents the GS QTAIM data for actinyl systems in the An(VI) and An(V) oxidation states. Across the actinide series, in both oxidation states, the ρ_{BCP}(An, O) and δ(An, O) metrics indicate an increasing actinyl bond covalency which correlates with decreasing bond lengths across the series. This finding is in good agreement with previous studies.[26, 27, 81, 94] For a given actinyl system, a change in oxidation state from An(VI) to An(V), leads to a decrease in actinyl covalency, with notable decreases in both ρ_{BCP}(An, O) and δ(An, O) upon reduction. This lower covalency coincides with a 0.07Å increase in the theoretical bond length for the actinyl(V) species. From an entirely electrostatic perspective, adding an additional electron to the actinide centre would reduce the effective nuclear charge of the actinide (shown previously by examining q(An) values in table 5.8), and therefore reduce its electronegativity. This would account for the lower ρ_{BCP}(An, O) and δ(An, O) values in the reduced species since the electron withdrawing ability of the actinide is diminished.

In the previous section, it was identified that reduction of the actinide centre does

Table 5.10: Ground-state QTAIM metrics for each actinyl An $M_{4/5}$-edge simulation in +6 and +5 oxidation states. Table reports the electron density at the An-O bond critical point ρ_{BCP}, delocalisation index between the an actinide and oxygen ligand δ(An, O), as well as localisation indexes for actinide and oxygen centres λ. Analysis is performed on RAS(SD) electron densities.

Simulation	$\boldsymbol{\rho_{BCP}}$	$\boldsymbol{\delta}$**(An, O)**	$\boldsymbol{\lambda}$**(An)**	$\boldsymbol{\lambda}$**(O)**
U(VI) M_4	0.35	1.86	86.64	7.79
Np(VI) M_5	0.37	1.89	87.76	7.69
Pu(VI) M_5	0.38	1.90	88.89	7.62
U(V) M_4	0.29	1.65	87.30	8.18
Np(V) M_5	0.30	1.67	88.41	8.10
Pu(V) M_5	0.31	1.68	89.53	8.03

not lead to a unitary increase in the localisation index, instead, table 5.10 reveals partial localisation onto the ligands as well as the metal centre. In all three actinyl GSs, the reduction from +6 to +5, leads to an increase of ∼0.7 and ∼0.4 in the localisation indices of the actinide and oxygen centres, respectively. The asymmetry in localisation, aligns with the decrease in actinide positive charge overall. The increased localisation of electrons onto all three centres in the actinyls comes with a ∼0.2 reduction to the δ(An, O) value of each bond. Overall, the GS QTAIM metrics highlight a deviation from the idea that a change in oxidation state amounts to localised change on the metal centre, but rather indicates how changes in oxidation state involves electronic changes across the system.

5.3.4.2 Covalency Determination from An $M_{4/5}$-edge XANES

5.3.4.2.1 QTAIM Analysis of the Core-Excited State

Figure 5.8 presents the ρ_{BCP}(An, O) and δ(An, O) values for the GS and key CESs associated with peaks in the XANES spectra reported in fig. 5.5. For a given actinyl system, the CES ρ_{BCP} values remain relatively similar or show a slight decrease in value

compared to the GS, changing by no more than 0.03 a.u. The largest decreases in ρ_{BCP} for a given system between the GS and CESs is associated with 3d$\rightarrow \sigma_u^*$ excitations (final peak). For these excitations the CESs present the largest re-distribution of electrons from bonding (RAS2) to anti-bonding orbitals (RAS3).

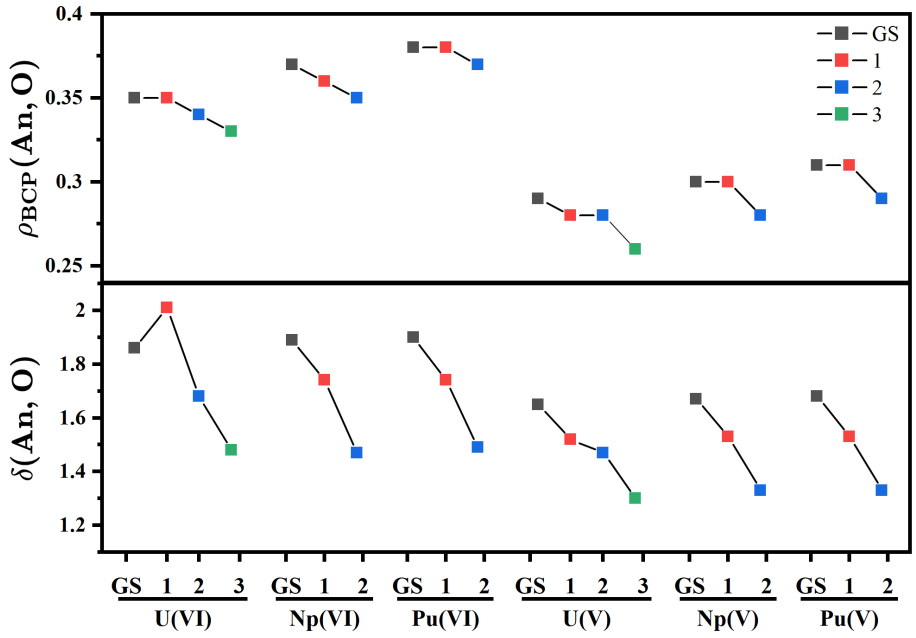

Figure 5.8: Plot of (top) electron density at the An-O bond critical point ρ_{BCP} and (bottom) delocalisation index between an actinide and oxygen centre δ(An, O) in the GS and for each key CES attributed to peaks (1,2 or 3) in table 5.6. ρ_{BCP} values are in atomic-units.

In the GS, ρ_{BCP} values increase across the actinide series for both the An(VI) and An(V) systems. The ρ_{BCP} values for the CESs plotted in fig. 5.8, show that in general, values also increase across the actinyl series. For instance, the final XANES peaks for uranyl to plutonyl all correspond to the 3d$\rightarrow \sigma_u^*$ excitation, and the resulting ρ_{BCP} value in the associated CES increases across these systems.

In the GS, the δ-values increase across the actinide series for both An(VI) and An(V) systems. However, unlike the GS and CES ρ_{BCP} values, there is no clear increasing or decreasing trend in δ-values that be discerned for the CESs across the actinide series in either oxidation state. The delocalisation index is found to be a more sensitive metric for changes in covalency between the GS and CESs, with this metric capturing changes in

Table 5.11: Changes in delocalisation index $\Delta\delta$(An, O) and localisation index $\Delta\lambda$ for actinide and oxygen centres, between the GS and CESs in different actinyl An $M_{4/5}$-edge simulations. Analysis is performed on RAS(SD) electron densities.

Simulation	**Peak**	Excitation	**$\Delta\delta$(An, O)**	**$\Delta\lambda$(An)**	**$\Delta\lambda$(O)**
U(VI) M_4	1	3d $\rightarrow$ $5f_{\delta/\phi}$	+0.15	+0.20	-0.26
	2	3d $\rightarrow$ π_u^*	-0.18	+0.38	-0.02
	3	3d $\rightarrow$ σ_u^*	-0.38	+0.62	+0.08
Np(VI) M_5	1	3d $\rightarrow$ $5f_{\delta/\phi}/\pi_u^*$	-0.15	+0.39	-0.06
	2	3d $\rightarrow$ σ_u^*	-0.42	+0.56	+0.15
Pu(VI) M_5	1	3d $\rightarrow$ $5f_{\delta/\phi}/\pi_u^*$	-0.16	+0.39	-0.06
	2	3d $\rightarrow$ σ_u^*	-0.41	+0.52	+0.15
U(V) M_4	1	3d $\rightarrow$ $5f_{\delta/\phi}$	-0.14	+0.41	-0.07
	2	3d $\rightarrow$ $5f_{\delta/\phi}/\pi_u^*$	-0.18	+0.41	-0.03
	3	3d $\rightarrow$ σ_u^*	-0.35	+0.55	+0.08
Np(V) M_5	1	3d $\rightarrow$ $5f_{\delta/\phi}/\pi_u^*$	-0.14	+0.32	-0.04
	2	3d $\rightarrow$ σ_u^*	-0.34	+0.46	+0.11
Pu(V) M_5	1	3d $\rightarrow$ $5f_{\delta/\phi}/\pi_u^*$	-0.14	+0.27	-0.02
	2	3d $\rightarrow$ σ_u^*	-0.35	+0.39	+0.15

bonding through all orbital interactions.

With the exception of the 3d$\rightarrow$ σ_u^* CESs and the 3d$\rightarrow$$5f_{\delta/\phi}$ CES in uranyl(VI) which is discussed separately, all other CESs in table 5.11 present $\Delta\lambda$(O) values which indicate effectively no change in electron localisation on the oxygen centre between the GS and CESs. For the 3d$\rightarrow$ σ_u^* CESs, an increase in λ(O) values is found, with Coulombic repulsion between electrons in the $5f_{\delta/\phi}$ and the σ_u^* orbitals thought to be responsible.

The rationalisation for substantial decrease in λ(O) and increase in δ(An, O) for the 3d→5f$_{\delta/\phi}$ CES in uranyl(VI) was outlined in chapter 4, and is thought to arise from electron donation to bonding interactions in order to balance the larger effective nuclear charge on the actinide due to insufficient shielding of the 3d core-hole. Furthermore, effectively no electron redistribution from the bonding orbitals to the anti-bonding orbitals occurs for this particular state (with a 0.07 reduction in the total population of the bonding orbitals), limiting the negative impact to bonding interactions.

A change in oxidation state has a notable effect on the strength of bonding interactions in both the GS and CESs, with a clear drop in both ρ_{BCP}(An, O) and δ(An, O) values in fig. 5.8 between the An(VI) and An(V) systems. While the magnitude of QTAIM metrics differ due to oxidation state, the similar changes in QTAIM metrics between the GS and CESs reported in table 5.11 for both An(VI) and An(V) systems indicates that the number of 5f$_{\delta/\phi}$ electrons has little influence on the core-excitation process, since similar charge redistribution is found in all three actinyl systems and between the +6 and +5 oxidation states.

5.3.4.2.2 Orbital Composition Analysis in the Core-Excited State

Investigation into the degree to which the bonding orbitals differ between the GS and CESs is continued from chapter 4, examining the actinyls in both the +6 and +5 oxidation states. In this chapter, additional orbital composition analysis methods were exhausted to obtain an informative picture of orbital changes. This ensures conclusions are not biased by the results of a single composition approach. In the previous chapter, a combination of AIM and NLMO results indicated a minimal change in the compositions for both the π- and σ-bonding orbitals in uranyl(VI) and neptunyl(VI). This suggests that M$_{4/5}$-edge XANES is a valid probe of GS covalency in those systems. For plutonyl, both π- and σ-bonding orbitals present greater An% contributions in the CES compared with the GS, representing an overestimation of the ground-state covalency when using the An M-edge as a covalency probe. The AIM and NLMO analysis performed for the actinyls(VI) in this chapter, set to theoretical bond lengths, reconfirm similar findings.

Figure 5.9 presents the changes in An% contributions to the (a) π- and (b) σ-bonding orbitals between the GS and the (a) 3d→ π_u^* and (b) 3d→ σ_u^* CESs, respectively. An

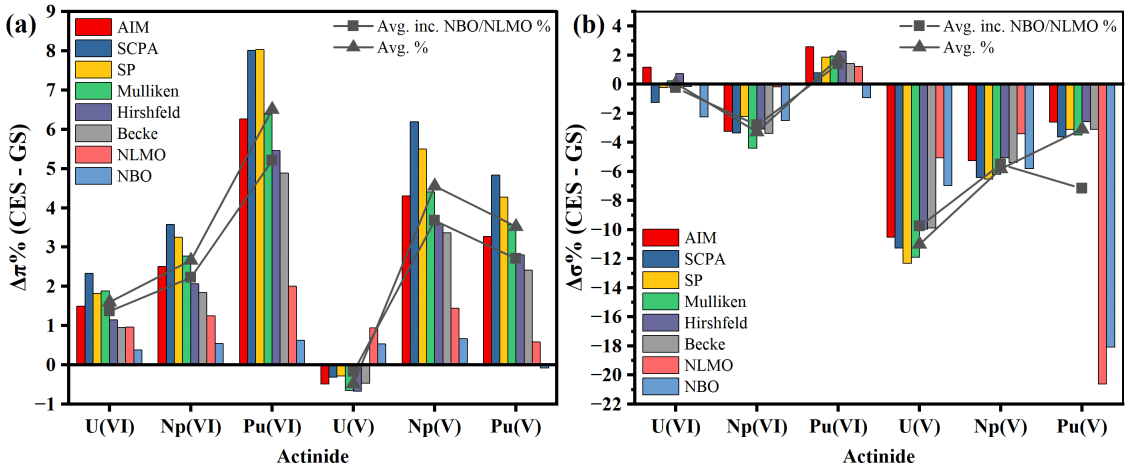

Figure 5.9: Calculated differences in actinide contributions to (a) π and (b) σ bonding orbitals between the ground and core-excited states. Orbital compositions were obtained using a variety of methods and two different averages were take, one including the NBO-type results and one without.

average across the methods both with and without natural bond orbital based approaches (NBO/NLMO) is taken to give a general average trend of composition changes. For the π-bonding orbitals, an increase in An% contribution in the CES is identified from uranyl(VI) to plutonyl(VI). The average An% compositions in the CES π-bonding orbitals remains within ∼3% of the GS for uranyl and neptunyl, but increases more substantially for plutonyl. The average An% compositions in the CES σ-bonding orbital remains effectively unchanged for uranyl, decreases by $\sim$ 3% for neptunyl and increases in plutonyl by $\sim$ 2%. For the actinyls in the +6 oxidation states, all methods predict largely comparable bonding orbitals in the GS and CESs for uranyl and neptunyl. The σ-bonding orbitals are also largely comparable for plutonyl between the GS and CESs, but changes in the π-bonding orbitals are significant. The same variety of orbital composition approaches was also utilized for the reduced actinyl(V) systems. Actinide contributions to the π-bonding orbitals in the CESs remain comparable to the GS for uranyl(V), but are significantly higher in the CESs for neptunyl(V) and plutonyl(V). An% contributions to the σ-bonding orbitals are reduced in the CESs compared to the GS, with the most substantial decrease being for uranyl(V) by as much as $\sim$ 12%, followed by neptunyl(V) ($\sim$ 6%) and plutonyl(V) ($\sim$ 3%) when excluding NBO and NLMO results.

On the whole, orbital composition approaches are all in good agreement for the relative changes in actinide contribution to the bonding orbitals between the GS and CESs. While the scale of values might differ, the overall trends lead to similar qualitative pictures of the changes that occur due to core-excitation. The NBO and NLMO approaches in most cases align with the results of the other methods. A key exception being for the compositional changes to the σ-bonding orbital in the actinyl(V) systems. Here, both the NBO and NLMO approach predict substantial decreases in the actinide contribution to the σ-bonding interactions between the GS and 3d$\rightarrow \sigma_u^*$ CES for the plutonyl(V) system. This anomaly in the data originates due to the non-existence of a σ-NLMO interaction, instead the approach finds a doubly occupied three centre σ-NLMO, suggesting a more delocalised nature to the interaction. Despite this, an An% was still obtained from the three-centre bonding orbital and plotted. A similar three-centre bonding orbital also arises in the NBO analysis.

In the previous chapter, orbital composition changes were thought to be largely impacted by two competing effects:

1. Occupation of anti-bonding orbitals of predominantly metal character in the CES perturbs charge density away from the actinides in the bonding orbitals.

2. Increased effective nuclear charge on the actinide centre due to the presence of the core-hole draws charge density to this centre.

The outlined effects were used to rationalise both the changes in composition for bonding orbitals between the O K-edge GS and CESs, as well as for the U(VI) M_4- and Np(VI) M_5-edge CESs. For instance, in both uranyl and neptunyl M-edge CESs, the two effects largely cancel, leaving the bonding orbitals in the GS and CESs relatively similar in composition. However, the rationalisation begins to break down for plutonyl(VI), whereby an increase in An% contributions to both the π- and σ-bonding orbitals is somewhat puzzling. In the CESs, it is assumed that the electron withdrawing effects due to the actinide core-hole will diminish as the number of 5f electrons increases, either due to a change in oxidation state or simply moving across the actinyl series. This implies that any changes to orbital compositions that increases An% contributions would not be accounted for via the first effect outlined above (1). Instead, some additional factors

must be influencing the charge distributions between the GS and CESs, such factors could include:

3. Coulombic effects arising from increasing electrons in the $5f_{\delta/\phi}$ orbitals, acting to 'push' charge density away from the actinide centre in the bonding orbitals.

4. The initial distribution of charge density in the ground-state bonding orbitals will impact the energetic favourability to perturb the orbitals upon core-excitation. For example, in orbitals with high oxygen character in the GS a 'push' of charge density toward the oxygen centres in the CES is associated with an energetically unfavourable change in the charge distribution all other things being equal.

Factor 3 was raised by Autschbach and co-workers, who identified potential Coulomb effects as impacting the changes in σ-covalency between the GS and CES for neptunyl and plutonyl.[27] For the second factor, assuming limited influence from the changes occurring in other orbitals, the nature of hybridisation for an orbital of interest in the GS is likely to influence the energetic favourability of a perturbation in orbital mixing when transitioning into the CES. For example, the π-bonding orbital charge density distribution can be characterised as ionic, since a greater amount of charge density resides on the ligands than on the metal. In this case, any influence that re-distributes charge away from the ligands in the π-bonding orbitals can be considered energetically favourable, while the opposite effect would be energetically unfavourable.

Providing a correct balance of all the influences outlined above to explain the orbital composition changes in fig. 5.9 is a challenge, especially as the number of electron interactions increases across the series and in the reduced species, hence the reason why simulations are utilized to quantitatively calculate changes in electronic structure. However, some qualitative explanations can be applied. For the +6 oxidation state, uranyl and neptunyl bonding orbital changes, as outlined in the previous chapter, can be explained by a cancellation of effects (1) and (2). In this chapter this largely holds, but the gradual increase in An% contribution to the π-bonding orbitals across the actinyl series in both the +6 and +5 oxidation states is attributed primarily to Coulombic interactions (3). Increased Coulomb interactions between electrons in the $5f_{\delta/\phi}$ orbitals and the π_u^* orbital repels charge density in the anti-bonding orbitals away from the metal centre,

which results in the opposite compositional change to the bonding orbitals as a response. This redistribution of charge density toward the actinide centres in the CES π-bonding orbitals is also an energetically favourable process, since it leads to a reduction in the ionic character of the orbitals compared to in the GS (4).

For the 3d→ σ_u^* CESs, a change in composition for the already covalent σ-bonding orbitals in the GS is an energetically unfavourable process. This energetic resistance to a change in the composition, combined with the effects outlined above (1 to 3), lead on the whole to a cancellation of effects for the actinyl(VI) systems, and the bonding orbitals remain similar between the GS and CES. For the σ-bonding orbitals in the actinyl(V) systems, the balance of effects leads on the whole to a decrease in actinide contributions to the orbitals in the 3d→ σ_u^* CESs.

While qualitative explanations have been applied to explain certain aspects of the results, care must be taken in interpreting the changes that occur within individual orbitals. QTAIM analysis metrics examined in this chapter are based on the total electron density, therefore these metrics give a full account of the changes that occur due to the differing electronic structures between the GS and CESs. On the other hand, changes to an individual orbital may be counter-intuitive. For example, QTAIM results reveal a net localisation of charge density onto the actinide centre in the CES. However, for a specific bonding orbital, there is no requirement that a similar charge redistribution toward the actinde centre must take place. Instead, it is the accumulation of all the particular and individual changes across the whole set of orbitals from the GS to the CES, which, through the electron density leads to a net charge density on the actinide centre.

5.3.4.2.3 XANES Peak Positions as Covalency Indicators

A number of studies have proposed a link between the energy separation of the 5f-$\sigma_u^*$and the 5f$_{\delta/\phi}$ peaks and the axial bond length.[11–13, 16–20] A larger separation (5f-σ_u^* shift) is interpreted as greater destabilisation of the the σ_u^* orbital, which as a result of the PFB mechanism, indicates a strengthening of the σ_u orbital covalency.[13, 18, 21, 22] From the studies, it is clear that a link between greater axial bond lengths and a reduced 5f-$\sigma_u^*$and 5f$_{\delta/\phi}$ peak separation can be established within a given actinyl. This includes changes in bond lengths due to the ligand environment but also changes due

to a reduction of the actinyl system from the +6 to the +5 oxidation state. Vitova et al. investigated changes in 5f-σ_u^* and 5f$_{\delta/\phi}$ $M_{4/5}$-edge peak separations between the actinyls(VI) and found, to their surprise, that peak separations were largest for uranyl and smallest in plutonyl, indicating a decrease in axial covalency across the series.[18] This was found puzzling since bond lengths contract across the series and recent studies report increasing covalency across the actinyl series.[24–26] Autschbach and co-workers utilized RAS approaches to simulate the $M_{4/5}$-edge of the actinyls.[27] Here it was found that the experimental trend reflected a decreasing σ_u covalency in the CESs rather than the GS, resolving the puzzle. Somewhat surprisingly, neither studies considered whether a contraction of the bond length is accounted for by changes in covalency or changes in actinide ionic radii. Table 5.12 reports the experimental and PBE0 derived actinyl bond lengths as well as the Shannon ionic radii.[99] Indeed, the change in experimental bond lengths (0.01 Å) across the series can be explained by a decrease in actinide ionic radius across the series. Since the theoretical bond lengths of the An(V) actinyls change by the same trend as the An(VI) actinyls, these too are suspected to be explained by changes in ionic radii.

Table 5.12: $[AnO_2(H_2O)_5]^{2+/+}$ An-O bond lengths from PBE0 optimisations and from experiment,[18, 76] and Shannon ionic radii of the actinide-ions in +6 and +5 state,[99] all values are reported in angstroms (Å).

System	Expt. An-O	PBE0 An-O	Ionic Radius
$[UO_2(H_2O)_5]^{2+}$	1.76	1.74	0.73
$[NpO_2(H_2O)_5]^{2+}$	1.75	1.72	0.72
$[PuO_2(H_2O)_5]^{2+}$	1.74	1.70	0.71
$[UO_2(H_2O)_5]^{+}$		1.81	0.76
$[NpO_2(H_2O)_5]^{+}$		1.79	0.75
$[PuO_2(H_2O)_5]^{+}$		1.77	0.74

Rather than focus on whether 5f-σ_u^* shifts correlate with the actinyl bond lengths,

this section aims to establish whether the shifts are indicators of axial covalency through comparison with QTAIM and orbital composition analysis.

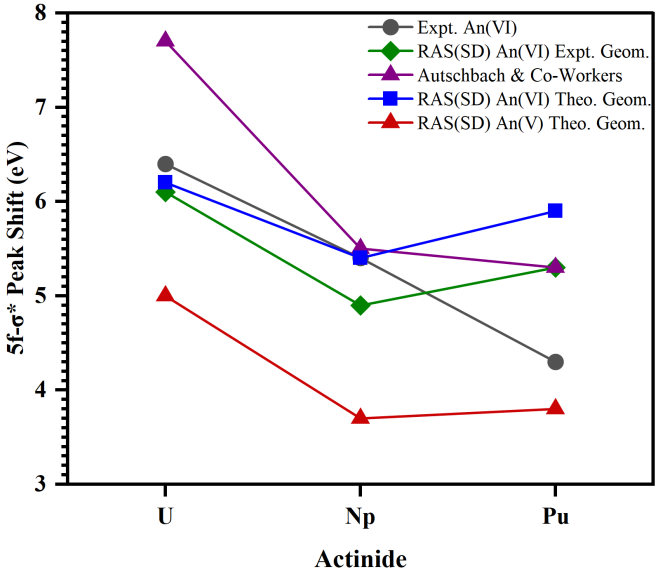

Figure 5.10: Energy shifts between the 5f-σ_u^* and 5f$_{\delta/\phi}$ peaks in An M$_{4/5}$-edge XANES simulated spectra for actinyl systems reported in fig. 5.5. Plot includes the experimental energy shifts from Vitova et al.,[18] and the predicted energy shifts from Sergentu et al.[27] Plot also includes energy shifts taken from fig. 4.4 for comparison.

Figure 5.10 presents the relative separation of the 5f-σ_u^* peak with respect to the 5f$_{\delta/\phi}$ peak from the experimental work of Vitova et al.[18] and the theoretical work of Autschbach and co-workers, [27] both of which examine trends in covalency for actinyls in the +6 oxidation state. Alongside the literature trends, the separations measured from the work in this chapter (figure 5.5) using actinyls informed by theoretical bond lengths and work from the previous chapter using experimentally informed bond lengths (figure 4.4) are plotted. The actinyl(V) data from this chapter is also plotted to examine trends across the actinyl series in the +5 oxidation state as well as examine changes in covalency for a given actinyl in the +6 and +5 oxidation states.

The experimental trend for An(VI) actinyls suggests a decreasing overlap driven covalency across the series since the 5f-σ_u^* peak shift decreases from uranyl to plutonyl. QTAIM analysis of the actinyl(VI) systems in the previous sections revealed an increasing

ρ_{BCP} across the actinyl series in the GS, suggesting an increasing overlap driven covalency. This also holds largely true for the actinyl(VI) systems informed by experimental bond lengths, but the QTAIM changes are less notable. Therefore the experimental trend appears to contradict the GS QTAIM results which suggest an increasing covalency across the series.

The predicted 5f-σ_u^* peak shifts for the theoretical and experimentally informed actinyl(VI) systems decreases from uranyl to neptunyl, but increases from neptunyl to plutonyl. The predicted peak shifts follow the experimental trend from uranyl to neptunyl, and correctly predict a lower shift for plutonyl compared to uranyl in both the experimental and theoretical actinyl(VI) sets. However, taking the predicted trend as a whole from uranyl to plutonyl, indicates that the 5f-shift for plutonyl is overestimated compared to the trend found in experiment. Similar results are found when examining the predictions of Autschbach and co-workers.[27]

Interpreting the theoretical actinyl(VI) 5f-σ_u^* peak shifts, suggests that the axial covalency of uranyl is greater than in neptunyl and plutonyl, while plutonyl has greater axial covalency than neptunyl. This does not fit with the GS QTAIM data since ρ_{BCP} values increase from U to Pu. Similarly, the DI values also increase across the series. While both metrics point to an increasing covalency from U to Pu, the change in values is not linear and hints that the covalency increases between U and both Np and Pu is greater than between Np and Pu. The predicted 5f-σ_u^* peak shifts for the theoretical actinyl(V) systems largely follow a similar trend to the actinyl(VI) systems. The shifts suggest a greater covalency for uranyl(V) compared to both neptunyl(V) and plutonyl(V), while a small increase in 5f-σ_u^* peak shift for plutonyl compared to neptunyl, indicates a slight increase in covalency for the former over the latter. QTAIM analysis reveals increasing ρ_{BCP} and δ(An, O) GS values from uranyl to plutonyl, which indicates a decreasing bond covalency from the former to the latter. In contrast to An(VI) systems, the changes in ρ_{BCP} increase linearly across the series. However, the QTAIM changes do not align with the predicted 5f-σ_u^* shifts in fig. 5.10.

As shown in fig. 5.8, the ρ_{BCP} values of the CES associated with the final 5f-σ_u^* peak increases across the series for both the +6 and +5 oxidation state actinyl systems. Therefore, the experimental trend does not reflect a decrease in overlap driven covalency

in the CESs across the actinyl series. This also applies to the predicted 5f-σ_u^* shifts for actinyls using theoretical bond lengths. The δ(An, O) data in both the actinyl(VI) and actinyl(V) systems suggest a decrease in covalency from uranyl to neptunyl, however this does not manifest as a larger 5f-σ_u^* peak shift for neptunyl compared with uranyl, instead the opposite is found. Overall, the increasing covalency indicated by QTAIM metrics across the actinyl series in the An(VI) and An(V) GSs, as well as in the CESs, do not correlate with 5f-σ_u^* shifts in fig. 5.10. A possible reason for the 5f-σ_u^* shifts not correlating with either ρ_{BCP} or δ(An, O) metrics could be due to the fact these metrics incorporate covalency contributions from both the σ_g and σ_u bonding orbital interactions. Instead of reflecting the overall axial covalency across the series, it is possible that the 5f-σ_u^* shifts only correlate with the specific covalency contribution from its σ_u bonding orbital. This requires further investigation in the future, perhaps by using symmetry decomposed QTAIM analysis.

For a given actinyl system, correlations between the simulated $M_{4/5}$-edge 5f-σ_u^* shifts and changes in covalency due to bond length or oxidation state are confirmed. For instance, all the 5f-σ_u^* shifts are lower in the experimentally informed actinyl(VI) structures compared to those informed by theory, with the ρ_{BCP} values in both the GS and 3d$\rightarrow \sigma_u^*$ CES also lower in the experimentally informed structures. The difference in ρ_{BCP} values between experimental and theoretical actinyl(VI) structures in both the GS and CES is on the order of 0.02 a.u., which increases to 0.03 for neptunyl(VI), and increases again to 0.04 for plutonyl, aligning with the increasing 5f-σ_u^* shift gap between the structures set to theoretical and experimental bond lengths across the series.

In fig. 5.10, the simulated 5f-σ_u^* peak shifts also decrease upon reduction of a given actinyl from the +6 to +5 oxidation state. This reduction in 5f-σ_u^* shifts in the reduced species also come with decreases in ρ_{BCP} and δ(An, O) GS values by up to 0.07 a.u. and 0.22, respectively. Simulations predict a drop of 1.2, 1.7 and 2.1 eV for U, Np and Pu actinyl 5f-σ_u^* shifts upon reduction from An(VI) to An(V). Oxidative reduction of uranyl from U(VI) to U(V) has been shown to reduce the 5f-σ_u^* shifts by between 1.5-2.2 eV in a number of studies,[11, 18, 20] and is comparable with the 1.2 eV predicted from fig. 5.10. Between Np(VI) and Np(V), the 5f-σ_u^* shift have been found to reduce by up to $\sim$3.3 eV, which is less consistent with the predicted 1.7 eV from simulations in this chapter.[20]

5.3.4.2.4 Covalency of the σ_u-Bonding Orbital

Focus in this section turns specifically to the σ_u bonding orbital, to examine whether the 5f-σ_u^* shifts correspond directly to σ_u orbital mixing. To ensure the picture of covalency is not biased by a single approach, a number of orbital composition schemes were explored. To facilitate comparison, the percentage of actinide contribution (An%) to the σ_u bonding orbital was converted into a quantitative measure of the deviation from ideal 50%:50% covalent mixing. This is defined as Λ_{mix}, where $\Lambda_{\text{mix}} = 1 - |\text{An\%} - 50\%|/50\%$. The parameter Λ_{mix} provides a scale from 0 to 1, where a value of 0 corresponds to a significant deviation from ideal covalent mixing, while a value of 1 indicates perfect 50%:50% mixing. The results of this measure for the actinyls in both +6 and +5 oxidation state as well as in the GS and CES is plotted in fig. 5.11.

In the GS, the σ_u covalency trends predicted by each method (excluding NBO and NLMO for now) are consistent with one another for both actinyls in the +6 (a) and +5 (b) oxidation states. For the +6 actinyls, the methods predict a decrease in σ_u covalency in the GS from uranyl to neptunyl, but is followed by a small increase from neptunyl to plutonyl. These results align more closely with the An(VI) simulated 5f-σ_u^* shift data rather than the experimental data, with the latter predicting a lower covalency for plutonyl compared to neptunyl. In fig. 5.11(b), all methods - excluding NLMO and NBO - predict an almost linear decrease in the σ_u bond covalency in the CES across the actinyl(VI) series. This trend aligns best with the experimental An(VI) 5f-σ_u^* shift data and the conclusion reached by Autschbach and co-workers using NLMO analysis.[27]

For the actinyl(V) systems, no experimental 5f-σ_u^* shift data is available. Most methods predict a gradual decrease in GS σ_u covalency across the An(V) actinyl series, which does not exactly align with the trend suggested by simulated 5f-σ_u^* shift data. Specifically, the shift data indicates a substantial decrease in covalency between uranyl(V) and neptunyl(V), followed by a slight increase in covalency for plutonyl(V). The GS Λ_{mix} data shown in fig. 5.11(c) is consistent with the actinyl(V) 5f-σ_u^* shift data in predicting greater σ_u covalency in uranyl(V) compared to the other systems. However, it does not reflect the large changes in the σ_u covalency between uranyl(V) and neptunyl(V), nor the minor increase in σ_u covalency between neptunyl(V) and plutonyl(V). For the CES Λ_{mix} data shown in fig. 5.11(d), methods provide differing predictions for σ_u covalency in the

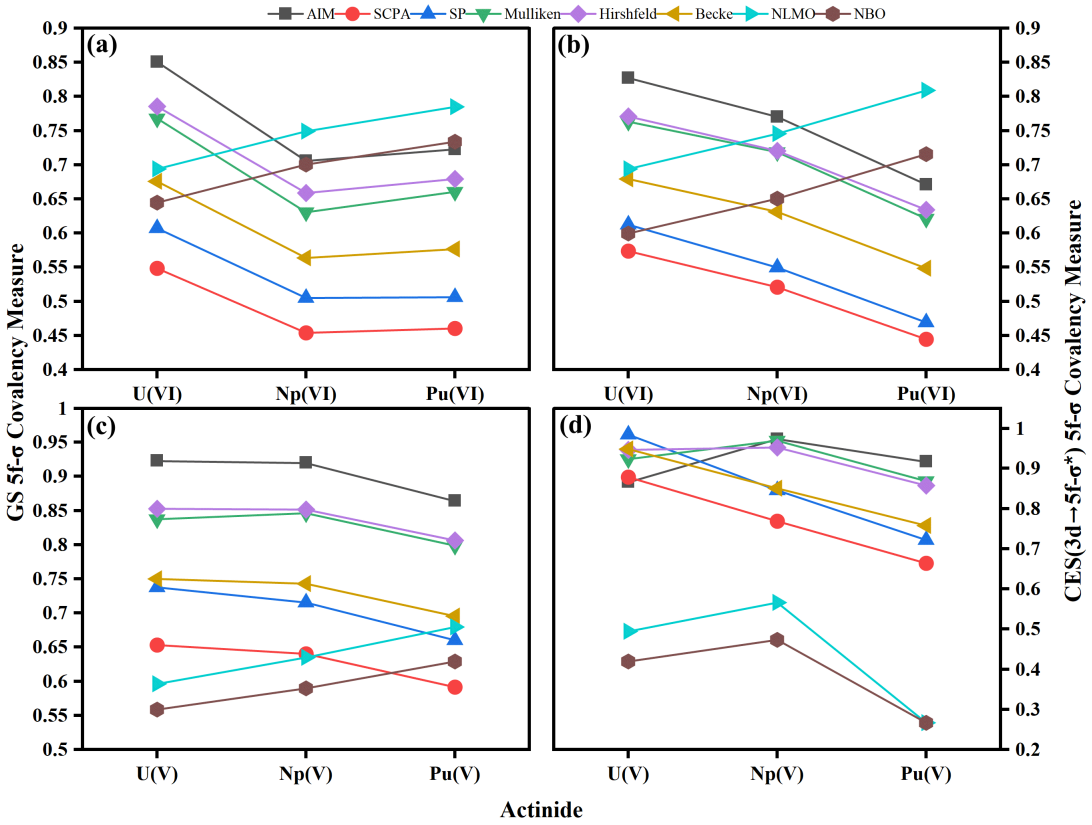

Figure 5.11: Orbital covalency of the actinyl σ_u bonding orbital in the GS (a,c) and 3d$\rightarrow \sigma_u^*$ CES (b,d) in the +6 (a,b) and +5 (c,d) oxidation states. The orbital covalency measure is obtained by calculating the degree to which the actinide contribution to the bonding orbital deviates from the idealised 50%:50% covalent mixing as follows: $\Lambda_{\text{mix}} = 1 - |\text{An}\% - 50\%|/50\%$. Giving a measure between 0 and 1, with 1 being exact 50%:50% covalent orbital mixing, while values < 1 correspond to deviations away from this covalency. An% contributions were obtained using a variety of orbital composition methods.

CES regarding neptunyl. The SCPA, Becke and SP approaches predict a linear decrease in the σ_u covalency across the series, which is consistent with the 5f-σ_u^* shift data indicating that uranyl(V) has greater covalency than neptunyl. However, the shift data suggests that covalency either remains similar or increases toward plutonyl, which is not reflected in the Λ_{mix} data. In contrast, the AIM, Mulliken, and Hirshfeld approaches predict an increase in σ covalency from uranyl to neptunyl, followed by a slight decrease toward plutonyl, which does not align with the 5f-σ_u^* shift data. Overall, there is no clear correlation between the

Λ_{mix} data for the CES in the actinyl(V) systems and the predicted 5f-shifts.

NLMO and NBO methods were also employed, predicting an increasing σ_u covalency for both the An(VI) and An(V) GSs across the acitnyl series, as well as in the An(V) CES. This trend continues for the An(V) CES between uranyl and neptunyl, but the covalency drops for plutonyl. This drop may be artificial, as no σ-bonding NLMO or NBO was identifiable; instead, a three-centre σ-interaction was found with a significantly lower An% contribution. Overall, the NBO-type approaches do not align with the covalency trends indicated by the Λ_{mix} data for the +6 and +5 actinyls systems, either in the GS or CES.

The results indicate the need for careful consideration when choosing a particular orbital composition method. In the majority of cases, the methods find qualitative agreement for trends, but as shown in the case of the An(V) actinyl CESs, disagreement in the trends can arise. The largest differences are found between the Mulliken-like approaches and the NBO approaches, predicting opposite trends in most cases. This is thought to arise since the NBO approach enables both 6d and 5f orbital contributions to the construction of the resulting σ-bonding NLMO or NBOs. Since the other methods only decompose the existing orbital into a set of atomic orbital contributions, the symmetry restrictions are not broken.

5.4 Conclusion

For the first time, a RASSCF approach has been employed to simulate the $M_{4/5}$-edge XANES spectra of actinyls in the +5 oxidation state. To the authors best knowledge, this study represents only the second instance where RASSCF has been used to simulate oxidation-state shifts in XANES due to oxidation state changes and is the first such application to actinides.[15] The resulting XANES profiles and peak assignments align with the available experimental data. A reduction of An(VI) to An(V), leads to a shift of approximately 2 eV, which, although an overestimate compared to experimental observations (0.4 - 0.6 eV),[11, 20, 91, 92] still reflects the correct red-shift behaviour expected from experiment.

The simulation results offer insight into the underlying mechanism driving oxidation-state shifts in XANES spectra due to oxidation state. These shifts can be attributed to the relative stability of the CES attributed to the main absorption edge in An(V) compared

to An(VI). A greater destabilisation of the An(VI) CES compared with the An(V) CES, is due to its higher electron affinity, which stems from an additional Coulomb interaction that raises the states energy. This is inline with the "$Q-U$ explanation" proposed by van der Laan and Kirkman.[98] This destabilisation of the An(VI) CES leads to a larger excitation energy between the GS and CES, and thus the absorption edge appears at higher energy relative to the An(V) actinyls in the $M_{4/5}$-edge spectrum. These findings corroborate the arguments made by Kubin et al.,[15] and provide a framework for understanding the oxidation-state shifts.

The QTAIM analysis of the GS reveals a trend of increasing covalency across the actinyl series for both the +5 and +6 oxidation states and the transition from An(VI) to An(V) is accompanied by a reduction in bond covalency. Upon core-excitation, the resulting CESs present a significant decrease in bond covalency due to the occupation of an anti-bonding orbital which lowers the actinyl bond order. These covalency changes are captured in the δ(An, O) values, which are found to be more sensitive metrics for covalency in this instance.

A variety of orbital composition methods were employed to assess changes in the bonding orbitals between the GS and CESs. For the actinyls in the +6 oxidation state, the π-bonding orbitals remain largely similar between the GS and CESs for uranyl and neptunyl, whereas plutonyl(VI) shows increased An% contributions in the CES. The σ-bonding orbitals are comparable across the GS and CESs for all three actinyl systems. Together the orbital composition results for the actinyl(VI) systems reconfirm the findings from chapter 4. For the actinyls in the +5 oxidation state, the π-bonding orbitals remain similar between the GS and CESs for uranyl(V), but neptunyl(V) and plutonyl(V) exhibit greater An% contributions in the CESs. Conversely, the σ-bonding orbitals in the CESs show reduced An% contributions for all three actinyl(V) systems. Various factors influence the extent to which bonding orbitals differ between the GS and CESs. However, connecting changes within a single orbital to the broader electronic structure variations between the GS and CES remains challenging. In this context, QTAIM analysis offers a more straightforward means for interpreting electronic structure changes. Overall, the results highlight that the validity of XANES as a probe of GS covalency is highly variable and dependent on both the orbitals being probed, the system in question and its oxidation

state.

The relationship between the separation of the $5f_{\delta/\phi}$ and σ_u^* peaks and actinyl covalency was explored in detail. Simulations confirm that the shifts in 5f-σ_u^* peaks serve as qualitative indicators of covalency for a given actinyl system. As for each actinyl, QTAIM data confirms a lower covalency for the reduced species, which correlates with the reduction in 5f-σ_u^* shifts from the +6 to +5 oxidation state. Furthermore, bond length changes were shown to influence these shifts; actinyl(VI) systems set to theoretically derived bond lengths, which are longer than experimental ones, exhibited reduced 5f-σ_u^* shifts, implying weaker covalency. The experimental findings of Vitova et al.[18] which indicated a decreasing actinyl covalency across the series, contrasts with QTAIM results in this chapter, which indicated an increasing covalency for both GS and CESs across the series. To investigate this further, the connection between the 5f-σ_u^* shifts and covalent mixing in the σ_u orbital was analysed using a variety of orbital schemes.

For actinyl(VI) systems, the covalency of the GS σ_u orbital correlates closely with the simulated 5f-σ_u^* shifts, while the CES σ_u orbital covalency aligns strongly with the experimental 5f-σ_u^* shifts. This finding is consistent with the conclusions drawn by Autschbach and co-workers,[27] and seemingly resolves the puzzle, with the experimental shifts reflecting a decreasing σ_u covalency in the CES which mirrors an increasing σ_u covalency in the GS. These findings suggest that the 5f-σ_u^* shifts are indicators of covalency for the σ_u bonding interaction in particular, rather than indicators of actinyl axial covalency as a whole. This could account for the lack of agreement between the 5f-σ_u^* shifts and QTAIM findings, since the metrics used in the latter give measures of covalency through all orbital interactions in the axial An-O bonds and do not specifically target the σ_u interaction. Although no experimental data exists for the reduced actinyl(V) systems, the predicted 5f-σ_u^* shifts follow a similar trend to those observed in actinyl(VI). However, no clear correlation was found between σ_u covalency, either in the An(V) GS or CES, and the predicted 5f-σ_u^* shifts.

In conclusion, the simulations presented in this chapter demonstrate the considerable challenges posed by RASSCF in simulating XANES for open-shell actinide systems. The results of these simulations affirm the robustness of the RAS(SD) methodology utilized across this thesis in providing accurate spectroscopic simulations.

References

[1] P. S. Bagus, B. Schacherl and T. Vitova, *Inorganic Chemistry*, 2021, **60**, 16090–16102, DOI: 10.1021/acs.inorgchem.1c01331.

[2] K. O. Kvashnina and S. M. Butorin, *Chem. Commun.*, 2022, **58**, 327–342, DOI: 10.1039/D1CC04851A.

[3] T. Vitova, J. C. Green, R. G. Denning, M. Löble, K. Kvashnina, J. J. Kas, K. Jorissen, J. J. Rehr, T. Malcherek and M. A. Denecke, *Inorganic Chemistry*, 2015, **54**, 174–182, DOI: 10.1021/ic5020016.

[4] S. M. Butorin, K. O. Kvashnina, A. L. Smith, K. Popa and P. M. Martin, *Chemistry – A European Journal*, 2016, **22**, 9693–9698, DOI: https://doi.org/10.1002/chem.201505091.

[5] S. M. Butorin, A. Modin, J. R. Vegelius, K. O. Kvashnina and D. K. Shuh, *The Journal of Physical Chemistry C*, 2016, **120**, 29397–29404, DOI: 10.1021/acs.jpcc.6b09335.

[6] S. M. Butorin, K. O. Kvashnina, J. R. Vegelius, D. Meyer and D. K. Shuh, *Proc. Natl. Acad. Sci.*, 2016, **113**, 8093.

[7] J. Kolorenč and K. O. Kvashnina, *MRS Advances*, 2018, **3**, 3143–3148, DOI: 10.1557/adv.2018.470.

[8] L. Köhler, M. Patzschke, S. Bauters, T. Vitova, S. M. Butorin, K. O. Kvashnina, M. Schmidt, T. Stumpf and J. März, *Chemistry – A European Journal*, 2022, **28**, e202200119, DOI: https://doi.org/10.1002/chem.202200119.

[9] M. Molinas, R. Faizova, A. Brown, J. Galanzew, B. Schacherl, B. Bartova, K. L. Meibom, T. Vitova, M. Mazzanti and R. Bernier-Latmani, *Environmental Science & Technology*, 2021, **55**, 4753–4761, DOI: 10.1021/acs.est.0c06633.

[10] Z. Pan, Y. Roebbert, A. Beck, B. Bartova, T. Vitova, S. Weyer and R. Bernier-Latmani, *Environmental Science & Technology*, 2022, **56**, 1753–1762, DOI: 10.1021/acs.est.1c06865.

[11] M. Zegke, X. Zhang, I. Pidchenko, J. A. Hlina, R. M. Lord, J. Purkis, G. S. Nichol, N. Magnani, G. Schreckenbach, T. Vitova, J. B. Love and P. L. Arnold, *Chem. Sci.*, 2019, **10**, 9740–9751, DOI: 10.1039/C8SC05717F.

[12] T. Vitova, I. Pidchenko, S. Biswas, G. Beridze, P. W. Dunne, D. Schild, Z. Wang, P. M. Kowalski and R. J. Baker, *Inorganic Chemistry*, 2018, **57**, 1735–1743, DOI: 10.1021/acs.inorgchem.7b02326.

[13] T. Vitova, R. Faizova, J. I. Amaro-Estrada, L. Maron, T. Pruessmann, T. Neill, A. Beck, B. Schacherl, F. F. Tirani and M. Mazzanti, *Chem. Sci.*, 2022, **13**, 11038–11047, DOI: 10.1039/D2SC03416F.

[14] P. Zimmermann, S. Peredkov, P. M. Abdala, S. DeBeer, M. Tromp, C. Müller and J. A. van Bokhoven, *Coordination Chemistry Reviews*, 2020, **423**, 213466, DOI: https://doi.org/10.1016/j.ccr.2020.213466.

[15] M. Kubin, M. Guo, T. Kroll, H. Löchel, E. Källman, M. L. Baker, R. Mitzner, S. Gul, J. Kern, A. Föhlisch, A. Erko, U. Bergmann, V. Yachandra, J. Yano, M. Lundberg and P. Wernet, *Chem. Sci.*, 2018, **9**, 6813–6829, DOI: 10.1039/C8SC00550H.

[16] L. Amidani, M. Retegan, A. Volkova, K. Popa, P. M. Martin and K. O. Kvashnina, *Inorganic Chemistry*, 2021, **60**, 16286–16293, DOI: 10.1021/acs.inorgchem.1c02107.

[17] M. O. J. Y. Hunault, G. Lelong, L. Cormier, L. Galoisy, P.-L. Solari and G. Calas, *Inorganic Chemistry*, 2019, **58**, 6858–6865, DOI: 10.1021/acs.inorgchem.9b00305.

[18] T. Vitova, I. Pidchenko, D. Fellhauer, P. S. Bagus, Y. Joly, T. Pruessmann, S. Bahl, E. Gonzalez-Robles, J. Rothe, M. Altmaier, M. A. Denecke and H. Geckeis, *Nature Communications*, 2017, **8**, 16053, DOI: 10.1038/ncomms16053.

[19] M. O. Hunault, D. Menut and O. Tougait, *Crystals*, 2021, **11**, DOI: 10.3390/cryst11010056.

[20] T. Vitova, I. Pidchenko, D. Schild, T. Prüßmann, V. Montoya, D. Fellhauer, X. Gaona, E. Bohnert, J. Rothe, R. J. Baker and H. Geckeis, *Inorganic Chemistry*, 2020, **59**, 8–22, DOI: 10.1021/acs.inorgchem.9b02463.

[21] L. C. Motta and J. Autschbach, *Nature Communications*, 2023, **14**, 4307, DOI: 10.1038/s41467-023-39626-8.

[22] N. Kaltsoyannis, *Inorganic Chemistry*, 2000, **39**, 6009–6017, DOI: 10.1021/ic000891b.

[23] I. Fryer-Kanssen and A. Kerridge, *Chemical Communications*, 2018, **54**, 9761–9764, DOI: 10.1039/C8CC06088F.

[24] D. Rios, M. del Carmen Michelini, A. F. Lucena, J. Marçalo and J. K. Gibson, *Journal of the American Chemical Society*, 2012, **134**, 15488–15496, DOI: 10.1021/ja305800q.

[25] A. F. Lucena, S. O. Odoh, J. Zhao, J. Marçalo, G. Schreckenbach and J. K. Gibson, *Inorganic Chemistry*, 2014, **53**, 2163–2170, DOI: 10.1021/ic402824k.

[26] N. Kaltsoyannis, *Dalton Trans.*, 2016, **45**, 3158–3162, DOI: 10.1039/C5DT04317D.

[27] D.-C. Sergentu, T. J. Duignan and J. Autschbach, *The Journal of Physical Chemistry Letters*, 2018, **9**, 5583–5591, DOI: 10.1021/acs.jpclett.8b02412.

[28] S. G. Balasubramani, G. P. Chen, S. Coriani, M. Diedenhofen, M. S. Frank, Y. J. Franzke, F. Furche, R. Grotjahn, M. E. Harding, C. Hättig, A. Hellweg, B. Helmich-Paris, C. Holzer, U. Huniar, M. Kaupp, A. Marefat Khah, S. Karbalaei Khani, T. Müller, F. Mack, B. D. Nguyen, S. M. Parker, E. Perlt, D. Rappoport, K. Reiter, S. Roy, M. Rückert, G. Schmitz, M. Sierka, E. Tapavicza, D. P. Tew, C. van Wüllen, V. K. Voora, F. Weigend, A. Wodyński and J. M. Yu, *The Journal of Chemical Physics*, 2020, **152**, 184107, DOI: 10.1063/5.0004635.

[29] C. Adamo and V. Barone, *The Journal of Chemical Physics*, 1999, **110**, 6158–6170, DOI: 10.1063/1.478522.

[30] M. Ernzerhof and G. E. Scuseria, *The Journal of Chemical Physics*, 1999, **110**, 5029–5036, DOI: 10.1063/1.478401.

[31] F. Weigend and R. Ahlrichs, *Phys. Chem. Chem. Phys.*, 2005, **7**, 3297–3305, DOI: 10.1039/B508541A.

[32] W. Küchle, M. Dolg, H. Stoll and H. Preuss, *The Journal of Chemical Physics*, 1994, **100**, 7535–7542, DOI: 10.1063/1.466847.

[33] M. L. Tarlton, O. J. Fajen, S. P. Kelley, A. Kerridge, T. Malcomson, T. L. Morrison, M. P. Shores, X. Xhani and J. R. Walensky, *Inorganic Chemistry*, 2021, **60**, 10614–10630, DOI: 10.1021/acs.inorgchem.1c01256.

[34] A. C. Behrle, A. Kerridge and J. R. Walensky, *Inorganic Chemistry*, 2015, **54**, 11625–11636, DOI: 10.1021/acs.inorgchem.5b01342.

[35] A. C. Behrle, A. J. Myers, A. Kerridge and J. R. Walensky, *Inorganic Chemistry*, 2018, **57**, 10518–10524, DOI: 10.1021/acs.inorgchem.8b00077.

[36] P. Rungthanaphatsophon, K. Stanistreet-Welsh, R. J. Ward, S. P. Kelley, W. W. Lukens, A. Kerridge and J. R. Walensky, *Organometallics*, 2023, **42**, 1404–1410, DOI: 10.1021/acs.organomet.3c00040.

[37] A. Klamt and G. Schüürmann, *J. Chem. Soc., Perkin Trans. 2*, 1993, 799–805, DOI: 10.1039/P29930000799.

[38] J. Olsen, B. O. Roos, P. Jo/rgensen and H. J. A. Jensen, *The Journal of Chemical Physics*, 1988, **89**, 2185–2192, DOI: 10.1063/1.455063.

[39] F. Aquilante, J. Autschbach, A. Baiardi, S. Battaglia, V. A. Borin, L. F. Chibotaru, I. Conti, L. D. Vico, M. Delcey, I. F. Galván, N. Ferré, L. Freitag, M. Garavelli, X. Gong, S. Knecht, E. D. Larsson, R. Lindh, M. Lundberg, P. Å. Malmqvist, A. Nenov, J. Norell, M. Odelius, M. Olivucci, T. B. Pedersen, L. Pedraza-González, Q. M. Phung, K. Pierloot, M. Reiher, I. Schapiro, J. Segarra-Martí, F. Segatta, L. Seijo, S. Sen, D.-C. Sergentu, C. J. Stein, L. Ungur, M. Vacher, A. Valentini and V. Veryazov, *The Journal of Chemical Physics*, 2020, **152**, 214117, DOI: 10.1063/5.0004835.

[40] F. Aquilante, L. D. Vico, N. Ferré, G. Ghigo, P.-å. Malmqvist, P. Neogrády, T. B. Pedersen, M. Pitoňák, M. Reiher, B. O. Roos, L. Serrano-Andrés, M. Urban, V. Veryazov and R. Lindh, *Journal of Computational Chemistry*, 2010, **31**, 224–247, DOI: 10.1002/jcc.21318.

[41] F. Aquilante, J. Autschbach, R. K. Carlson, L. F. Chibotaru, M. G. Delcey, L. D. Vico, I. F. Galván, N. Ferré, L. M. Frutos, L. Gagliardi, M. Garavelli, A. Giussani, C. E. Hoyer, G. L. Manni, H. Lischka, D. Ma, P. Å. Malmqvist, T. Müller, A. Nenov, M. Olivucci, T. B. Pedersen, D. Peng, F. Plasser, B. Pritchard, M. Reiher, I. Rivalta,

I. Schapiro, J. Segarra-Martí, M. Stenrup, D. G. Truhlar, L. Ungur, A. Valentini, S. Vancoillie, V. Veryazov, V. P. Vysotskiy, O. Weingart, F. Zapata and R. Lindh, *Journal of Computational Chemistry*, 2016, **37**, 506–541, DOI: 10.1002/jcc.24221.

[42] B. O. Roos, R. Lindh, P.-Å. Malmqvist, V. Veryazov and P.-O. Widmark, *The Journal of Physical Chemistry A*, 2005, **109**, 6575–6579, DOI: 10.1021/jp0581126.

[43] B. O. Roos, R. Lindh, P.-Å. Malmqvist, V. Veryazov and P.-O. Widmark, *Chemical Physics Letters*, 2005, **409**, 295–299, DOI: 10.1016/j.cplett.2005.05.011.

[44] *The Journal of Physical Chemistry A*, 2004, **108**, 2851–2858, DOI: 10.1021/jp031064+.

[45] A. Wolf, M. Reiher and B. A. Hess, *The Journal of Chemical Physics*, 2002, **117**, 9215–9226, DOI: 10.1063/1.1515314.

[46] B. A. Hess, *Physical Review A*, 1986, **33**, 3742–3748, DOI: 10.1103/PhysRevA.33.3742.

[47] B. A. Hess, *Physical Review A*, 1985, **32**, 756–763, DOI: 10.1103/PhysRevA.32.756.

[48] M. Douglas and N. M. Kroll, *Annals of Physics*, 1974, **82**, 89–155, DOI: 10.1016/0003-4916(74)90333-9.

[49] B. A. Hess, C. M. Marian, U. Wahlgren and O. Gropen, *Chemical Physics Letters*, 1996, **251**, 365–371, DOI: 10.1016/0009-2614(96)00119-4.

[50] V. Sauri, L. Serrano-Andrés, A. R. M. Shahi, L. Gagliardi, S. Vancoillie and K. Pierloot, *Journal of Chemical Theory and Computation*, 2011, **7**, 153–168, DOI: 10.1021/ct100478d.

[51] S. Vancoillie, H. Zhao, V. T. Tran, M. F. A. Hendrickx and K. Pierloot, *Journal of Chemical Theory and Computation*, 2011, **7**, 3961–3977, DOI: 10.1021/ct200597h.

[52] J. Finley, P.-Å. Malmqvist, B. O. Roos and L. Serrano-Andrés, *Chemical Physics Letters*, 1998, **288**, 299–306, DOI: 10.1016/S0009-2614(98)00252-8.

[53] J. P. Zobel, J. J. Nogueira and L. González, *Chemical Science*, 2017, **8**, 1482–1499, DOI: 10.1039/C6SC03759C.

[54] N. Forsberg and P.-Å. Malmqvist, *Chemical Physics Letters*, 1997, **274**, 196–204, DOI: 10.1016/S0009-2614(97)00669-6.

[55] G. Ganguly, D.-C. Sergentu and J. Autschbach, *Chemistry – A European Journal*, 2020, **26**, 1776–1788, DOI: 10.1002/chem.201904166.

[56] D.-C. Sergentu and J. Autschbach, *Dalton Transactions*, 2022, **51**, 1754–1764, DOI: 10.1039/D1DT04075H.

[57] D.-C. Sergentu and J. Autschbach, *Chemical Science*, 2022, **13**, 3194–3207, DOI: 10.1039/D1SC06454A.

[58] R. Polly, B. Schacherl, J. Rothe and T. Vitova, *Inorganic Chemistry*, 2021, **60**, 18764–18776, DOI: 10.1021/acs.inorgchem.1c02364.

[59] P. Å. Malmqvist, B. O. Roos and B. Schimmelpfennig, *Chemical Physics Letters*, 2002, **357**, 230–240, DOI: 10.1016/S0009-2614(02)00498-0.

[60] J. Autschbach, *Comments on Inorganic Chemistry*, 2016, **36**, 215–244, DOI: 10.1080/02603594.2015.1121874.

[61] K. Stanistreet-Welsh, *Molcas2Molden: Molcas INPORB to MOLDEN Convertor*, https://github.com/k-stanistr-wel/Molcas2Molden, 2023.

[62] J. development team, *Jmol: an open-source Java viewer for chemical structures in 3D*, http://www.jmol.org/, 2023.

[63] T. Lu and F. Chen, *Journal of Computational Chemistry*, 2012, **33**, 580–592, DOI: 10.1002/jcc.22885.

[64] Z. Wenli, *Molden2AIM: A utility program which can be used to create AIM-WFN, AIM-WFX, and NBO-47 files from a Molden file*, https://github.com/zorkzou/Molden2AIM, 2023.

[65] T. A. Keith, *AIMAll*, version 19.02.13, TK Gristmill Software, 2019.

[66] F. L. Hirshfeld, *Theoretica chimica acta*, 1977, **44**, 129–138, DOI: 10.1007/BF00549096.

[67] R. S. Mulliken, *The Journal of Chemical Physics*, 1955, **23**, 1833–1840, DOI: 10.1063/1.1740588.

[68] R. S. Mulliken, *The Journal of Chemical Physics*, 1955, **23**, 1841–1846, DOI: 10.1063/1.1740589.

[69] R. S. Mulliken, *The Journal of Chemical Physics*, 1955, **23**, 2338–2342, DOI: 10.1063/1.1741876.

[70] A. D. Becke, *The Journal of Chemical Physics*, 1988, **88**, 2547–2553, DOI: 10.1063/1.454033.

[71] E. W. Stout and P. Politzer, *Theoretica chimica acta*, 1968, **12**, 379–386, DOI: 10.1007/BF00525915.

[72] P. Ros and G. C. A. Schuit, *Theoretica chimica acta*, 1966, **4**, 1–12, DOI: 10.1007/BF00526005.

[73] L. Tian and C. Feiwu, *Acta Chimica Sinica*, 2011, **69**, 2393–2406.

[74] E. D. Glendening, C. R. Landis and F. Weinhold, *Journal of Computational Chemistry*, 2013, **34**, 1429–1437, DOI: https://doi.org/10.1002/jcc.23266.

[75] A. E. Reed and F. Weinhold, *The Journal of Chemical Physics*, 1985, **83**, 1736–1740, DOI: 10.1063/1.449360.

[76] P. J. Hay, R. L. Martin and G. Schreckenbach, *The Journal of Physical Chemistry A*, 2000, **104**, 6259–6270, DOI: 10.1021/jp000519h.

[77] G. A. Shamov and G. Schreckenbach, *The Journal of Physical Chemistry A*, 2005, **109**, 10961–10974, DOI: 10.1021/jp053522f.

[78] S. O. Odoh and G. Schreckenbach, *The Journal of Physical Chemistry A*, 2011, **115**, 14110–14119, DOI: 10.1021/jp207556b.

[79] S. Spencer, L. Gagliardi, N. C. Handy, A. G. Ioannou, C.-K. Skylaris, A. Willetts and A. M. Simper, *The Journal of Physical Chemistry A*, 1999, **103**, 1831–1837, DOI: 10.1021/jp983543s.

[80] G. La Macchia, I. Infante, J. Raab, J. K. Gibson and L. Gagliardi, *Phys. Chem. Chem. Phys.*, 2008, **10**, 7278–7283, DOI: 10.1039/B810744K.

[81] D. Rios, M. C. Michelini, A. F. Lucena, J. Marçalo, T. H. Bray and J. K. Gibson, *Inorganic Chemistry*, 2012, **51**, 6603–6614, DOI: 10.1021/ic3001625.

[82] L. Gagliardi and B. O. Roos, *Inorganic Chemistry*, 2002, **41**, 1315–1319, DOI: 10.1021/ic011076e.

[83] P. G. Allen, J. J. Bucher, D. K. Shuh, N. M. Edelstein and T. Reich, *Inorganic Chemistry*, 1997, **36**, 4676–4683, DOI: 10.1021/ic970502m.

[84] S. D. Conradson, *Applied Spectroscopy*, 1998, **52**, 252A–279A, DOI: 10.1366/0003702981944599.

[85] J. M. Combes, C. J. Chisholm-Brause, G. E. J. Brown, G. A. Parks, S. D. Conradson, P. G. Eller, I. R. Triay, D. E. Hobart and A. Miejer, *Environmental Science & Technology*, 1992, **26**, 376–382, DOI: 10.1021/es00026a020.

[86] R. G. Denning, *The Journal of Physical Chemistry A*, 2007, **111**, 4125–4143, DOI: 10.1021/jp071061n.

[87] S. Matsika and R. M. Pitzer, *The Journal of Physical Chemistry A*, 2000, **104**, 4064–4068, DOI: 10.1021/jp993767q.

[88] S. Matsika, Z. Zhang, S. R. Brozell, J.-P. Blaudeau, Q. Wang and R. M. Pitzer, *The Journal of Physical Chemistry A*, 2001, **105**, 3825–3828, DOI: 10.1021/jp003085z.

[89] B. Schacherl, C. Joseph, P. Lavrova, A. Beck, C. Reitz, T. Pruessmann, D. Fellhauer, J.-Y. Lee, K. Dardenne, J. Rothe, H. Geckeis and T. Vitova, *Analytica Chimica Acta*, 2022, **1202**, 339636, DOI: https://doi.org/10.1016/j.aca.2022.339636.

[90] K. O. Kvashnina, A. Y. Romanchuk, I. Pidchenko, L. Amidani, E. Gerber, A. Trigub, A. Rossberg, S. Weiss, K. Popa, O. Walter, R. Caciuffo, A. C. Scheinost, S. M. Butorin and S. N. Kalmykov, *Angewandte Chemie International Edition*, 2019, **58**, 17558–17562, DOI: https://doi.org/10.1002/anie.201911637.

[91] R. Bès, K. Kvashnina, A. Rossberg, G. Dottavio, L. Desgranges, Y. Pontillon, P. Solari, S. Butorin and P. Martin, *Journal of Nuclear Materials*, 2018, **507**, 145–150, DOI: https://doi.org/10.1016/j.jnucmat.2018.04.046.

[92] G. Leinders, R. Bes, J. Pakarinen, K. Kvashnina and M. Verwerft, *Inorganic Chemistry*, 2017, **56**, 6784–6787, DOI: 10.1021/acs.inorgchem.7b01001.

[93] P. S. Bagus, C. J. Nelin, K. M. Rosso, B. Schacherl and T. Vitova, *Inorganic Chemistry*, 2024, **63**, 1793–1802, DOI: 10.1021/acs.inorgchem.3c03158.

[94] P. Zhang, Y.-X. Wang, P. Zhang, S.-A. Wang and S.-X. Hu, *Inorganic Chemistry*, 2020, **59**, 11953–11961, DOI: 10.1021/acs.inorgchem.0c00535.

[95] S. Bahl, S. Peuget, I. Pidchenko, T. Pruessmann, J. Rothe, K. Dardenne, J. Delrieu, D. Fellhauer, C. Jégou, H. Geckeis and T. Vitova, *Inorganic Chemistry*, 2017, **56**, 13982–13990, DOI: 10.1021/acs.inorgchem.7b02118.

[96] T. Vitova, I. Pidchenko, D. Fellhauer, T. Pruessmann, S. Bahl, K. Dardenne, T. Yokosawa, B. Schimmelpfennig, M. Altmaier, M. Denecke, J. Rothe and H. Geckeis, *Chem. Commun.*, 2018, **54**, 12824–12827, DOI: 10.1039/C8CC06889E.

[97] S. D. Conradson, K. D. Abney, B. D. Begg, E. D. Brady, D. L. Clark, C. den Auwer, M. Ding, P. K. Dorhout, F. J. Espinosa-Faller, P. L. Gordon, R. G. Haire, N. J. Hess, R. F. Hess, D. W. Keogh, G. H. Lander, A. J. Lupinetti, L. A. Morales, M. P. Neu, P. D. Palmer, P. Paviet-Hartmann, S. D. Reilly, W. H. Runde, C. D. Tait, D. K. Veirs and F. Wastin, *Inorganic Chemistry*, 2004, **43**, 116–131, DOI: 10.1021/ic0346477.

[98] G. van der Laan and I. W. Kirkman, *Journal of Physics: Condensed Matter*, 1992, **4**, 4189, DOI: 10.1088/0953-8984/4/16/019.

[99] R. D. Shannon, *Acta Crystallographica Section A*, 1976, **32**, 751–767, DOI: 10.1107/S0567739476001551.

Chapter 6

Conclusion and Outlook

One of the key aims of this thesis was to establish the ability of RASSCF approaches to simulate both O K-edge and actinide $M_{4/5}$-edge XANES. These XANES edges are amongst two of the most commonly used for probing covalency, and in the case of $M_{4/5}$-edge, are also utilised for determining actinide oxidation state. To this end, the thesis successfully presents O K-edge and An $M_{4/5}$-edge XANES simulations for actinyls(VI/V) across the series from uranyl to plutonyl.

In chapter 3, the RAS(SD) methodology was outlined in detail, and is subsquently adapted for use in chapters 4 and 5. The RAS(SD) approach is first shown (chapter 3) in the simulation of O K-edge for uranyl using progressively more representative models of the $Cs_2UO_2Cl_4$ crystal used in the experiment reported by Denning et al.[1] Models included $[UO_2]^{2+}$, $[UO_2Cl_4]^{2-}$, and a $Cs_2UO_2Cl_4$ point-charge model. While the $[UO_2Cl_4]^{2-}$ model lead to a simulated spectrum with predicted peaks and relative separations that most accurately aligned with experiment, all three models were sufficient in generating the correct three peak spectral profile in the targeted 530-545 eV region to within 1.5 eV of experiment. The process of assigning simulated peaks to a particular core-excitation was outlined in detailed, with the simulated O K-edge assignments aligning with those of previous studies. Chapter 3 highlights how XANES peaks can be comprised of multiple transitions making assignment to a single core-excitation challenging. Additionally, the core-excited states themselves present highly multiconfigurational character manifesting as substantial electron re-distribution from the bonding orbitals to the anti-bonding orbitals, and is found to increase at higher excitation energy. This feature appears to persist

across actinyl simulations performed in the studies that comprise this thesis, in both O K-edge and An $M_{4/5}$-edge simulations, suggesting that this may be a general feature of the RAS(SD) methodology. Results also indicate that the core-excitation transition strength may not be directly linked to the amount of oxygen 2p-character in the anti-bonding orbital but rather rely more on the larger overall changes in electronic structure between the GS and CESs. While this was only investigated for uranyl O K-edge simulations, this finding could also hold true in the other systems and in additional edges.

In chapter 4, an additional set of O K-edge simulations were performed using $[AnO_2]^{2+}$ models set to experimental bond lengths for actinyls ranging from uranyl to plutonyl. Unlike uranyl, the simulations of neptunyl and plutonyl represent predictions that await experimental verification. The same features from the spectral profile of the uranyl O K-edge spectrum appear for neptunyl and plutonyl, but peaks broaden across the series due to an increased density of states made possible by partially occupied non-bonding 5f-orbitals. In this chapter, An $M_{4/5}$-edge XANES simulations are introduced with the aim of replicating the experimental spectra reported by Vitova et al.[2] Using experimentally informed bond lengths, An $M_{4/5}$-edge XANES simulations for $[AnO_2]^{2+}$ models generated spectra with relative peak separations to within 1 eV of experiment.

In the final results chapter (chapter 5), simulations of An $M_{4/5}$-edge XANES were continued but on An(VI) and An(V) $[AnO_2]^{2+/+}$ models with bond lengths set to those from DFT optimised $[AnO_2(H_2O)_5]^{2+/+}$ systems, which are expected to form in the aqueous conditions typically used in experiments. No direct comparison with experiment was made since no An $M_{4/5}$-edge spectra have been reported for a consistent set of actinyl(V) systems. The results from this chapter demonstrate the capability of RASSCF to correctly simulate the expected red-shift behaviour of XANES spectra due to a reduction of An(VI) to An(V) in a given actinyl system. To the authors best knowledge, this is only the second instance of RASSCF predicting a XANES oxidation-state shift and the first instance of doing so for An $M_{4/5}$-edge XANES. The shift was rationalised by the relative stability of the CESs, with a higher An(VI) CES resulting from an additional Coulomb interaction that raises its state energy, and as a result, increases the excitation energy compared with the An(V) system. Hence, the An(VI) absorption edge appears at higher excitation energies in the $M_{4/5}$-edge XANES spectra compared to An(V).

QTAIM analysis across the three different chapters offers insight into the nature of covalency in the actinyls. Across the actinyl series, both in the +6 and +5 oxidation states, QTAIM metrics point to an increasing bond covalency. Alternatively, the reduction of actinyls from An(VI) to An(V) leads to a lowering of the bond covalency as was to be expected when adding an additional electron to the system. Regardless of the XANES edge simulated, upon core-excitation, actinyl covalency decreases in the CES since the occupation of an anti-bonding orbital lowers the overall An-O bond order. The greatest reductions in covalency between the GS and CESs is found for those states which exhibit the most substantial multiconfigurational character, since in these states, significant re-distribution of electrons from the bonding orbitals to the anti-bonding orbitals occurs and decreases the bond order. These findings come from examining the changes in delocalisation index, which were found to be the most sensitive metric for quantifying changes in covalency. While electron sharing in the An-O bonds is reduced in both the O K-edge and An $M_{4/5}$ -edge CESs, the localisation of electrons differs. In O K-edge CESs, the electrons localise onto all three atomic centres, while for An $M_{4/5}$ -edge CESs, localisation occurs primarily onto the actinide centre. The difference in electron localisation is attributed primarily to the location of the core-hole and its influence on charge density.

The validity of ligand K-edge and actinide $M_{4/5}$-edge XANES as GS covalency probes relies on the assumption that the bonding orbitals in the probed CES and GS do not differ in composition due to orbital relaxation. As such, the second aim of this thesis was to establish if XANES is a valid probe of GS actinyl covalency. In chapters 3 and 4, orbital composition analysis was utilised to examine bonding orbitals in the GS and O K-edge CESs for the $[AnO_2]^{2+}$ systems. In both chapters, a reduction in actinide contribution to the actinyl bonding orbitals in the CESs of up to 13% was calculated using the AIM method. This represents an underestimation of the actinide contribution to GS covalency when probing CESs via O K-edge XANES. This underestimation remains even in the case whereby a more representative model of experiment is utilised, such as in the $Cs_2UO_2Cl_4$ model used for chapter 1, which returned a reduction in An% contribution to the bonding orbitals of up to 7%.

In chapters 4 and 5, orbital composition analysis of the GS and An $M_{4/5}$-edge CESs

was performed. For actinyl(VI) systems, the bonding orbitals are found to be largely comparable between the GS and CESs for uranyl and neptunyl. In plutonyl, the An% contribution to the bonding orbitals is up to 5% greater in the CESs when using the AIM method. This represents an overestimation of the actinide contribution to GS covalency when probing CESs in $M_{4/5}$-edge spectra. The orbital composition results across chapters 3 to 5 for both the O K-edge and An $M_{4/5}$-edge simulations provides an upper and lower bound to the actual actinide contribution to GS bonding orbitals, An_{GS}%, compared to the measured contribution from either edge $An_{K\text{-}/M\text{-edge}}$% as follows: $An_{K\text{-edge}}\% \leq\leq An_{GS}\% \leq An_{M\text{-edge}}\%$. In actinyl(V) systems, results indicate that the An% contribution to the π_u- and σ_u-bonding orbitals will be overestimated in the former and underestimated in the latter, when probing the respective CESs via XANES. While various qualitative factors are thought to influence the changes in bonding orbitals between the GS and CESs, connecting changes within a single orbital to the broader electronic structure variations between the GS and CES remains challenging.

The relative separation of peaks in An $M_{4/5}$-edge XANES spectra have been utilised as indicators of covalency rather than peak intensity. An investigation as to whether a relationship can be established between the axial bond covalency and the relative separation of the $5f_{\delta/\phi}$ and 5f-σ_u^* peaks was performed. Due to the influence of the 'pushing from below' mechanism, an enhancement of 5f-covalency in the σ_u bonding orbital comes along with a destabilisation of the σ_u^* orbital, which manifests in the XANES spectrum as a larger peak separation (larger 5f-σ_u^* shift). In chapter 5, it is found that for a given actinyl system, the 5f-σ_u^* shift is a valid indicator of changes to GS covalency due to oxidation state or a change in bond length. Across the actinyl series, the experimental 5f-σ_u^* shifts are found to correlate best with the σ_u-covalency in the CES, which finds agreement with a previous theoretical study by the Autschbach and co-workers.[3] However, the simulated 5f-σ_u^* shifts were found to correlate best with the covalency trends of the GS σ_u orbital, while no correlation could be established for actinyl(V) systems. Examining the covalency trends outlined by QTAIM analysis and those of the 5f-σ_u^* shifts, it is concluded that the the 5f-σ_u^* shifts are indicators of σ_u orbital covalency specifically, and are not general indicators of overall bond covalency. To improve the detail of results, future studies could focus on the application of symmetry decomposed QTAIM, which could enable the

targeting of the specific bonding interactions that contribute most to covalent bonding.

The RASSCF method outlined in this thesis can be adapted to other systems of interest. To date, RASSCF XANES simulations have been performed for actinide sandwich complexes and actinide hexachloride systems with active spaces similar in size to those used in this thesis. Ultimately, given the costs associated with RASSCF calculations, XANES simulations using these approaches will be constrained to systems with high symmetry and those with reasonable valance spaces that be encompassed by the active-space without increasing the number of orbitals and active electrons too far beyond what has been achieved in this thesis (18 orbitals, 16 electrons). To extend these simulations to a more broad set of systems, an option is to apply minimal structural alterations to low symmetry systems to increase their symmetry as was done in chapter 3 for the $Cs_2UO_2Cl_4$ crystal. For more complex and larger systems, a compromise for applying RASSCF simulations could be to perform them on an idealized versions of the central unit of interest, with larger ligand structure removed to give an approximate XANES spectrum that captures the key core-excitation processes. However, this would come at the cost of accurate prediction of peak positions. Whilst actinide systems have been focused upon in this thesis, these approaches can also be readily applied to lanthanide and transition metal complexes as well as organic chemistry molecules.

In conclusion, the research presented in this thesis has laid a foundation from which to apply the RASSCF methodology and analysis schemes to different actinide systems of varying covalency. To date, RASSCF XANES studies have focused on systems where the actinide centre changes but the ligands remain the same, leaving an obvious gap in the literature that requires filling. An additional avenue would be to explore simulating different XANES edges apart from K- and M-edges, since L-edge is also readily used in experiment. Future work could also adapt the current RASSCF methodologies for XANES simulations, to instead simulate resonant inelastic X-ray spectroscopy (RIXS) since more experimental high-resolution XANES spectra tend to be obtain from RIXS experiments and would enable more direct comparison between simulation and experiment. Finally, the RASSCF approach outlined in this thesis is highly adaptable, and could equally be applied to other types of spectroscopy that access the core-excited state.

References

[1] R. G. Denning, J. C. Green, T. E. Hutchings, C. Dallera, A. Tagliaferri, K. Giarda, N. B. Brookes and L. Braicovich, *The Journal of Chemical Physics*, 2002, **117**, 8008–8020, DOI: 10.1063/1.1510445.

[2] T. Vitova, I. Pidchenko, D. Fellhauer, P. S. Bagus, Y. Joly, T. Pruessmann, S. Bahl, E. Gonzalez-Robles, J. Rothe, M. Altmaier, M. A. Denecke and H. Geckeis, *Nature Communications*, 2017, **8**, 16053, DOI: 10.1038/ncomms16053.

[3] D.-C. Sergentu, T. J. Duignan and J. Autschbach, *The Journal of Physical Chemistry Letters*, 2018, **9**, 5583–5591, DOI: 10.1021/acs.jpclett.8b02412.